NUMERICAL MODELLING OF PARTICULATE AND FIBRE REINFORCED COMPOSITES

A thesis submitted for

the degree of Doctor of Philosophy

by

Matthew G. Knight, BEng (Hons)

Department of Mechanical Engineering

Brunel University, UK.

September 2002

Abstract

This thesis presents research into the micromechanical modelling of composite materials using numerical techniques. Composite materials are generally examined from two points of view: macromechanics and micromechanics, owing to their inherent heterogeneous nature. In this research, the material behaviour is examined on a microscopic scale, as the properties of interest, i.e. strength and toughness, are dependent on local phenomena. In general, the strength and toughness of composite materials are not as well understood as the simpler elastic properties, because in many cases the modes of failure under a given system of external load are not predictable in advance.

Previous research in this field has typically involved specially designed experiments, theoretical/statistical studies, or the use of numerical models. In this study, advanced implementations of numerical methods in continuum mechanics, i.e. the boundary element and the finite element methods are employed to gain a greater understanding of composite behaviour. The advantage of using numerical methods, as opposed to experimental studies, is that the geometric and material characteristics can be investigated parametrically, in addition to the reduced time and expense involved. However, to model the complete behaviour of real composites is still not possible, due to the degree of complexity and uncertainty involved in modelling the various mechanisms of damage and failure, etc. and also due to the immense computational cost. Therefore, simplified models must be employed which are limited by their assumptions.

For the preliminary studies within this thesis, geometrically simplified models are presented to provide an understanding of the influence of embedding second phase inclusions on the local stress fields, and also to validate the numerical techniques with readily available analytical solutions. These models are then extended to accommodate additional phenomena, such as inclusion interaction, spatial inclusion arrangement, material formulation, i.e. consisting of two- and three-phases of various material properties. The influence of such factors on the local stress concentrations, which play an important role in determining the strength of the composite, is analysed through a series of parametric studies. The localised toughening of composites is also considered through novel investigations into the interaction between a propagating crack with inclusions and microcracks.

Through the development of the numerical models a more realistic representation of composite behaviour is achieved, which in turn, provides an improved knowledge of the factors that control strength and toughness. Such information is invaluable to composite material designers, who presently rely heavily on experimental studies to develop composite materials.

List of Publications

- **Knight, M. G., de Lacerda, L. A., Wrobel, L. C.** and **Henshall, J. L.** (2002a), Parametric study of the contact stresses around spherical and cylindrical inclusions, *Computational Materials Science*, **25**, 115-121.

- **Knight, M. G., de Lacerda, L. A., Wrobel, L. C.** and **Henshall, J. L.** (2002b), A parametric study of inclusion interaction in particulate- and fibre-reinforced materials using the boundary element technique, *Journal of Strain Analysis*, **37**, 47-58.

- **Knight, M. G., Wrobel, L. C.** and **Henshall, J. L.** (2002c), Micromechanical response of fibre-reinforced materials using the boundary element technique, *Submitted for publication*.

- **Knight, M. G., de Lacerda, L. A., Wrobel, L. C.** and **Henshall, J. L.** (2002d), A study of the interaction between a propagating crack and an uncoated/coated elastic inclusion using the BE technique, *International Journal of Fracture*, **114**, 47-61.

Acknowledgements

I would like to express my sincere gratitude to Prof. Luiz C. Wrobel, Prof. John L. Henshall and Dr. Luiz A. de Lacerda for their guidance, incentive and support during the period of my research. The Engineering and Physical Sciences Research Council (EPSRC) are gratefully acknowledged for their financial support.

I am also very grateful to my fiancée, Samantha for her tireless love and encouragement. Finally, I must thank my daughter Leila for giving me many sleepless nights, but also many days of joy.

Table of Contents

List of Notation

Some of the key variables used in this report are listed below. Where appropriate, some symbols may have more than one meaning.

Italic and Mathematical Symbols

a_o	Initial crack length
$[A]$	Matrix containing the integrals of T_{ij}
$[A^*]$	Modified form of $[A]$
$[B]$	Matrix containing the integrals of U_{ij}
$C_{ij}(P)$	Matrix of constants dependent on the geometry at the boundary point P
$[c]$	Vector composed from the prescribed nodal values multiplied by their corresponding influence coefficients
d	Inter-fibre/particle separation distance (ligament thickness), or the crack offset from the centreline
D	Normalised distance from the central inclusion towards the neighbouring inclusion
$D_{kij}(P,Q)$	Third-order tensor multiplying the traction vector
E	Young's modulus
f_i	Body force vector
$[F]$	External force vector
G	Energy release rate at the crack tip
G_i	Galerkin vector
H, L	Numerical model dimensions
k	Bulk modulus
K	Stress concentration factor
K_c	Fracture toughness
K_I, K_{II}, K_{III}	Stress intensity factor for fracture modes I, II, III
$[k]$	Stiffness matrix
n	Unit outward normal at the boundary
p	Load point inside the solution domain
P	Load point moved to the boundary
q	Field point inside the solution domain
Q	Field point moved to the boundary
r	Radius of the central inclusion, or the radius of the inclusions (general)
r, θ, z	Cylindrical coordinate system
R	Radius of the neighbouring inclusions
$r(p,q)$	Distance between points p and q
$r(p,Q)$	Distance between points p and Q
$S_{kij}(P,Q)$	Third-order tensor multiplying the displacement vector
t	Inclusion coating thickness

t_i	Traction vector
$t_i\,(Q)$	Tractions along the boundary of the real problem
$T_{ij}\,(p,Q)$	Kelvin (fundamental) traction tensor
$[t]$	Matrix containing the tractions of the real problem
u_i	Displacement vector
$u_i\,(Q)$	Displacements along the boundary of the real problem
$U_{ij}\,(p,Q)$	Kelvin (fundamental) displacement tensor
$[u]$	Matrix containing the displacements of the real problem
V_f	Volume fraction of inclusions
x, y, z	Cartesian coordinate system
$[x]$	Vector containing a mixture of unknown displacements and tractions

Greek Symbols

α	Thermal expansivity
α, β	Constants depending on the material properties of the two phases
α, β, γ	Three parameters of the Weibull reliability function
δ	Angle between a plane containing the two fibre centres and the applied load
δ_{ij}	Kronecker delta function
$[\delta]$	Displacement vector
ε_{ij}	Strain components
γ_{ij}	Shear strain components
η	Contact angle
θ	Crack-tip propagation angle
φ, θ	Angles along the interface of the inclusion
μ	Shear modulus of the particular phase, or the friction coefficient
ρ	Density
σ_*	Tensile strength
σ_{ij}	Stress components
σ_o	Externally applied stress
τ_{ij}	Shear stress components
υ	Poisson's ratio
ξ	Adjustable parameter (Halpin-Tsai expression)

Sub- and Superscripts

c	Central inclusion
f	Fibre phase
i	Inclusion phase (general)
m	Matrix phase, or the element number
n	Neighbouring inclusion
n, t	Surface normal and tangential directions, respectively
*	Effective properties of the multiphase material

Chapter 1: Introduction

1.1 Background

There are many situations in engineering where no single material will be suitable to meet a particular design requirement. However, by combining two (or more) materials enhanced mechanical properties can be achieved, and hence, provide a feasible solution to the materials-selection problem. In this context, such multiphase materials are known as *composites*. An overview of composite classification, material combinations, physical properties, benefits and micromechanics is discussed in Chapter 2.

Industrial Sector	*Examples*
Aerospace	wings, fuselage, antennae, helicopter blades, landing gears, seats, floors, interior panels, fuel tanks, rocket motor cases, nose cones, launch tubes
Automobile	body panels, cabs, spoilers, consoles, instrument panels, lamp-housings, bumpers, leaf springs, drive shafts, gears, bearings
Boats	hulls, decks, masts, engine shrouds, interior panels
Chemical	pipes, tanks, pressure vessels, hoppers, valves, pumps, impellers
Domestic	interior and exterior panels, chairs, tables, baths, shower units, ladder
Electrical	panels, housings, switchgear, insulators, connectors
Leisure	motor homes, caravans, trailers, golf clubs, racquets, protective helmets, skis, archery bows, surfboards, fishing rods, canoes, pools, diving boards, playground equipment.

Table 1.1 Some applications of polymer matrix composites, *Matthews and Rawlings (1994).*

Composites make up a very broad and important class of engineering materials, which are used in a wide variety of applications. Some of the main applications are within the aerospace, transportation, electrical, medical and leisure industries (see Table 1.1). For example, aircraft engineers are increasingly searching for structural materials that have low density, are strong, stiff, abrasion and impact resistant, and are not easily corroded. Figure 1.1 illustrates the use of composites in the construction of the latest versions of the

Harrier aircraft, giving rise to a 25% weight saving in the airframe compared to an all-metal construction (*Kelly (1994)*).

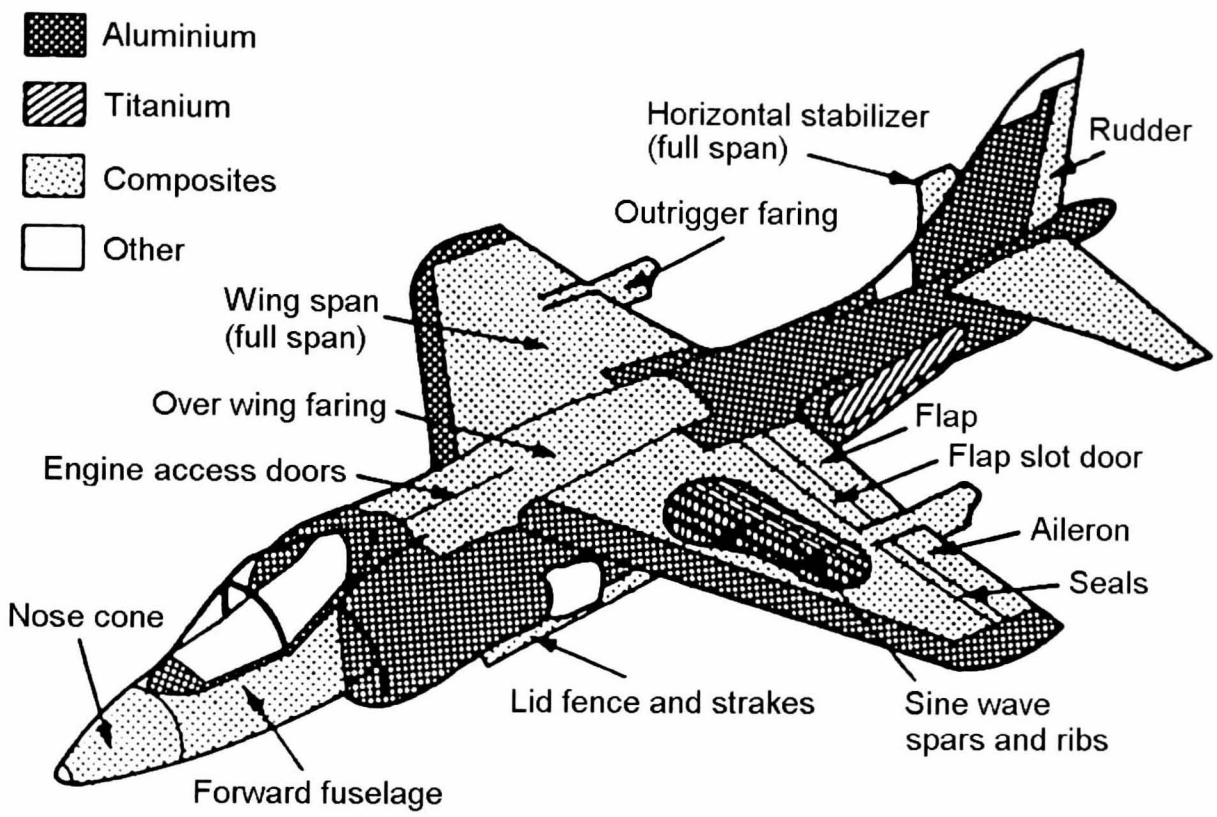

Figure 1.1 A diagram showing the types of materials and their locations within the AV-8B Harrier aircraft, *Kelly (1994)*.

Over the past century, there has been considerable research on the analysis and prediction of the mechanical properties of such materials. The standard lower and upper bound rule of mixture estimates form the most widely used analytical approach for estimating the bulk properties of composite materials. This approach, with minor phenomenologically based modifications, such as for example *Halpin and Tsai (1967)*, can be used to predict with reasonable accuracy the Young's and shear moduli of the material under perfect bonding conditions between the inclusion and matrix. This approach generally provides reasonable estimates of the moduli, but there will be inaccuracies to a greater or lesser extent. These can result from, for example, the presence of an interphase, which may develop during manufacture due to chemical reactions between the contacting fibre and matrix material, or such effects as crenulation and debonding.

The predictions of other bulk properties of these materials, such as strength and toughness, are subject to much greater variability. In general, the solution to complex stress analysis problems involves the use of a numerical method of continuum mechanics, such as the Finite Element (FE) or Boundary Element (BE) approach. (An overview of the FE and BE numerical techniques is presented in Chapter 3.) Nevertheless, at present it is still not possible to numerically simulate the complete behaviour of real composites, due to the degree of complexity and uncertainty involved in modelling the various mechanisms of damage and failure, etc. and also due to the immense computational time and resources required.

1.2 Aims and Objectives

The research presented in this thesis concentrates on the implementation of numerical methods to investigate the micromechanical response of composite materials. The purpose of this study is to provide an improved knowledge of the influence of reinforcement architecture, material properties of the phases, and interfacial conditions between the constituents on the local behaviour. Based on such information a greater understanding of the factors that control composite strength and toughness can be assessed, with a view to designing composite materials with improved physical properties. Therefore, less experimental work would then be required to develop materials with properties that are more closely optimised for the particular specification required.

For the preliminary studies, geometrically simple models will be presented to provide an understanding of the influence of embedding second phase inclusions on local stress fields, and to allow validation of the numerical methods with readily available analytical solutions. Two numerical techniques are employed within the following study, i.e. the BE approach, in the form of an in-house developed Boundary Element Analysis program, and the FE method, using a commercial Finite Element Analysis software package (ANSYS).

The various models will then be extended to accommodate additional phenomena, such

as inclusion interaction, spatial inclusion arrangement and material composition, i.e. consisting of two- and three-phases of various material properties. The influence of such factors on the local stress concentrations, which plays an important role in determining the strength of the composite, will be considered through a series of parametric studies. In addition, the interaction between a propagating crack with inclusions and microcracks will also be investigated in terms of localised toughening mechanisms.

Through the development of the numerical models a more realistic representation of the behaviour of composites is anticipated. Information from such models will hopefully be invaluable to composite material designers, who presently rely heavily on relatively expensive experimental work to develop composite materials.

1.3 Summary of Thesis

The thesis consists of nine chapters. After this introductory chapter, Chapter 2 presents an overview of composite materials, in terms of classification, possible material combinations, physical properties, benefits and finally a comprehensive review of published micromechanical modelling techniques and theory. In Chapter 3, the two most popular numerical techniques in continuum mechanics, namely finite element and boundary element methods, are briefly reviewed, followed by a comparison between the two approaches. Lastly, an in-house developed boundary element analysis program suitable for both two-dimensional (plane strain and plane stress) and axisymmetric, linear-elastic problems, involving contact (conforming or non-conforming, frictionless or frictional) and fracture (stationary or propagating) is described. This program is implemented within the next five chapters.

Chapter 4 analyses the interfacial stresses around a single, circular inclusion embedded within a remotely stressed matrix, using the FE and BE techniques. Two interfacial conditions are considered, i.e. fully bonded or non-bonded. From such work a thorough understanding of the significance of second phase inclusions on the localised stress distributions is realised, for a range of controlling factors. In addition, as analytical

solutions are readily available for such problems, the accuracy and reliability of the BEA program can be verified.

Chapter 5 extends the work of the previous chapter and studies the effect of inclusion interaction within a composite model, using the FE and BE methods. The localised stress distributions are calculated around an embedded inclusion within a matrix, which is affected by the presence of two further inclusions, one on either side. Once again, two interfacial conditions are considered, i.e. fully bonded or non-bonded. From this research the importance of inclusion interaction is highlighted.

Chapter 6 analyses the transverse tensile response of a unidirectional composite, using the BE approach, where the effects of fibre distribution and constituent material properties are parametrically examined. Numerical simulations include several simple geometric arrangements, i.e. idealised square and hexagonal placed fibres. These models are then extended to accommodate random distributions, so that the effects of fibre clustering on the localised stress distributions could be investigated.

Chapter 7 studies the interaction between a propagating crack and an uncoated or coated inclusion, using the BE method. Crack tip energetics and trajectory are analysed for a range of controlling factors, with the aim of maximising the localised toughening effect, i.e. crack deflection process, in a composite.

Chapter 8 extends the work of the previous chapter and studies the effect of inclusion interaction and localised microcracking within a unidirectional composite, using the BE technique. Two typical composite materials, i.e. glass fibre reinforced polyester and carbon fibre reinforced epoxy, and also a glass-carbon hybrid composite are analysed. Crack tip energetics and local stress fields are considered, with emphasis on the toughening processes.

The final chapter, Chapter 9, presents the conclusions drawn as a result of the research presented herein. In addition, recommendations for further development of the research

are discussed.

Chapter 2: Composite Materials

2.1 Introduction

In the continuing quest for improved performance, which may be specified by various criteria including reduced weight, increased strength and lower cost, currently used materials frequently reach the limit of their usefulness. Thus, material scientists and engineers are always striving to produce either improved traditional materials or completely new materials. Composites are an example of the latter category.

The principle of composite materials is not new, they have a long history of usage. For example, straw was used by the Israelites to strengthen mud bricks and plywood was used by the Egyptians when they realised that wood could be rearranged to achieve superior strength and resistance to thermal expansion, as well as to swelling caused by the absorption of moisture. More recently, concrete (a mixture of gravel held together by mortar) has become a versatile and familiar building material. In addition to these synthetic composites there are naturally occurring composites, of which the best-known examples are wood and bone. Wood can be considered to consist of fibrous chains of cellulose in a matrix of lignin, while bone is essentially a composite containing hard inorganic crystals (osteones) in an organic matrix called collagen.

Within the last forty years there has been a rapid increase in the production of synthetic composites. The spur to this expansion was the development in the UK of carbon fibres and in the USA of boron fibres in the early 1960s. These new fibres, which have high elastic constants, gave a significant increase in the stiffness of composites over well-established glass fibre containing materials, and hence made possible a wide range of applications for composites. One of the key factors was the very high strength-to-weight and stiffness-to-weight ratios possessed by these new composites. Similarly, the development of high strength silicon carbide (SiC), and alumina (Al_2O_3) fibres, which maintain their properties at elevated temperatures, initiated much of the current interest in

composites based on metals and ceramics, *Matthews and Rawlings (1994)*.

2.2 Definitions and Classification

As stated in Section 1.1, a composite is a mixture of two or more distinct 'constituents' or 'phases'. However, this definition is not sufficient and three other criteria have to be satisfied before a material can be said to be a composite. First, both constituents have to be present in reasonable proportions, say greater than 5%. Secondly, it is only when the constituent phases have different properties, and hence the composite properties are noticeably different from the properties of the constituents, that we have come to recognise these materials as composites. Lastly, conventionally the constituent phases must be combined physically with the proviso that they are separated by a distinct interface. Thus, most metallic alloys and many ceramics do not fit this definition because their multiple phases are formed as a consequence of heat treatment or similar process.

Many composite materials are composed of just two phases. The constituent that is continuous, and is often but not always, present in the greater quantity in the composite, is termed the 'matrix phase'. The normal view is that it is the properties of the matrix that are improved on incorporating another constituent to produce a composite. A composite may have a ceramic, metallic or polymeric matrix, depending on the application and physical properties required. The mechanical properties of these three classes of material differ considerably as demonstrated in Table 2.1. As a generalisation, polymers have low strengths and Young's moduli, ceramics are strong, stiff and brittle, and metals have intermediate strengths and moduli together with good ductilities, i.e. they are not brittle.

The second constituent is referred to as the 'reinforcing phase' or 'reinforcement', as it enhances or reinforces the mechanical properties of the matrix. In most cases the reinforcement is harder, stronger and stiffer than the matrix, although there are some exceptions; for example, ductile metal reinforcement in ceramic and rubberlike reinforcement in a brittle polymer matrix. The properties exhibited by various types of

reinforcement are presented in Table 2.2.

Matrix	Density ρ (Mg/m^3)	Young's modulus E (GPa)	Poisson's ratio υ	Tensile strength σ_* (GPa)	Thermal expansivity α $(10^{-6}\,K^{-1})$
CERAMICS					
Silicon Carbide, SiC	3.4	400	0.20	0.4	4
Alumina, Al_2O_3	3.8	380	0.25	0.5	8
METALS					
Aluminium, Al	2.7	70	0.33	0.2-0.6	24
Magnesium, Mg	1.8	45	0.35	0.1-0.3	27
Titanium, Ti	4.5	110	0.36	0.3-1.0	9
POLYMERS					
Epoxy resin	1.1-1.4	3-6	0.38-0.40	0.035-0.1	60
Polyester	1.2-1.5	2.0-4.5	0.37-0.39	0.04-0.09	100-200
Nylon 6.6	1.14	1.4-2.8	0.30	0.06-0.07	90
Polypropylene	0.90	1.0-1.4	0.30	0.02-0.04	110

Table 2.1 Selected properties for different types of matrix. (Adapted from *Hull and Clyne (1996)*)

Reinforcement (fibrous)	Density ρ (Mg/m^3)	Young's modulus E (GPa)	Poisson's ratio υ	Tensile strength σ_* (GPa)	Thermal expansivity α $(10^{-6}\,K^{-1})$
SiC, monofilament	3.0	400	0.20	2.4	4.0
Boron, monofilament	2.6	400	0.20	4.0	5.0
High modulus (HM) carbon	1.95	axial 380 radial 12	0.20	2.4	axial –0.7 radial 10
High strength (HS) carbon	1.75	axial 230 radial 20	0.20	3.4	axial –0.4 radial 10
E-glass	2.56	76	0.22	2.0	4.9
Nicalon™	2.6	190	0.20	2.0	6.5
Kevlar™ 49	1.45	axial 130 radial 10	0.35	3.0	axial –6 radial 54

Table 2.2 Selected properties for different types of reinforcements. (Adapted from *Hull and Clyne (1996)*)

Composites can be classified into three main categories – particulate, fibre and laminar, based on the shapes of the materials. Concrete, a mixture of mortar and gravel, is a particulate composite; fibreglass, containing glass fibres embedded in a polymer, is a fibre-reinforced composite; and plywood, having alternating layers of wood veneer, is a laminar composite (Figure 2.1).

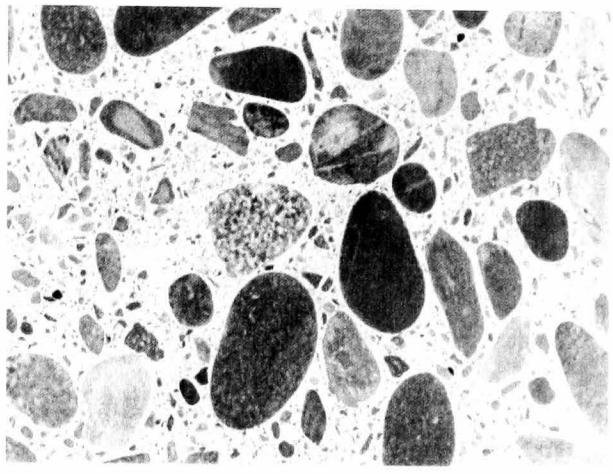

(a)

(b)

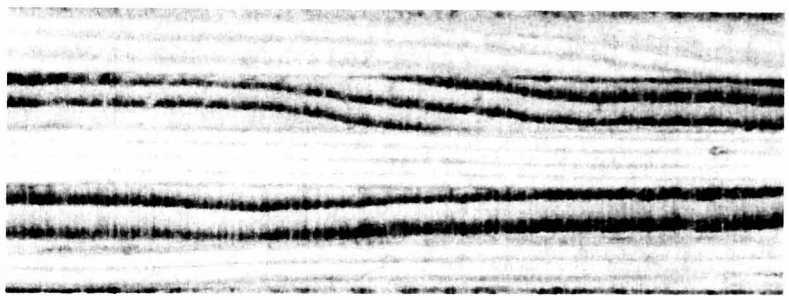

(c)

Figure 2.1 **Some samples of composite materials: (a) Concrete is a particulate composite containing gravel in a cement matrix (reduced 50%). (b) Fibreglass is a fibre-reinforced composite containing glass fibres in a polymer matrix (x300). (c) Plywood is a laminar composite of layers of wood veneer (x3),** ***Askeland (1996).***

Particulate reinforcements have dimensions that are approximately equal in all directions. The shape of the reinforcing particles may be spherical, cubical (or cuboid), platelet or any regular or irregular geometry. The arrangement of the particulate reinforcement may be random or with a preferred orientation. In the majority of particulate reinforced composites the orientation of the particles is considered, for practical proposes, to be

random (Figure 2.2(a)).

A fibrous reinforcement is characterised by its length being much greater than its cross-sectional dimension. However, the ratio of length to the cross-sectional dimension, known as the aspect ratio, can vary considerably. High aspect ratio, long fibre composites are termed 'continuous', whereas composites fabricated using short fibres of low aspect ratio are termed 'discontinuous'. The orientation of the discontinuous fibres may be preferred or random (Figures 2.2(b) and (c)), while continuous fibre composites are generally aligned in either one or two directions, termed 'unidirectional' (Figure 2.2(d)) or 'woven mat' respectively.

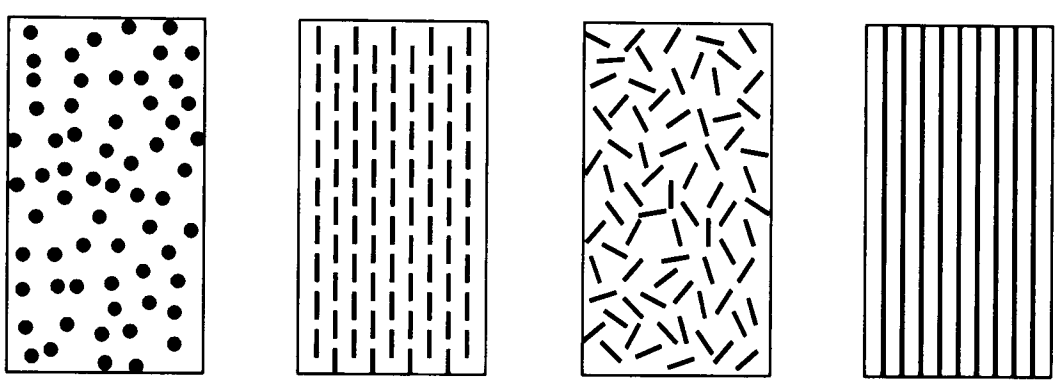

(a) (b) (c) (d)

Figure 2.2 Examples of composites: (a) particulate, random; (b) discontinuous fibres, unidirectional; (c) discontinuous fibres, random; (d) continuous fibres, unidirectional. (*Matthews and Rawlings (1994)*)

A laminar composite is composed of two dimensional sheets or panels that have a preferred high-strength direction such as is found in wood and continuous and aligned fibre-reinforced composites. The layers are stacked and subsequently cemented together such that the orientation of the high-strength direction varies with each successive layer. For example, adjacent wood sheets in plywood are aligned with the grain direction at right angles to each other. Laminations may also be constructed using fabric material such as cotton, paper, or woven glass fibres embedded in a plastic matrix.

In addition to the aforementioned three main types of composites, other important types of composite exist, e.g. sandwich structures. Sandwich materials consist of two strong outer sheets, or faces, separated by a layer of less-dense material, or core. An important example is the honeycomb structure used in aircraft applications (Figure 2.3). Bonding thin aluminium strips at selected locations and then expanding produces a very low-density, honeycomb shaped, cellular panel that, by itself, is unstable. However, when an aluminium facing sheet is adhesively bonded to either side of the honeycomb a very stiff, rigid, strong, and exceptionally lightweight sandwich panel is obtained.

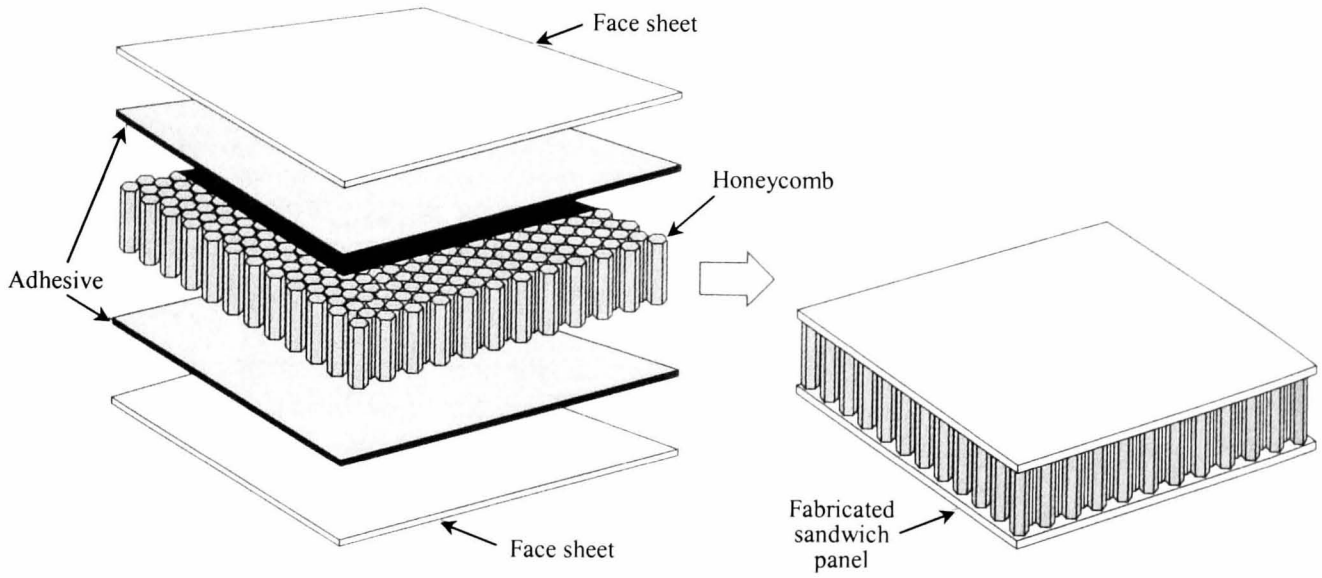

Figure 2.3 Schematic diagram showing the construction of a honeycomb core sandwich panel, *Callister (1994).*

For the remainder of this chapter only particulate and fibre-reinforced composites will be considered because of the direct relevance to forthcoming numerical simulations.

2.3 Characteristics of Composites

Composite materials have many mechanical behaviour characteristics that are different from those of more conventional engineering materials. Most common engineering materials are considered as both homogeneous and isotropic. The terms homogeneous and isotropic implies that the material has uniform properties throughout and that the material properties are the same in every direction, respectively. In contrast, particulate

composites are inhomogeneous, yet can be considered to be isotropic if the particles are uniformly distributed. Whereas, fibre reinforced composites are inhomogeneous and may be either isotropic in the case of discontinuous random fibre composites, or anisotropic in the case of unidirectional fibre composites. This potential for controlled anisotropy of stiffness and strength allows the tailoring of a composite material to meet a particular structural requirement with little waste of material capability.

As stated previously, improved material properties can also be achieved in forming a composite. Some of the typical properties include; stiffness, strength, weight, impact resistance, corrosion resistance, thermal conductivity, and fatigue life. Naturally, not all of these properties are improved at the same time, nor is there usually any requirement to do so. To measure the relative mechanical advantage of composite materials the *specific stiffness* and *specific strength* are commonly considered. The specific stiffness is the ratio between the Young's modulus and the density, and the specific strength is the ratio between the tensile strength and the density. Composite materials generally have a high specific modulus and strength, as shown in Figure 2.4, which means the weight of certain components can be reduced. This is a factor of great importance in moving components,

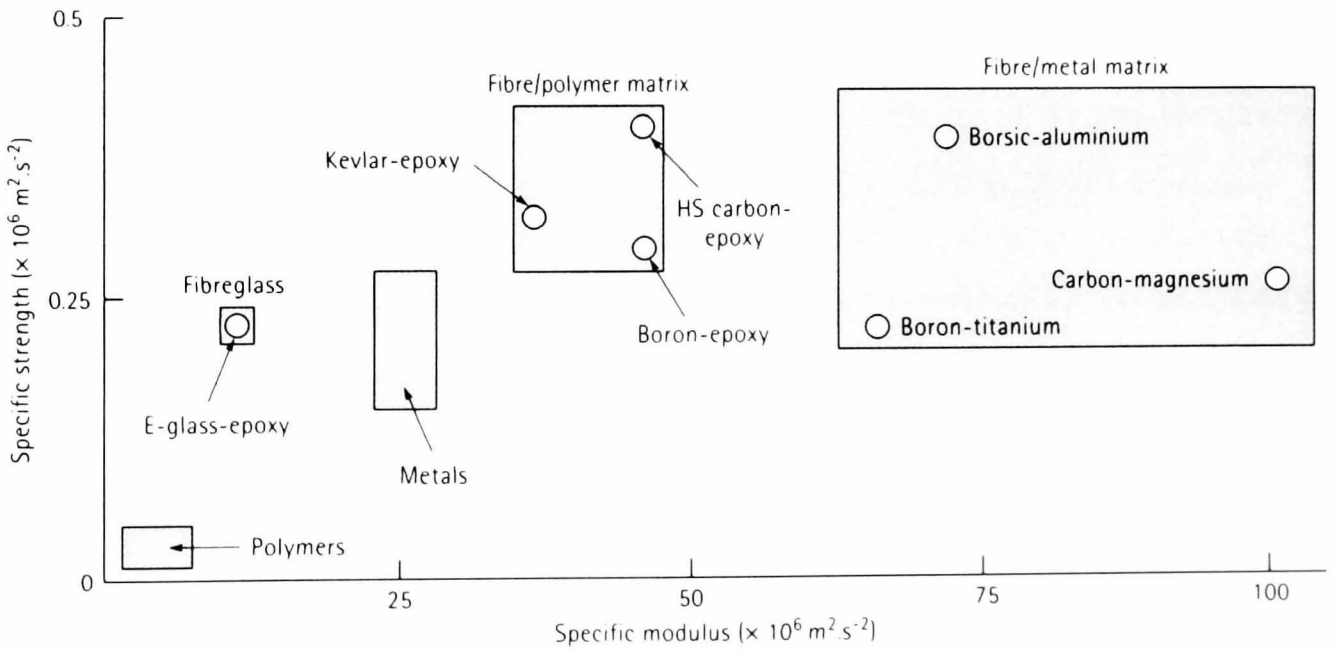

Figure 2.4 **A comparison of the specific modulus and specific strength of several composite materials with those of metals and polymers, *Askeland (1996).***

especially in all forms of transport where reduction in weight results in greater efficiency leading to energy and hence cost savings.

Other mechanical parameters for comparing the performance of composites include resistance to fracture, fatigue, impact, and creep.

Most properties of a composite are a complex function of a number of parameters, of which these include:

- The properties of the reinforcement phase
- The properties of the matrix phase
- The volumetric ratio of the respective phases in the composite (dispersed phase volume fraction)
- The geometry and orientation of the reinforcement phase
- Bond strength between the phases

As, in most cases, the reinforcement is the stiffer and stronger constituent, therefore it is the principal load bearer. Hence, depending on the volume fraction of reinforcements and the bond strength with the matrix, which allows the transfer of load from the matrix, the properties of the composite will be strongly influenced by the properties of the reinforcement utilized. For example, by increasing the stiffness of the reinforcement it would be expected that the stiffness of the resultant composite would also increase.

Although matrices by themselves generally have low mechanical properties as compared to the reinforcements, the matrix influences many mechanical properties of the composite. These properties include transverse modulus and strength (in the case of fibre composites), shear modulus and strength, compressive strength, interlaminar shear strength, thermal expansion coefficient, thermal resistance, and fatigue strength. For example, if the thermal expansion coefficient of the matrix is higher than that of the reinforcement, and the manufacturing temperatures are higher than the operating temperatures, the matrix will radially shrink more the reinforcement. This causes the

matrix to compress around the reinforcement, generating compressive 'residual' stresses at the interface, which in turn affect the composite properties.

The ratio of reinforcement to matrix derives largely from the manufacturing process used. However, it is also influenced by the type of matrix system used, and the form in which the reinforcements are incorporated. In general, since the mechanical properties of the reinforcements usually have higher values than those of the matrix, the greater the reinforcement volume fraction, the better the mechanical properties of the resultant composite. In practice, the amount of reinforcement that can be incorporated in a given matrix is limited by a number of factors. For example, with particulate reinforced metals, the reinforcement content is usually kept to less than 40 vol. % because of processing difficulties and increasing brittleness at higher contents. On the other hand, the volume fraction of WC particles in carbide tools can exceed 90%. The processing methods for fibre-reinforced polymers are capable of producing composites with a high proportion of fibres, and the upper limit of about 70 vol. % is set by the need to avoid inter fibre contact, which results in fibre damage.

The geometry and orientation of the reinforcement phase is also important, as it is one of the major parameters in determining the effectiveness of the reinforcement. Particulate reinforcements generally have an aspect ratio close to unity, however their relative size can vary significantly. For equiaxed particles, the composite behaves essentially as an isotropic material whose elastic properties are independent of direction. In addition, the orientation of the particles would have little effect on the composites behaviour.

For particle diameters that are in the range of 0.01 to 0.1 μm dispersion strengthening occurs, as the small-dispersed particles hinder or impede the motion of dislocations. Thus, plastic deformation is restricted such that yield and tensile strengths, as well as hardness, improve. For coarse particles (>0.1 μm) the particle-matrix interactions cannot be treated on the atomic or molecular level, and hence do not effectively block slip. These composites are used to produce unusual combinations of properties rather than improved

strength.

Fibrous reinforcements can be either long or short, depending on the processing method and/or the application requirements. Long continuous fibres have a high aspect ratio, and short discontinuous fibres have a low aspect ratio. Long fibres provide many benefits over short fibres. These include impact resistance, low shrinkage, improved surface finish, dimensional stability, and controlled anisotropic behaviour. However, short fibres provide low cost, are easy to work with, and have fast cycle time fabrication procedures.

The chemical and strength characteristics of the interface between the phases are particularly important in determining the properties of the composite. The interfacial bond strength has to be sufficient for load to be transferred from the matrix to the reinforcements if the composite is to be stronger than the unreinforced matrix. On the other hand, if toughness is a requirement of the composite, the interface must not be so strong that it does not fail and allow toughening mechanisms such as debonding and fibre pull-out to take place.

2.4 Micromechanics of Composite Materials

Because of the inherently heterogeneous nature of composite materials, they are conveniently studied from two points of view: macromechanics and micromechanics. Macromechanics is the study of material behaviour wherein the material is presumed homogeneous, and the effects of constituent materials are detected only as averaged apparent macroscopic properties. In this thesis, macromechanics will not be considered, hence for a more formal treatment of the underlying concepts see e.g. *Jones (1999)*.

The term micromechanics implies the study of material behaviour wherein the interaction of the constituent phases is examined on a microscopic scale to determine their effect on the properties of the composite. There are many theoretical micromechanics models that have been developed and applied to predict the effective properties of composite materials in terms of size, shape, volume fraction and distribution of the constituent

phases. In particular, predictions of elastic properties such as Young's modulus, shear modulus, and the Poisson's ratio of two-phase materials have been studied extensively, and comparisons with experimental data have been widely examined, as discussed in detail in the following sections.

2.4.1 Particulate Reinforced Composites

Linear Elastic Properties

The first major publication to analyse the bulk properties of heterogeneous materials was by *Eshelby (1957)*, but this was restricted to the special case when the volume fraction of the inclusions is very small and it can be assumed that they do not interact. Clearly, interaction has a strong role to play and one of the earliest papers in this particular field to include finite inclusion concentration was by *Paul (1960)*, who constructed Voigt-Reuss type bounds (*Voigt (1889)* and *Reuss (1929)*) using variational theorems of the theory of elasticity and an admissible stress and displacement system. While Paul's treatment was based on arbitrary phase geometry, and these bounds have the advantage of being exact, they were generally too far apart to give a good estimate of the effective Young's modulus (E^*).

Following this publication a number of authors proposed refinements to the analytical models, using a variety of techniques, so that the elastic modulus could be calculated more accurately and efficiently from the moduli of the constituents. *Hashin (1962)* and *Hashin and Shtrikman (1963)* developed a concentric spheres model, using again variational theorems of the theory of elasticity. These authors developed a model whereby an assemblage of spherical inclusions and a surrounding matrix described the material. The inclusions being of various sizes such that the inclusion-matrix combination of spheres completely filled the volume of the composite (see Figure 2.5). They then stated that the effective elastic modulus could be conveniently defined by means of the strain energy stored within the inclusion-matrix assemblage when subjected to gross uniform

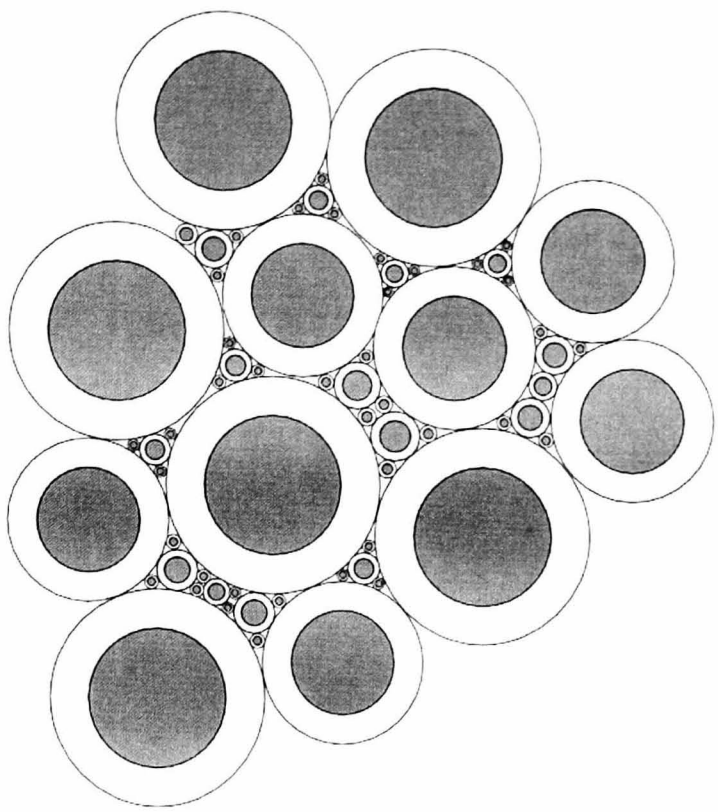

Figure 2.5 Philosophy of the concentric spheres model, *Christensen (1979).*

strains or stresses. Hence, with the use of variational principles for non-homogeneous linear elasticity, in terms of the elastic polarization tensor, the strain energy was then bounded and thus also the effective elastic moduli. The expressions derived by Hashin and Shtrikman for the effective Young's modulus (E^*) bounds are as follows:

$$E_n^* = \frac{9k_n^*\mu_n^*}{(3k_n^* + \mu_n^*)} \tag{2.1}$$

in which,

$$k_n^* = k_n + \frac{V_{f\,3-n}}{\dfrac{1}{k_{3-n} - k_n} + \dfrac{3V_{f\,n}}{3k_n + 4\mu_n}} \tag{2.2}$$

$$\mu_n^* = \mu_n + \frac{V_{f\,3-n}}{\dfrac{1}{\mu_{3-n} - \mu_n} + \dfrac{6(k_n + 2\mu_n)V_{f\,n}}{5\mu_n(3k_n + 4\mu_n)}} \tag{2.3}$$

where n = 1,2, and E_1^*, k_1^*, and μ_1^*, are lower bound effective properties of Young's

modulus, bulk and shear modulus respectively, while E_2^*, k_2^*, and μ_2^*, are upper bound effective properties. For property terms without an asterix the subscript denotes the material phase, where the matrix is given the subscript 1 and the inclusions the subscript 2. Finally, V_f corresponds to the volume fraction of the appropriate phase.

The bulk modulus bounds obtained by Hashin coincided with those of Paul, whereas the shear modulus bounds were much closer together than those obtained by Paul. However, the results were strictly valid only for a material consisting of a matrix in which certain special distributions of spherical inclusions are embedded. The subsequent paper by Hashin and Shtrikman improved the technique to account for arbitrary phase geometry, and gave a better estimate for the effective modulus, when compared with experimental results, so long as the moduli ratio between the different phases is not too large.

Hill (1965) and *Budiansky (1965)* then independently presented self-consistent analytical models for multiphase materials. This technique estimates the macroscopic elastic modulus by taking account of the inhomogeneity of stress and strain in a manner similar to the *Hershey (1954)* and *Kröner (1958)* self-consistency theory of crystalline aggregates. In essence, the method involves viewing each phase of the composite as being lumped as a single ellipsoidal inclusion in an infinite medium possessing the unknown effective properties. Applying uniform stress and strain conditions at infinity then allows the determination of the average conditions in the inclusion. After this operation is performed for all phases, the average conditions are known in terms of the individual phase properties and the effective properties. Hence, the average conditions in the entire composite are known and the effective moduli can be calculated from the averages.

Although the self-consistent method for multiphase media seems straightforward, there are some problems with it. For instance, the predicted effective shear modulus (μ) becomes zero at a volume fraction of $V_f = 0.5$ in the case of voids; and μ becomes infinite at a volume fraction of $V_f = 0.4$ in the case of rigid inclusions. This result cannot be too surprising, as this method takes enormous liberties with the geometry of the material

combination. To calculate the averages needed for each phase, the geometry is successively rearranged to view the phase under consideration as an inclusion, even if in reality the phase is completely continuous. Of course, the scheme is not a geometric model at all; it is merely a convenient and appealing operational scheme, which unfortunately can give erroneous results.

The approach of *Walpole (1966)*, also based on a variational principle, is analogous to the Hashin and Shtrikman method; with the exception that Walpole used a single-averaging approximation, unlike the double-averaging method used by Hashin and Shtrikman. The bounds by Hashin and Shtrikman stem from the extremum principles proposed by themselves earlier, whereas Walpole based his work around classical extremum principles. Hence, as Walpole infers, his rigorous treatment would seem more incisive and also more generalised than the method proposed by Hashin and Shtrikman.

Mori and Tanaka (1973) then introduced a method that linked eigen strain, equivalent inclusion, back stress concepts, and complex energy considerations. This model primarily relies on Eshelby's solution of the misfitting inclusion to determine the average stresses and strains in the matrix and inclusion, and hence, the effective properties of the multiphase material. The Mori-Tanaka method is completely different from the other models discussed, as it does not admit a physical description, at least not at the same level, but involves complex manipulations of the field variables along with other special concepts, such as back stress. Recently, however, this technique was improved by *Benvensite (1987)*, who reformulated the Mori-Tanaka theory using a much more direct approach to define and compute the effective moduli. This mean-field approach, which is still referred to as the Mori-Tanaka theory, has emerged as one of the most versatile methods developed in recent years and has been used widely to model multiphase media with relative success.

A majority of the analytical methods available today are only variants of the above models and as shown by *Weng (1990)*, there are fundamental connections between them.

For instance, the equivalent polarisation stress and strain in the Mori-Tanaka theory are exactly those chosen by Hashin-Shtrikman and Walpole; and the average stress and strain of the matrix phase in the Mori-Tanaka theory are equal to the image stress and strain imposed on the approximate fields by Walpole. Hence, for a multiphase composite with aligned, identically shaped inclusions, the derived moduli are believed to be generally reliable, with most cases lying on or within the respective bounds. It also points to the conditions where the theory can be safely applied without violating the bounds.

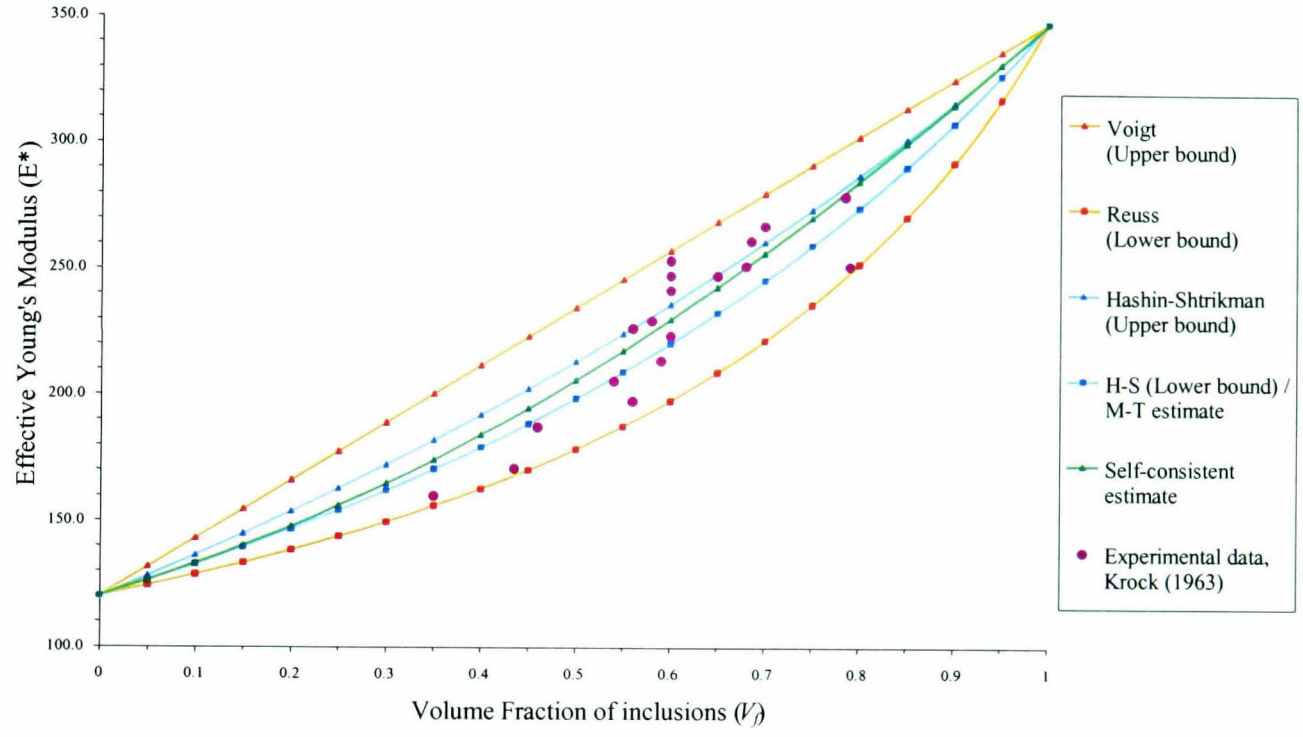

Figure 2.6 Comparison between the classical analytical models and experimental data for a composite of tungsten particles dispersed within a copper matrix.

A critical review of the bases and assumptions of the classical models mentioned above, as well as the accuracy of their predictions relative to experimental data is available elsewhere, see *Christensen (1990)*. However, plotted in Figure 2.6 is a simple comparison between the classical analytical approaches and experimental data for the particular case of copper-tungsten composite, in which tungsten is the particulate phase. From this graph it is noticeable that the bounds obtained by Hashin and Shtrikman are much closer together, and hence more useful than those of the simple Voigt-Reuss bounds. This

improvement is due the fact that the H-S bounds incorporate important morphological information about the microstructure, i.e. phase geometry. It is also apparent that the Mori-Tanaka estimate corresponds to the lower of the H-S bounds, which was also noticed by *Willis (1977)* and *Christensen (1990)*, and that the self-consistent estimate lies between all the above-mentioned bounds. Comparing these schemes with the experimental data from *Krock (1963)*, a high degree of scatter is observed, and hence it would be difficult to draw any conclusions as to which method is more accurate.

Although these analytical models are attractive because they offer better physical insight, any attempt to extend them to complex geometries invariably leads to mathematical intractability. However, in recent years, the growing accessibility of fast computers has allowed the development of advanced computational techniques to replace the time-consuming analytical procedures. Among the various numerical methods available, the most popular are the Finite Difference Method (FDM), the Finite Element Method (FEM) and the Boundary Element Method (BEM), with the latter two techniques described in detail within Chapter 3. Many of the initial numerical models published are restricted to a unit-cell approach, in which the real structure is approximated by a periodic array of certain regular geometries, e.g. *Agarwal and Broutman (1974)*. However, these models are generally not valid when the spatial and the size distribution of the reinforcement are random, as in real particulate composites. Hence, more recently other numerical approaches have been proposed which claim to model randomly distributed particulate composites, such as *Guild and Young (1989)* who combined finite element analysis and spatial statistical techniques (Voronoi cells); and also *Ramakrishnan et al. (1996)*, who incorporated FEM and generalised plane strain techniques to model the three-dimensional behaviour of a randomly distributed composite, using a two-dimensional approximation. Results from these and other similar numerical models have, in most cases, compared favourably with experimental data; however, to date no single approach has been universally recognised to simply and accurately model the elastic response of real particulate composites, for all possible situations.

Strength and Failure Criteria

In this part of the literature review, attention is concentrated on predicting the applied stress at which damage and failure occur within particulate reinforced composite materials. Failure of composite materials is a complex and important topic, and studies of failure are an ongoing activity. In general, there are many issues and controversies surrounding the subject of composite failure. Failure may occur due to ductile yielding or brittle cracking of the matrix, or through inclusions debonding and separating from the matrix, or even by inclusions fracturing under localised stress concentrations, etc. Clearly, many different mechanisms must be considered when studying failure and, in reality, failure is often a combination of several of these mechanisms or modes. Failure can simply be the final event in a complex and difficult to understand process of damage initiation and accumulation within the material.

While it is important to understand the mechanisms of failure, for many applications it is very difficult to detail each step of the failure process and so it would become almost impossible to incorporate every mode of failure into the design. A simpler alternative is to use an empirical failure criterion, which is essentially a set of equations with parameters adjusted to fit experimental data of failure of a simple sample. As particulate reinforced materials can be generally assumed to be isotropic and homogeneous at a macroscopic scale, the failure criteria developed for metals has been typically applied directly. The most common failure criteria are those of von Mises for ductile materials and the maximum principal stress or strain for brittle materials.

The von Mises criterion corresponds to yield occurring when the distortional (shape-changing) strain energy stored in the material reaches a critical value. This may be expressed as:

$$(\sigma_1 - \sigma_2)^2 + (\sigma_2 - \sigma_3)^2 + (\sigma_3 - \sigma_1)^2 < 2\sigma_Y^2 \qquad (2.4)$$

where σ_1, σ_2 and σ_3 are the three principal stresses within the composite, and σ_Y is the yield strength of a simple test specimen. Whereas, the maximum principal stress or strain

criterion can simply be written as:

$$\sigma_1 < \sigma_{1u} \qquad or \qquad \varepsilon_1 < \varepsilon_{1u} \tag{2.5}$$

where σ_1, ε_1 are the maximum principal stress and strain within the composite, and σ_{1u}, ε_{1u} are the (ultimate) failure stress or strain of a simple test specimen. The maximum principal stress criterion is generally more widely used, as information regarding the component design stresses are usually more readily available. However, in many situations, the maximum strain criterion is regarded as the safer option.

Thus far, strength has been characterised as a macroscopic property of the composite material, without regard to the individual constituents. In the previous section, many useful means of predicting the macroscopic stiffness properties in terms of the moduli of the individual phases are reported. One would expect that a similar procedure could be adopted to predict the macroscopic strength of composite materials in terms of the strength properties of the individual constituents. Unfortunately, this approach to strength characterisation is nowhere near as highly developed as the corresponding stiffness characterisation. The reasons are many, and research is very active in this area. Aspects that affect the macroscopic strength of composites include the statistical variability of material properties caused by the original manufacturing operation, or by subsequent handling, which introduces inherent flaws within the material and also the various environmental effects, which can weaken the chemical bond between phases.

Toughness

Previously, the mechanical property of strength, which is related to the stresses at which damage and failure occur in composites, was discussed. However, in many situations, the amount of energy absorbed by the material under load is equally important and this measure of fracture resistance is given the name 'toughness'. The effect of second phase particulates on fracture toughness has been studied by many authors in the past, with emphasis on the mechanisms of crack bowing and deflection (*Lange (1970)*, and *Faber*

and Evans (1983)), debonding at the matrix-reinforcement interface (*Beaumont (1988)*), microcracking (*Miyata et al. (1992)*), and crack shielding (*McMeeking and Evans (1982)*) i.e. crack bridging, or transformation toughening. However, the interrelation between particle parameters, toughness and strength is still not fully understood.

Considering an idealised composite, which contains particles whose Young's modulus is greater than the matrix, the overall strength should increase, but inadvertently the toughness generally decreases. In contrast, composites containing particles whose Young's modulus is less than the matrix can store a greater amount of energy density and are significantly tougher, but they are also relatively weak. In reality, however, the toughness of a composite is controlled by many factors, and hence, this rule is not necessarily observed experimentally.

Low fracture toughness within some next generation, high-strength composites has been one of the main obstacles to a large-scale application. Hence, recent numerical and experimental studies have attempted to optimise both strength and toughness of these multiphase materials. One such approach involves coating the second-phase inclusions with a ductile interphase layer. Numerical results from *Lu and Zhang (1995)* indicate that debonding has a strong tendency to be initiated when the rigidity of uncoated particles are higher than that of the matrix and thus, the toughness of the material is difficult to enhance. However, if these rigid particles are coated with a ductile layer, the stress field in the matrix will be strongly affected and as a result, matrix yielding becomes the dominant mode of micro-damage. Then, both the toughening effect and the reinforcing effect on the particle-filled material can be improved. Another approach, which has recently been investigated, is composites that contain mixtures of both high and low Young's moduli particles, *Hornsby and Premphet (1997,1998)*.

2.4.2 Fibre Reinforced Composites

Linear Elastic Properties

Considerable research has also been conducted in the analysis of the micro-mechanical properties of fibre-reinforced composites, as a result of the development of advanced composite materials. Perhaps the most widely used analytical approach for estimating the effective properties of composite materials is the `rule of mixtures', which is based on the premise that the material can be treated as if it were composed of parallel slabs of the two constituents bonded together, with relative thicknesses in proportion to the volume fraction of matrix and fibre. The theory behind this approach can be found in various texts, such as *Hull and Clyne (1996)*, hence only the elastic stiffness equations in the direction of the fibres (axial) and perpendicular to the fibres (transverse) are given below:

Axial stiffness:

$$E_1 = (1 - V_f)E_m + V_f E_f \tag{2.6}$$

Transverse stiffness:

$$E_2 = \frac{E_m E_f}{(1 - V_f)E_f + V_f E_m} \tag{2.7}$$

where V_f is the volume fraction of fibres, and E_m, E_f are the values of Young's modulus for fibre and matrix respectively. This technique has been experimentally proven to reasonably predict the Young's and shear moduli in the direction of the fibres when the composite has a strong bond between the fibres and matrix, with only minor deviations arising when the Poisson's ratios of the two phases are not equal. However, this model is a poor predictor of the effective properties in a direction perpendicular to the fibres.

Prediction of the transverse stiffness of a composite from the elastic properties of the constituents is far more difficult than the axial stiffness. In addition, experimental measurement of transverse stiffness is more prone to error, partly as a result of higher stresses in the matrix, which can, for example, cause polymeric matrices to creep under

modest applied loads. Also, the non-uniform distribution of stress and strain during loading means that the simple rule of mixtures method is inadequate. The `rule of mixtures' model generally gives an underestimate of the Young's modulus and can only really be treated as a lower bound. Various empirical or semi-empirical expressions designed to give more accurate estimates have been proposed. One of the most successful is that due to *Halpin and Tsai (1967)*. This technique is not based on rigorous elasticity theory, but broadly takes account of enhanced fibre load bearing, relative to the equal stress assumptions within the rule of mixtures model. Their expression for the transverse stiffness is:

$$E_2 = E_m \frac{(1+\xi\eta V_f)}{(1-\eta V_f)} \tag{2.8}$$

in which,

$$\eta = \frac{E_f - E_m}{E_f + \xi E_m} \tag{2.9}$$

where ξ is an adjustable parameter, generally of the order of unity. The expression given in Eq. (2.8) gives the correct values in the limits of $V_f = 0$ and $V_f = 1$ and in general gives good agreement with experiments over the complete range of fibre content.

Another important method of analysing filamentary composites consists of assuming that the fibres are arranged in a regular periodic array (see Figure 2.7). In this method, the resulting elasticity problem is solved either by a series development or by some numerical scheme. The resulting elastic fields are then averaged to give expressions for the desired elastic constants.

One of the earliest applications of this approach appears to be due to *Hashin and Rosen (1964)*, who obtained bounds and expressions for the effective elastic moduli of reinforced materials using a concentric cylinders model and variational theorems of the theory of elasticity. This model is the two-dimensional counterpart of the three-dimensional concentric spheres model introduced in Section 2.4.1. Results have

been presented for both hexagonal and random fibre arrays.

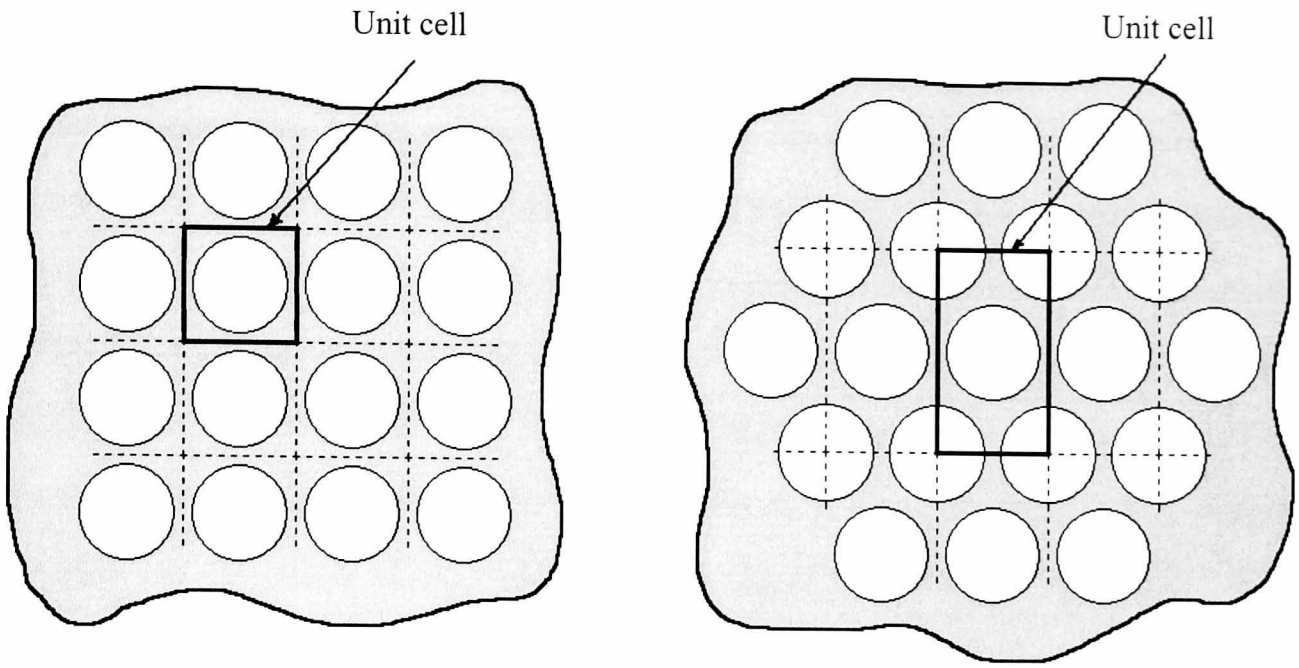

(a) Square-packed array

(b) Hexagonal-packed array

Figure 2.7 Concept of unit cells, *Hyer (1998).*

Following the work of Hashin and Rosen, various other authors also proposed analytical models in order to derive the effective elastic constants for fibrous composite materials. *Whitney and Riley (1966)* used the classical theory of linear elasticity for the determination of the elastic constants. In this work, Airy's stress functions were applied to the composite unit cell. *Chen and Cheng (1967)* also used the classical theory of linear elasticity for the determination of elastic constants. For the solution of the differential equations of linear elasticity, an infinite series, a least squares method, and a Fourier method have been employed. They investigated only a hexagonal fibre arrangement. *Adams and Doner (1967b)* represented the governing equilibrium equations and stress-displacement relations by using finite differences. The composite was subjected to normal stress components in the direction perpendicular to the fibre axes for the evaluation of transverse stiffness. *Chow and Hermans (1969)* obtained the elastic constants by expressing these as a series expansion, in terms of the volume fraction of the fibres. The coefficients of this series were estimated with the use of a 'reflection theory'.

More recently, literature in this particular field has incorporated novel numerical techniques, as discussed previously. However, in general they remain restricted to the unit-cell approach, because in the case of composites of aligned fibres this assumption can be considered to be reasonable. For example, *Eischen and Torquato (1993)* applied the boundary element method (BEM) to a simplified unit-cell for the determination of effective elastic moduli of a fibrous composite material. An idealised hexagonal array of infinitely long fibres was considered and a variety of inclusions either stiffer or weaker than the matrix; and a wide range of volume fractions of fibres have been examined. *Chati and Mitra (1998)* then extended this work to account for transversely isotropic materials and the effects of crenulations and interfacial debonding of the fibres.

In most cases, the results from these and other similar numerical models compare well with experimental data, however as with particulate composites, no single approach has been universally recognised to simply and accurately model the elastic response of real fibre-reinforced composites, for all situations.

Strength and Failure Criteria

The application of an arbitrary stress state to a unidirectional composite can lead to failure by one or more basic failure processes. The three most important types of failure are:

- Axial tensile failure
- Transverse tensile failure
- Shear failure

Axial tensile failure occurs when large tensile stresses are applied parallel to the fibres, σ_1, which leads to fibre and matrix fracture, with the fracture path normal to the fibre direction. Transverse tensile failure occurs when tensile stresses are applied perpendicular to the fibre axes, σ_2, and shear failure can be caused by external applied shear stresses, τ_{12}. In these cases, fracture may occur entirely within the matrix, at the fibre/matrix interface or primarily within the fibres. To predict the strength of a composite, values of the failure (ultimate) stresses σ_{1u}, σ_{2u} and τ_{12u} have to be determined.

In addition to the stated tensile failure modes, failure in compression is feasible. However, within this thesis discussion will concentrate on the three main modes stated above.

- **Axial tensile failure**

Understanding of failure under an applied tensile stress parallel to the fibres is relatively simple, provided that both constituents behave elastically and fail in a brittle manner. They then experience the same axial strain and hence sustain stresses in the same ratio as their Young's moduli. Two cases can be identified, depending on whether matrix or fibres have the lower strain to failure.

If the matrix has the lower failure strain ($\varepsilon_{mu} < \varepsilon_{fu}$), the composite stress is given by the simple rule of mixtures, for strains up to ε_{mu}

$$\sigma_1 = V_f\sigma_f + (1-V_f)\sigma_m \qquad (2.10)$$

Above this strain, however, the matrix starts to undergo microcracking and the composite subsequently extends with little further increase in the applied stress. As matrix cracking continues, the load is transferred progressively to the fibres. If the strain does not reach ε_{fu} during this stage, further extension causes the composite stress to rise and the load is now carried entirely by the fibres. Final fracture occurs when the strain reaches ε_{fu}, so that the composite failure stress σ_{1u} is given by $V_f\sigma_{fu}$. Alternatively, if the fibres break before matrix cracking has become sufficiently extensive to transfer the entire load to them, then the strength of the composite is given by:

$$\sigma_{1u} = V_f\sigma_{fmu} + (1-V_f)\sigma_{mu} \qquad (2.11)$$

where σ_{fmu} is the fibre stress at the onset of matrix cracking ($\varepsilon_1 = \varepsilon_{mu}$).

If the fibres have the lower failure strain ($\varepsilon_{mu} > \varepsilon_{fu}$), the fibres fail first at a composite strain of ε_{fu}. Further straining causes the fibres to break up into progressively shorter lengths and the load is transferred to the matrix. Subsequent failure then occurs at an applied stress of $(1-V_f)\sigma_{mu}$. If matrix fracture takes place while the fibres are still bearing

some load, then the composite failure stress is:

$$\sigma_{1u} = V_f \sigma_{fu} + (1 - V_f)\sigma_{mfu} \tag{2.12}$$

where σ_{mfu} is the matrix stress at the onset of fibre cracking.

Application of this analysis to real systems that fail essentially in a brittle manner has shown that the fibre strength is dominant in determining the axial strength of the composite and the product $V_f\sigma_{fu}$ provides a reliable estimate of σ_{1u}, *Hull and Clyne (1996)*. Note that it is unrealistic to apply these calculations to ductile metallic and thermoplastic matrices, which normally depart from linear elastic behaviour well before failure occurs.

Although the above conclusion about estimation of σ_{1u} is often valid, the overall treatment represents a gross simplification. In reality, microcracking of the matrix does not result in the matrix becoming completely unloaded and fibres still carry some stress even after they have broken into short lengths. Further assumptions in the above treatment are that the fibre strength is a constant and that the fibres fail in isolation from each other. In fact, most types of fibre exhibit a range of strengths, due to presence of flaws, which may occur randomly along the length of the fibre. The variability in strength is greater when the fibre displays a low Weibull modulus, *Weibull (1951)*. The Weibull modulus is an important parameter for characterising the strength distribution exhibited by the fibre (or any other brittle material). A major factor determining fibre strength is the damage that fibres sustain when they rub against each other during processing operations. To minimise this damage, fibres (e.g. glass) are usually treated with a 'size' at an early stage of manufacture. This is a thin coating applied to the fibres by spraying with water containing an emulsified polymer. The size serves several proposes: (a) to protect the surface of the fibres from damage, (b) to lubricate the fibres so that they can withstand abrasion during subsequent processing operations, (c) to impart anti-static properties and (d) to provide a chemical link between the glass surface and the matrix to increase the interfacial bond strength.

In practice, when a load is applied parallel to the fibres, the first failure is at the weakest point. If the stress redistribution associated with this failure is not sufficient to cause adjacent fibres to break, the applied stress increases and further fractures occur randomly throughout the material. Several models have been proposed to treat this process; e.g. *Rosen (1965)* developed a 'cumulative weakening' model, and *Zweben and Rosen (1970)* presented a 'fibre break propagation' model. However, these models have limited predictive power, because the stress field around a fractured fibre is sensitive to details of interfacial properties and to matrix yielding and fracture behaviour, which can be influenced by a wide variety of factors.

Prediction of stress fields around cracks by the use of numerical modelling has proven useful in exploring what is likely to occur after a fibre has fractured or when a crack approaches a fibre. Pioneering work of this type was carried out by *Cook and Gordon (1964)*, who highlighted the possibility of fibre/matrix decohesion in front of a crack. Interfacial debonding would then blunt the crack tip, tending to prevent the crack from simply slicing through the fibres it encounters in the crack plane. This *crack-blunting* mechanism is important in raising the toughness of a composite, as discussed subsequently. More recently, work has explored the significance of fibre/matrix stiffness mismatch, plastic flow in the matrix, interfacial sliding, etc. For example, the work of *He et al. (1993)* numerically modelled the stress field around a cracked fibre in a hexagonal array, under axial loading.

- **Transverse tensile failure**

It is not possible to make a simple estimate of σ_{2u}, comparable with the estimate of σ_{1u} described previously. The transverse strength is influenced by many factors, such as the nature of the interfacial bonding, the fibre distribution, the presence of voids, etc. In general, the transverse strength is less than the axial strength and less that of the unreinforced matrix, often significantly so. A consequence of this is that the transverse plies in a crossply laminate usually start to crack before the parallel plies, even though

they are less stiff and so carry less load.

The fibres make little contribution to the strength; conversely, they inherently introduce high local stresses and strains within the matrix, due to the constraint of the fibres on the matrix. If the interfacial bonding is weak, then cracks tend to form at the interface and link up through highly stressed sections of matrix. A process of this type is illustrated in the micrographs of Figure 2.8. If, on the other hand, there is strong resistance to interfacial decohesion, cracks will tend to form in the matrix close to the interface where there is a concentration of stress and a high degree of triaxial constraint, so that matrix plasticity is inhibited.

An estimate of the effect of the presence of the fibres on the transverse strength can be obtained by treating the fibres in the composite as a set of cylindrical holes and considering the reduction in load-bearing cross-section thus introduced. (This is not accurate, since the presence of even completely debonded fibres would lead to a different stress distribution in the matrix than would the case for holes, but the approach is useful as a guide.) For a simple square array of holes, consideration of the maximum reduction in matrix cross-sectional area leads to the following expression for the transverse strength of a lamina having a volume fraction V_f of fibres,

$$\sigma_{2u} = \sigma_{mu}\left[1-2\left(\frac{V_f}{\pi}\right)^{1/2}\right] \tag{2.10}$$

A comparison between predictions from this equation and experimental data for Al(6061)/Borsic composites can be found in *Prewo and Kreider (1972)*. [Note Borsic is the term used to describe boron fibres coated with silicon carbide (SiC)]. In this case, the model gives good agreement with experiment.

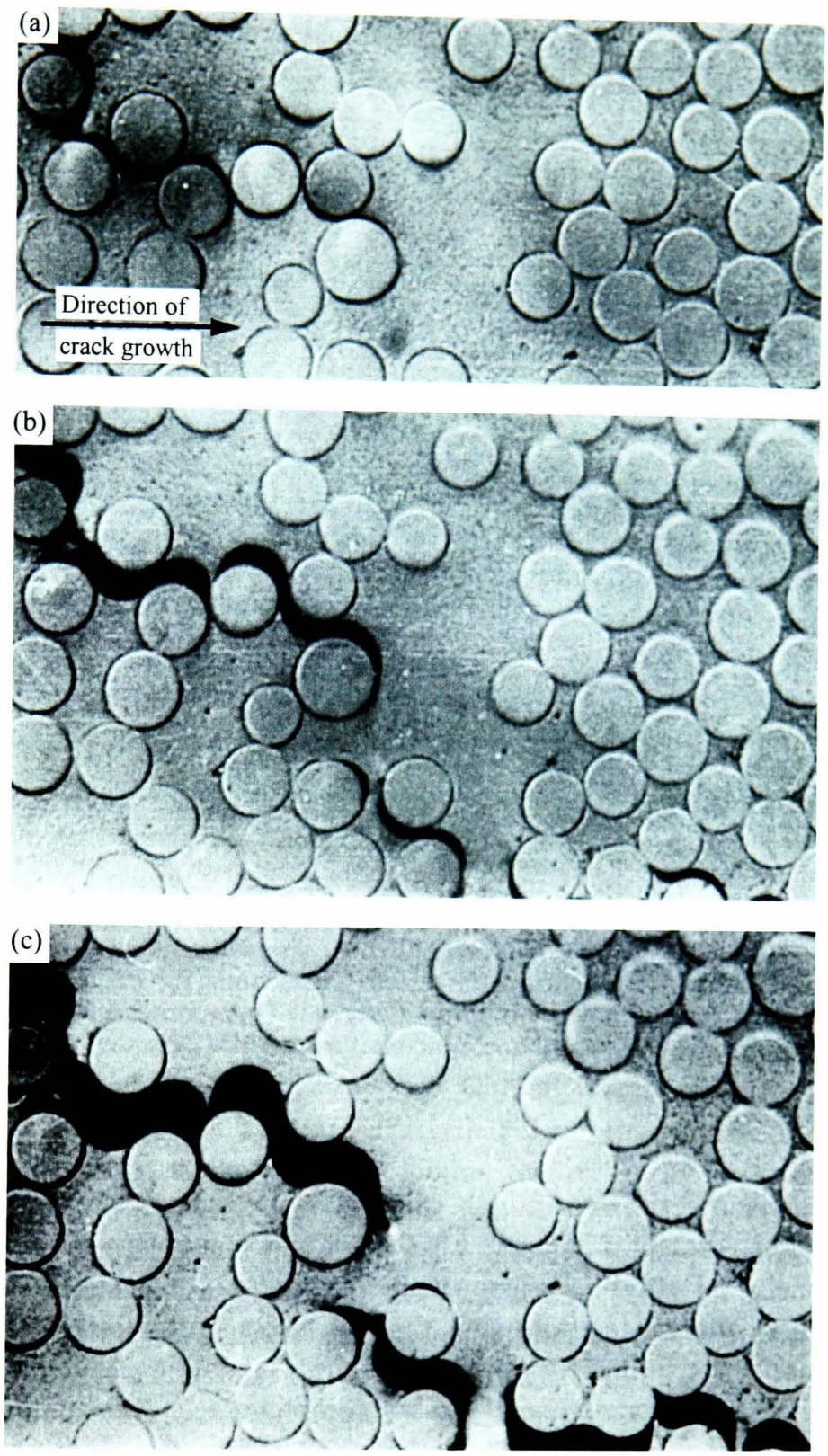

Figure 2.8 SEM micrographs illustrating the propagation of a transverse crack in a polyester/glass lamina, *Jones (1981).*

There is much interest in improving the transverse properties of laminae, particularly the failure strain. Among the possibilities that have been considered is the provision of a very compliant (e.g. rubber) layer on the fibre surface, so as to reduce the strain localisation and constraint imposed on the matrix. Unfortunately, a layer sufficiently thick to increase

significantly the transverse failure strain tends to have an adverse effect on other properties, such as the shear stiffness.

- **Shear failure**

No analytical expression is available to predict the effect of fibre content on τ_{12u}. *Adams and Doner (1967a)* have used finite difference methods to deduce how the shear stress concentration factor should vary with fibre volume fraction. Unless the fibre volume fraction is very high (when constraint on the matrix deformation becomes severe), this factor is quite close to unity and τ_{12u} is expected to have a value close to τ_{mu} for the matrix.

Typical experimental failure data for each of the respective failure modes are summarised in Table 2.3. Note that there are both practical and theoretical difficulties to be overcome in obtaining such data.

Composite	Axial strength σ_{1u} (MPa)	Transverse strength σ_{2u} (MPa)	Shear strength τ_{12u} (MPa)
Polyester / 50% glass	700	20	50
Epoxy / 50% carbon (HM)	1000	35	70
Epoxy / 50% Kevlar^{TM}	1200	20	50

Table 2.3 Typical experimental failure data for laminae based on thermoset matrices, *Hull and Clyne (1996).*

In each of the failure modes a uniaxial stress state is considered. However, the general practical design problem often involves a biaxial, if not a triaxial state of stress. Thus, a logical method of using uniaxial strength information obtained in practical material coordinates is required for analysis of multiaxial loading problems. As fibre reinforced

materials are generally assumed to be anisotropic, modified failure criteria, similar to the failure criteria used in metal design, have been proposed. The most popular among these criteria are:

- Maximum stress criterion,
- Maximum strain criterion,
- Tsai-Hill failure criterion.

These criteria are simply empirical statements of the process of degradation and failure of the material, with parameters adjusted to fit experimental data of failure of a simple sample. A comprehensive review of the popular approaches adopted has been published by *Rowlands (1985)*.

- Maximum stress criterion

The maximum stress criterion is a simple failure theory, which predicts failure when at least one of the stresses within the material (σ_1-axial stress, σ_2-transverse stress, τ_{12}-shear stress in the 1-2 plane) exceeds the corresponding experimental value of strength. Symbolically, the maximum stress criterion states that a fibre-reinforced material will not fail if at every point:

$$\sigma_{1u}^{C} < \sigma_1 < \sigma_{1u}^{T}$$

$$\sigma_{2u}^{C} < \sigma_2 < \sigma_{2u}^{T} \qquad (2.11)$$

$$\tau_{12} < \tau_{12u}^{S}$$

where $\sigma_{1u}^{T}, \sigma_{2u}^{T}$ are the experimentally determined tensile failure stresses in the 1 (axial) direction and the 2 (transverse) direction respectively, similarly σ_{1u}^{C} , σ_{2u}^{C} are the experimentally determined compressive failure stresses. Finally, τ_{12u}^{S} is the shear failure stress in the 1-2 plane.

- Maximum strain criterion

The maximum strain criterion is the direct counterpart of the maximum stress criterion,

and is defined by:

$$\varepsilon_{1u}^{C} < \varepsilon_1 < \varepsilon_{1u}^{T}$$

$$\varepsilon_{2u}^{C} < \varepsilon_2 < \varepsilon_{2u}^{T} \qquad (2.12)$$

$$\gamma_{12} < \gamma_{12u}^{S}$$

where ε_{1u}^{T}, ε_{2u}^{T} are the experimentally determined tensile failure strains in the 1 (axial) direction and the 2 (transverse) direction respectively, similarly ε_{1u}^{C}, ε_{2u}^{C} are the experimentally determined compressive failure strains. Finally, γ_{12u}^{S} is the shear failure strain in the 1-2 plane.

- **Tsai-Hill failure criterion**

This criterion is similar to the von Mises criterion for plasticity of metals but adapted for anisotropic materials, *Tsai (1965)*. For unidirectional composites, this criterion may be written:

$$\left(\frac{\sigma_1}{\sigma_{1u}}\right)^2 + \left(\frac{\sigma_2}{\sigma_{2u}}\right)^2 - \frac{\sigma_1\sigma_2}{(\sigma_{1u})^2} + \left(\frac{\tau_{12}}{\tau_{12u}}\right)^2 < 1 \qquad (2.13)$$

This expression defines an envelope in stress space: if the stress state (σ_1, σ_2 and τ_{12}) lies outside this envelope, i.e. if the sum of the terms on the left-hand side is equal to or greater than unity, then failure is predicted.

The maximum stress and the maximum strain criteria are quite widely used because of their simplicity, but generally they only have significance for one-dimensional stress and strain states, and their use in multidimensional states must be made with caution. The Tsai-Hill criterion was developed specifically to address this shortcoming and considers the interaction between stress components. However, the Tsai-Hill criterion still has some drawbacks, such as the differences in behaviour due to tensile and compressive loading are not taken into account and that the mode of failure is no longer identified, as in the case of the maximum stress or strain criterion. These limitations were highlighted by *Tsai*

and Wu (1971), who proposed a more complex criterion involving both tensile and compressive failure stresses and an interaction parameter. Although the Tsai-Wu failure criterion seems to fit well the experimental data available, it still lacks a physical micromechanical basis.

Toughness

Establishing the toughness of fibre-reinforced materials suffers from similar difficulties to those posed by particulate composites. In addition, there are the effects of fibre pull-out which must be considered. The fundamental process behind fibre pull-out can be categorised into two main stages. Firstly, due to matrix cracking, load that was once carried by the matrix is transferred by shear to the fibres, which are still intact. These shear forces eventually become so large that the bond between fibre and matrix fails, and interfacial cracks propagate away from the matrix crack surface. The next stage involves continued load transfer between fibre and matrix through frictional contact, inducing non-uniform stresses along the debonded fibre. As the fibre strength varies along its length, the fibre is able to break some distance from the matrix crack-plane where the

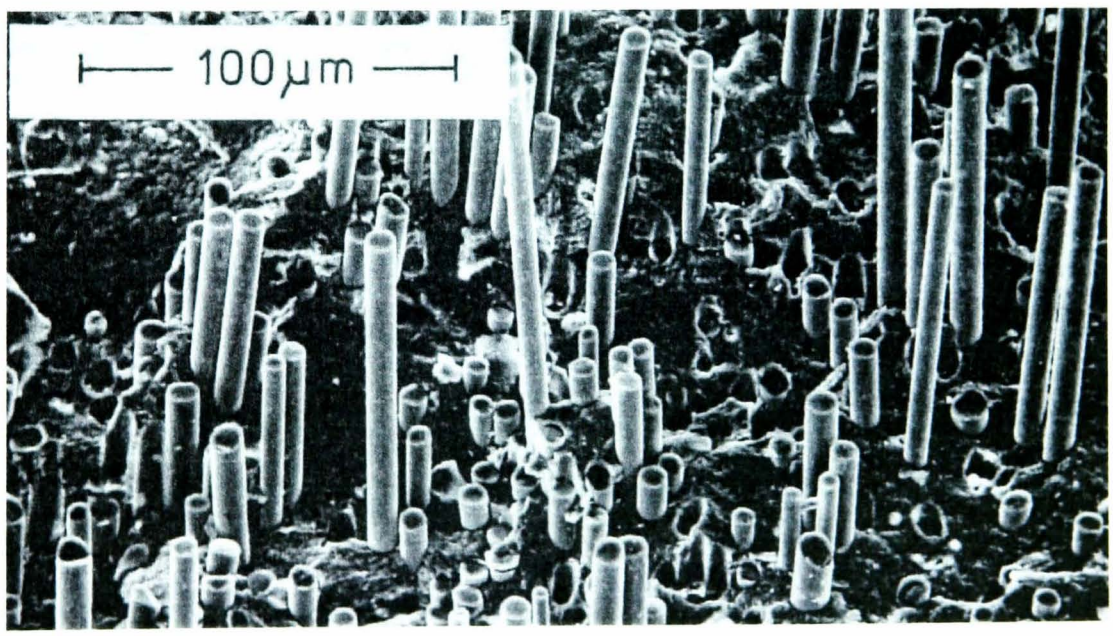

Figure 2.9 **Fibre pull-out along the fracture surface of a glass-ceramic reinforced with SiC fibres, *Matthews and Rawlings (1994)***

stress is highest. Hence, after fracture, the composite typically shows a matrix crack-plane with fibres protruding from it (Figure 2.9).

Depending on the interfacial roughness, contact pressure and sliding distance, this process can absorb large quantities of energy, and hence, the potential for contribution to the overall toughness is substantial. Extensive studies have been conducted within this field (e.g. *Wells and Beaumont (1985)* and *Chiang (2000)*), and from these models a greater understanding of the processes that affect toughness has been achieved.

2.5 Summary

Composites are composed of two or more materials joined to give a combination of properties that cannot be attained in any of the original materials. Natural composites, such as wood, and some synthetic composites, have been used by humans for thousands of years, but the major developments have taken place in recent times. Many types of composites are currently available, of which there are three main classes: particle-reinforced, fibre-reinforced, and laminar composites.

The properties of composites are influenced by the properties of the constituents, the microstructure (which includes the volume fraction and morphology of the reinforcement) and the properties of the matrix-reinforcement interface. Over the past century, there has been considerable research on the analysis and prediction of the mechanical properties of such materials. Development of micromechanical models has allowed such mechanical properties as Young's moduli, shear moduli, and Poisson's ratio to be estimated to a high degree of accuracy. In contrast, the prediction of other bulk properties, such as strength and toughness, is subject to a reasonable level of variability.

More recently, numerical methods such as the finite difference (FD), finite element (FE) or boundary element (BE) approach have been employed. Nevertheless, at present it is still not possible to numerically simulate the complete behaviour of real composites, due to the degree of complexity and uncertainty involved in modelling the various

mechanisms of damage and failure, and also due to the immense computational time and resources required.

Chapter 3: Numerical Methods in Continuum Mechanics

3.1 Introduction

Without numerical techniques, it would be almost impossible to solve practical engineering problems analytically with a reasonable degree of accuracy. The main numerical techniques in continuum mechanics are: the Finite Difference (FD), Finite Element (FE) and the Boundary Element (BE) methods, as shown in Figure 3.1.

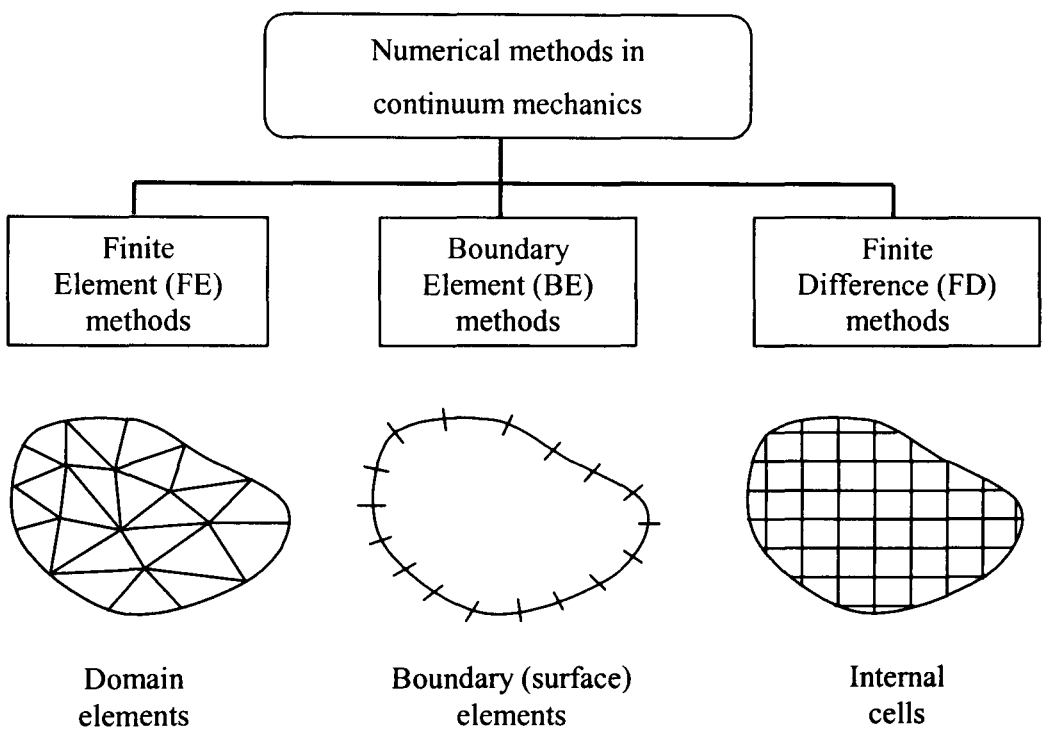

Figure 3.1 Classification of numerical methods in continuum mechanics, *Becker (1992).*

The finite difference method is the simplest of the three approaches and is relatively easy to program, however, it is generally not suitable for modelling problems with irregular geometries due to the regularity of the grid structure. Furthermore, because it is difficult to vary the size of the difference cells in particular regions, this method is not suitable for problems of rapidly changing variables, such as stress concentration problems.

Nowadays, finite difference methods are popular for heat transfer and fluid flow problems, rather than stress analysis; hence, no further discussion of this approach will be given in this thesis.

The finite and boundary element methods, in comparison, can easily accommodate practical engineering problems of complex geometries. In addition, mesh density can be simply varied to obtain good accuracy in regions of rapidly changing variables.

Each of these numerical techniques is based on the principle that it is possible to derive some equations and relationships that describe accurately the behaviour of a small differential part of the body. For linear-elastic stress analysis, the following relationships are applied within the development of these methods (tensor notation):

1. **Strain definitions** (strain-displacement equations)

$$\varepsilon_{ij} = \frac{1}{2}\left(\frac{\partial u_i}{\partial x_j} + \frac{\partial u_j}{\partial x_i}\right) \tag{3.1}$$

2. **Hooke's law** (stress-strain, constitutive equations)

$$\sigma_{ij} = \frac{2\mu\upsilon}{1-2\upsilon}\delta_{ij}\varepsilon_{kk} + 2\mu\varepsilon_{ij} \tag{3.2}$$

where μ is the shear modulus, υ is the Poisson's ratio and δ_{ij} is the Kronecker delta function whose properties are

$$\delta_{ij} = \begin{cases} 0 & i \neq j \\ 1 & i = j \end{cases}$$

3. **Equilibrium of a differential element** (differential equations of stress)

$$\frac{\partial \sigma_{ij}}{\partial x_j} + f_i = 0 \tag{3.3}$$

where f_i is the body force vector.

By dividing the entire body, or just the surface in the case of boundary element analysis, into a large number of smaller 'parts' or 'elements', and using further relationships inherent to each method to link or assemble the parts together, it is possible to obtain a reasonably accurate prediction of the values of variables, such as stresses and displacements in the body. As the sizes of these elements are made smaller, the numerical solution generally becomes more accurate, with the only limiting factor for linear analyses being the computational time and resources available.

In this chapter, the two most popular techniques in continuum mechanics, namely finite element and boundary element methods, are briefly reviewed, and the advantages and disadvantages of the two methods are then discussed.

3.2 Finite Element (FE) Technique

Many books have been written on Finite Element Analysis and, therefore, the complex mathematical processes will not be covered within this thesis; see *Cook (1995)* and *Mottram and Shaw (1996)*. Instead, a brief explanation of the technique and its procedures will be discussed to allow the reader to comprehend the terminology used within later sections.

In this approach, the problem under consideration is divided into a number of small segments of a simple basic shape. This is known as 'spatial discretisation', with each of the simpler shapes being known as an 'element', and the whole collection of elements being known as a 'mesh' (see Figure 3.2). For each element, the relevant properties of the element are then predicted in a simple way. In the case of structural analysis, the relationship between forces, displacements, strains and finally, stresses are evaluated, following the theory of elasticity (Eqs. 3.1-3). Then the elemental properties, defined by the element equations, are reconnected at fixed points known as 'nodes'. These are effectively glue points that hold elements together, to produce a set of simultaneous algebraic equations, which hold the properties and interactions for the entire system. In

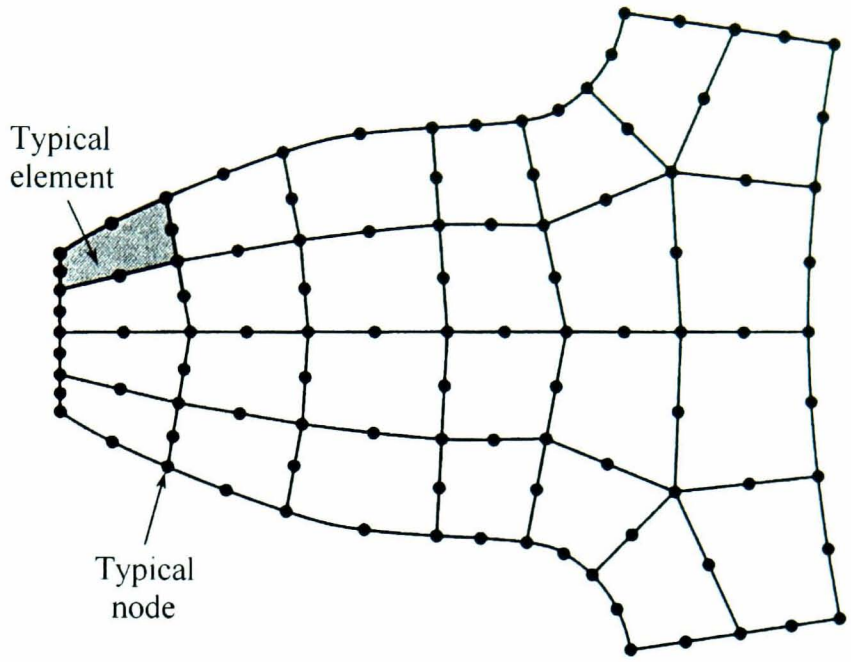

Figure 3.2 A Finite Element model of an irregular-shaped geometry, *Cook (1995).*

the case of stress analysis, these equations are nodal equilibrium equations, which can then be solved to find the inherent field quantity. There may be several hundred or several thousand such equations, which means that computer implementation is mandatory.

3.2.1 Review of the FE formulation

To further define the finite element approach, the following summary illustrates the steps involved in a typical FE formulation:

1. Discretise the problem under consideration into a mesh of finite elements linked together at nodal points. These elements can be triangular or quadrilateral (for two-dimensional problems), or tetrahedral and brick-elements (for three-dimensional problems), depending on the geometry of the physical problem.

2. Define how the geometry and variables change over each element (e.g. linearly or quadratically) by using a suitable shape function. Increasing the order of variation of an element should produce more accurate solutions, however more nodal points

are assigned to each element, resulting in higher computational expense. Hence, the analyst must decide whether it is better to use many simple (lower order) elements or a few complicated (higher order) elements to model the physical problem.

3. Use the three governing equations for linear-elastic structural mechanics (Eqs. 3.1-3) to derive the strains and stresses within each element from the unknown displacements. Compatibility is automatically satisfied between elements, because the displacements are chosen as the unknown variables. Then, use either a variational (energy) formulation or a direct equilibrium of forces approach to derive the elemental stiffnesses using the following relationship:

$$\sum_{m} [k]_m [\delta]_m = [F] \tag{3.4}$$

where m represents the element number, $[k]_m$ is the element stiffness matrix, $[\delta]_m$ is the element displacement vector and $[F]$ is the vector containing all the external forces.

4. Assemble the overall system of equations that characterises the physical problem. Since the summation of the stiffnesses is carried out only on elements sharing particular nodes, the overall stiffness matrix will be sparsely populated. Then apply the boundary conditions for the problem, which can take the form of prescribed displacements, stresses or pressures.

5. Use either direct or iterative algorithms to solve the overall system of linear equation to obtain the nodal displacements. The choice of solver depends mainly on the size of the problem under consideration. Direct methods (e.g. Gaussian elimination) are exact schemes that are generally more suitable for solving small to medium systems of equations. Whereas, iterative methods (e.g. Gauss-Seidel, and Preconditioned Conjugate Gradient (PCG)) are approximate schemes that allow very large systems to be solved efficiently.

6. Then calculate further field variables, such as nodal or elemental stresses, strain energy density, from the derived displacements.

3.3 Boundary Element (BE) Technique

The literature describing this powerful technique in detail has grown in popularity in recent years (see *Brebbia et al. (1984)*, *Becker (1992)*, and more recently *Wrobel and Aliabadi (2002)*). Hence, the full mathematical content of the theory will not be addressed; instead, a brief explanation of the technique and the fundamental mathematical procedures will be described such that the terminology used within later sections is clearly defined.

In this approach, only the surface or boundary of the problem under consideration is considered, as the name implies. The boundary is divided into a number of small segments over which the transformed governing differential equations, in the form of integral identities, are numerically integrated. As in the finite element approach, provided that the boundary conditions are satisfied, a system of linear algebraic equations emerges, for which a unique solution can be obtained.

3.3.1 Review of the BE formulation

To illustrate the Boundary Element approach, the following steps summarise the procedures and analytical formulation involved in a typical BE analysis:

1. Starting from the three governing equations for linear-elastic structural mechanics (Eqs. 3.1-3), combine the three relations into one single differential equation in terms of displacements (*Navier equation*):

$$\frac{\partial^2 u_i}{\partial x_j \partial x_j} + \left(\frac{1}{1-2\upsilon}\right)\frac{\partial^2 u_j}{\partial x_i \partial x_j} = \frac{-f_i}{\mu} \tag{3.5}$$

2. Then obtain the 'fundamental solution' for the differential equation. This is a solution that satisfies the differential equation of displacements (Navier) and at the same time has properties that are physically meaningful. The Navier equation in the form shown in Eq. 3.5, is difficult to solve analytically, hence, the above-mentioned equation must be converted into a biharmonic relationship for which analytical solutions can be easily sought. This is achieved by expressing the displacement vector in terms of a *Galerkin vector* (G_i),

$$u_i = \frac{\partial^2 G_i}{\partial x_j \partial x_j} - \left(\frac{1}{2(1-\upsilon)}\right)\frac{\partial^2 G_j}{\partial x_i \partial x_j} \tag{3.6}$$

and then substituting Eq. 3.6 back into the Navier equation 3.5 as follows:

$$\nabla^4 G_i = \nabla^2(\nabla^2 G_i) = \frac{-f_i}{\mu} \tag{3.7}$$

Next, consider the problem of a single concentrated force applied in the interior of an infinite domain, which is known as the *Kelvin problem* (see *Love (1944)*). Assume that a unit force is applied at a point p; find the effect of this force on another point q anywhere in the domain. The solution must satisfy two conditions:

(i) All stresses must vanish as the distance between p and q tends to infinity.

(ii) The stresses must be 'singular' at p itself (i.e. tend to infinity as the distance between p and q tends to zero).

It can be verified (see *Cruse (1977)*) that the following Galerkin vector is a solution of Eq. 3.7 and satisfies both the above-mentioned physical conditions:

$$G_i = \frac{1}{8\pi(1-\upsilon)} r(p,q) \tag{3.8}$$

where the function $r(p,q)$ is the physical distance between points p and q. Substituting Eq. 3.8 into Eq. 3.6, and dividing the displacement vector

components into tensor functions the *displacement kernel* is obtained, as follows:

$$U_{ij}(p,q) = \frac{1}{16\pi\mu(1-\upsilon)}\left[\frac{1}{r(p,q)}\right]\left[(3-4\upsilon)\delta_{ij} + \frac{\partial r(p,q)}{\partial x_i}\frac{\partial r(p,q)}{\partial x_j}\right] \tag{3.9}$$

The fundamental solution (Eq. 3.9) is a three-dimensional solution for a point load in an infinite medium. However, by considering the point load as a line load, or as a ring load, the two-dimensional and axisymmetric fundamental solutions can be obtained, respectively (see Appendix A).

3. Use the reciprocal work theorem (*Betti's theorem*). This theorem states that if two stress states (a) and (b) exist that satisfy equilibrium, then the work done by the forces of system (a) on the displacements of system (b) is equal to the work done by the forces of (b) on the displacements of (a), as follows:

$$\sum_p F_p^{(a)} u_p^{(b)} = \sum_p F_p^{(b)} u_p^{(a)} \tag{3.10}$$

where p is any point with a force F. If the external forces are confined to the surface (S) only, then the following integral equation can be obtained after some mathematical manipulation:

$$\int_S t_i^{(a)} u_i^{(b)} dS = \int_S t_i^{(b)} u_i^{(a)} dS \tag{3.11}$$

where i = 1, 2, 3 (corresponding to the Cartesian coordinates x, y, z, in a three-dimensional problem). Then, choose the (a) system to be the fundamental solution (known) and the (b) system to be the actual problem (unknown). The result is the *Somigliana identity for displacements*, *Somigliana (1885)*:

$$u_i(p) = -\int_S T_{ij}(p,Q)u_j(Q)dS + \int_S U_{ij}(p,Q)t_j(Q)dS \tag{3.12}$$

where u_i and t_i are displacements and tractions along the boundary of the real problem, U_{ij} is the *displacement kernel* given by Eq. 3.9, and T_{ij} is the *traction*

kernel arising from the fundamental solution. The *traction kernel* can be derived by differentiating the *displacement kernel* and substituting in the Hooke's law equation (Eq. 3.2), as follows:

$$T_{ij}(p,Q)=\frac{-1}{8\pi(1-\upsilon)r^2(p,Q)}\left[\frac{\partial r(p,Q)}{\partial n}\right]\left[(1-2\upsilon)\delta_{ij}+3\frac{\partial r(p,Q)}{\partial x_i}\frac{\partial r(p,Q)}{\partial x_j}\right]$$

$$-\frac{1-2\upsilon}{8\pi(1-\upsilon)r^2(p,Q)}\left[\frac{\partial r(p,Q)}{\partial x_j}n_i-\frac{\partial r(p,Q)}{\partial x_i}n_j\right] \qquad (3.13)$$

where n is the unit outward normal at the boundary point Q. The corresponding two-dimensional and axisymmetric *traction kernels* can be found in Appendix A.

Finally, by approaching the source point p to the boundary, and after a limiting process, the boundary integral equation (BIE) relating the displacements and tractions at the surface (boundary) can be obtained:

$$C_{ij}(P)u_j(P)=-\int_S T_{ij}(P,Q)u_j(Q)dS+\int_S U_{ij}(P,Q)t_j(Q)dS \qquad (3.14)$$

where C_{ij} is a matrix of constants dependent on the geometry at the boundary point P.

4. Divide the surface into segments or boundary elements. Use shape functions to describe the geometry and variables over each element. These shape functions, as with the FE method, may be linear, quadratic or higher order. Because analytical integrations are not practical due to the complexity of the integral functions, numerical integration is performed using the Gaussian quadrature technique. Special schemes are necessary to integrate the singular terms when the load point P coincides with the field point Q. This is because for a 3D problem the fundamental tensors U_{ij} and T_{ij} contain terms of the orders $O(r^{-1})$ and $O(r^{-2})$, respectively. By summing the integrals over each element, the total surface integral can be evaluated.

5. Form the system matrix using a method called collocation, which involves applying Eq. 3.14 with the load point P placed in turn at each boundary node. The load point P is first placed at node 1, which yields a set of three equations (for a 3D problem) relating to all N nodes on the surface. Then the load point P is placed at node 2, yielding another set of three equations, and so on until a set of $3N$ equations is formed. The resulting system of linear equations is of the following form:

$$[A][u]=[B][t] \tag{3.15}$$

where the matrices $[A]$ and $[B]$ contain the integrals of T_{ij} and U_{ij}, respectively, and where vectors $[u]$ and $[t]$ contain the displacements and tractions of the real problem, respectively.

6. Apply the boundary conditions. These take the form of either prescribed displacements or tractions. By rearranging the linear equations such that all the unknown variables are on the left-hand side, and all the known variables are on the right-hand side, the following modified system of equations is obtained:

$$[A^*][x]=[c] \tag{3.16}$$

where the vector $[x]$ contains a mixture of unknown displacements and tractions and the matrix $[A^*]$ is a modified form of $[A]$. The right-hand side vector $[c]$ is composed from the prescribed nodal values, multiplied by their corresponding influence coefficients.

7. Solve the overall system of linear equations. Since the system matrix is unsymmetric and fully populated with non-zero coefficients, direct solution techniques (e.g. Gaussian elimination, and LU decomposition), or specialised iterative methods (e.g. Generalised Minimal Residual method (GMRES), *Saad and Schultz (1986)*) should be used.

8. Then using the computed boundary displacements and tractions, further field variables can be calculated at the boundary and internal points.

3.4 Comparison between the Finite and Boundary Element techniques

Both the Finite Element (FE) and the Boundary Element (BE) approaches are very versatile and can easily accommodate geometrically complex problems. However, there are also fundamental differences and distinct advantages between the two methods in particular situations.

In general, the BE technique involves less data preparation time than the FE method, as a direct result of the 'surface' modelling approach adopted. As the dimensionality of the problem is reduced by one, the analyst should require less time to prepare and check the data, and subsequent changes in meshes are made easier. This advantage is particularly important in problems where re-meshing is required, such as preliminary design studies and crack propagation. The BE technique produces a higher resolution of stresses, because there are no further approximations imposed on the solution at interior points, i.e. the solution is continuous inside the domain. Hence, if the boundary discretisation models exactly the surface displacements and tractions for the body, and if the integration process is exact, the displacements and tractions calculated within the body will also be exact at all points. This makes the BE method very suitable for modelling problems of rapidly changing stresses, such as stress concentration, contact and fracture problems. Furthermore, in many engineering problems the analyst is only interested in the highest stress values that usually occur at the surface. Therefore, in these situations, the FE method would be less efficient as field variables are calculated at every nodal point. Finally, the BE method can also be used to model incompressible, rubber-like materials without numerical difficulties (*Becker (1992)*).

However, in certain situations involving non-linear problems, e.g. plasticity, the BE

method also requires localised internal discretisation and so, the main advantage of this technique is reduced. The FE approach is also more suitable than the BE method for problems which require thin shell analysis. Furthermore, as there seems to be very few user-friendly stress analysis BEM software packages, the power of this numerical method has been restricted.

A summary of the advantages and disadvantages of the two techniques is presented in Table 3.1.

	Finite Element Method (FEM)	**Boundary Element Method (BEM)**
Advantages	Complex analysis software (including pre- and post-processors) is commercially available Non-linear analysis can be incorporated within the FE method in a routine manner More suitable for problems requiring thin shell analysis	The order of accuracy of the stress analysis is high (no further approximations are imposed on the solution at interior points) Less data preparation time for a given problem (as a direct result of the 'surface' modelling approach) Less unwanted information (field variables at internal points are optional) Easily applicable to incompressible materials
Disadvantages	Stresses are not calculated directly, but from force/displacement behaviour, which limits the accuracy of the derived stresses Analyses requiring re-meshing, particularly if frequent (e.g. due to crack growth), are very time consuming Contact analysis requires approximations	Boundary Element Analysis software is less commercially developed Non-linear effects, such as plasticity, are more difficult to incorporate (interior modelling is unavoidable, and hence, the method loses its main advantage of a reduction in dimensionality) Changing the degree of dimensionality requires different fundamental solutions of the governing equations

Table 3.1 Comparison between the Finite and Boundary Element techniques with particular regard to stress analysis.

3.5 In-house Developed Boundary Element Analysis Program

For the physical problems considered within the following chapters, an in-house developed Boundary Element Analysis program and, for verification purposes, a commercial Finite Element Analysis software package (ANSYS 5.6), have been used to examine the different facets of the research. The BEA program is suitable for both two-dimensional (plane strain and plane stress) and axisymmetric problems, and allows the use of constant, linear and quadratic boundary elements. Furthermore, the code can model linear-elastic problems involving contact (conforming or non-conforming, frictionless or frictional) and fracture (stationary or propagating). The program has three main parts: a pre-processor, an analysis block, and a post-processor, Figure 3.3.

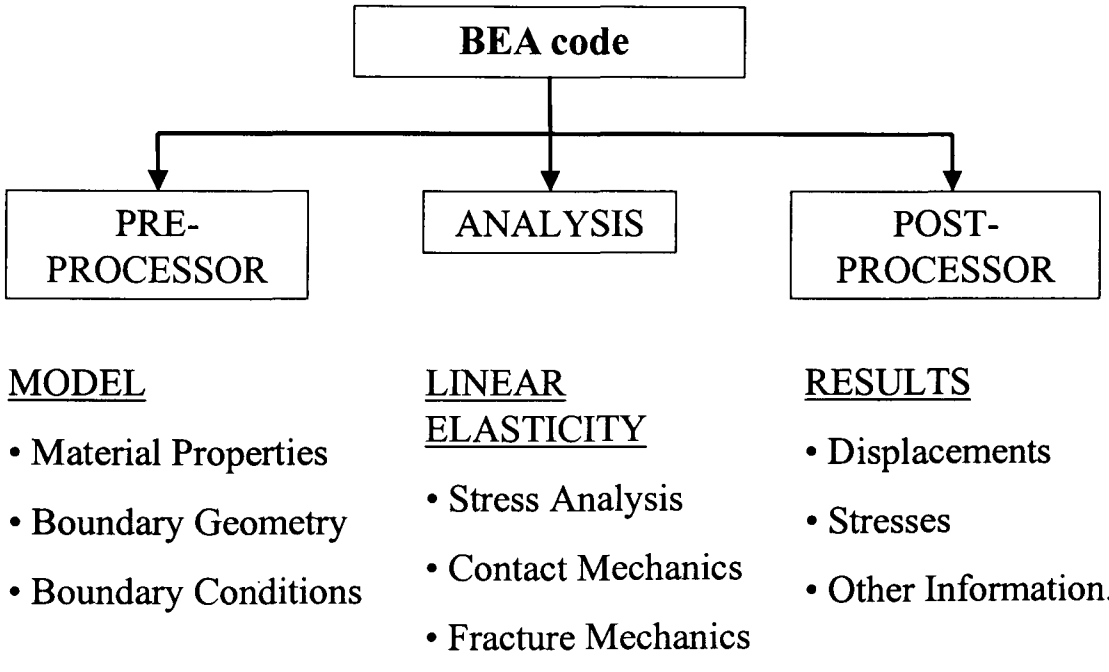

Figure 3.3 Outline of the in-house developed BEA program

The BE program is particularly well suited to the types of problems considered within the following chapters, which involve linear stress analysis, frictionless and frictional contact, and crack growth.

3.5.1 Stress Analysis

In the present BE program, a typical stress analysis problem follows steps 4-8 indicated in section 3.3.1. Surface modelling is accomplished using linear, circular and parabolic shape functions, which are then meshed using constant, linear or quadratic elements. The discretisation may be homogeneous or refined along the boundaries using a geometric-progression spacing algorithm, depending on the problem.

In addition, an iterative solver (GMRES) has been implemented within the program to substantially reduce the computational time to solve large systems of equations. For instance, a problem involving 8000 degrees of freedom (d.o.f.) solved on a typical Pentium III, 600 MHz desktop computer took in the region of six hours using the existing LU decomposition method (direct method), compared to approximately forty minutes using GMRES.

3.5.2 Contact Analysis

For contact problems the BE method has certain advantages because, while the standard FE technique only utilizes displacement degrees of freedom, the BE technique employs degrees of freedom in terms of both displacements and surface forces. Therefore, compatibility of displacements and equilibrium of forces can be directly enforced at the contacting surfaces.

Classification of Contact

Contact problems may be categorised by the degree of resistance of the two surfaces to sliding (*frictionless* and *frictional* contact), the undeformed contact geometry (*conforming* and *non-conforming* contact), and the development of the contact area (*advancing* and *receding* contact).

Frictionless contact is an idealised contact mode, which can be associated with well-lubricated smooth surfaces. It is assumed that the contacting surfaces are able to

slide over each other without any resistance along the tangential direction (i.e. parallel to the contact interface). In the absence of friction, stresses in the tangential direction are zero and the evolution of contact is independent of loading history (i.e. frictionless problems in linear elasticity are therefore linear). *Frictional* contact is a more realistic mode in which the sliding movement in the tangential direction of a point in contact is restricted by the frictional forces (tangential shear stresses) at the point of contact, which in turn depend on the normal component of the forces (normal stresses) exerted at the same point. The relationship between the tangential and normal components of forces results in a nonlinear behaviour between the sliding movement of the contact surfaces and the external load. In frictional contact, the contact conditions are either *stick* (i.e. no relative tangential displacements), or *slip* (i.e. sliding against resistance in the tangential direction).

Conforming contact refers to the type of problem in which the contacting surfaces 'match' each other in the unloaded state. For example, a flat punch resting on a flat foundation, or a perfect-fit pin in a hole, are conforming contact problems. A key feature of this type of contact problem is that the extent of the contact area is independent of the load. For this reason, the load can be applied in a single step. *Non-conforming* contact refers to problems with different profiles for the contacting surfaces. The main feature is that the size of the initial contact area will change once the bodies are subjected to external loading/unloading, hence a load step incrementation process is required. This type of problem can rarely be solved analytically, and is the most challenging for computational methods.

Advancing or *progressive* contact is relevant to most contact problems, as in most non-conforming contact problems the bodies initially touch at a point or along a line, and the area of contact grows with increasing load. *Receding* contact refers to a type of problem in which the contact is initially over an appreciable area, and when loaded it will deform in such a way that the contact area is decreased. For example, a perfect-fit pin in a hole will initially touch around the whole circumference, but when the surrounding

material is loaded perpendicular to the pin axis, the contact area is reduced as a gap develops between the pin and the hole.

In practice, other types of contact in addition to above will exist, e.g. rolling contact. However, the contact problems considered in Chapters 4 and 5 can be considered to be frictionless or frictional, conforming and receding.

Numerical Modelling Concept

The numerical modelling of practical contact problems is generally more complicated than other problems for the following reasons:

1. Although the material behaviour of each contacting body may be assumed linear, contact problems are nevertheless non-linear because the contact area does not change linearly with the applied load.
2. In most practical problems, the actual contact area is not known in advance and can only be estimated as part of the solution.
3. In frictional contact problems, the behaviour may be load history dependent. This means that the load must be applied in small steps (increments) until the final load is reached.

In a typical contact problem, at least two bodies are involved. Generally, when the bodies come into contact, only parts of each boundary are in contact with each other, therefore their total boundaries (S) may be divided into regions of potential contact (S_c) and non-contact (S_{nc}), as shown in Figure 3.4, i.e.

$$S = S_{nc} + S_c \tag{3.17}$$

The non-contact areas, after discretisation, are conventionally composed of nodes with two prescribed values and two unknowns each. Whereas, the potential contact areas are discretised by matching the nodal points of each contacting body, forming contact node pairs with eight unknown variables each. To account for these eight unknowns, four additional equations (accounting for equilibrium and compatibility conditions) are

necessary at each contact node pair to produce a well-defined mathematical model. Equilibrium conditions enforce equal and opposite tractions along and across the mating surfaces, and compatibility conditions enforce continuity of displacements in the normal contact direction (i.e. no overlap).

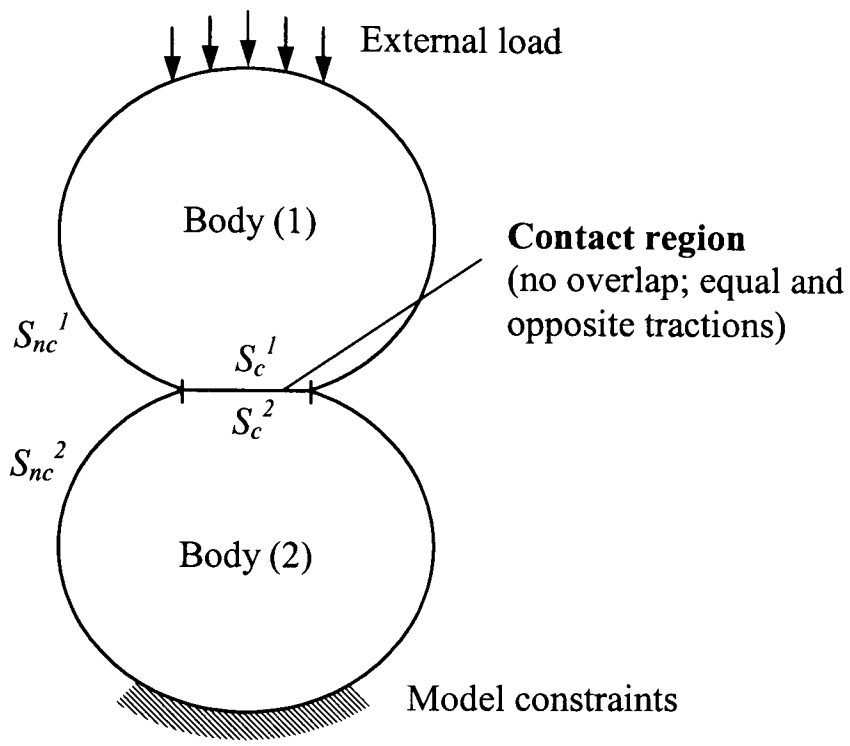

Figure 3.4 Schematic representation of two bodies in contact.

For a given contact state, the contact conditions of a contact node pair may be represented by any one of three modes of contact: *separation*, *slip* and *stick*. Separation mode defines node pairs that remain apart, slip mode indicates node pairs that are in contact and experience a relative tangential displacement, and stick mode relates to node pairs in contact that are restrained in the tangential direction (frictional contact only). Each of these contact modes can be defined mathematically at each node pair (*a* and *b* say) as follows (*de Lacerda and Wrobel (2000)*):

Equilibrium -	$t_t^{(a)} - t_t^{(b)} = 0,$	$t_n^{(a)} - t_n^{(b)} = 0$	Separation/Slip/Stick mode
Compatibility -	$t_t^{(a)} = 0,$	$t_n^{(a)} = 0$	Separation mode

$$t_t^{(a)} \pm \mu t_n^{(a)} = 0, \qquad u_n^{(a)} + u_n^{(b)} = 0 \qquad \text{Slip mode}$$

$$u_t^{(a)} + u_t^{(b)} = 0, \qquad u_n^{(a)} + u_n^{(b)} = 0 \qquad \text{Stick mode}$$

where t_t and t_n are the tangential and normal tractions, u_t and u_n are the tangential and normal displacements, respectively, expressed in local coordinates, and μ is the friction coefficient of the mating surfaces.

To arrive at the system matrix, each domain is treated separately to form the matrices of Eq. 3.15. At the contact region, these two systems of equations share the boundary variables, that is the equations are coupled according to the relevant contact conditions above and must be solved simultaneously. Once the boundary conditions are applied and the equations are rearranged such that all the unknown variables are on the left-hand side, and all the known variables are on the right-hand side, a unified system of equations is generated (Eq. 3.16).

As the extent of contact may not be known *a priori*, it must be determined as part of the solution. This means most contact problems require an iterative solution procedure to obtain the correct contact area and stick-slip zone. After each iteration, the following three checks can be performed:

1. *Edge overlap check.* The displacements of the pairs of elements just outside the assumed contact area are checked to determine whether overlap has occurred. The detection of overlap is an indication that the contact area is too small for the given load, and the overlapped element pairs must be included in the contact area in the next iteration.

2. *Tensile stress check.* All contacting element pairs are checked to determine if tensile stresses have been generated. The detection of tensile stresses in the contacting elements is an indication that the contact area is too large for the given load and these elements must be released from contact in the next iteration.

3. *Friction slip check.* If friction is present, relative sliding of the two bodies in contact will occur when the tangential traction at any point in the interface exceeds the product of the normal traction at that point and the friction coefficient, as follows:

$$|t_t| \geq |\mu t_n| \qquad \text{Slip mode}$$

$$|t_t| < |\mu t_n| \qquad \text{Stick mode}$$

In such problems, the element pairs are assumed to be in stick mode for the first iteration. This allows the sign of the tangential traction to be determined for the next iteration (where slip will be allowed).

During the iterative process, coefficients in $[A^*]$ and $[c]$ of Eq. 3.16, derived from inside the contact zone only, may change from one iteration to the next; the number of changes in matrix $[A^*]$ is small because the number of elements whose contact conditions change is usually a small fraction of the total. Under normal procedures the entire system of equations would have to be reordered for the next iteration, in order to accommodate the changes in the contact zone. Repetition of this procedure, until the final solution is found, would be inefficient.

In order to solve the updated system of equations efficiently, a high-speed reanalysis algorithm, based on the Sherman-Morrison formula (*Press et al. (1992)*) has been implemented. This algorithm only requires one full LU decomposition of the complete system of BE equations, for the first load step. Updated solutions for subsequent load steps can be quickly obtained, from the solution of the previous step, by using specific correction factors. The algorithm is very efficient for receding contact problems, with and without friction, of the type studied here, *de Lacerda and Wrobel (2000)*.

Figure 3.5 shows the algorithm implemented within the BEA code for contact analysis (total loading).

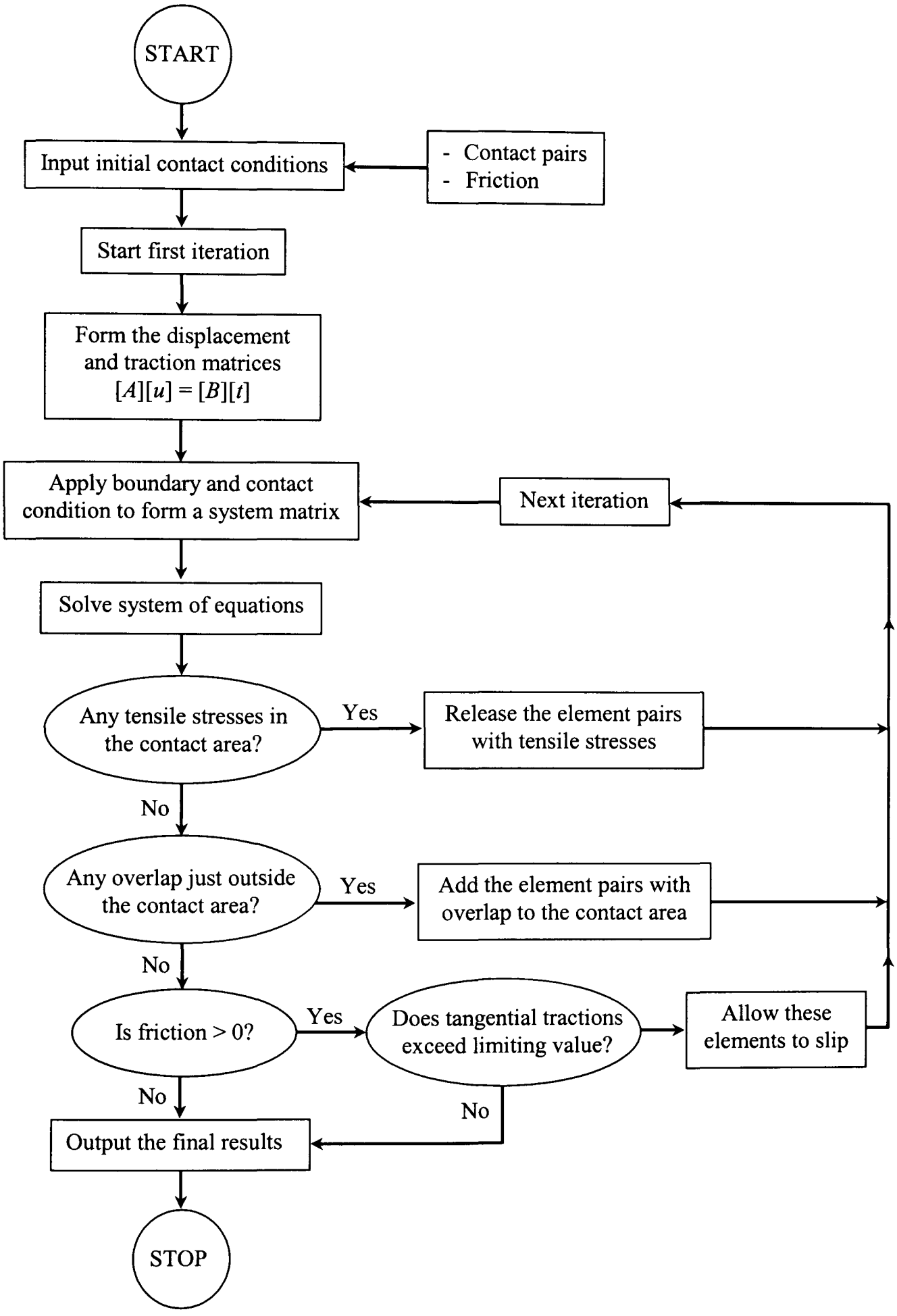

Figure 3.5 Flow chart for the contact iterations.

3.5.3 Fracture Analysis

Fracture problems involving crack growth can be efficiently analysed using the dual BE technique, as the extension of the crack may be modelled simply by inserting further elements at the crack tip in the appropriate directions. Whereas, within most of the present FE formulations, there is a need for continual remeshing to follow the crack extension (*Swenson and Ingraffea (1988)* and *Kocer and Collins (1998)*), which can make this method rather time-consuming and computationally wasteful. Remeshing implies redefining part of the mesh of the numerical model and consequently, the redefined elements must have their matrices recomputed before the system of algebraic equations corresponding to the current configuration of the structure can be solved.

Linear Elastic Fracture Mechanics (LEFM)

In the present BEA program, linear elastic fracture mechanics (LEFM) theories are applied (*Irwin (1957)*). This assumes that the material containing a crack will have infinite stresses at the tip. In practice, however, such infinite stresses do not occur, and the material yields at the crack tip, creating a plastic zone surrounding the crack tip. LEFM theories assume that the size of this plastic zone is small compared to other crack dimensions (rather than ignoring the effect of plasticity); hence, only brittle fracture can be adequately modelled.

In addition, the fundamental postulate of LEFM is that the behaviour of cracks (i.e. whether it grows or not, and how fast it grows) can be determined solely by the value of the *stress intensity factors*, K_I, K_{II}, and K_{III}. (The stress intensity factor should not be confused with the 'stress concentration factor', which is the value of a stress at a stress raiser, i.e. a notch or hole, divided by the nominal stress. The stress intensity factor is not a stress value as such, but a measure of how close the crack is to its critical length (when it starts propagating)). The subscript denotes the modes of deformation of the cracked body. These modes are characterised by the movements of the upper and lower crack surfaces with respect to each other, and are shown in Figure 3.6; they are referred to as:

opening or *tensile mode* (mode I), where the two crack surfaces are pulled apart; *sliding* or *in-plane shearing mode* (mode II), where the crack surfaces slide over each other along the crack line; and *tearing* or *out-of-plane shearing mode* (mode III), where the crack surfaces slide over each other perpendicular to the crack line. Note that mode III deformation is not possible within the present BEA program, as only two-dimensional problems can be modelled.

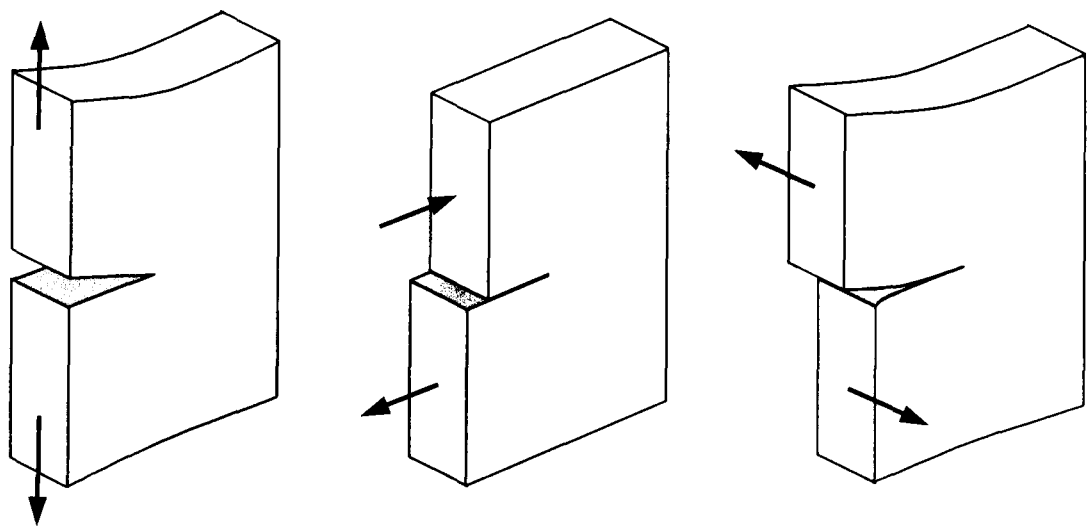

Mode I (opening mode) | Mode II (sliding mode) | Mode III (tearing mode)

Figure 3.6 The basic deformation modes for a cracked body, *Wrobel and Aliabadi (2002).*

From these three basic modes any crack deformation can be represented by an appropriate superposition:

$$K_{eq} = f(K_I, K_{II}, K_{III}) \tag{3.18}$$

where K_{eq} is an equivalent stress intensity factor, defined in a mixed-mode analysis. In general, K_{eq} will be a function of the crack size and shape, the modes of loading and the geometrical configuration of the structure. As K_{eq} reaches a critical value (known as K_c), catastrophic structural failure occurs, i.e. the crack is presumed to grow in an uncontrollable manner through a fracturing process. K_c is often referred to as the *fracture toughness* of the material, and is a material property independent of the geometry or applied loads. Hence, the structure can be designed to be safe from fracture by ensuring

that $K_{eq} < K_c$.

Numerical Modelling Concept

The crack surfaces of a typical fracture problem are modelled in the BEA program using coincident boundaries. However, using the standard boundary element formulation based on the displacement boundary integral equation (Eq. 3.14), nodal coincidences along the crack boundaries give rise to an ill-posed problem, in which a single equation is available for two load points. The equation for the load point located on one side of the crack is identical to that of the opposite load point located on the other side of the crack, as they both have the same coordinates and integration path. Some special techniques have been devised to overcome this difficulty. Among these, the most important are: the crack Green's function method, *Snyder and Cruse (1975)*; the displacement discontinuity method, *Crouch (1976)*; the subregions method, *Blandford et al. (1981)* and the dual boundary element method, *Portela et al. (1993)*, and *de Lacerda and Wrobel (2001)*. Of these techniques the dual boundary element method is the most general procedure, and is adopted within the present BEA program.

The dual boundary element method overcomes the crack modelling difficulty by introducing an additional traction boundary integral equation along the crack, as follows:

$$\frac{1}{2}t_j(P) = -n_i(P)\int_S S_{kij}(P,Q)u_k(Q)dS + n_i(P)\int_S D_{kij}(P,Q)t_k(Q)dS \qquad (3.19)$$

where n_i is the unit outward normal to the boundary at point P, and S_{kij} and D_{kij} contain the derivatives of U_{ij} and T_{ij}, respectively. Hence, the displacement boundary integral equation (Eq. 3.14) is applied to load points on one surface of the crack, and the traction boundary integral equation (Eq. 3.19) to load points on the other crack surface. Although the integration path is still the same for coincident load points, the respective boundary integral equations are now distinct, giving rise to a mathematically well-posed formulation.

In a physical fracture problem, discontinuous linear elements are employed for discretisation of the cracks. Discontinuous elements have their edge nodes shifted towards the centre of the element, enforcing smoothness at the boundary nodes, which in turn allows the traction boundary integral equation (Eq. 3.19) to be uniquely defined.

For crack-growth problems, an incremental crack-extension analysis is required to predict the crack path. Note that the process of crack propagation is assumed to be 'quasi-static', and dynamic effects are not taken into account. Quasi-static implies that the crack is stationary at each crack increment, therefore the problem can be considered to be time independent. For each increment of the analysis, in which the crack extension is modelled with new boundary elements, the dual boundary element method is applied for the stress analysis and the modified crack closure method (*de Lacerda and Wrobel (2001)*) is used for the evaluation of the crack tip stress intensity factors. The modified crack closure integral method evaluates the stress intensity factors, using the normal and tangential stresses in front of the crack tip and also the relative normal and tangential displacements along the crack path. The energetics of the crack tip may also be estimated using other techniques, which include: the *J*-integral method, *Portela et al. (1993)*; from localised stress fields near the crack tip, *Kocer and Collins (1998)*, and from a global energy approach, which evaluates the work done by the external loads, *Bush (1997)*. As stated earlier, if the equivalent stress intensity factor (K_{eq}) is higher than the fracture toughness (K_c) of the material, the crack will grow until $K_{eq} < K_c$.

The maximum principal stress criterion is used to calculate the crack growth direction, as it is the most commonly used fracture criteria in the literature. This criterion predicts that the crack will grow perpendicularly to the principal stress direction at the crack tip. Knowledge of the stress intensity factors (K_I, K_{II}) is sufficient to calculate this direction (*de Lacerda and Wrobel (2001)*):

$$\theta = 2\tan^{-1}\left[\frac{1}{4}\left(\frac{K_I}{K_{II}} \pm \sqrt{\left(\frac{K_I}{K_{II}}\right)^2 + 8}\right)\right] \tag{3.19}$$

where θ is measured from the crack axis ahead of the crack tip. Notice that the predicted angle does not take into account the length of the increment, so a correction is necessary to adjust this orientation. This predictor-corrector technique is an iterative procedure, which can be used very efficiently with the dual boundary element method and an *LU* solver, *Portela et al. (1993)*.

Once this direction is defined, a crack increment is added to the system: one pair of boundary elements with length comparable to the tip element size. This procedure constitutes an extremely easy re-meshing approach. Moreover, the added pair of elements only contributes with a few extra rows and columns to the system of equations (see Figure 3.7), which can be very efficiently solved using an incremental *LU* decomposition method. This algorithm only requires one full *LU* decomposition of the complete system of BE equations corresponding to the initial configuration. Then, by decomposing the newly formed rows and columns, the solutions for subsequent crack increments can be quickly obtained.

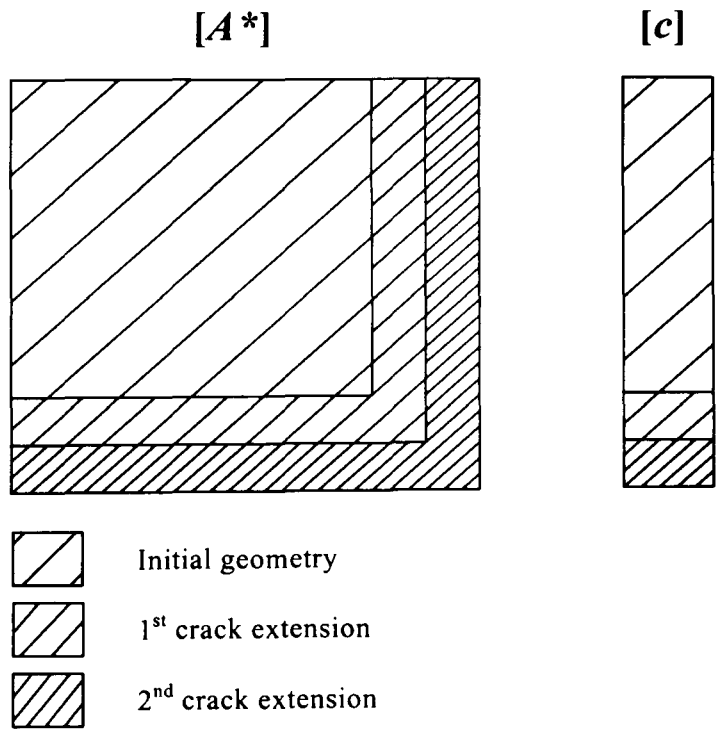

Figure 3.7 Incremental generation of the system of equations, *Portela (1993)*.

3.6 Summary

The main numerical simulations in the present studies are concerned with two-dimensional linear stress analyses of multi-domain problems involving localised stress concentrations, contact mechanics (frictionless or frictional, conforming and receding) or fracture mechanics (stationary or quasi-static crack growth) for two- or three-phase composite materials. These particular topics have been selected because of their relevance to engineering situations involving important classes of composite materials, e.g. glass fibre or carbon fibre reinforced plastics. As noted in this chapter, there are three principal techniques for such analyses, i.e. finite difference (FD), finite element (FE) and boundary element (BE). The BE method is more appropriate in this research because of its surface modelling approach. The consequences of this are that the contact conditions are more precisely modelled and that quasi-static crack propagation requires very simple re-meshing, thus its analysis is computationally efficient. In contrast, there are other types of applications, such as non-linear analysis, where the FE formulation is more suitable.

The BE method is employed in the form of an in-house developed program. This code is suitable for both two-dimensional (plane strain and plane stress) and axisymmetric problems, and allows the use of constant, linear and quadratic boundary elements. Furthermore, the code can model linear-elastic problems involving contact (conforming or non-conforming, frictionless or frictional) and fracture (stationary or propagating).

For verification purposes, a commercial Finite Element Analysis software package (ANSYS 5.6) is also employed. Both linear stress and contact analysis can be modelled, however it is not well suited for analysing crack growth.

Chapter 4: Interfacial Stresses around Spherical and Cylindrical Inclusions

4.1 Introduction

Modelling of the bulk properties of composites, such as elastic moduli, can be performed with a good degree of accuracy in many situations. However, to be able to determine other properties of these materials, such as strength, it is necessary to develop a thorough understanding of the localised stress distributions. Previous studies have highlighted the significance of second phase inclusions on the localised stress distributions for a range of limited conditions (*Goodier (1933)*, *Stippes et al. (1962)*, *Wilson and Goree (1967)*, and *Lui and Nauman (1990)*). However, a full evaluation of the problem for a wide range of controlling factors is still lacking. For example, there have been no previous studies that have parametrically investigated the influence of Poisson's ratio, or analysed the development of fully frictional contact conditions. Consequently, the purpose of this chapter is to analyse the disturbing effect of fully- and non-bonded, spherical and cylindrical inclusions on an otherwise uniformly stressed elastic solid, using the BE technique.

A further reason behind these analyses is to establish a BE computer model, which gives accurate and reliable results compared to that of a commercial FE package and other previous numerical and analytical models. This means that when the BE program is used for more complex and novel analyses; there can be a good degree of confidence in the results.

4.2 Model Description

4.2.1 Geometry and Materials

This problem concerns the localised stress distributions produced around a spherical (particle) or cylindrical (fibre) inclusion within an infinite matrix under fully bonded or contact conditions, with or without friction. The simple inclusion geometry (i.e. circular) was chosen since it is a reasonable representation of the most commonly used fibres, e.g. glass and carbon, and allows comparisons with readily available analytical solutions. Studies of more complex inclusion shapes under fully-bonded conditions can be found, for instance, in *Biswas et al (1997)*. The stress distributions have been examined as a function of:

- Elastic moduli ratio (E_i/E_m), where $i \equiv$ inclusion and $m \equiv$ matrix,
- Poissons ratios (υ_i or υ_m),
- Relative particle/matrix dimensions, and
- Interfacial conditions (i.e. fully bonded/non-bonded, with or without friction).

The term 'fully-bonded' implies that displacements will be continuous across the interface between the different phases, and that no separation can occur. Whereas, the term 'non-bonded' implies that the interface is free to slide or separate, and that within the contact region the normal components of displacements must be continuous.

The material phases are assumed to be homogeneous and isotropic, and behave purely elastically.

4.2.2 Finite Element and Boundary Element Modelling

The FE and BE meshes for this axisymmetric (in which case the inclusions represent particles) and plane strain (which is equivalent to the inclusions representing fibres) problem, have been carefully designed with finer elements placed along the interface between the inclusion and the dissimilar matrix. This is to ensure that the stress gradients

at and close to the interface between the two phases are accurately captured. Typical BE meshes comprised approximately 300 linear elements in the contact region (non-bonded) or 180 quadratic interface elements (fully-bonded), and 20 quadratic elements along external boundaries, whereas the FE meshes comprised approximately 4500, six node plane quadratic elements and 180 surface-to-surface quadratic contact elements (non-bonded). Figures 4.1-2 shows typical BE and FE meshes of the problem under consideration, respectively.

In the particular models shown, the matrix is subjected to a unit tensile, uniaxial stress (σ_o) in the z-direction (axisymmetric) or in the y-direction (plane strain), and due to the symmetry of the problem, only a quarter of the problem needs to be modelled with symmetry boundary conditions applied along the r, z (axisymmetric) or x, y (plane strain) axes. It should be noted that along the lines of symmetry the BE model need not be discretised and hence, the boundary curve of the matrix becomes an open one. The inclusion-matrix diameter ratio of 0.2 was specifically chosen to correspond with the work of *Park et al.(1995)*, as they believed this ratio adequately represented an infinite

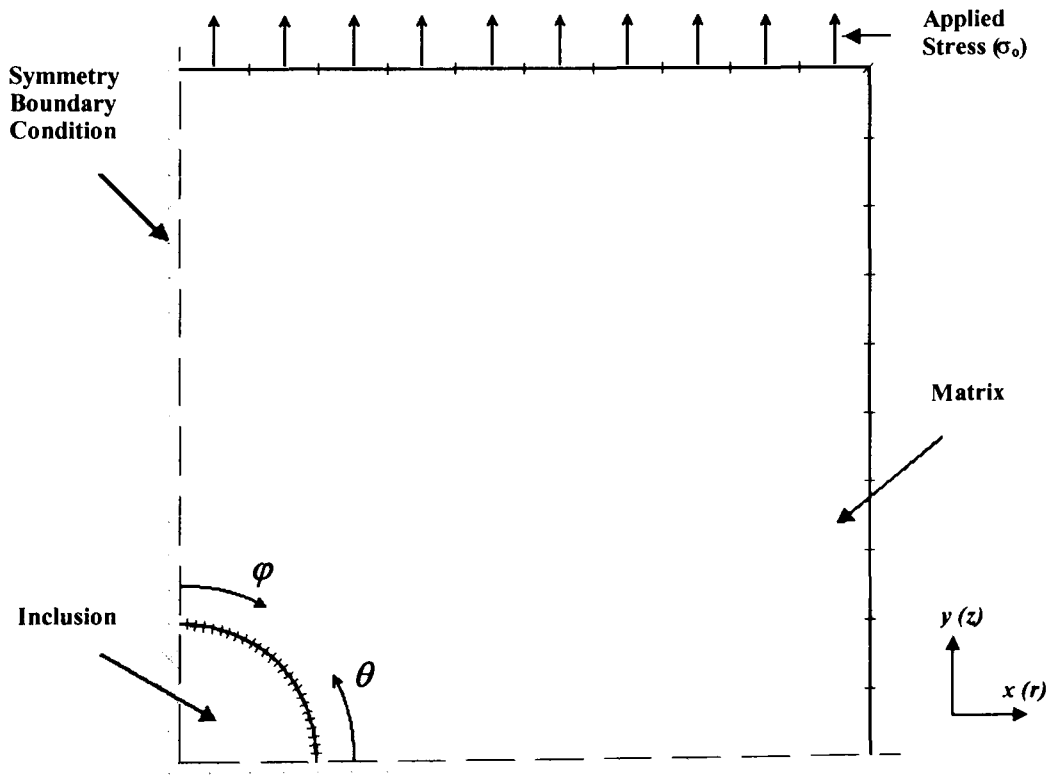

Figure 4.1 Typical 2D Boundary Element model of a single fibre/particle within a finite matrix under an externally applied load. Model axes are z, r (axisymmetric) and y, x (plane strain).

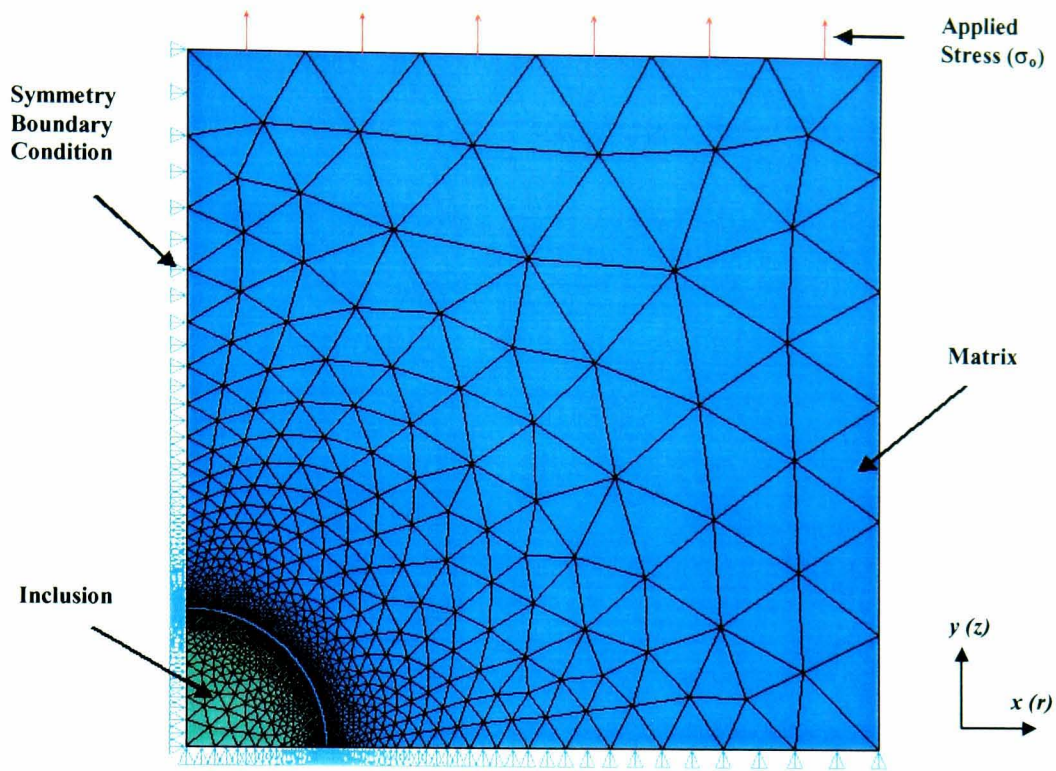

Figure 4.2 **Typical 2D Finite Element model of a single fibre/particle within a finite matrix under an externally applied load. Model axes are *z*, *r* (axisymmetric) and *y*, *x* (plane strain).**

matrix model; however, as discussed later, this is only true for the axisymmetric problem.

4.3 Results and Discussion

In the first part of this subsection, the simple case of a fully-bonded inclusion embedded within a dissimilar matrix will be considered, then following this analysis, the more complicated problem involving non-bonded contact will be addressed. Note that the results presented along the interface between particle/fibre and matrix are normalised with respect to the applied stress (σ_o).

4.3.1 Fully-Bonded Problem

The emphasis of this chapter is to analyse the interfacial stresses within the physical problem. In addition, brief consideration will also be given to the distribution of stresses within the inclusion and embedding matrix. The first principal stress (S1) was measured,

as it is widely regarded as a good indicator of the onset of failure in brittle materials subjected to tensile loading, *Beer and Johnston (1992)*. Figure 4.3 shows contour plots of the variation of the first principal stresses within the particle and fibre models, respectively. Typical material properties were chosen for both models, i.e. an elastic moduli ratio of ten, and Poisson's ratios of 0.3 for both phases.

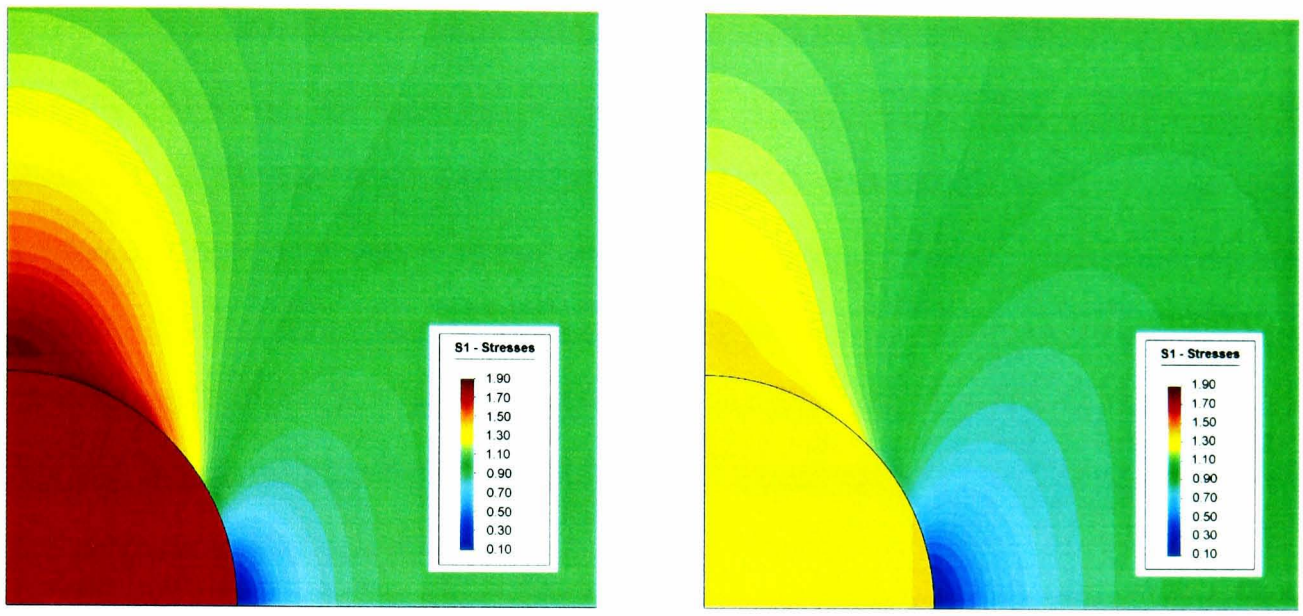

(a) (b)

Figure 4.3 Contour plot indicating the variation of first principal stress (S1) within the particle (a), and fibre (b) inclusion model. (*Fully-bonded*, $E_i/E_m = 10$, $\upsilon_i = \upsilon_m = 0.3$)

From this figure it is noticeable that the highest concentrations of stress, in both cases, are within the matrix near the interface along the vertical axis and at the interface at approximately $\varphi = 22^{\circ}$. In addition, the stresses within the inclusions are nearly uniform (approximately 97 percent of the maximum stress), which is due to the relative rigidity of the inclusion. Finally, the magnitudes of the stresses are found to be higher in the particle model, when compared to the corresponding fibre inclusion model. Note that the results presented in Figure 4.3 are practically identical to the corresponding z-direction (axisymmetric) or y-direction (plane strain) stress distributions (not shown).

Effect of Relative Inclusion Stiffness

Figure 4.4 shows the computed normal interfacial stress (σ_n) distribution around a particle/fibre inclusion for a range of material properties (E_i/E_m). Results obtained from both the FE and BE techniques are presented.

This clearly shows that as the inclusion becomes more rigid relative to the matrix material ($E_i/E_m > 1$), the stresses generally become more tensile with a maximum value at $\varphi = 0^\circ$. Curiously, however, the stresses near $\varphi = 90^\circ$ become slightly compressive due the contraction of the matrix perpendicular to the applied load caused by the Poisson's ratio chosen ($\upsilon_i = \upsilon_m = 0.3$). As the inclusion becomes less rigid ($E_i/E_m < 1$) this effect is then reversed. Similar trends are produced for both the particle and fibre inclusion, but the stress concentration effect is more noticeable with the particle inclusion. Finite Element (FE) and Boundary Element (BE) results are also compared within Figure 4.4 and very good agreement is achieved.

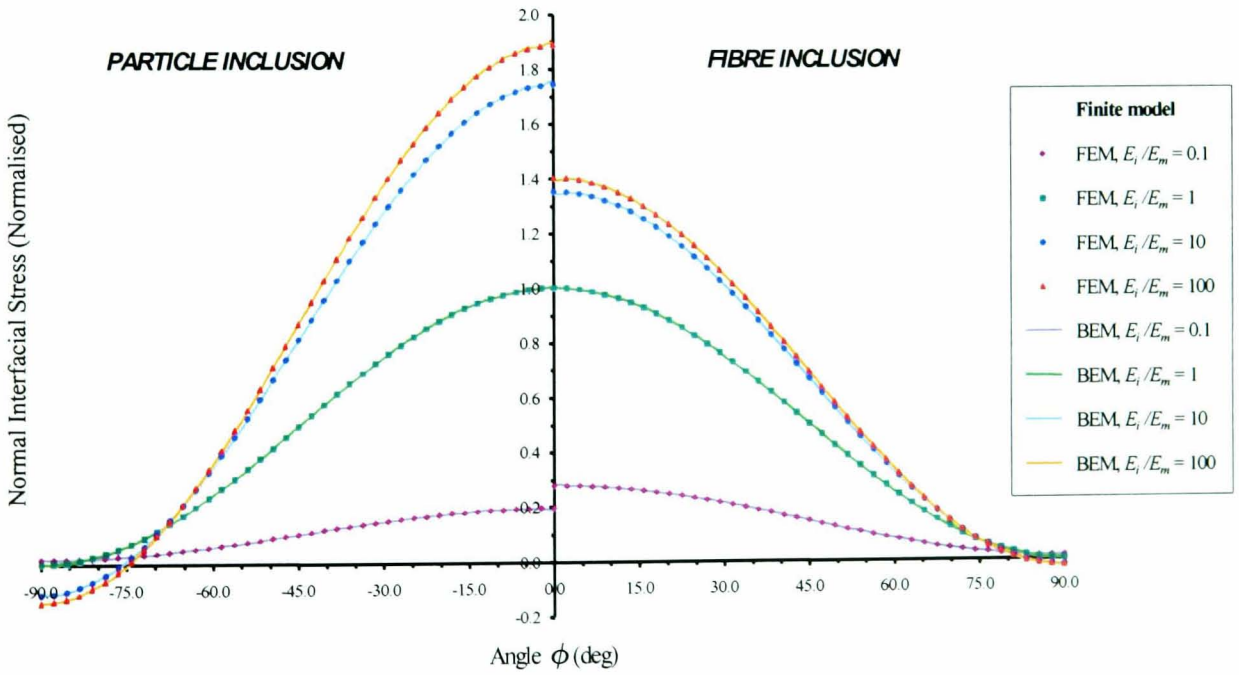

Figure 4.4 **Effect of the elastic moduli ratio (E_i/E_m) on the normal interfacial stress (σ_n) distribution under uniaxial tension. (*Fully-bonded*, $\upsilon_i = \upsilon_m = 0.3$)**

Effect of Model Geometric Dimensions

To analyse whether the inclusion-matrix diameter ratio of 0.2 adequately represented an infinite matrix model, a convergence study was conducted to examine the changes in the normal interfacial stress as the geometrical ratio decreased (i.e. the external boundaries are moved further away from the interface region). The normal interfacial stresses from the 'finite model' (inclusion-matrix diameter ratio of 0.2) are plotted against the converged results for an 'infinite model' in Figure 4.5.

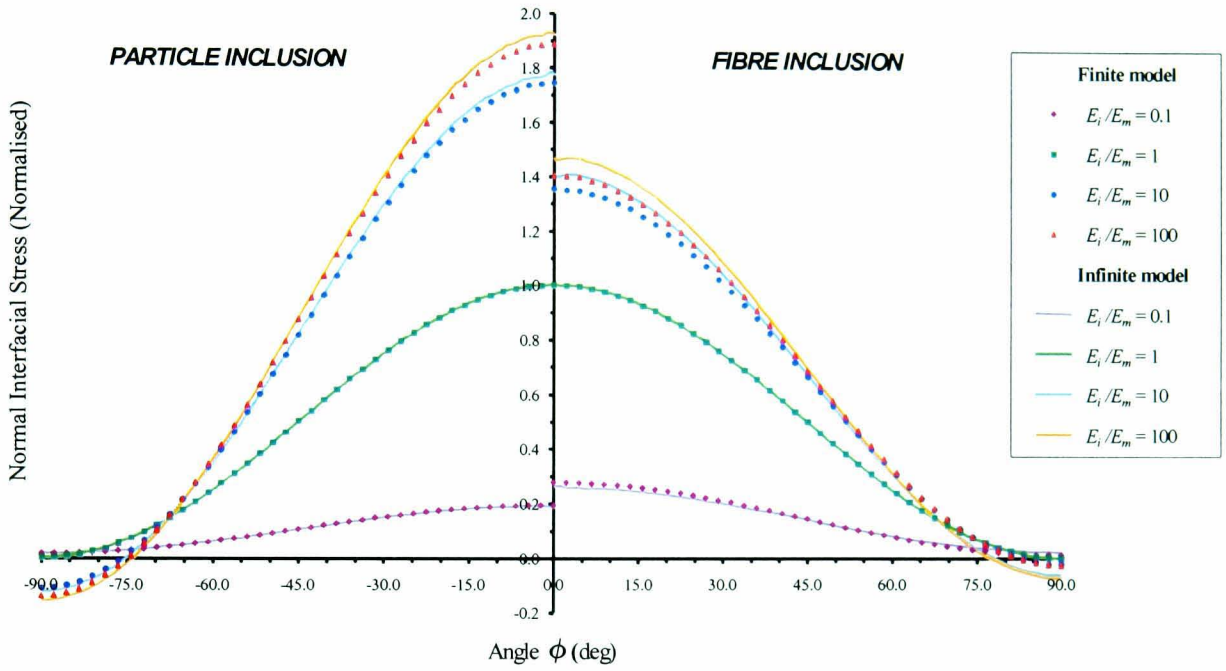

Figure 4.5 Effect of the relative inclusion/matrix dimensions on the normal interfacial stress (σ_n) distribution under uniaxial tension. (*Fully-bonded*, $\upsilon_i = \upsilon_m = 0.3$)

Although, the level of accuracy of the finite model is generally high, the difference is more noticeable for a fibre inclusion where the error in σ_n is as high as 4.7%. Many authors have proposed analytical solutions for a bonded inclusion embedded within a dissimilar, infinite media undergoing uniaxial tension, previously. For the fibre inclusion problem, normal stresses at the interface between the phases can be calculated as follows (see *Goodier (1933)*, and *Muskhelishvili (1977)*):

$$\sigma_n = \frac{\sigma_o}{2}\left[\alpha + \beta \cos 2\varphi\right] \tag{4.1}$$

in which,

$$\alpha = \frac{2\mu_i(1-\upsilon_m)}{\mu_i + \mu_m(1-2\upsilon_i)} \tag{4.2}$$

$$\beta = \frac{4\mu_i(1-\upsilon_m)}{\mu_m + \mu_i(3-4\upsilon_m)} \tag{4.3}$$

where σ_o is the applied stress at infinity and α, β are constants dependent on the material properties of the two phases. Considering the extreme case of a nearly rigid inclusion, i.e. E_i/E_m = 100 and $\upsilon_i = \upsilon_m$ = 0.3, the values of 1.394 and 1.547 are calculated for the constants α and β respectively from Eqs. 4.2-3. Substituting these constant values into Eq. 4.1 normal stress values of 1.4707 and -0.0763 are obtained at ϕ = 0° and 90°, respectively. Comparing these theoretical values with the results obtained from the infinite BE model, i.e. σ_n = 1.471 and -0.076, good agreement is achieved (see Figure 4.5).

For the particle inclusion problem, normal stresses at the interface between the phases can be calculated using the following α, β constants, substituted into Eq. 4.1 (see *Goodier (1933)*, and *Lui and Nauman (1990)*):

$$\alpha = \frac{2\mu_i(1+\upsilon_i)(1-\upsilon_m)}{(1+\upsilon_m)\left[2\mu_m(1-2\upsilon_i)+\mu_i(1+\upsilon_i)\right]} + \frac{5\mu_i(1-\upsilon_m)}{\mu_m(7-5\upsilon_m)+2\mu_i(4-5\upsilon_m)} \tag{4.4}$$

$$\beta = \frac{15\mu_i(1-\upsilon_m)}{\mu_m(7-5\upsilon_m)+2\mu_i(4-5\upsilon_m)} \tag{4.5}$$

Considering a nearly rigid inclusion, as before, normal stress values of 1.9199 and -0.1573 at ϕ = 0° and 90°, respectively are obtained for the analytical expressions. Comparing these theoretical values with the results obtained from the infinite BE model, i.e. σ_n = 1.918 and -0.157, good agreement is also achieved (see Figure 4.5).

Effect of Poisson's Ratio

The effect of Poisson's ratio mismatch on the normal interfacial stress will now be considered. From the numerical BE results shown in Figure 4.6 it is noticeable that for

$\upsilon_i / \upsilon_m < 1$ the stresses along the interface of both the fibre and particle reduce, whereas for $\upsilon_i / \upsilon_m > 1$ the stresses increase. This can be verified analytically using the expression above.

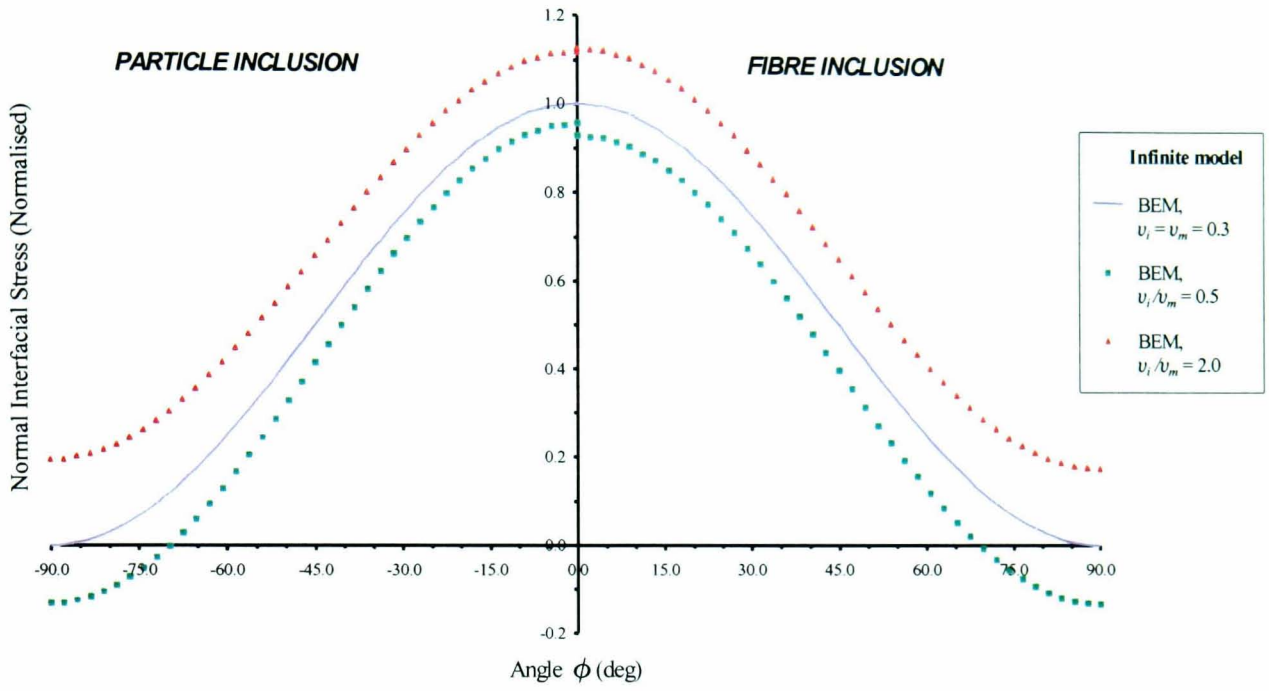

Figure 4.6 Effect of a Poisson's ratio mismatch (υ_i / υ_m) on the normal interfacial stress distribution (σ_n) under uniaxial tension. (*Fully-bonded*, $E_i/E_m = 1$)

4.3.2 Non-Bonded (Contact) Problem

Contact problems can be classified in several categories, depending upon the initial contact conditions and the progressive change of contact status. The geometries and loading situations covered within this report can be classified as non-Hertzian, conformal, receding contact problems, since the initial undeformed bodies fit exactly or closely together and the contact region reduces as the load is applied. However, it can be shown that when the contact region is established (for an infinitely small applied load), the angle (η) defining the extent of contact becomes independent of the level of loading, and the stresses are then proportional to the applied stresses for all material combinations, *Keer et al. (1973)*.

Under non-bonded, contact interfacial conditions, it can be seen from the numerical

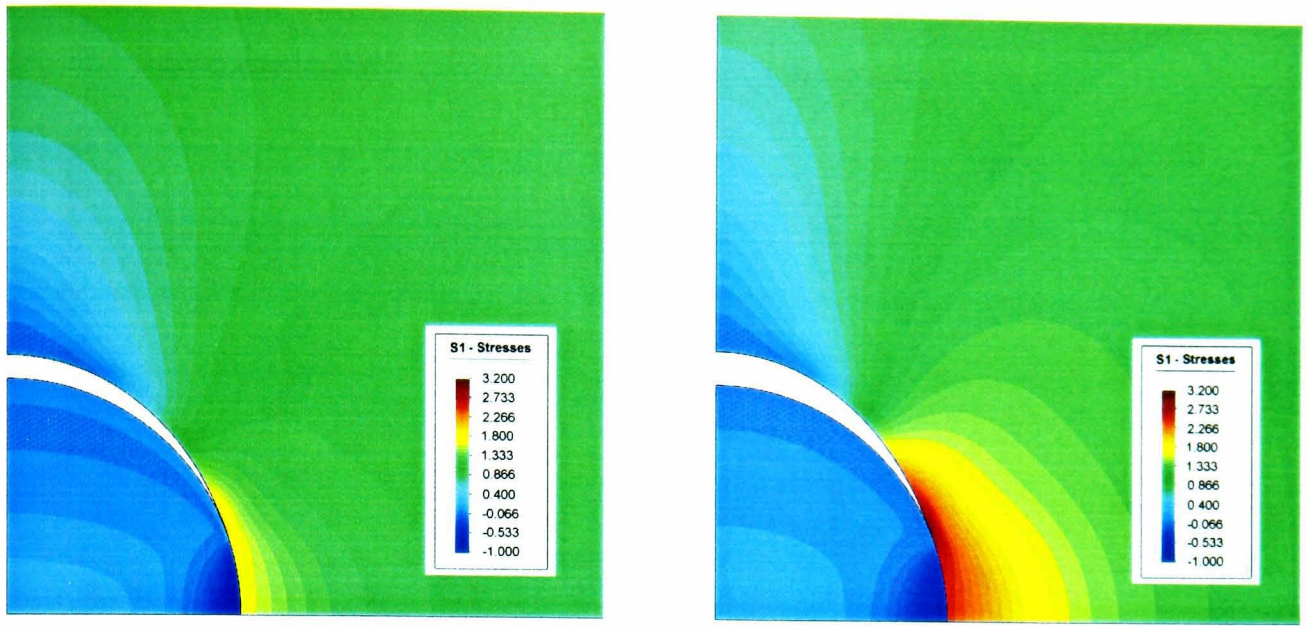

(a) (b)

Figure 4.7 Contour plot indicating the variation of first principal stress (S1) within the particle (a), and fibre (b) inclusion model. (*Non-bonded*, $E_i/E_m = 10$, $\upsilon_i = \upsilon_m = 0.3$, $\mu = 0$)

models that the inclusion and matrix are free to separate (see Figure 4.7). However, due to the contraction of the model perpendicular to the applied load, contact is maintained over a small proportion of the interfacial area. Figure 4.7 shows the variation in the first principal stresses (S1) within the particle and fibre models, respectively, using the corresponding material properties of the fully bonded problem (Figure 4.3). From this figure a stress concentration is present within the matrix phase in the contact zone, and the maximum stress occurs at the point of separation between the matrix and inclusion. In addition, the magnitude of the stress concentration is higher in the case of the fibre inclusion model.

Effect of Relative Inclusion Stiffness

Figure 4.8 shows the computed normal contact stress distribution (σ_n) around the particle/fibre inclusion arising from a remote uniaxial tensile stress for a range of material properties. Results from both the FE and BE techniques show good correspondence, although the sensitivity of the FE solutions to non-homogeneous discretisation along the contact surface and rapid refinement into the contact zone was particularly noted.

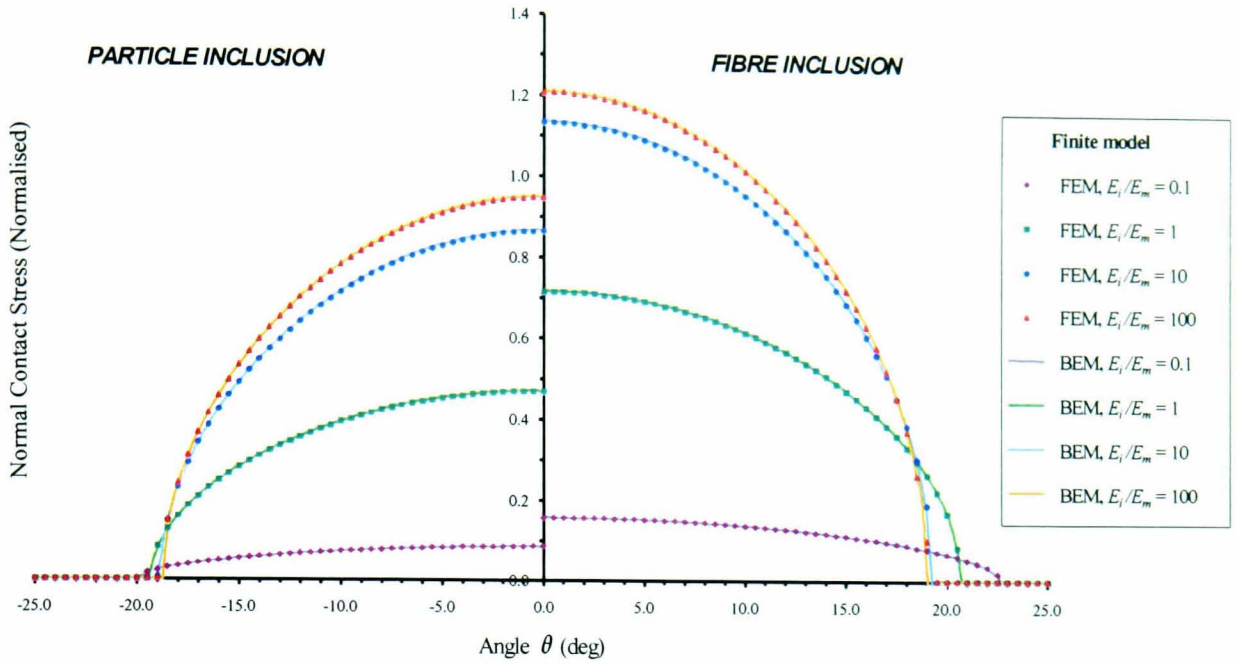

Figure 4.8 Effect of the elastic moduli ratio (E_i/E_m) on the normal contact stress distribution (σ_n) under uniaxial tension. (*Non-bonded*, $\upsilon_i = \upsilon_m = 0.3$, $\mu = 0$)

Furthermore, this figure clearly shows that as the particle or fibre inclusion becomes more rigid compared to the matrix ($E_i/E_m > 1$), the normal contact stress shows a marked increase and the contact angle (η) slightly decreases. However, as the inclusion becomes less rigid compared to the matrix ($E_i/E_m < 1$), the situation is then reversed. For the fibre inclusion problem, the contact stresses are larger for all Young's moduli ratios, and the contact angle changes more significantly.

Effect of Model Geometric Dimensions

To analyse the size effect of the model a convergence study was conducted, in a similar manner to the fully-bonded problem, to examine the changes in the normal interfacial stress as the geometrical ratio decreased. The normal contact stresses from the finite model (inclusion-matrix diameter ratio of 0.2) are plotted against the converged results representing an infinite model (inclusion-matrix diameter ratio as low as 0.083) in Figure 4.9.

From these tests it was clear that the inclusion-matrix diameter ratio of 0.2 only

adequately represented an infinite matrix model for the particle inclusion problem. For the fibre inclusion problem, the contact stress dropped by between 11.7-18.7%, the difference being greatest for low modulus ratios. *Man (1994)* also identified this effect and conducted a similar convergence study, which is in agreement with the results presented in this work. He concluded that contact problems in particular are very sensitive to size effects and care should be taken when modelling remote boundaries.

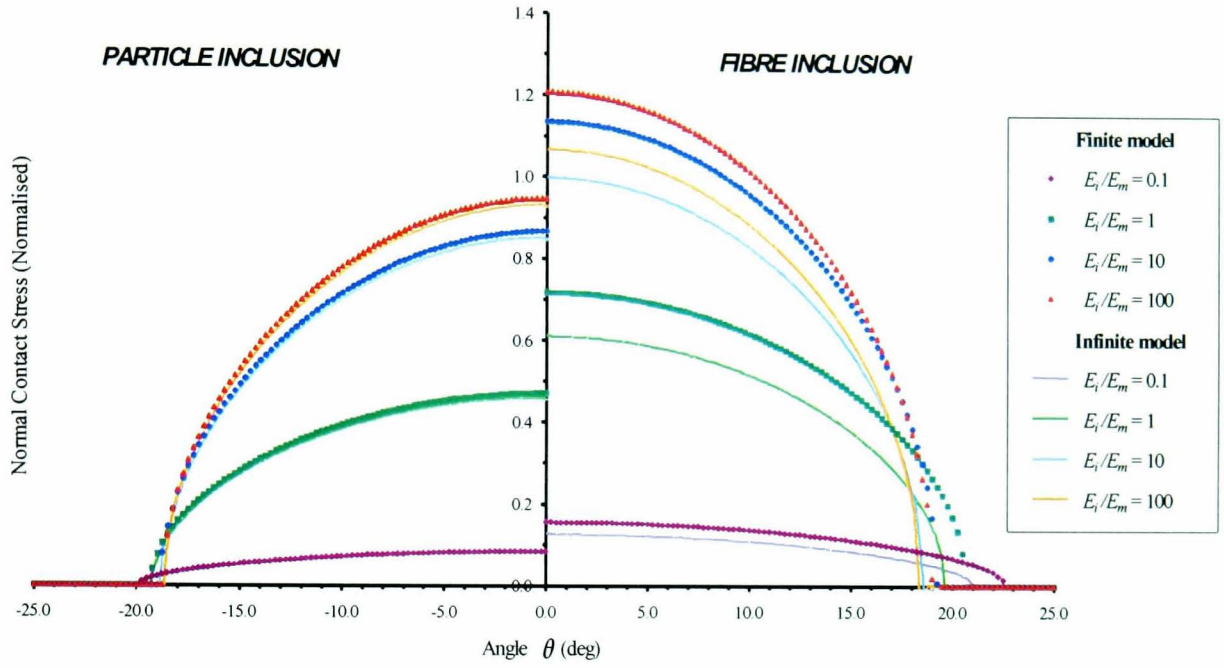

Figure 4.9 Effect of the relative inclusion/matrix dimensions on the normal contact stress (σ_n) distribution under uniaxial tension. (*Non-bonded*, $\upsilon_i = \upsilon_m = 0.3$, $\mu = 0$).

Such size effects may also explain some of the discrepancies in other published results, such as *Dandekar and Conant (1992)* who modelled the geometry with an inclusion-matrix diameter ratio of 0.167 and found slightly higher contact stresses than those from the analytical solution. The authors assumed that this discrepancy was due to the approximations involved within the analytical solution; however, in light of the results presented here, this statement is probably incorrect.

A number of authors have previously proposed analytical solutions for a non-bonded inclusion embedded within a dissimilar, infinite media undergoing uniaxial tension. For the axisymmetric particle inclusion problem, normal contact stresses and contact angles

at the interface between the phases have been obtained by *Wilson and Goree (1967)*, whereas for the plane strain fibre inclusion, similar solutions are given by *Stippes et al. (1962)*. In Wilson and Goree, analytical values of $\sigma_n = 0.457$ at $\theta = 0^\circ$ and a contact angle of $\eta = 19.6^\circ$, were given for the special case of $E_i/E_m = 1$ and $\upsilon_i/\upsilon_m = 1$, whilst in Stippes et al., $\sigma_n = 0.609$ at $\theta = 0^\circ$ and a contact angle of $\eta = 19.62^\circ$, were proposed assuming the properties of each of the phases are the same. In both cases, these results compare favourably with the infinite BE models presented in Figure 4.9.

Effect of Poisson's Ratio

Next, the effect of the Poisson's ratio was considered, as shown in Figure 4.10. It can be seen from the numerical results that the Poisson's ratio for both materials has a significant effect on σ_n and η in the case of the particle inclusion problem, with the values of σ_n and η increasing as the materials becomes more incompressible ($\upsilon_i = \upsilon_m = \sim 0.5$). However, for the fibre inclusion problem there was little or no effect. Analytically, the contact conditions can be shown to be independent of the Poisson's ratio in the case of a plane

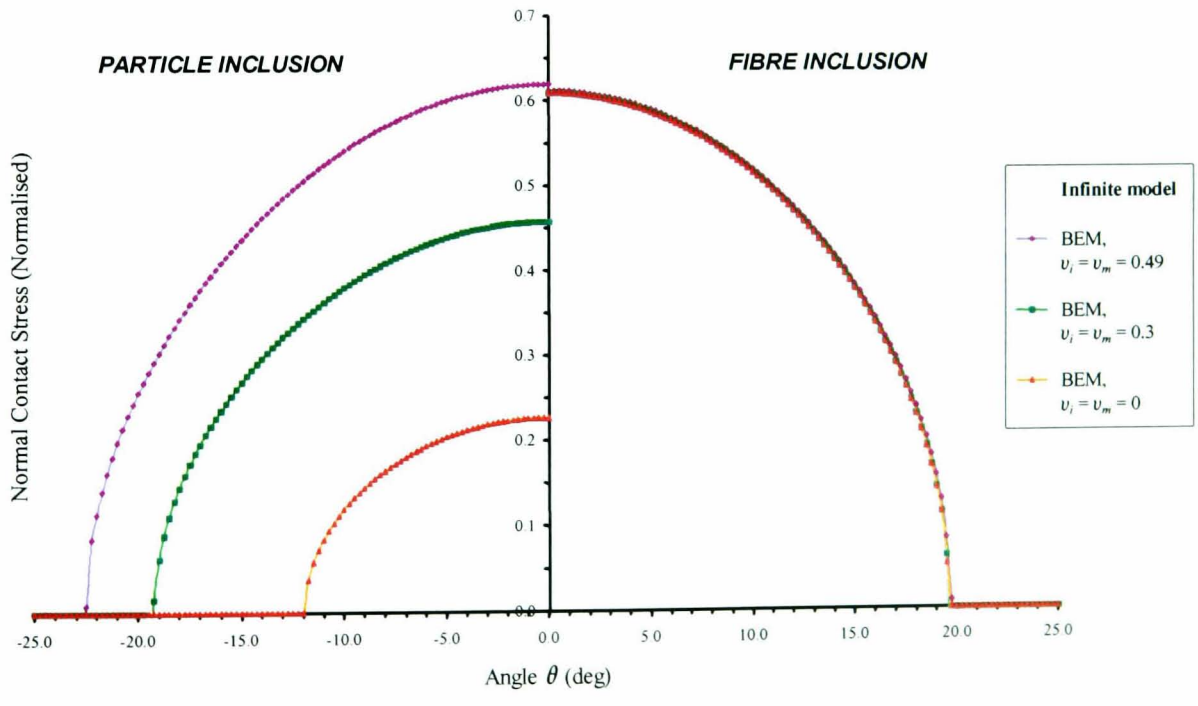

Figure 4.10 Effect of the Poisson's ratio (υ) on the normal contact stress (σ_n) distribution under uniaxial tension. (*Non-bonded*, $E_i/E_m = 1$, $\mu = 0$)

strain fibre, *Keer et al. (1973)*. However, in the case of the particle inclusion, no analytical verification could be found to justify or disprove the results presented. Hence, through further comparison with FE results (not shown), the trends presented for the particle inclusion were shown to be correct.

Poisson's ratio mismatch affects the contact stresses and angle, producing higher compressive stresses and contact angle at the interface of the particle for $\upsilon_i / \upsilon_m < 1$. Interestingly, this trend is reversed in the case of the fibre (see Figure 4.11). Once again these trends can be verified analytically (see *Wilson and Goree (1967)*, and *Keer et al. (1973)*), for the case of the particle and fibre inclusion, respectively.

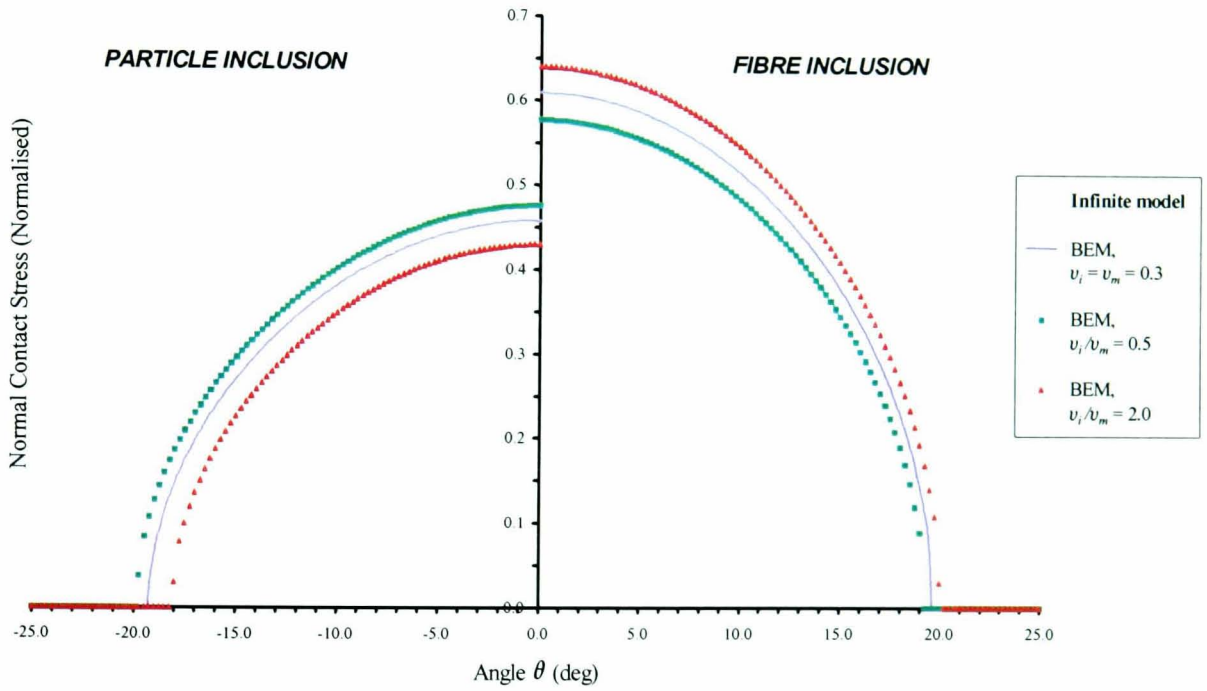

Figure 4.11 Effect of a Poisson's ratio mismatch (υ_i / υ_m) on the normal contact stress (σ_n) distribution under uniaxial tension. (*Non-bonded*, $E_i/E_m = 1$, $\mu = 0$)

Effect of Frictional Contact Conditions

Next, the frictional behaviour of the single inclusion models was also obtained. The normal stress (σ_n) and tangential shear stress (τ_{nt}) distributions for various coefficients of friction (μ) values are plotted in Figure 4.12. The result of including friction, in the case of both the particle and fibre inclusion is to lower the maximum compressive stress and in

particular for low values of μ, to shift the maximum stress away from the line of symmetry $\theta = 0^{\circ}$. Also, as μ increases the contact angle increases slightly. This general behaviour is due to the presence of a stick zone, which grows as the friction coefficient rises and extends from the line of symmetry to the point in which $\sigma_n = \tau_{nt} / \mu$. In the two extremes, the contact is all in slip-mode for $\mu = 0$, and the contact is all in stick-mode for $\mu \to \infty$. Similar trends have been reported in the literature (*Man (1994)*), for the single value of $\mu = 0.6$, using the BE technique.

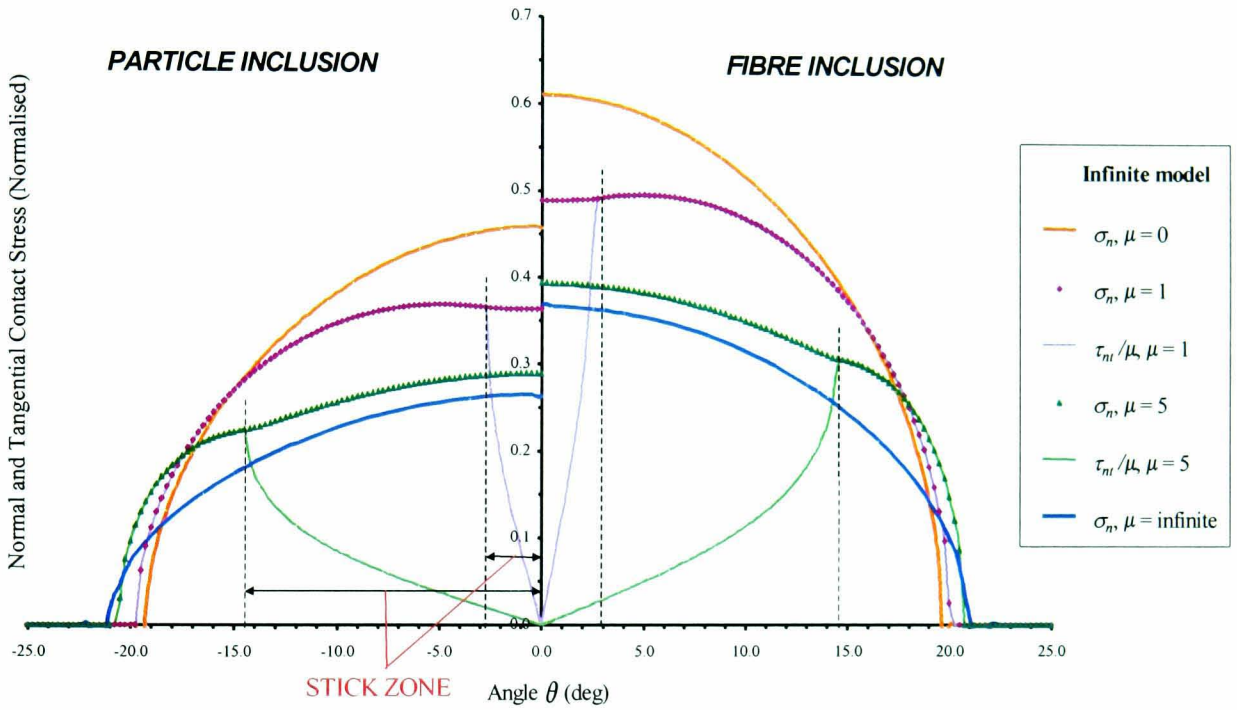

Figure 4.12 Effect of the friction coefficient (μ) on the normal stress (σ_n) and tangential shear stress (τ_{nt}) distribution under uniaxial tension. (Non-bonded, $E_i/E_m = 1$, $\upsilon_i = \upsilon_m = 0.3$)

4.4 Summary

In this chapter, the localised stress distributions for a cylindrical (fibre) or spherical (particle) inclusion embedded in a remotely stressed dissimilar matrix are investigated using computational techniques. Results obtained parametrically examine the effect of the constituent material properties on the interfacial stresses under two interfacial conditions: fully bonded and non-bonded, with or without friction. To summarise, the main results obtained in this chapter are listed below:

Fully-bonded interfacial conditions

- As the elastic modulus mismatch rises from unity ($E_i / E_m > 1$) a stress concentration is present at the interface of the inclusion. However, for the same material combination the effect is more pronounced in the case of the particle inclusion.
- Poisson's ratio mismatch slightly affects the interfacial stresses, producing higher stresses at the interface of the particle and fibre for $\upsilon_i / \upsilon_m > 1$, and lower stresses when $\upsilon_i / \upsilon_m < 1$.

Non-bonded, with or without friction, interfacial conditions

- Higher compressive contact stresses are produced at the interface of the particle and fibre when E_i / E_m rises. However, for the same material combination contact stresses are more pronounced in the case of the fibre inclusion.
- For the particle, the contact stresses are dramatically affected by the Poisson's ratio chosen for both materials. Maximum compressive stresses and contact angles are achieved when the materials become almost incompressible ($\upsilon_i = \upsilon_m = 0.49$). For the fibre, however, the Poisson's ratio has no effect.
- Poisson's ratio mismatch affects the contact stresses and angle, producing higher compressive stresses and contact angle at the interface of the particle for $\upsilon_i / \upsilon_m < 1$. Interestingly, this trend is reversed in the case of the fibre.
- The result of including high friction coefficients is to lower the maximum compressive stress and increase the contact angle.

The BE method is shown to be versatile, accurate and computationally inexpensive when modelling this kind of problem and results have been found to correlate well with FE simulations. Also, comparisons of the results with previously published analytical FE and BE analyses have generally shown good agreement.

Chapter 5: A Parametric Study of the Interaction of Three Inclusions

5.1 Introduction

In the previous chapter, the significance of the localised stress distribution in the interfacial region of second phase inclusions was described for the special case of a single inclusion within an infinite matrix (*Knight et al. (2002a)*). These results are pertinent to materials in which the volume fraction (V_f) of second phase is very low, such that the inclusions are non-interacting. However, most engineering composites have volume fractions of between 0.2-0.6, in which case the effects of inclusion interactions cannot be ignored. This chapter will address this situation, by analysing the effect of inclusion interaction within a composite material using the boundary element technique. Spherical and cylindrical inclusions will be considered, under either fully bonded, or non-bonded interfacial conditions (*Knight et al. (2002b)*). Similar models, considering only the case of fully bonded inclusions, have been developed using analytical methods (*Shelley and Yu (1966)*, *Goree (1967)*, *Yu and Sendeckyj (1974)*, and *Chen and Acrivos (1978)*), which are of less general applicability.

For verification, the results have been found to correlate well with finite element simulations, and where possible, comparison of the results with analytical models shows good agreement.

5.2 Model Description

5.2.1 Geometry and Materials

This chapter analyses the localised stress distributions produced around an embedded inclusion within a matrix, which is affected by the presence of two further inclusions, one

on either side. The matrix is subjected to a remote uniaxial tensile stress, and the interfacial and ligament stresses have been determined as functions of:

- Inter-fibre/particle separation distance (d),
- Interfacial conditions (fully bonded or non-bonded, frictionless contact),
- Relative size of neighbouring inclusions, and
- Relative stiffnesses of neighbouring inclusions.

As in the previous chapter, the different material phases are assumed to be homogeneous and isotropic, and behave purely elastically.

5.2.2 Finite Element and Boundary Element Modelling

The BE and FE meshes for the present axisymmetric and plane strain models have been developed such that smaller elements are placed along the interface between the inclusion and the dissimilar matrix. This is to ensure accurate results along the central inclusion

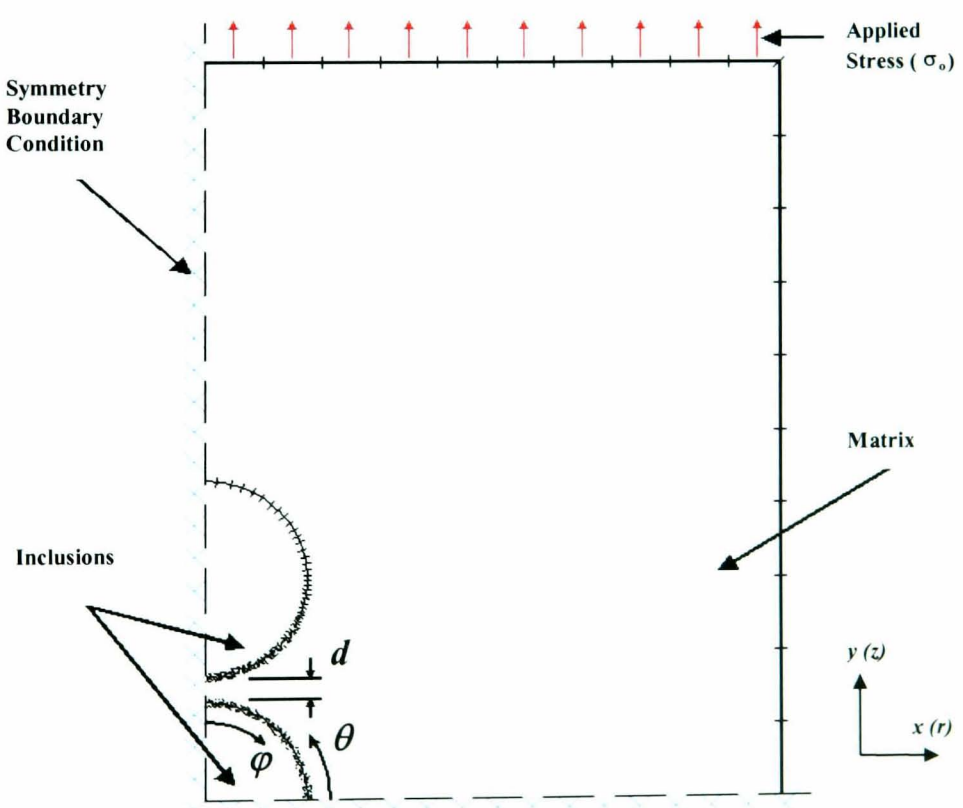

Figure 5.1 **Typical 2D Boundary Element model of three fibres/particles interacting within a finite matrix under an externally applied load. Model axes are z, r (axisymmetric) and y, x (plane strain).**

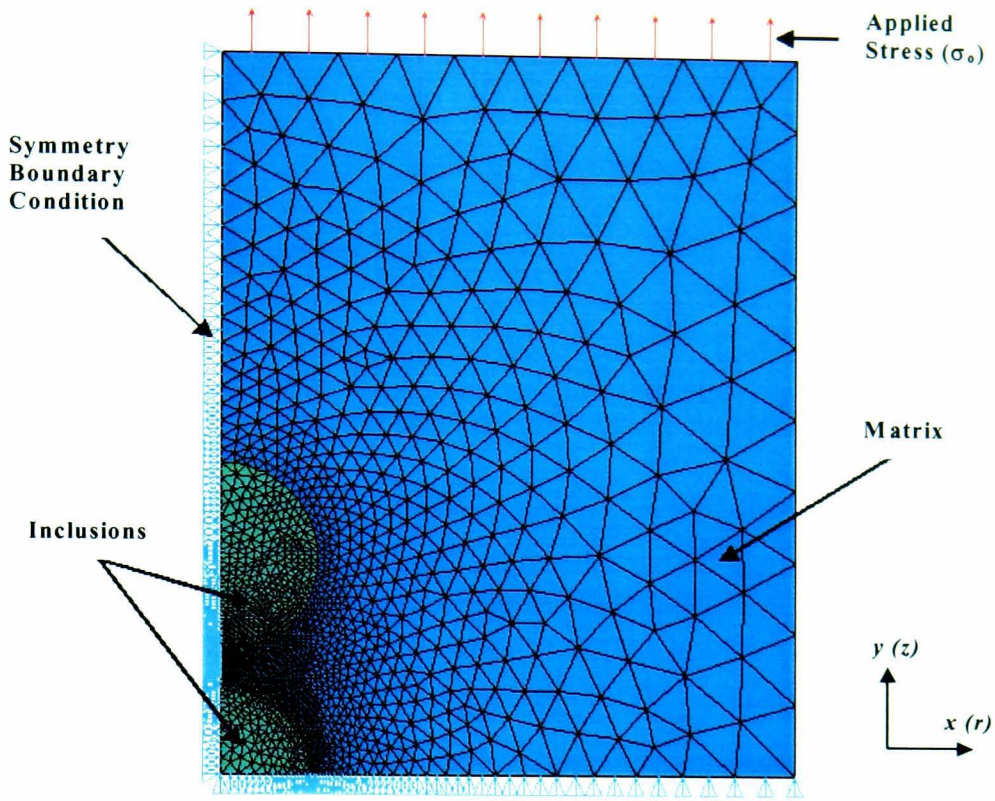

Figure 5.2 **Typical 2D Finite Element model of three fibres/particles interacting within a finite matrix under an externally applied load.**

interface and ligament, especially when the inclusions are nearly touching. Typical BE meshes comprised 520 linear elements in the contact region (non-bonded) or 270 quadratic interface elements (bonded), and 20 quadratic elements along the external boundaries, whereas the FE meshes comprised 9,500 six-node plane quadratic elements and 520 surface-to-surface quadratic contact elements (non-bonded). Figures 5.1 and 5.2 are typical examples of the BE and FE meshes, respectively.

In the particular models shown, the radius of the central inclusion (r) and the neighbouring inclusion (R) are equal ($R = r$). Furthermore, the matrix is subjected to a unit tensile, uniaxial stress (σ_o) in the z-direction (axisymmetric) or in the y-direction (plane strain), and once again, only one quarter of the geometry needs to be modelled, due to the symmetry of the problem. The external boundary dimensions have been chosen such that the results converge to that of an infinite matrix problem, and the material properties used in these analyses are $E_i / E_m \rightarrow$ infinity (i.e. rigid inclusions), and $\upsilon_i = \upsilon_m = 0.3$, where the subscript i = inclusions and m = matrix. The main reason for the choice

of rigid inclusions is that this enables the maximum values for the local stresses for stiffer inclusions to be determined.

5.3 Results and Discussion

In this section, firstly the problem of three fully bonded inclusions within an infinite matrix is considered, followed by the more complex analysis involving multiple contacting inclusions. Note that the results presented along the interface between the central particle/fibre and matrix, and within the matrix ligament between the inclusions are normalised with respect to the applied stress (σ_o).

5.3.1 Fully-Bonded Problem

As in the previous chapter, consideration will be given first to the distribution of stresses within the inclusion and embedding matrix, before an in-depth analysis of the interfacial and ligament stresses. Figure 5.3 shows contour plots of the variation of the first principal stresses (S1) within the particle and fibre models, respectively. In the particular models shown, the radius of the central inclusion (r), the radius of the neighbouring inclusion (R), and the inter-fibre/particle separation distance (d) are all equal. In addition, the material properties selected correspond with the single inclusion models featured in figures 4.3 and 4.7.

In both models, a high stress region is present within the matrix ligament between the central and neighbouring inclusions, and two separate stress maxima can be seen close to the material interfaces along the vertical axis. Relatively high stresses are also found within the inclusions, in particular at the interfacial zone closest to its neighbouring inclusion. Finally, the magnitudes of the stresses are found to be higher in the particle model, when compared to the corresponding fibre inclusion model.

Comparing these results with those of the single-inclusion model (Figure 4.3), it is clear that for this particular geometrical configuration the neighbouring inclusions strongly

influence the stress distribution present around the central inclusion.

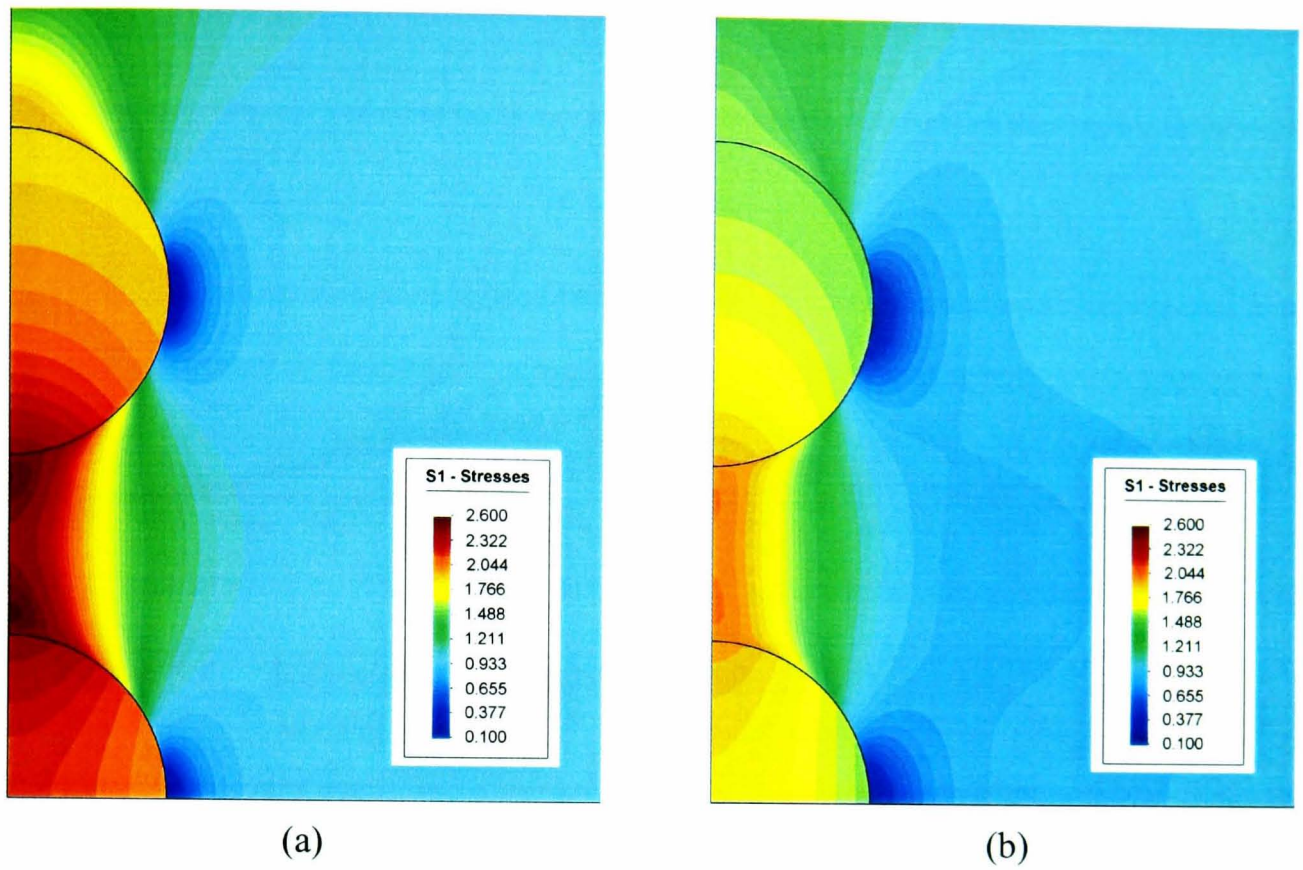

Figure 5.3 Contour plot indicating the variation of first principal stress (S1) within the particle (a), and fibre (b) inclusion model. (*Fully-bonded*, $E_i/E_m = 10$, $\upsilon_i = \upsilon_m = 0.3$, $R = r = d$)

Effect of Inter-fibre/particle Separation

Figures 5.4 and 5.5 show the computed normal interfacial stress (σ_n) around the central inclusion and the z-direction (axisymmetric) or y-direction (plane strain) stress within the matrix ligament between the inclusions, respectively (Model 1, $R = r$). As indicated within these figures, the results are presented for both particle and fibre inclusions, and for validation purposes, values have been obtained using both the BE and FE techniques. The results from both numerical techniques show good correspondence, although the time required for model preparation was generally longer for the FE method.

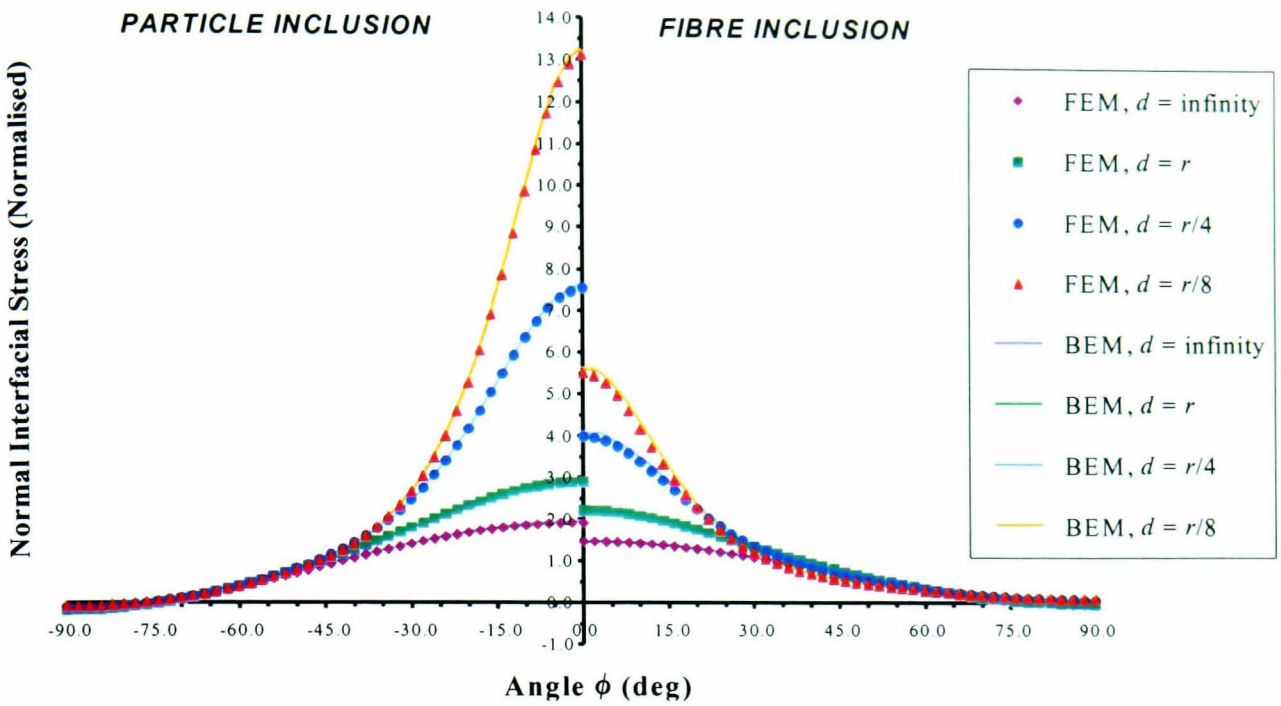

Figure 5.4 **Effect of the separation distance between inclusions on the normal interfacial stress (σ_n) distribution. (*Fully Bonded*, $E_i/E_m \approx$ infinity, $\upsilon_i = \upsilon_m = 0.3$)**

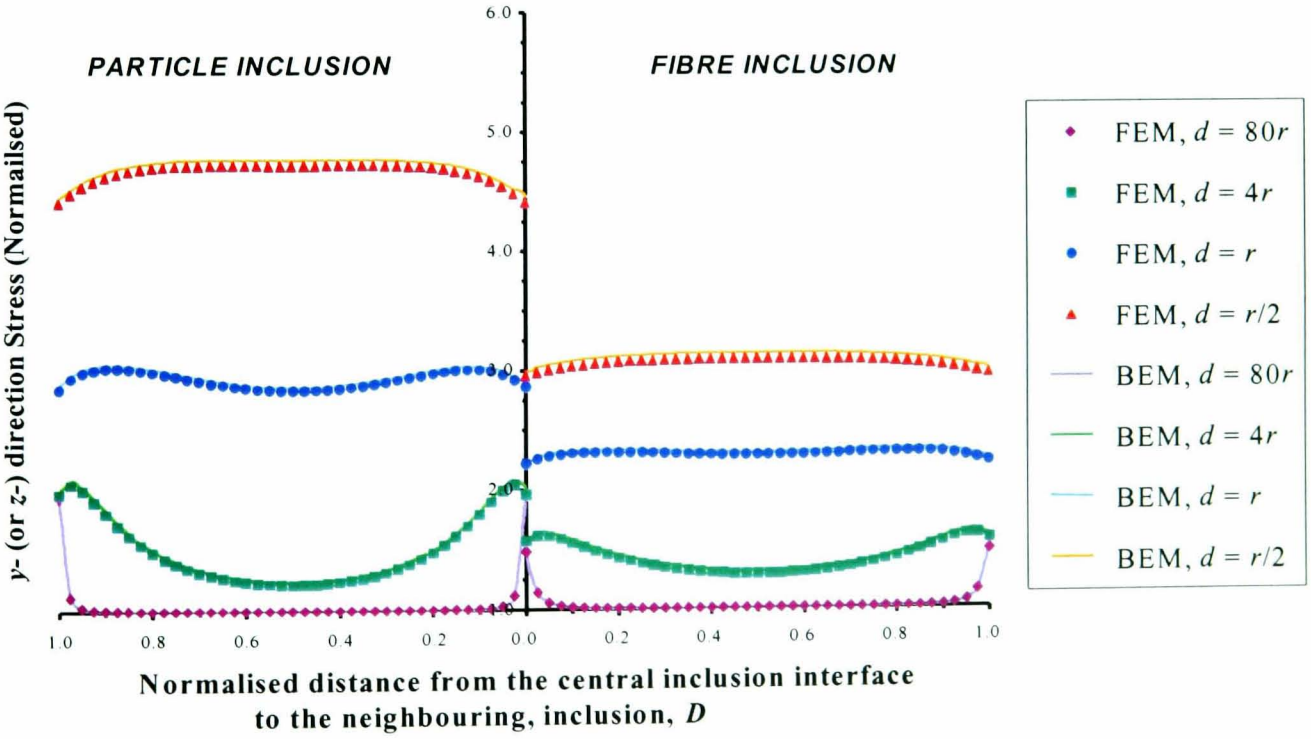

Figure 5.5 **Effect of the separation distance between inclusions on the ligament stress distribution. (*Fully Bonded*, $E_i/E_m \approx$ infinity, $\upsilon_i = \upsilon_m = 0.3$)**

The results in Figure 5.4 clearly show that the stress normal to the interface for the central inclusion is a maximum when $\varphi = 0^{\circ}$ for both the particulate and fibre inclusions.

As the (rigid) central and neighbouring inclusions move closer together the maximum value of the normal interfacial stress increases significantly. The stress concentration effect caused by the inclusion interaction is more pronounced for particles than for fibres, with its value increasing from 1.94 to 13.18 and 1.48 to 5.66 respectively, as the inclusion separation distance (d) decreases from infinity to r / 8. Also, as the inclusions come into close proximity, as Figure 5.5 shows, the position of the maximum value of the (normalised) ligament stress moves from the interfacial region to the centre of the ligament. The stress concentration in the ligament increases from 1.94 to 4.77 for the particle and 1.48 to 3.14 for the fibre as the separation decreases from infinity to r / 2.

Similar trends have been reported in the analytical papers of *Goree (1967)* and *Shelley and Yu (1966)* for the interaction of cylindrical and spherical inclusions, respectively, under uniaxial tension. However, in both publications only a limited range of results has been given.

Effect of Relative Inclusion Size

To analyse the effects arising from the interaction of dissimilar sized inclusions, two further models were considered where the radius of the central inclusion was fixed and the radius of the neighbouring inclusions was either doubled or halved. Although this choice is relatively arbitrary it is considered that the results of the analyses will be indicative of the effects to be expected in practice, arising from variations in inclusion sizes within a material.

Figure 5.6 shows the variation of normal interfacial stress around the central inclusion with angle φ. These results were obtained for a model consisting of two large inclusions moving into close proximity with a smaller inclusion (Model 2, $R = 2r$). Comparison of Figures 5.4 and 5.6 shows that for the latter case, i.e. dissimilar sized inclusions, the

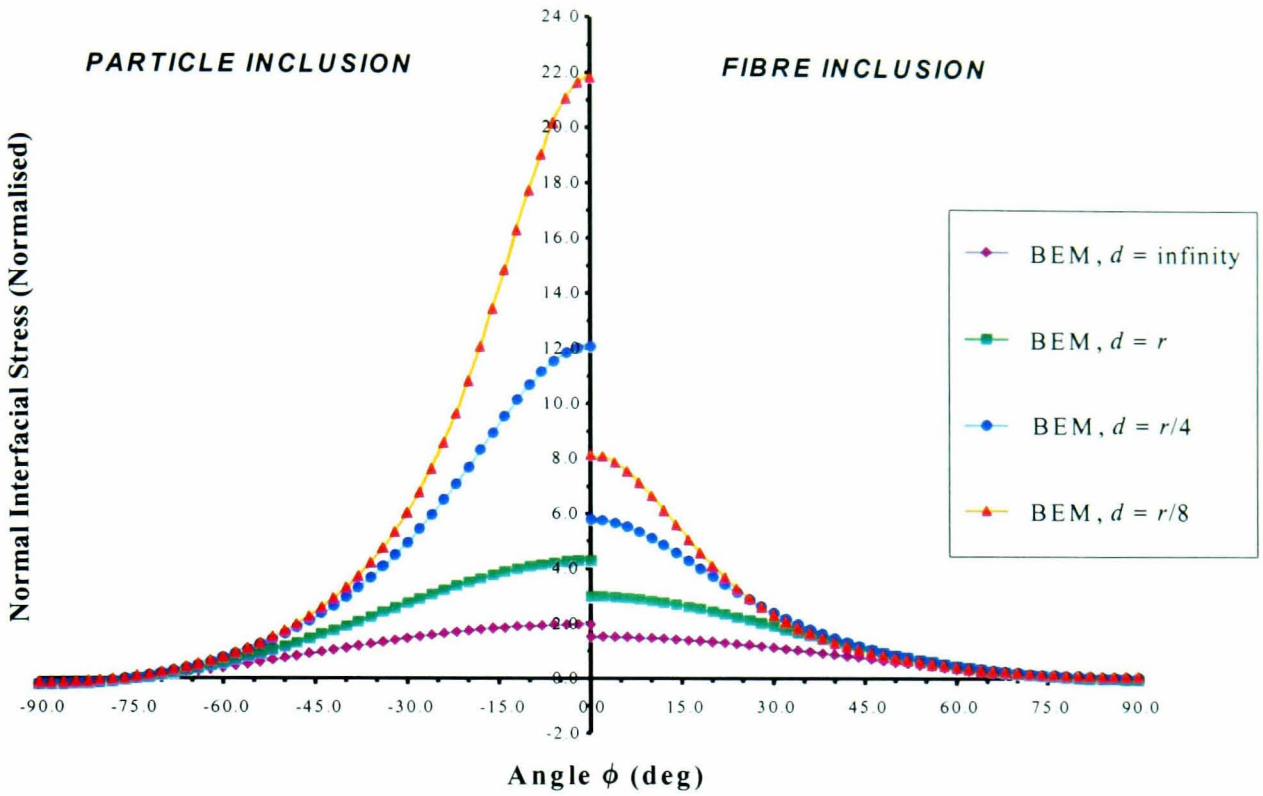

Figure 5.6 **Effect of the separation distance between different sized inclusions (R=2r) on the normal interfacial stress distribution. (*Fully Bonded*, $E_i/E_m \approx$ infinity, $\upsilon_i = \upsilon_m = 0.3$)**

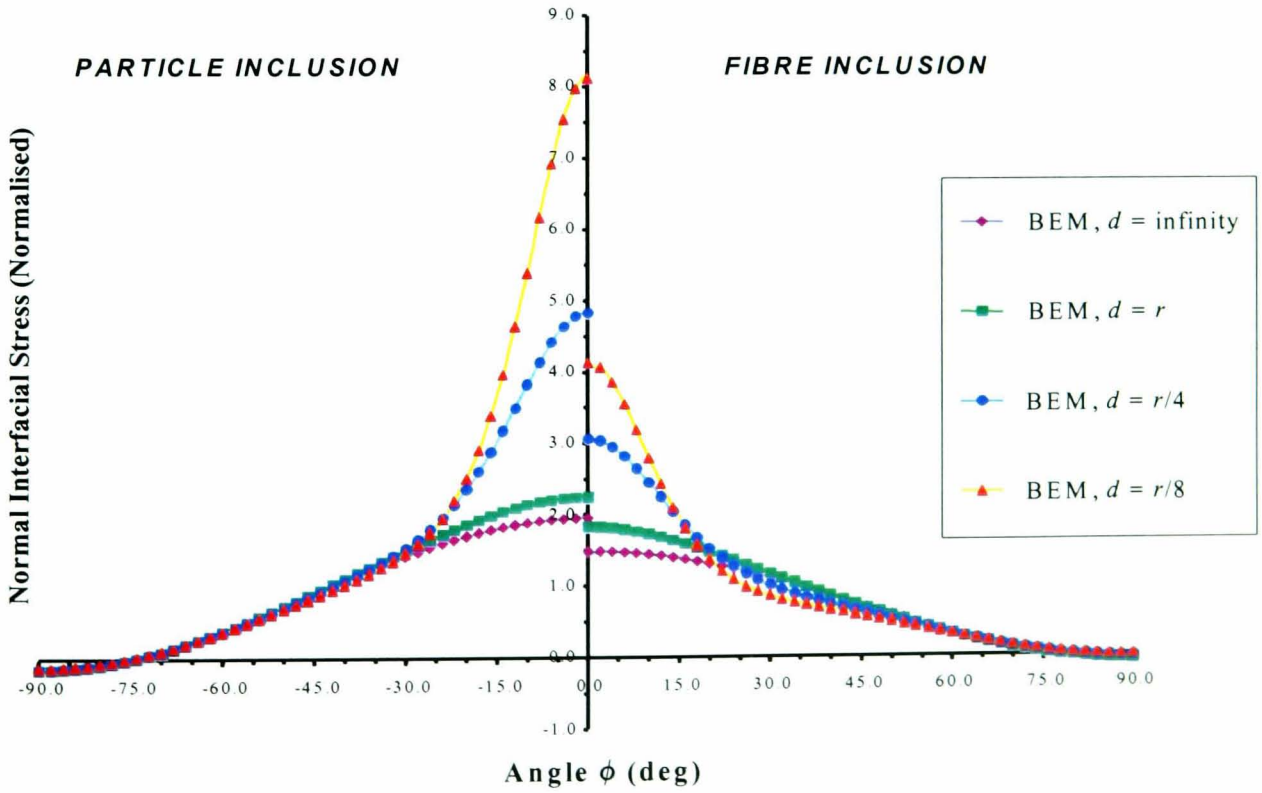

Figure 5.7 **Effect of the separation distance between different sized inclusions (R=r/2) on the normal interfacial stress distribution. (*Fully Bonded*, $E_i/E_m \approx$ infinity, $\upsilon_i = \upsilon_m = 0.3$)**

influence of the neighbouring inclusions becomes apparent at a greater separation distance and also the stress concentration is noticeably increased, from 13.2 to 21.8 and 5.66 to 8.11 for the particle and fibre respectively at $d = r / 8$.

Figure 5.7 shows the results obtained for the normal interfacial stress when considering two small inclusions moving into close proximity with a larger inclusion (Model 3, $R = r / 2$). As expected, the results show the opposite trend to those given by ($R = 2r$), and hence, the stress distributions observed around the central inclusion are relatively unaffected by the presence of the neighbouring inclusions, until the inclusions are virtually touching.

The maximum ligament stresses for each of the models discussed can also be seen in Figure 5.8. From this graph, it is clearly noticeable that the stresses within the ligament increase substantially as the inclusions come into close proximity, irrespective of their relative size differences. However, the effect is more pronounced in the case of two large

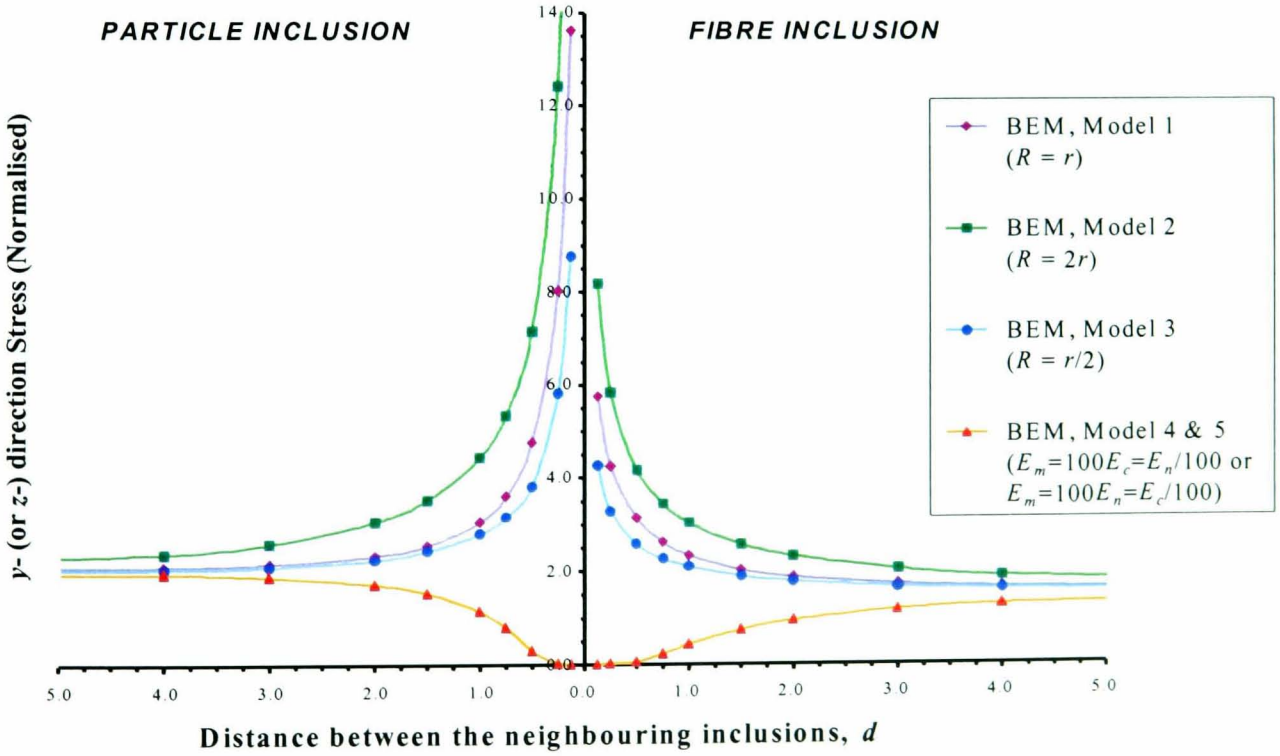

Figure 5.8 **Effect of the separation distance between different sized or moduli inclusions on the maximum ligament stress. (*Fully Bonded*)**

inclusions with a relatively small inclusion between them (Model 2, $R = 2r$).

The results presented for different sized inclusions, therefore, indicate a relative increase in the stress concentration at the surface of the smaller inclusion and a relative decrease at the surface of the larger inclusion, for the same separation distance. Thus, to minimise the overall stress concentrating effect caused by the interaction of rigid inclusions, as little variation as possible in the inclusion sizes is recommended in the design/manufacture of a particulate or fibre reinforced composite material.

Effect of Relative Inclusion Stiffness

Next, the localised effect of relatively high and low Young's modulus inclusions interacting was studied. This has direct relevance to the recent development of improved fracture toughness composites that contain mixtures of both high and low Young's moduli particles (*Hornsby and Premphet (1997,1998)*). Considering an idealised composite, which contains particles whose Young's modulus is greater than the matrix, it would generally be expected that the overall strength would increase, but inadvertently the toughness generally decreases. In contrast, composites containing particles whose Young's modulus is less than the matrix may be significantly tougher, but they are also generally relatively weak. Therefore, by manufacturing a material with a dispersion of high and low Young's moduli inclusions, both strength and toughness could possibly be enhanced, due to the combined reinforcing and toughening effects of the three-phase system.

By considering two further models (Models 4 and 5), in which the central and neighbouring inclusions are assigned Young's moduli values $E_m = 100E_c = E_n/100$ or $E_m = 100E_n = E_c/100$ (where the subscripts m = matrix, c = central inclusion, and n = neighbouring inclusion) and consisting of equal sized inclusions ($R = r$), the effect of relative inclusion stiffness has been investigated (Figures 5.9 and 5.10).

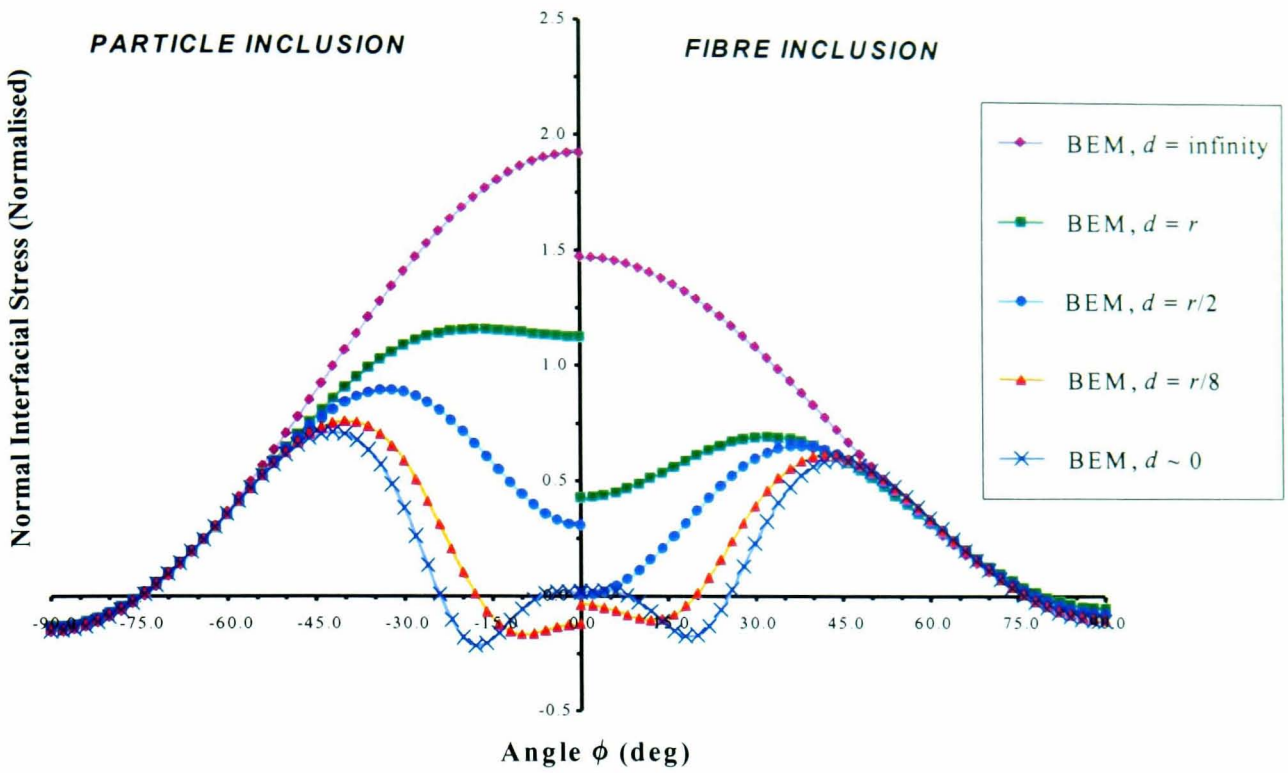

Figure 5.9 **Effect of the separation distance between differing moduli inclusions ($E_m = 100E_c = E_n/100$) on normal interfacial stress distribution. (*Fully Bonded*, $\upsilon_i = \upsilon_m = 0.3$)**

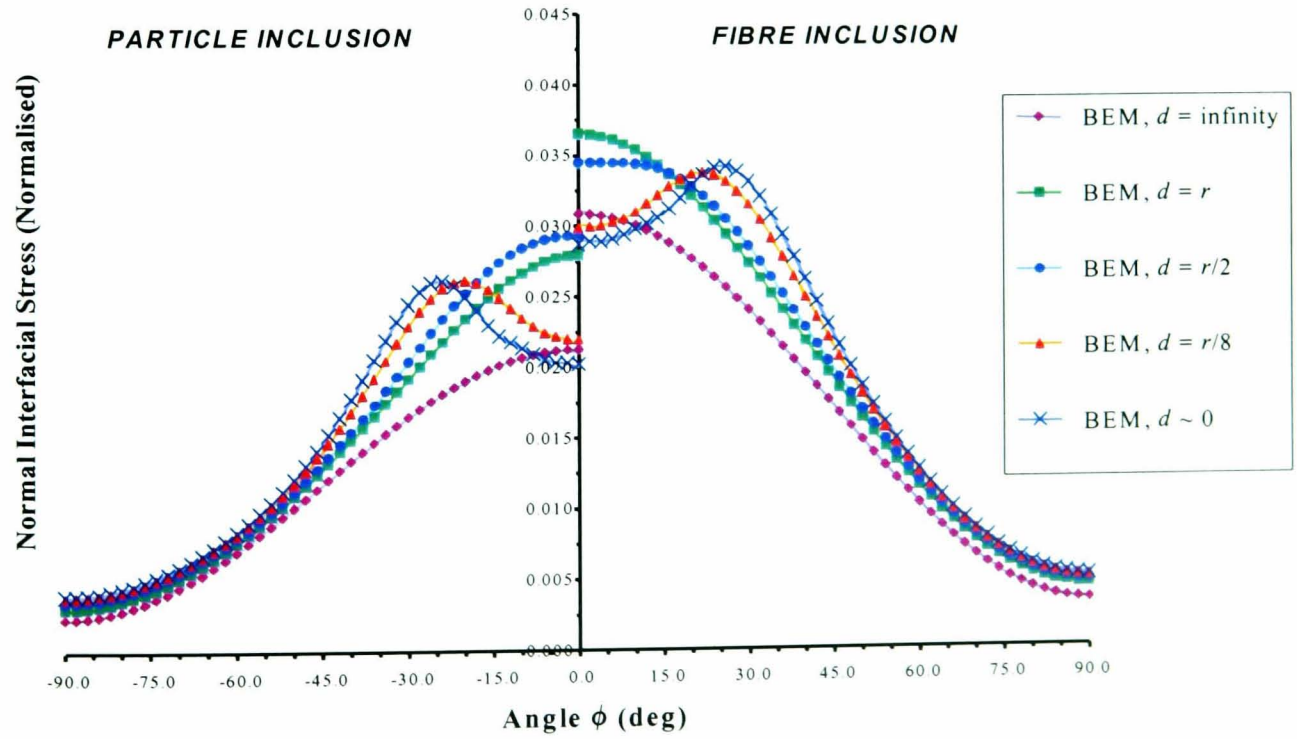

Figure 5.10 **Effect of the separation distance between differing moduli inclusions ($E_m = 100E_n = E_c/100$) on the normal interfacial stress distribution. (*Fully Bonded*, $\upsilon_i = \upsilon_m = 0.3$)**

Figure 5.9 shows the normal stress at the interface between the central inclusion and the matrix for a relatively stiff ($E_c \gg E_m$) inclusion surrounded by two relatively compliant ($E_n \ll E_m$) inclusions. Whereas, the results presented in Figure 5.10 are for the opposite case, being a relatively compliant ($E_c \ll E_m$) central inclusion surrounded by two relatively stiff ($E_n \gg E_m$) inclusions. From these two plots, it can be noted that the stress distribution at the interface of the high moduli inclusion falls dramatically, and for the low moduli inclusion the values increase slightly as the inclusions come into close proximity.

Furthermore, the interfacial stresses are much lower around the more compliant inclusion, and in both cases the maximum stress is shifted away from the symmetry axis by approximately 45° and 25°, respectively.

The maximum ligament stress corresponding to both models can be seen in Figure 5.8. The results obtained closely follow the corresponding values shown in Figure 5.9, at $\varphi = 0^{\circ}$, therefore, confirming previous observations and indicating that the stress concentration is local to the high moduli inclusion.

In practical terms these results would seem to be very beneficial, as the stress concentration present at the high moduli inclusion interface is effectively removed. This is indicated by the drop in the maximum interfacial stress to values less than the applied stress, at separations of less than one radius (Figure 5.9). Hence, micro-cracks, which often nucleate in and around second phase materials, would require a higher applied stress for initiation, which in turn, could improve the strength of the composite.

5.3.2 Non-Bonded (Contact) Problem

For the problem of three non-bonded inclusions, contact interfacial conditions, it can be seen that the inclusion and matrix are allowed to separate (see Figure 5.11). However, due to the contraction of the model perpendicular to the applied load, contact is maintained over a proportion of the interfacial area. In the contact region, extending from the x-axis, a stress-concentrating effect is noticeable, which gives rise to the maximum stress present

within the matrix phase. As shown in Figure 5.11, the magnitude of the stress concentration is higher in the case of the fibre inclusion model for the same geometrical and material properties.

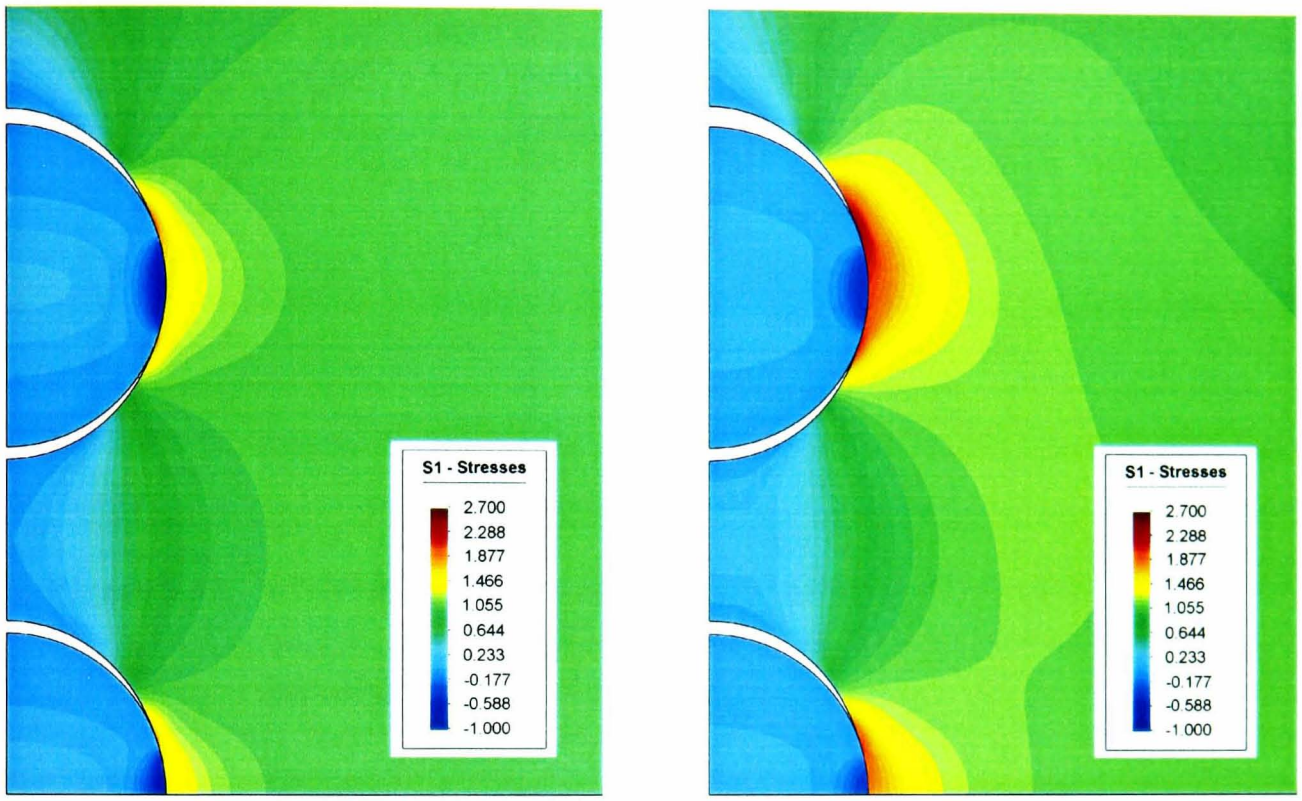

(a) (b)

Figure 5.11 Contour plot indicating the variation of first principal stress (S1) within the particle (a), and fibre (b) inclusion model. (*Non-bonded*, $E_i/E_m = 10$, $\upsilon_i = \upsilon_m = 0.3$, $\mu = 0$, $R = r = d$)

Effect of Inter-fibre/particle Separation

Figures 5.12 and 5.13 show the variation of the normal contact stresses around the central inclusion and the stress distribution in the matrix ligament between the inclusions, respectively, with angle θ (Model 6, $R = r$). As would be expected the normal contact stress is a maximum for $\theta = 0^{\circ}$, i.e. normal to the applied stress. The contact stress decreases with increasing angle until it reaches zero, i.e. separation of the matrix and inclusion occurs for values of θ between approximately 12° and 19°. The validation of the analyses is of greater significance in this case than for the bonded analyses described above. This arises from the fact that the separation point is not known *a priori*, but the

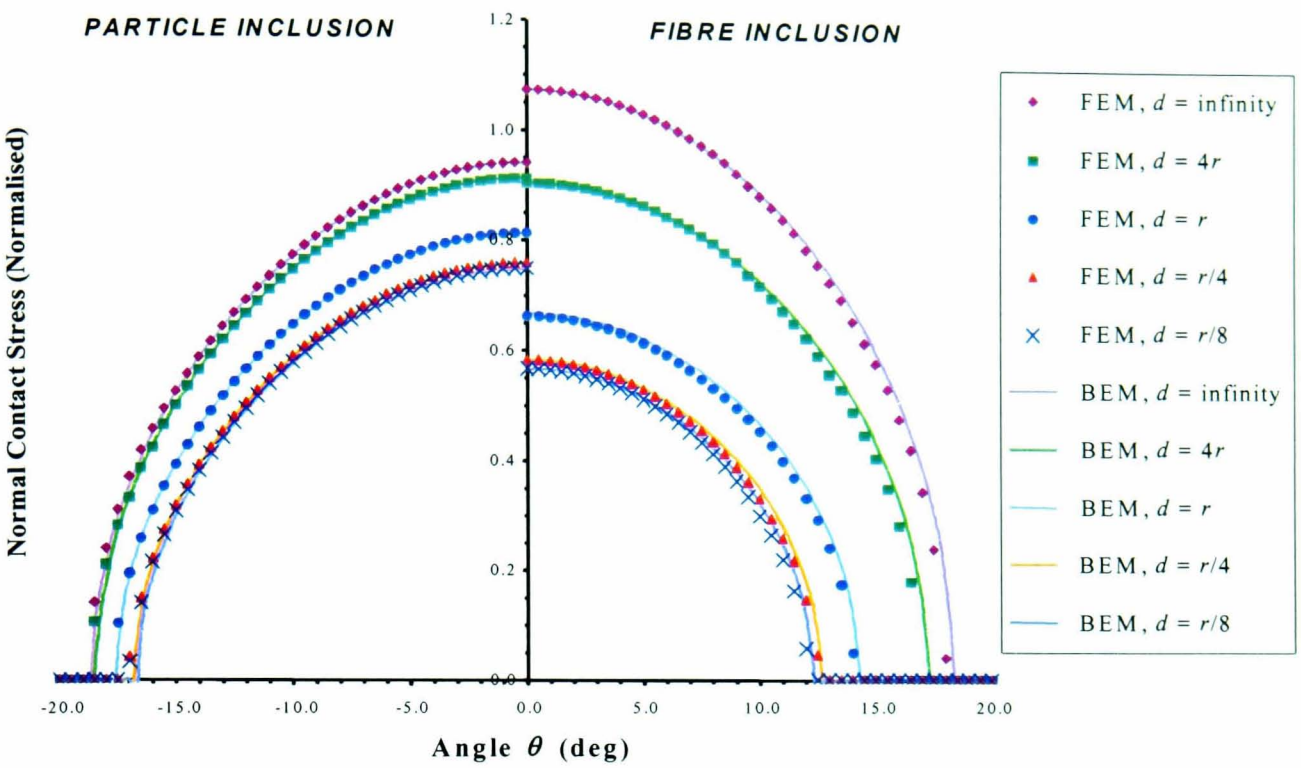

Figure 5.12 **Effect of the separation distance between the inclusions on the normal contact stress distribution. (*Non-Bonded*, E_i / E_m ≈ infinity, $\upsilon_i = \upsilon_m = 0.3$, $\mu = 0$)**

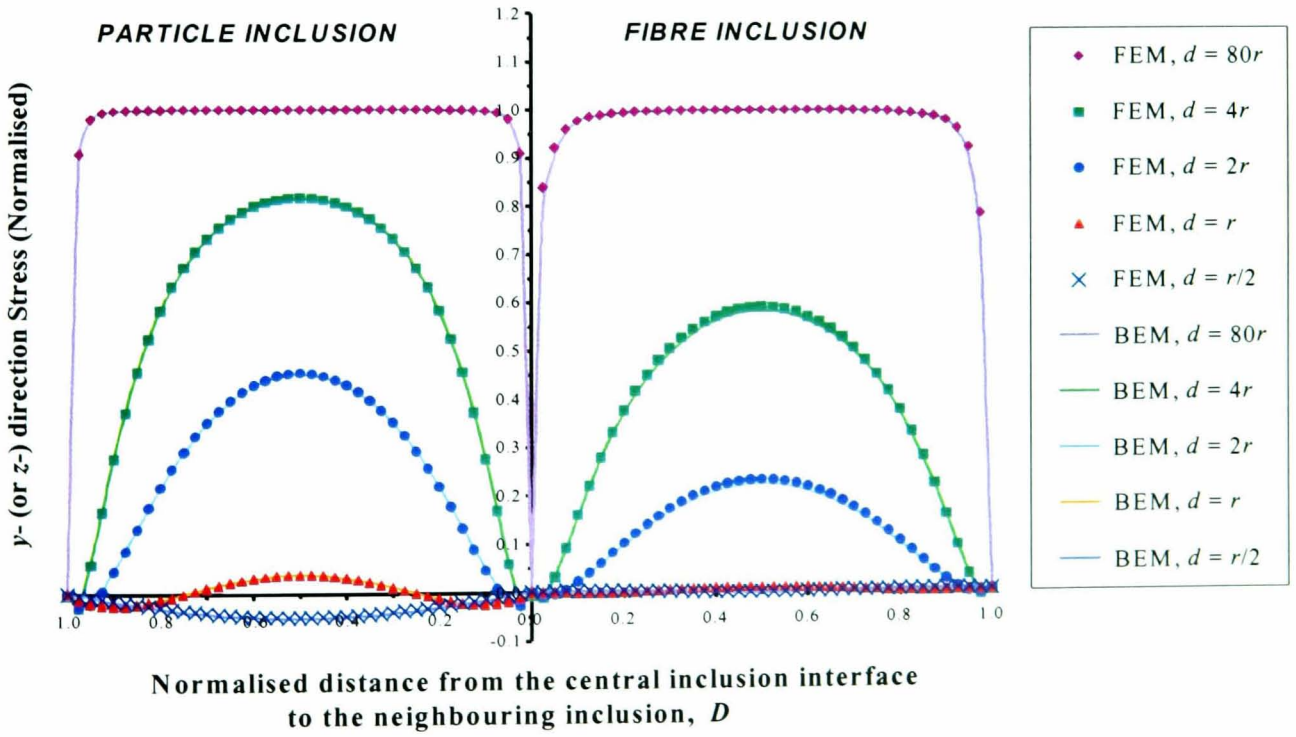

Figure 5.13 **Effect of the separation distance between the inclusions on the ligament stress distribution. (*Non-Bonded*, E_i / E_m ≈ infinity, $\upsilon_i = \upsilon_m = 0.3$, $\mu = 0$)**

mesh adjacent to the separation zone needs to have a small element size, since there are steep gradients in the stresses in this region. Hence, the mesh size and spacing were varied until stable results were obtained. Stress values were obtained using both the FE and BE techniques, with the results from the two different numerical techniques showing good correspondence. The time required for model preparation and solution was generally longer for the FE method, primarily due to the implementation of efficient reanalysis algorithms within the BE method, as described by *de Lacerda and Wrobel (2000)*.

Furthermore, from Figure 5.12 it can be noticed that as the rigid inclusions move closer together, the normal contact stresses and contact angle within the interface of the central inclusion decrease for both the particle and fibre analyses, and converge towards a lower limit. Within the ligament the stresses diminish as the inter-fibre/particle separation distance (d) reduces to a near-touching situation (Figure 5.13). Therefore, it would appear that the ligament becomes 'stress-free', as the rigid inclusions come into close proximity. The trends shown in both plots are also more pronounced with fibres than with particles.

Effect of Relative Inclusion Size

The effect of relative inclusion size has also been considered, in a similar manner to that of the fully bonded case. As can be seen from Figure 5.14, the normal contact stresses fall dramatically as the separation decreases (Model 7, $R = 2r$). In particular, in the case of cylindrical (fibre) inclusions the contact stresses around the central (smaller) inclusion become zero for separation distances of less than two radii, which suggests a complete loss of contact between the inclusion and the matrix. The results for two small inclusions moving into close proximity with a larger inclusion (Model 8, $R = r / 2$) are shown in Figure 5.15. As expected, the results show the opposite trend to those given by $R = 2r$, and hence, the stress distributions observed are relatively unaffected by the presence of the neighbouring inclusions, until the inclusions are virtually touching.

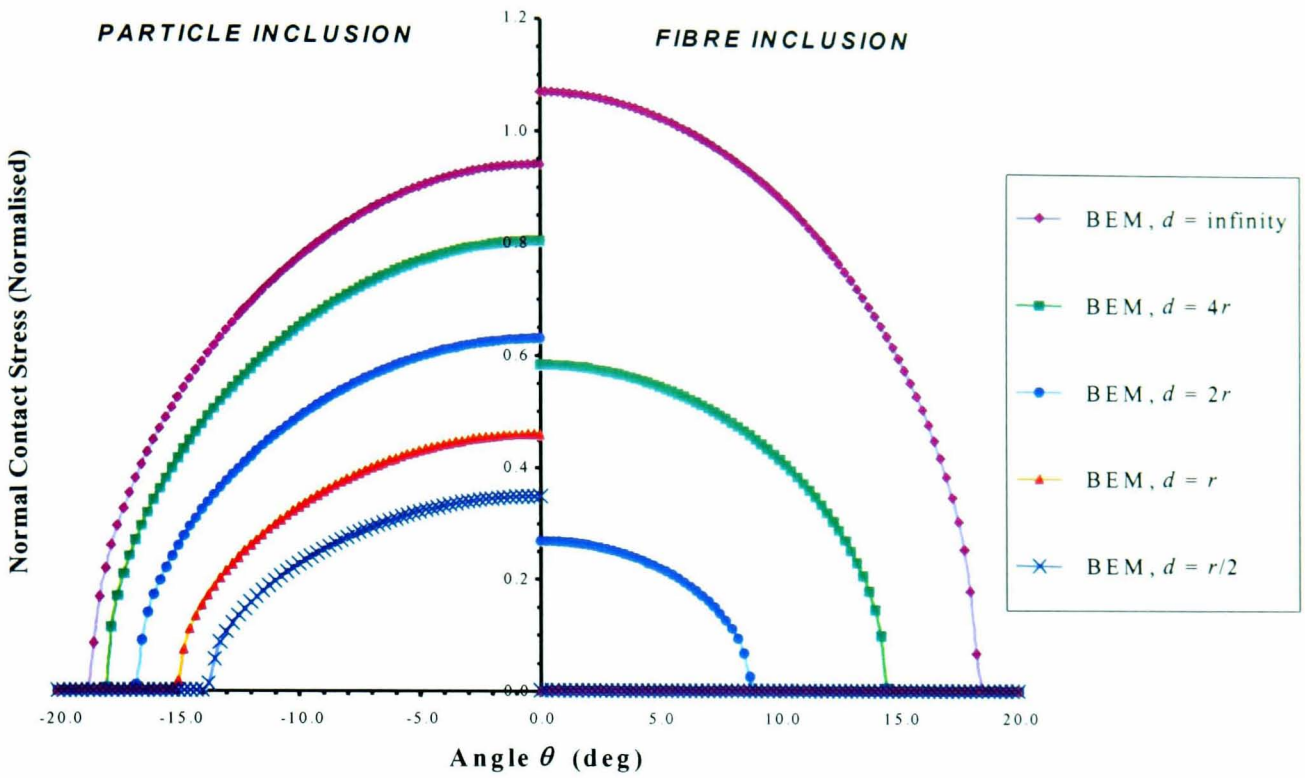

Figure 5.14 **Effect of the separation distance between different sized ($R = 2r$) inclusions on the normal contact stress distribution. (*Non-Bonded*, $E_i / E_m \approx$ infinity, $\upsilon_i = \upsilon_m = 0.3$, $\mu = 0$)**

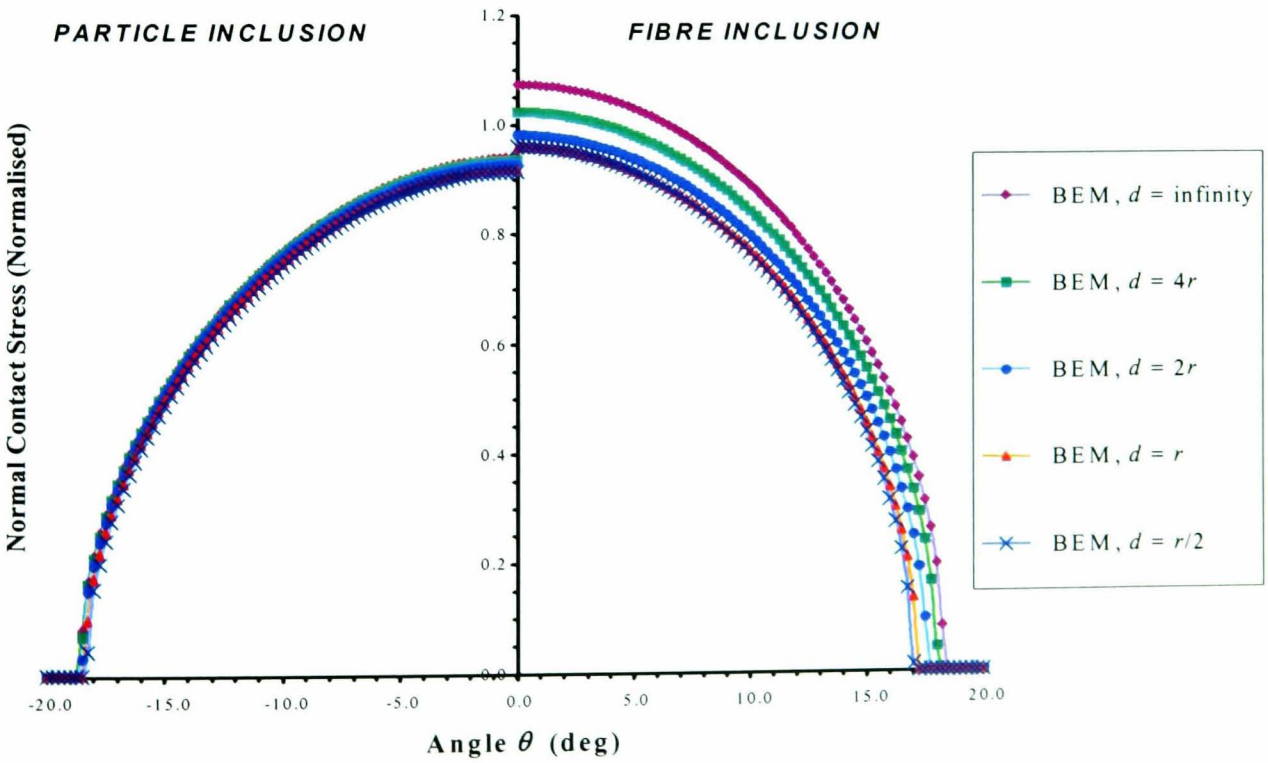

Figure 5.15 **Effect of the separation distance between different sized ($R = r/2$) inclusions on the normal contact stress distribution. (*Non-Bonded*, $E_i / E_m \approx$ infinity, $\upsilon_i = \upsilon_m = 0.3$, $\mu = 0$)**

The maximum ligament stresses for each of the models discussed are presented in Figure 5.16. From this graph, it is clearly noticeable that the stresses within the ligament also drop substantially as the inclusions come into close proximity, irrespective of their relative size differences. However, the effect is more pronounced in the case of two large inclusions surrounding a relatively small inclusion ($R = 2r$).

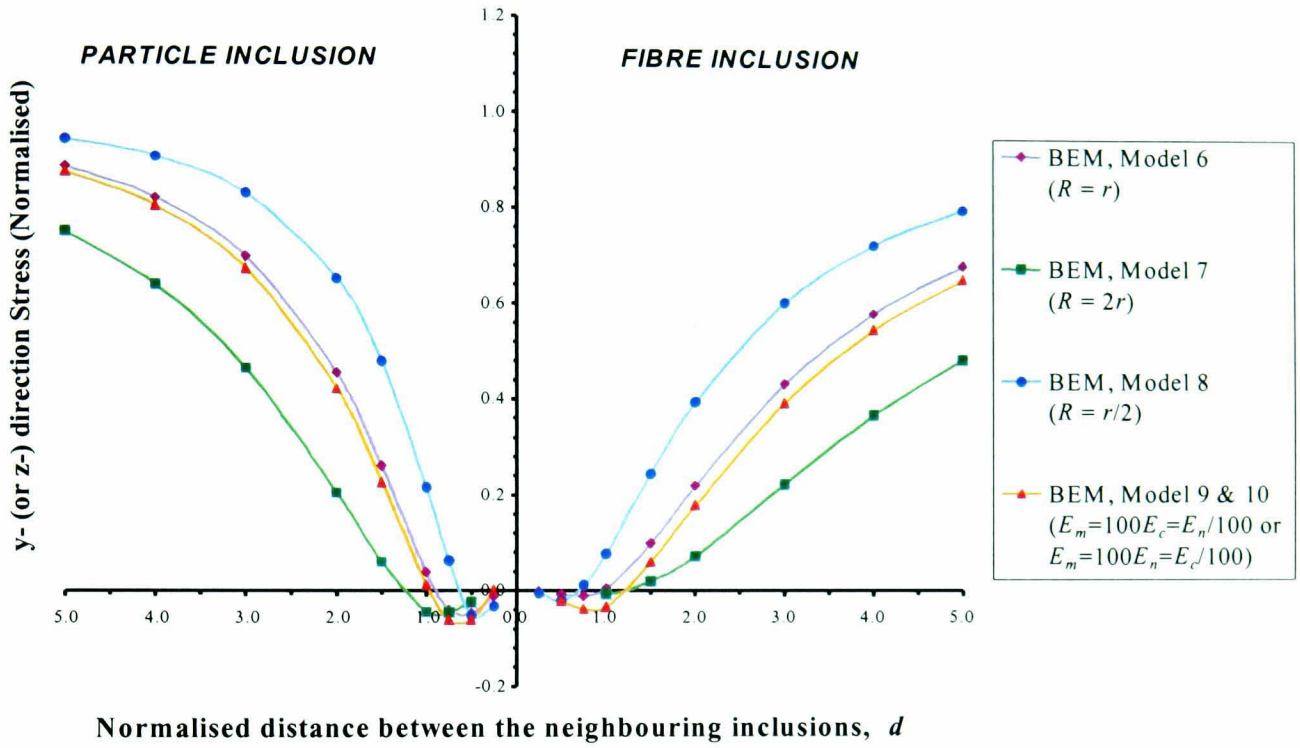

Figure 5.16 Effect of the separation distance between different sized or moduli inclusions on the maximum ligament stress. (*Non-Bonded*)

The significance of these tests is to observe the 'shielding' effect of the larger inclusions, or possibly even clusters of inclusions, which causes the load to bypass the central region occupied by the smaller inclusion. Therefore, in practical terms these results would suggest that in certain materials manufactured with low interfacial adhesion (non-wetting) and a high variation in inclusion size or inclusion clustering, debonding of neighbouring solitary inclusions might be prevalent. Clearly, experimental testing would be required to substantiate this hypothesis.

Effect of Relative Inclusion Stiffness

Finally, the localised effects of high and low Young's modulus inclusions were also obtained under contact conditions (Models 9 and 10, where $R = r$ for both models and where $E_m = 100E_c = E_n/100$ and $E_m = 100E_n = E_c/100$, respectively). Figures 5.17 and 5.18 depict the angular variation of the normal contact stresses at the interface of the matrix and central inclusion, for models 9 and 10 respectively. The results shown in Figure 5.17 are broadly similar to those presented in Figure 5.11 for rigid inclusions, and in both cases the effect of inter-inclusion spacing is greater for fibres than for particles. The contact stresses are much lower for the more compliant central inclusion, Figure 5.18, as would be expected. Also, in all the investigated cases of non-bonding inclusions, the effect of the interaction between the inclusions is to reduce the contact stresses and angle.

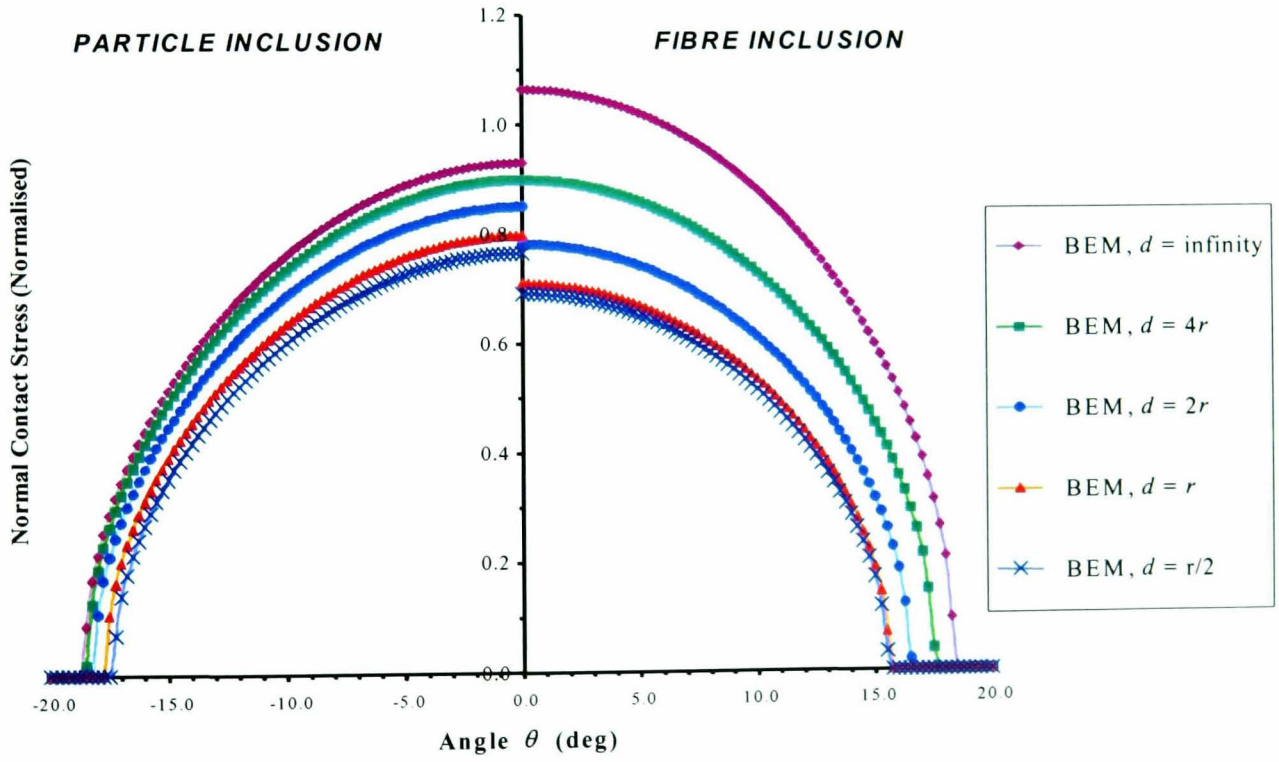

Figure 5.17 Effect of the separation distance between differing moduli inclusions ($E_m = 100E_c = E_n/100$) on the normal interfacial stress distribution. (*Non-Bonded*, $\upsilon_i = \upsilon_m = 0.3$, $\mu = 0$)

The effects of these variations on the resultant ligament stresses can be seen in Figure 5.16. As noted in the previous section, when the neighbouring inclusions come into closer proximity to the central one, the ligament stresses approach zero.

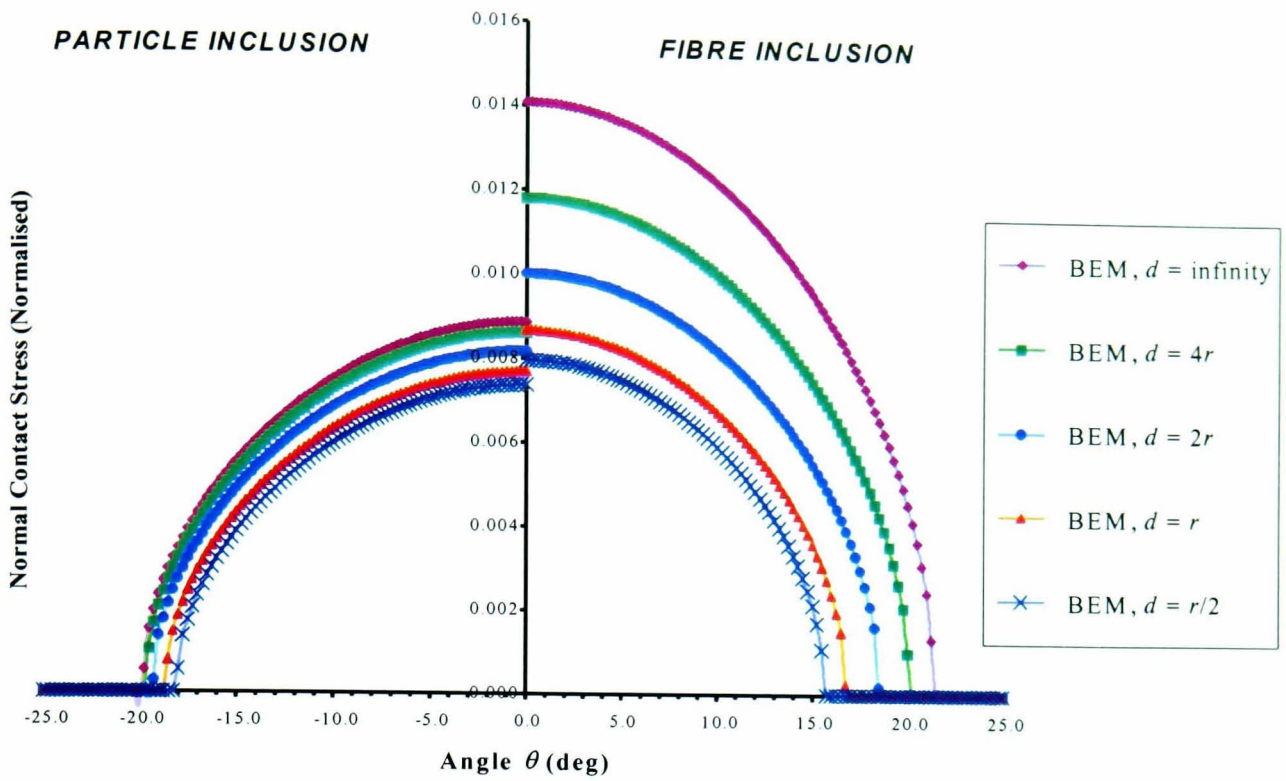

Figure 5.18 **Effect of the separation distance between differing moduli inclusions ($E_m = 100E_n = E_c/100$) on the normal interfacial stress distribution. (*Non-Bonded*, $\upsilon_i = \upsilon_m = 0.3$, $\mu = 0$)**

5.4 Summary

In this study, the localised stress distributions for multiple cylindrical (fibre) or spherical (particle) inclusions interacting within a dissimilar matrix are investigated using computational techniques. Results obtained are for two interfacial conditions (fully-bonded and non-bonded, frictionless contact) and calculated stresses are given within the interfacial zone of the central inclusion and across the ligament between the neighbouring inclusions.

The main results obtained from this study are:

Fully bonded interfacial conditions

- As the inclusions move closer together the stresses within the interface closest to the neighbouring inclusion, and also within the ligament, increase markedly. The effect is more noticeable with the particle inclusions.

- Considering inclusions of different sizes, the stress concentrations observed increase at the surface of the smaller inclusion and decrease at the surface of the larger inclusion, for the same separation distance. Hence, to minimise the overall stress raiser effect caused by the interaction of rigid inclusions, a low variation in inclusion size is recommended in the material design.

- Finally, combinations of relatively high and low Young's moduli inclusions were studied. From these results it was clear that the presence of a low modulus inclusion close to a high modulus inclusion dramatically reduced the stress concentrations to a point at which the stress raiser was removed. In practical terms these results would seem to be very beneficial, as micro-cracks which often nucleate in and around second phase materials would have a lower probability of initiation.

Non-bonded, frictionless contact interfacial conditions

- As the inclusions move close together the stresses and contact angle within the interface decrease. The effect is more apparent for the fibre inclusions. Within the ligament the first principal stress decreases to close to zero as $d \rightarrow 0$.

- Considering inclusions of different sizes, the computed contact stresses around the smaller inclusion are significantly affected by the size difference, particularly in the case of cylindrical (fibre) inclusions. In this case, the contact stress becomes zero for separation distances of less than two radii, indicating a 'shielding' effect, which causes a complete loss of contact between the inclusion and the matrix. Therefore, it is recommended, once again, that a low variation in inclusion size be used in the material design.

- Finally, combinations of relatively high and low Young's moduli inclusions were studied. In both the high and low moduli inclusions the contact angle and stresses reduced, with the effect being more noticeable with the fibre inclusions.

Chapter 6: A Parametric Study of the Interaction of Multiple Inclusions

6.1 Introduction

In this chapter, the BEA program has been implemented to analyse the transverse tensile response of a 'composite construct', where the effects of fibre distribution and constituent material properties are examined parametrically (*Knight et al. (2002c)*). A composite construct refers to a simplified model that closely represents the local behaviour within a real composite material. Hence, a unidirectional fibre composite is simplified to a two-dimensional model representing the geometrical characteristics within an arbitrary cross-sectional plane perpendicular to the fibre axes, where the fibres are assumed to be equally sized and circular, and distributed either periodically or randomly within the embedding matrix.

The purpose of this work is to apply a numerical tool to a parametric investigation of the micromechanics of composite materials, and thus provide an improved knowledge of the influence of fibre arrangement and phase properties on the local stresses. A range of geometrical parameters and materials properties has been modelled with a view to designing composite materials with improved properties that are more closely optimised for the particular specification required.

The numerical simulations include several simple geometric arrangements, i.e. square and hexagonally arranged fibres. These models are then extended to accommodate random distributions, so that the effects of fibre clustering on the localised stress distributions could be investigated. In addition, a range of material combinations, i.e. relatively stiff or flexible fibres or a mixture of both, relative to the matrix, is considered. An embedded cell approach (ECA) is employed to apply far field loading, as discussed in

Section 6.2.1, and a statistical method, based on the Weibull distribution, has been used to describe the distribution of stress concentrations, as discussed in Section 6.3.2. The results presented in this chapter pertain to calculations where the matrix and fibres follow an elastic response, and the interface between the fibres and the matrix is fully bonded.

6.2 Model Description

6.2.1 Embedded Cell Approach (ECA)

The embedded cell approach is a combination of macro- and micromechanics modelling, which aims at predicting the microfields in inhomogeneous materials at high spatial resolution. This technique approximates the real inhomogeneous material by a model consisting of a core containing a discrete phase arrangement ('local heterogeneous region'), which is embedded within some outer region to which far field loads or displacements are applied. A schematic depiction of the technique can be seen in Figure 6.1. The material characteristics of the inner core can range from relatively simple idealised configurations to highly detailed experimentally obtained phase arrangements. The outer region may be described by some macroscopic constitutive law (*Wulf et al.*

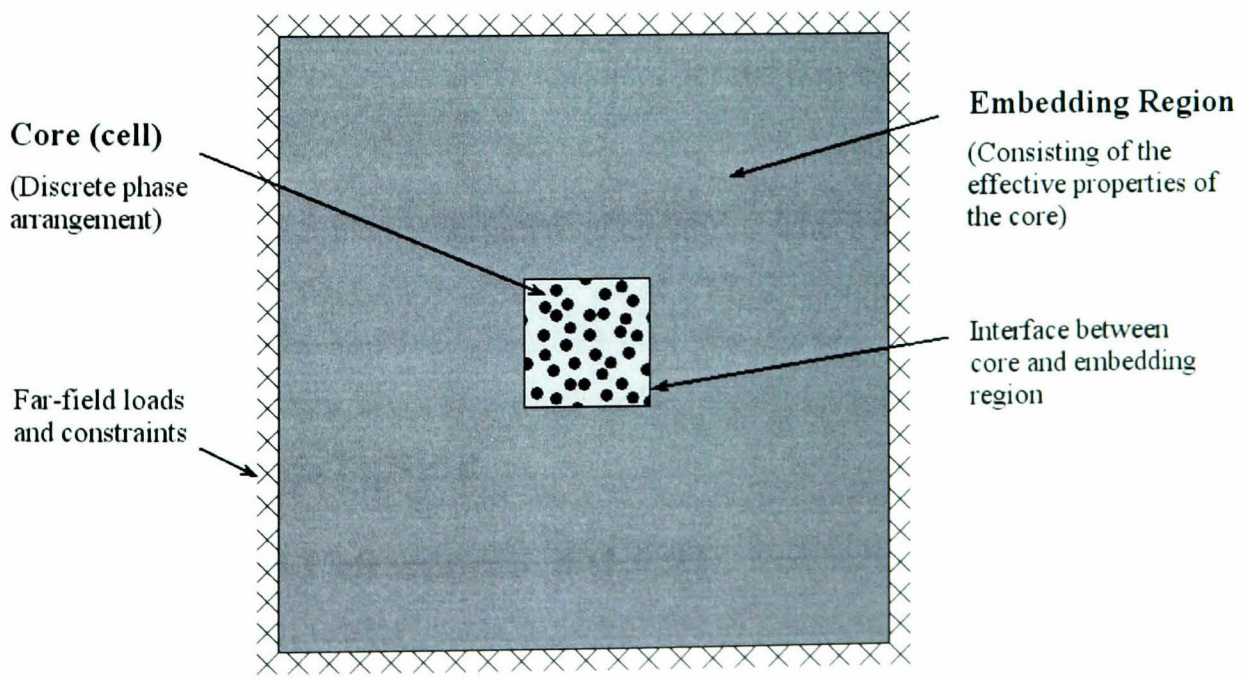

Figure 6.1 Concept of the Embedded Cell Approach (ECA)

(1996) and *Monaghan and Brazil (1997)*), determined self-consistently from the behaviour of the core (*Chen et al. (1994)* and *Dong and Schmauder (1996)*), or it may take the form of a coarse description and/or discretisation of the global phase arrangement (*Sautter et al. (1993)*). In the present study the outer region will be described using a standard constitutive law in the case of the two-phase composite, and determined self-consistently from the behaviour of the core for the three-phase composite, as discussed in Section 6.2.2.

ECAs have been successfully used for materials characterisation, and they are also very well suited for studying regions of special interest, e.g. local evolution of damage around a crack tip (*Wulf et al. (1996)*). However, a suitable description of the outer region must be chosen, so that errors in the accommodation of stresses and strains are avoided. Some care is also required with respect to spurious a 'boundary layer' that may occur at the interface between the core and the surrounding material, *Böhm (2000)*. The boundary layer is a transition zone between the homogenised deformation of the embedding region and the typically inhomogeneous response of the core. Hence, the localised stresses within this zone, which are evaluated from the displacements, would not necessarily reflect the stress distributions of the central core, as discussed in Section 6.3.1. As a rule, the boundary layer has a thickness of about an inclusion diameter for elastic materials, but they may be longer ranged for nonlinear material behaviour (*Böhm (2000)*).

6.2.2 Geometry and Materials

The distribution of the unidirectional fibres within a matrix has been modelled using several different packing arrangements, which can be classified into two groups: (i) embedded cells containing regularly spaced periodic fibre arrangements and (ii) embedded cells containing randomly distributed fibres. For the embedded cells with uniformly spaced fibre arrangements, the fibres were packed in square or hexagonal arrays as shown in Figure 6.2. These two idealised distributions are the most common arrangements used in many previous 'unit-cell' analyses (*Foye (1966)*, *Adams and Doner*

(1967b), *Aboudi (1989)*, *Guild and Young (1989)*, and *Achenbach and Zhu (1989)*).

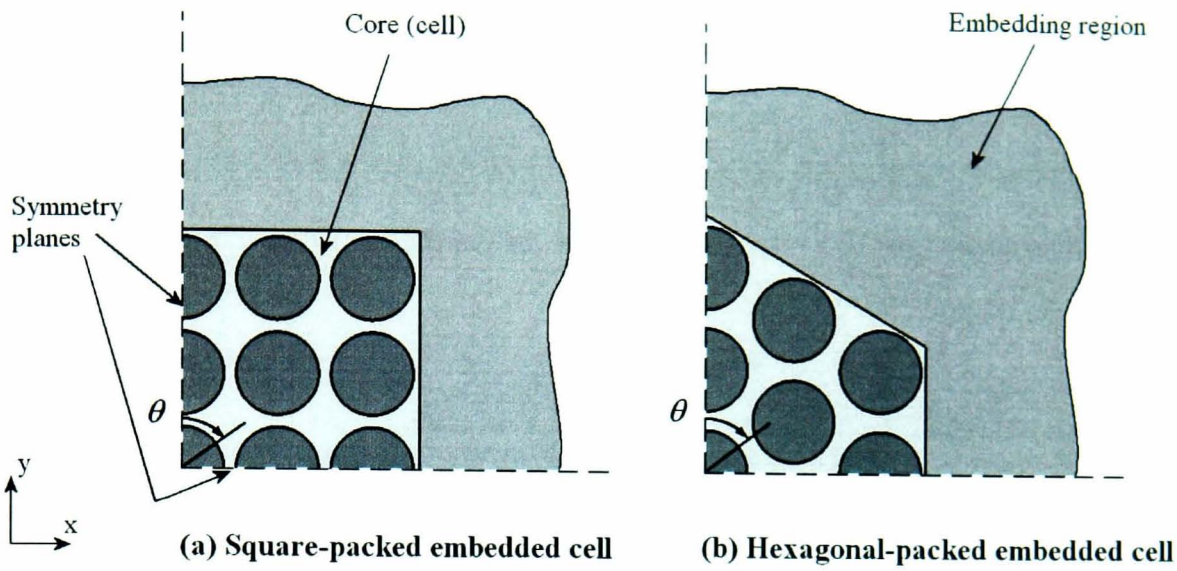

Figure 6.2 **Schematic of regularly spaced periodic fibre packing arrangements. (a) 25 square packed fibres, and (b) 19 hexagonally packed fibres**

For the square (SQ) and hexagonal (HEX) periodic arrangements, as shown in Figures 6.2(a) and 6.2(b), respectively, only one-quarter of the problem needs to be modelled, due to the symmetry. Along these symmetry planes the BE model need not be discretised and symmetry boundary conditions are applied. In the particular models shown, 25 and 19 equally sized fibres form the square and hexagonal lattices, respectively. However, as discussed later in Section 6.3.1, further models of differing numbers of inclusions are analysed to quantify the 'boundary layer' produced by the ECA. In each case, the embedding region is subjected to a remote unit tensile stress (σ_o) in the y-direction, at a sufficient distance from the core such that free surface effects can be neglected.

In addition to the uniformly spaced fibre arrangements in Figure 6.2, numerical simulations were conducted using embedded cells containing 60 equally sized, randomly (RAND) distributed fibres, as shown in Figure 6.3. These random-fibre embedded cells were generated using an in-house developed program. Within this program, the stipulated fibre volume fraction and number of inclusions determines the size of the embedded cell, and the location of each fibre is randomly selected such that fibres neither overlap with

each other nor with the cell boundaries. Note that by restricting fibres from overlapping with the cell boundaries, modelling the problem is greatly simplified. However, the localised fibre volume fraction close to the cell walls becomes lower than that of the central region (or kernel), as shown later. The effect of this geometric non-uniformity is discussed in Section 6.3.2. Furthermore, the ligament size (distance between the fibres) is controlled such that numerical problems could be avoided, as discussed in Section 6.2.3.

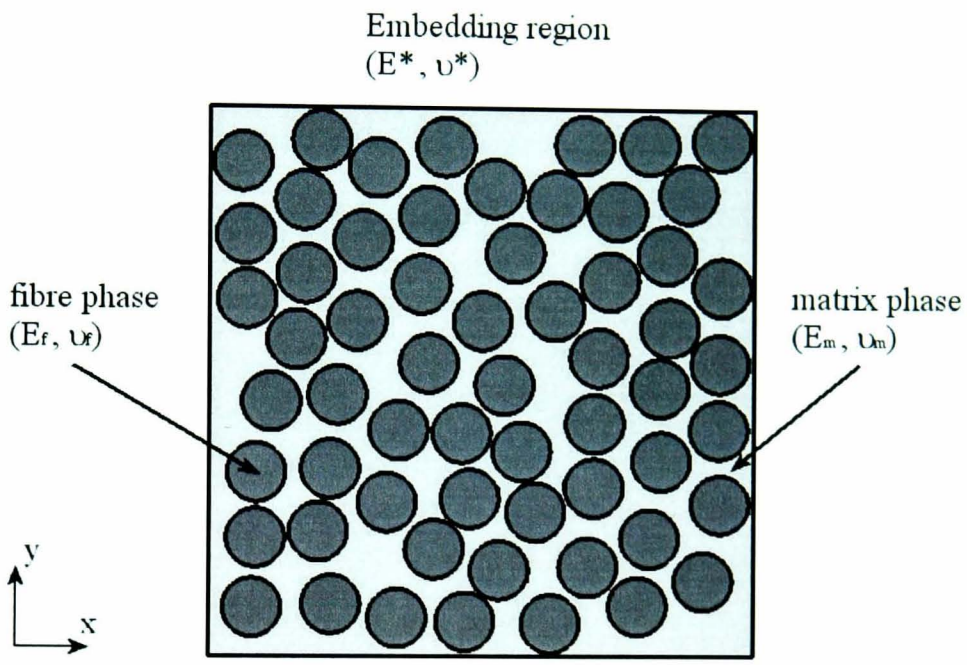

Figure 6.3 Schematic representation of an embedded cell containing 60 randomly distributed fibres.

Although the number of fibres chosen does not guarantee that the sample size accurately represents the response of a real composite, previous studies have confirmed that the representative volume element (RVE) selected is sufficient in size to adequately capture the behaviour of an inhomogeneous material (*Nakamura and Suresh (1993)*, *Drugan and Willis (1996)*, and *Gusev (1997)*).

In this study, ten different randomly distributed embedded cells are analysed so that a sample of results could be used within a statistical analysis, without increasing the model size and computational resources required. In addition, by conducting multiple simulations, a greater insight into the effect of random inclusion dispersion could then be achieved.

Representative material properties were chosen for the analysis, such that the results may be examined parametrically. Hence, the overall trends presented are equally valid for any fibre-reinforced composite with similar materials and interfacial characteristics. The volume fraction of fibres (V_f) used within the numerical models is 0.2, 0.4 and 0.6 for the periodic arrangements, and 0.54 (which corresponds to a kernel fibre volume fraction of approximately 0.6, as shown in Section 6.3.2) for the random arrangements. These values were deemed to cover the scope of typical reinforcement concentrations for fibre-reinforced composites, with the emphasis on the higher concentration (V_f = 0.6) used within both the periodic and random models.

For the two-phase composite models considered, the Young's modulus ratio selected for the constituents is $E_f / E_m = 10$, and the Poisson's ratio $\upsilon_f = \upsilon_m = 0.3$, where the subscript f = fibres and m = matrix. Further studies then consider the effect of varying the Young's moduli ratio (E_f / E_m), and Poisson's ratio mismatch (υ_f /υ_m) on the localised stress concentrations. The cases considered were:

- the fibres are nearly rigid ($E_f / E_m = 100$),
- the fibres are compliant ($E_f / E_m = 0.1$),
- the fibres have a higher Poisson's ratio than the matrix ($\upsilon_f = 0.4$, $\upsilon_m = 0.2$), and
- the fibres have a lower Poisson's ratio than the matrix ($\upsilon_f = 0.2$, $\upsilon_m = 0.4$).

In the first two models the Poisson's ratio of each constituent is 0.3, whereas, the latter models have an elastic moduli ratio of 10.

For the two-phase models considered, the material properties (E^*, υ^*) employed for the embedding region were obtained using semi-empirical expressions proposed by *Halpin and Tsai (1967)*, as follows:

$$M^* = M_m \frac{1+\xi\eta V_f}{1-\eta V_f} \tag{6.1}$$

where

$$\eta = \frac{M_f - M_m}{M_f + \xi M_m} \tag{6.2}$$

in which:

M = Material property (E_2, G_{12}, υ_{12})
V_f = Fibre-volume fraction
ξ = Adjustable parameter (depends on the fibre geometry, packing geometry, and loading conditions)

Although the given expressions only form an approximate representation of more complicated micromechanics models, in general they give good agreement with experiment over the complete range of fibre content (*Wolfenden and Wolla (1989)*). The only difficulty in using the Halpin-Tsai equations is in the determination of a suitable value of ξ. For the present study, $\xi = 2$ was used in the transverse material calculations, as it was found to give excellent agreement with *Foye's (1966)* results for fibres with square cross sections in a diamond array, and *Adams and Doner's (1967b)* results for circular fibres in a square array.

Finally, three-phase composite models comprising mixtures of both stiff and compliant fibres relative to that of the matrix were also analysed. This has direct relevance to the recent development of improved fracture toughness composites that contain mixtures of both high and low Young's moduli particles (*Hornsby and Premphet (1997,1998)*). Considering an idealised composite, which contains particles whose Young's modulus is greater than the matrix, it would generally be expected that the overall strength would increase, but inadvertently the toughness generally decreases. In contrast, composites containing particles whose Young's modulus is less than the matrix may be significantly tougher, but they are also generally relatively weak. Therefore, by manufacturing a material with a dispersion of high and low Young's moduli inclusions, both strength and toughness could possibly be enhanced, due to the combined reinforcing and toughening effects of the three-phase system. The material properties chosen were a 50:50 mixture of stiff fibres ($E_f / E_m = 10$), and compliant fibres ($E_f / E_m = 0.1$), with each constituent having a Poisson's ratio of 0.3. Ten arrangements were analysed, whose geometric characteristics were kept constant, however the distribution of fibre moduli was randomly

varied.

For the three-phase models considered, the elastic property (E^*) employed for the embedding region was determined self-consistently from the behaviour of the core. Note that the Poisson's ratio chosen for each phase is 0.3, therefore the effective Poisson's ratio, υ^*, must also be 0.3. The reason for this approach is due to the deficiency in accurate and reliable macroscopic constitutive laws governing the behaviour of three-phase composites. In this approach the core is assumed to be macroscopically homogenous, which allows the elastic response of the core to be evaluated from its boundary displacements. Ideally the elastic response of the core should be equivalent to that of the embedding region, therefore from an initial guess for the embedding region elastic constant an iterative procedure is adopted to obtain a value of E^*.

6.2.3 Boundary Element Modelling

The BEM meshes for the plane strain models (which are equivalent to the inclusions representing fibres) have been carefully developed, such that finer elements are placed along the fibre/matrix interfaces in regions where the fibres are nearly touching. This is to ensure accurate results where possible high stress gradients occur. Typical BEM meshes comprised of up to 3000 and 6500 linear elements for the periodic and randomly distributed models, respectively. Figure 6.4 illustrates a typical BEM discretisation used to represent a random-fibre composite undergoing transverse deformation, and Figure 6.5 shows the local mesh refinements in regions where fibres come into close proximity with each other.

In the full model shown (Figure 6.4), the upper and lower edges of the embedding region are subjected to a unit tensile stress (σ_o) in the y direction, and the model geometry is defined by: $H/L = 10.7$, $r/L = 0.107$, where H, L and r represent the embedding region size, cell size and the fibre radius, respectively. In addition, each fibre has the same radius, and the minimum ligament length is defined as ten percent of the fibre radius. The latter

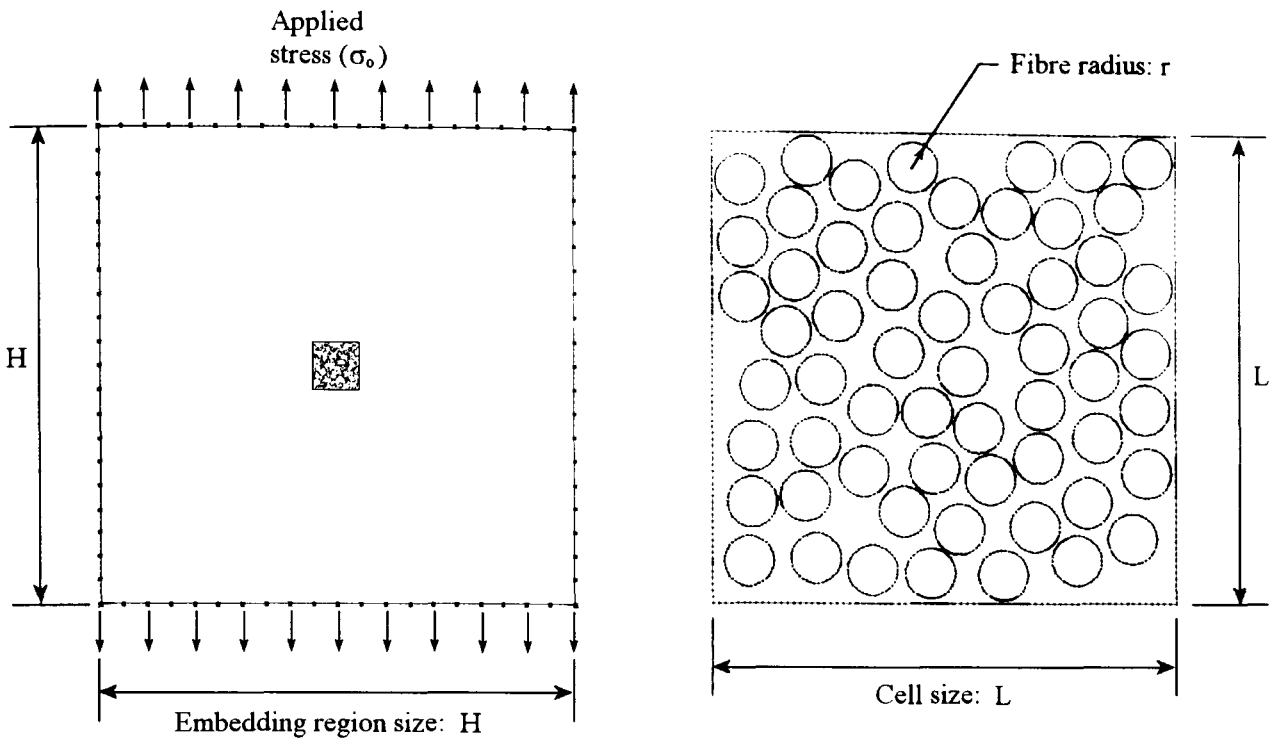

Figure 6.4 **Typical 2D BEM model, showing (a) the full discretised model and (b) an enlarged view of the embedded cell. (*H/L = 10.7, r/L = 0.107*)**

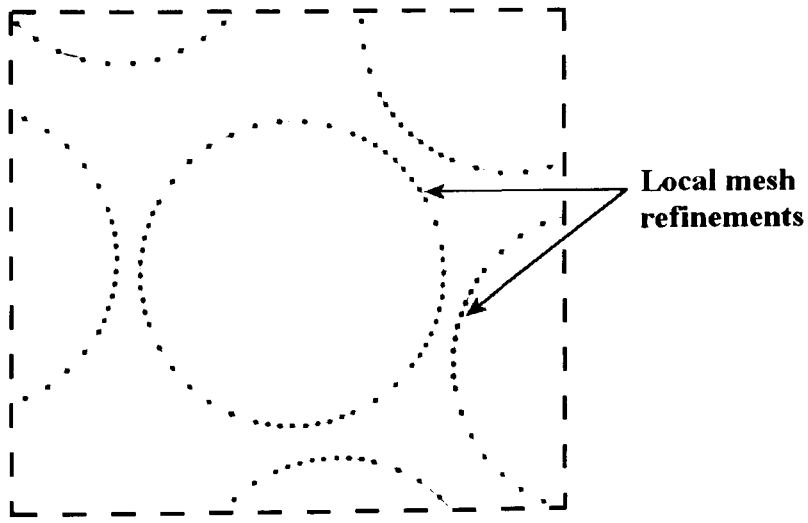

Figure 6.5 **Close-up view BEM discretisation, indicating localised mesh refinements for near-touching boundaries.**

condition is stipulated such that the ligament size is of the same order of magnitude or greater than the elemental size in those regions. The reason for this restriction is to avoid the stresses becoming unbounded when the fibres touch, hence the problem to be

considered has a contiguity (C) value of zero. Contiguity is a measure of inter-fibre contact between the embedded inclusions, *Lee and Gurland (1978)*.

To validate the model solution, a convergence study was undertaken using a number of models of different mesh densities. From this study, the boundary element meshes that are adopted within this thesis were found to give mesh-independent results. In addition, the results were found to correlate well with FE simulations (not shown).

6.3 Results and Discussion

In this section, firstly embedded cell models containing regularly spaced periodic fibre arrangements are considered, followed by the more complex analysis involving embedded cells containing 60 randomly distributed fibres. The regular arrays are employed as benchmark studies to validate the modelling techniques and the numerical method. The random-fibre representations are used to investigate further the roles played by fibre distribution and constituent material properties on the localised response of 'real' fibre-reinforced materials.

6.3.1 Periodic Arrangements

Effect of Cell Size and Spurious 'Boundary Layer'

To quantify the 'boundary layer' produced by the ECA, a number of simulations were conducted using increasing size embedding cells (RVEs), which have a fibre volume fraction of 0.6. For the square (SQ) arrangement, the normal stress (σ_n) and the tangential shear stress (τ_{nt}) were taken around the central fibre within a single, nine, and twenty-five inclusion RVEs, as shown in Figure 6.6(a). The corresponding results for a single, seven, and nineteen inclusion hexagonal (HEX) arrangements can be seen in Figure 6.6(b). Note that, in all cases, the stresses have been normalized by the applied stress (σ_o).

From these figures, it is noticeable that the distributions presented for the two larger embedded cells are very similar, however the values obtained from a single inclusion

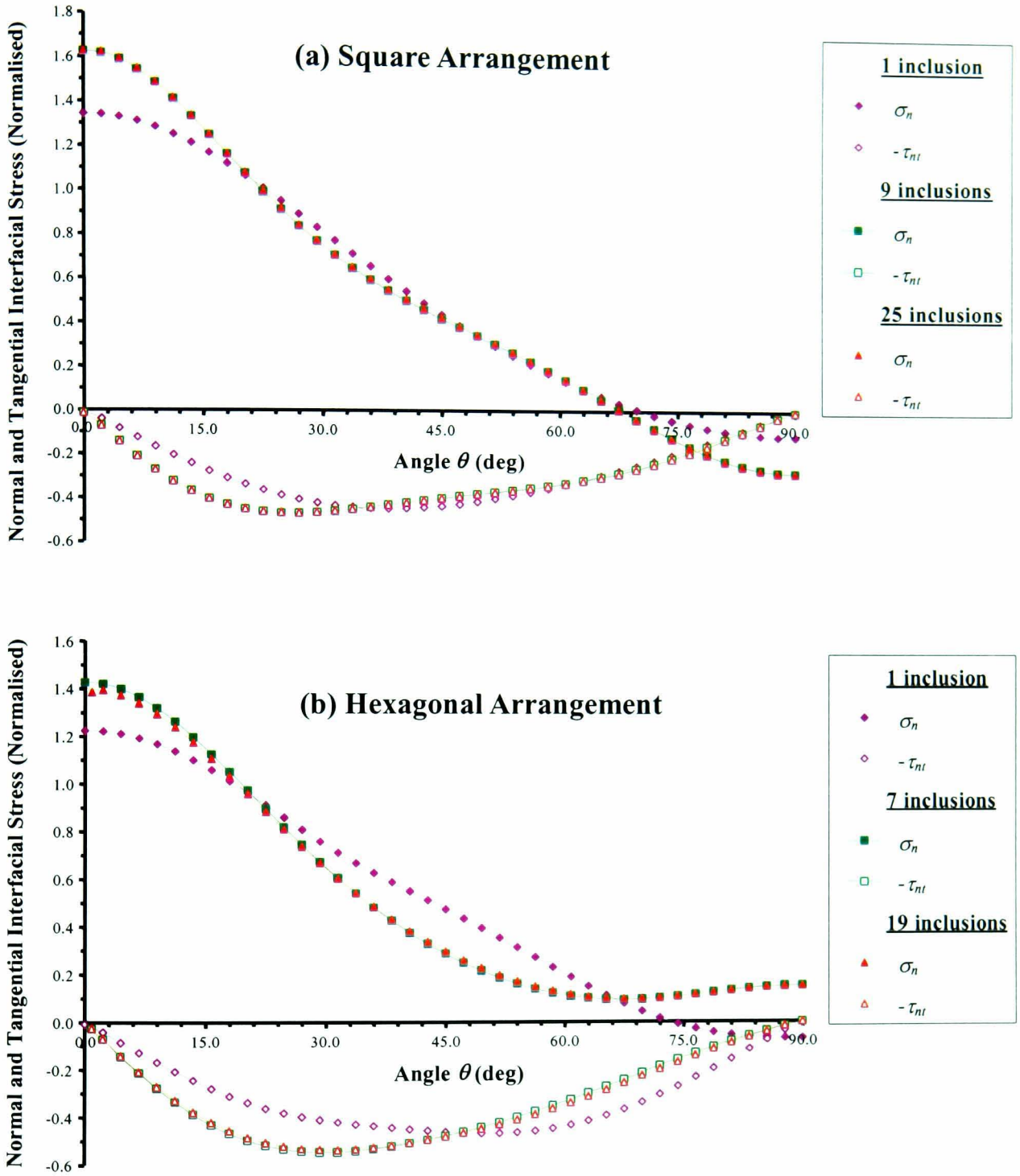

Figure 6.6 **Effect of the periodic cell size on the normal stress (σ_n) and tangential shear stress (τ_{nt}) distribution around the central inclusion. ($V_f = 0.6$, $E_f / E_m = 10$, $\upsilon_f = \upsilon_m = 0.3$)**

model are clearly dissimilar. This would suggest that, in both cases of square and hexagonal packing, the single inclusion model is insufficient in size to capture the localised behaviour, with the boundary layer introducing a noticeable effect. Nevertheless, for the resulting trends of the two larger embedded cells to be so similar, the boundary

layer must be limited to a range of approximately one inclusion diameter, which is in agreement with *Böhm (2000)*.

Validation of the Modelling Techniques and the Numerical Method

A comparison between the results presented for the largest embedded cells and the authors' FEM simulations using unit cell models with periodic boundary conditions, generally shows good agreement (see Figure 6.7). A range of volume fractions were analysed and the slight differences between the results have been found to be due to the approximated effective properties of the embedding region. As expected, the normal interfacial stresses (σ_n) are highest at $\theta = 0^\circ$, the direction of the imposed tensile stress, and the magnitude of these stresses increases as the volume fraction rises, with values being slightly higher for the square packing than the hexagonal array. At $\theta = 90^\circ$, the square-packed array predicts that the normal stress becomes compressive, whereas in the hexagonal array it remains tensile. The interfacial shear stress (τ_{nt}) rises to a maximum for values of θ between 20° and 45° in both the square and hexagonal arrays.

Further studies considering periodic arrangements with different material properties were also undertaken, analysing the effect of varying the elastic moduli ratio (E_f / E_m) and Poisson's ratio mismatch (υ_f / υ_m) on the local stress concentrations. Discussion of these results, as well as a direct comparison with random arrangements, is given in Section 6.3.2.

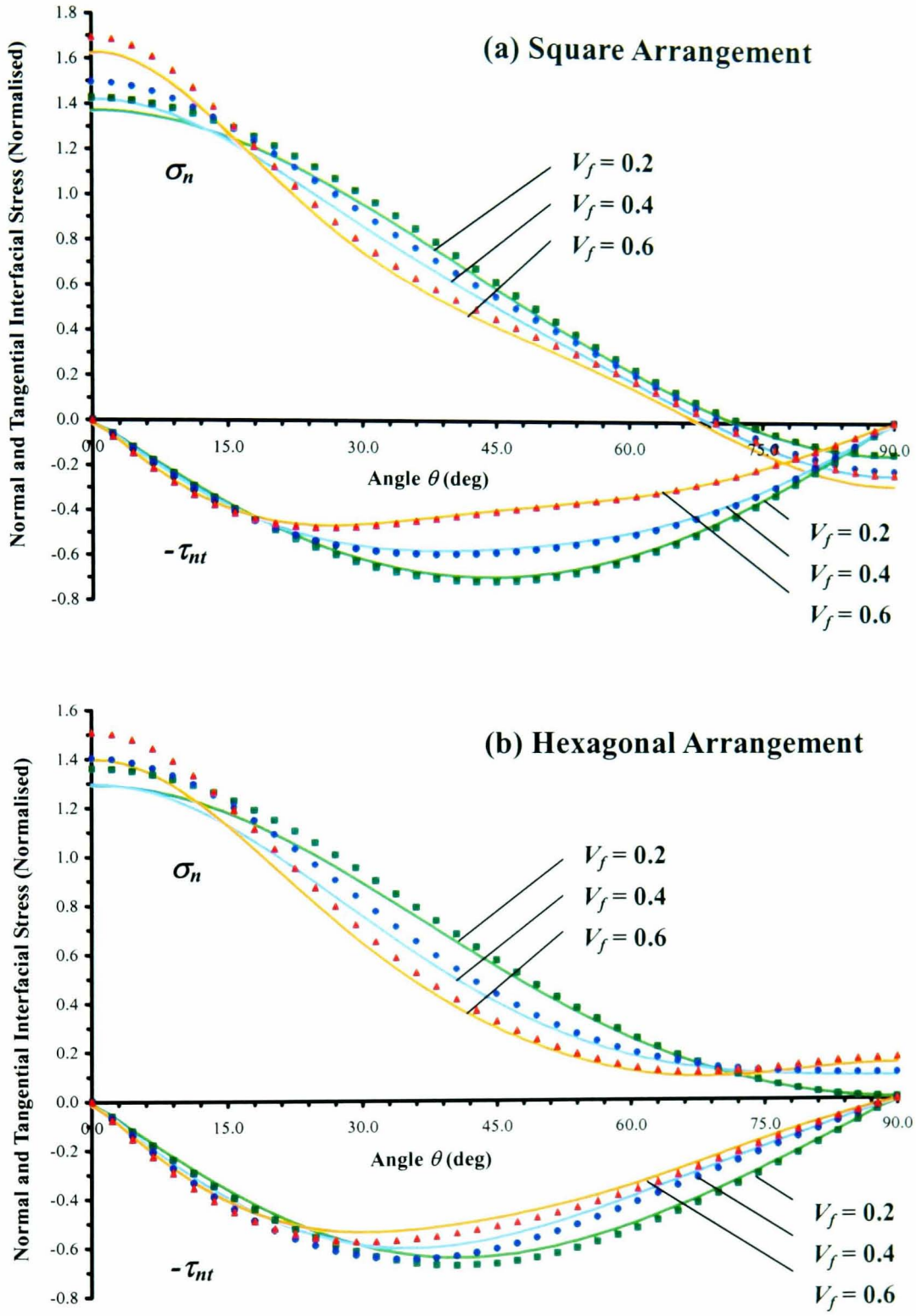

Figure 6.7 **Comparison between BEM embedded cell models (symbols), and FEM unit cell models, with periodic boundary conditions (lines). ($E_f / E_m = 10$, $\upsilon_f = \upsilon_m = 0.3$)**

6.3.2 Random Arrangements

Geometric Characterisation of the Model

As mentioned in Section 6.2.2, the random-fibre embedded cell models were generated such that fibres do not overlap with the cell boundaries. Hence, the localised fibre volume fraction close to the cell walls would be expected to be less than that of the central region (or kernel). Therefore, to analyse the extent of this geometric variation, 'test' windows were placed within the embedded cell and the resulting samples' fibre volume fraction (V_f) were numerically evaluated. The test window initially took the dimensions of the embedded cell, and the window boundaries were shifted inwards from the cell boundaries in steps of $0.1r$, calculating V_f at each step. The variation of V_f within 10 random (RAND) embedding cells can be seen in Figure 6.8. When the test window exactly matches the embedded cell, the average volume fraction of fibres is obtained. However, as the test window shrinks towards the central region (or kernel), the concentration of

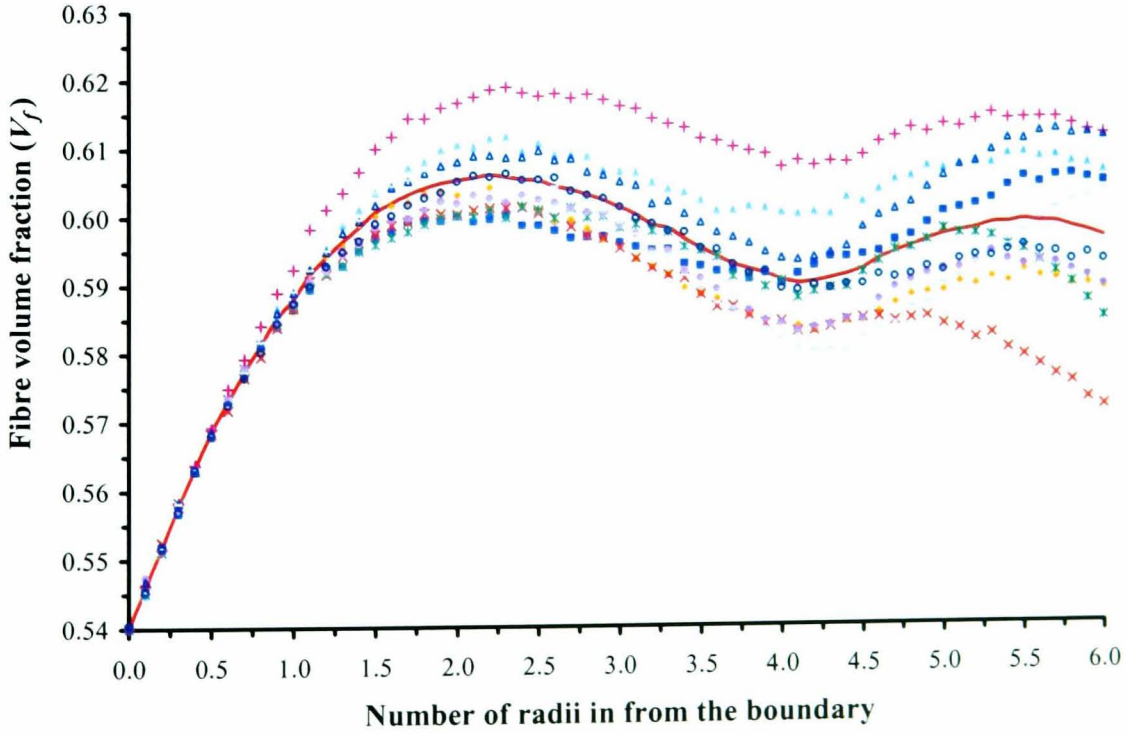

Figure 6.8 **The variation in the fibre volume fraction (V_f) within 10 random embedding cells. (*Symbols indicate the individual geometric models analysed and the line shows the average variation*)**

fibres increases in each model to a reasonably constant value at about one-inclusion diameter in from the cell walls. Although slightly deceptive in the figure due to its scaling, a consistency of the geometric characteristics is shown. The average kernel volume fraction ($V_f \approx 0.6$) has a variation of less than 2%, and all ten arrangements are within a 5% scatter band.

From these statistical variations, and the observations found within the previous section regarding the size of the 'boundary layer' produced by the ECA, results taken within one-inclusion diameter from the cell walls are less representative. Hence, with subsequent analyses, results will only be taken within the embedded cell kernel.

Local Analysis of the Composite

Figure 6.9 shows a contour plot of the variation of the first principal stress (S1) within a typical random-fibre embedded cell model. Many interesting features are noticeable from this figure. For instance, tensile bands seem to be formed linking fibres which have centres aligned in a direction close to that of the applied load. This is clearly seen on the left-hand side of the figure, where two visible fibre chains (shaded in green through to red) are shown. This would indicate that the load is being transferred between neighbouring inclusions in such a way that direct load paths are formed, linking the upper and lower surfaces of the cell. Within these bands, high values for the local stresses can also be found at the fibre/matrix interface or within the matrix ligament, for inclusions that are nearly touching and are closely aligned with the applied stress. These stress concentrations are typically twice the applied stress, but can be even greater.

For a periodic arrangement, consideration of the stress distribution within and around a single representative inclusion is sufficient to characterize the overall stress state. However, for the random arrays, the consideration of the stress distribution is not as straightforward. Hence, alternative methods of considering and describing the results have to be used. As there is no standard conventional approach to this, new methods of

general applicability are proposed, with the present results being used as particular examples.

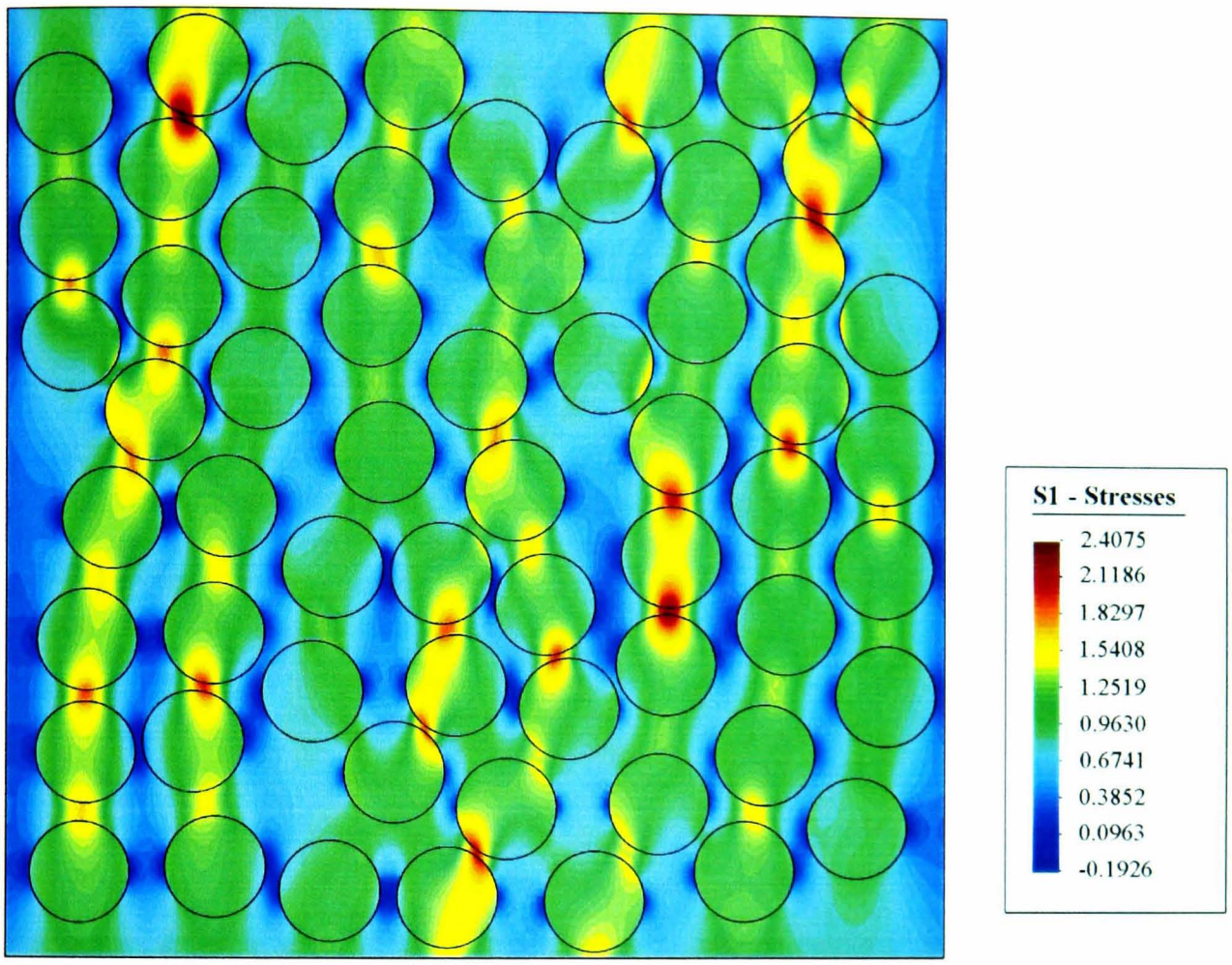

Figure 6.9 Contour plot of the variation of the first principal stress (S1) within a typical random-fibre embedded cell model. ($V_f = 0.54$, $E_f / E_m = 10$, $\upsilon_f = \upsilon_m = 0.3$)

From observations of the stress raiser locations and the local geometric arrangements of the fibres, it would seem that the magnitude of the stress concentrations are dependent on both the ligament length (d) (distance between the two neighbouring fibres that have a common high-stress region, in units of r), and their angle (δ) relative to the applied load (angle between a plane containing the two fibre centres and the applied load). To investigate this phenomenon, maximum first principal stresses $(S1)_{max}$ were taken from each fibre and its surrounding matrix, within the kernel of ten random arrangements, as well as the corresponding values for d and δ. Figure 6.10 shows two scatter graphs, which relate to; (a) the results obtained within the fibres and (b) the results obtained from the

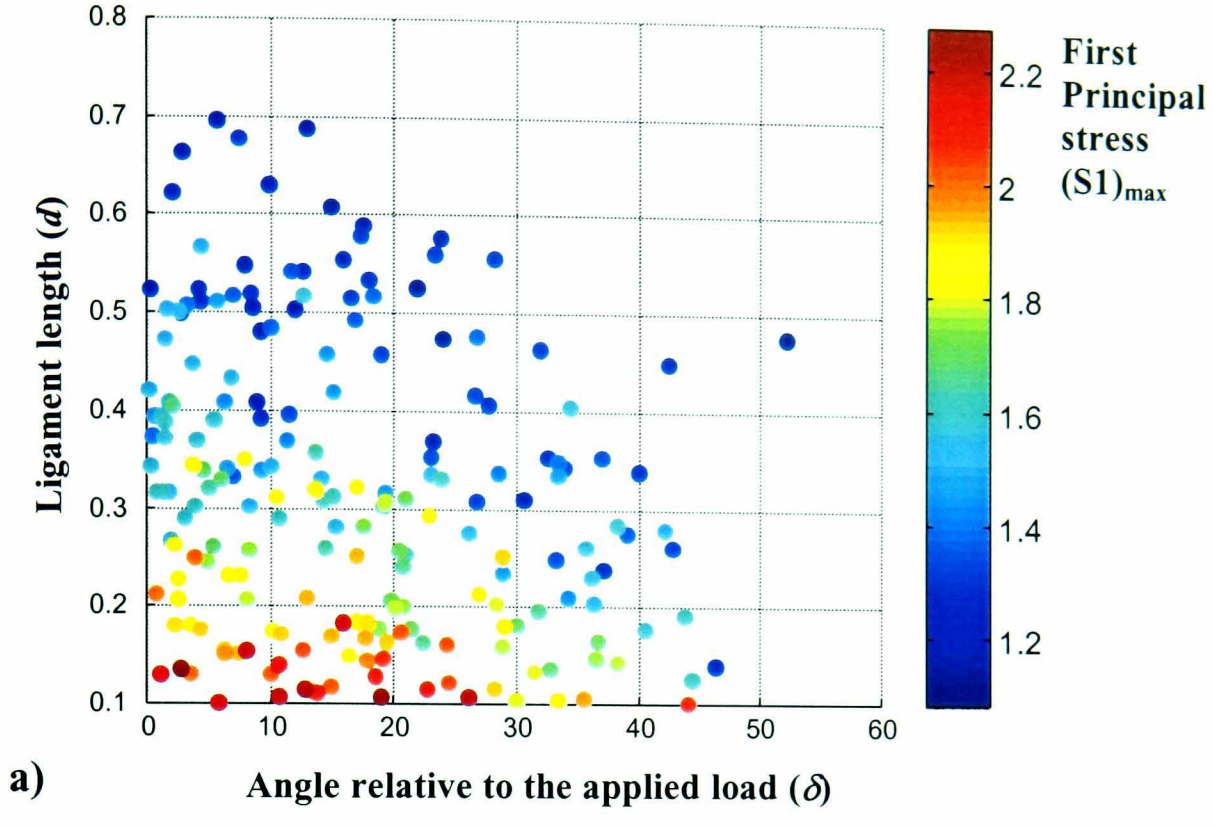

Figure 6.10 **Scatter graph showing the dependence of the localised maximum first principal stresses $(S1)_{max}$ within the 10 random arrangements on the ligament length and the alignment of the fibres relative to the applied load.** (***Values are taken within (a) the fibres, and (b) the matrix).***

surrounding matrix. In Figure 6.10(a), the maximum fibre values were always at the interface between the inclusion and matrix, whereas, the maximum matrix values, Figure 6.10(b), were either taken from the interface or within the ligament. In addition, the results tended to be slightly higher within the matrix, when compared to the corresponding values within the fibres.

Trends indicated within these figures seem to suggest that the magnitudes of the stress concentrations have a strong dependence on the ligament length (d), and to a lesser extent on the angle (δ) relative to the applied load. For example, data points that are distant from the two axes have lower values of stress than points close to the origin, and points of highest stress (shaded in red) are generally within a band $d = 0.1\text{-}0.2r$ and $\delta = 0\text{-}30^{\circ}$.

To examine the data shown in Figure 6.10 in terms of statistical variations, the applicability of a Weibull analysis (*Weibull (1951)*) was considered. This distribution was chosen because it is generally used to analyse the failure statistics for brittle materials. A cumulative probability distribution was obtained by summing the number of stress results above a certain stress concentration factor (K) and dividing this value by the total number of results in the set. This process was carried out over the range of stress concentrations, in intervals of 0.05, as shown in Figure 6.11. The triangular and diamond shaped symbols indicate the raw data corresponding to the matrix and fibres, respectively.

To obtain a curve fit to the data points, the standard three-parameter Weibull reliability function was employed, where the general form of the function $R(x)$ is given by:

$$R(x) = \mathrm{e}^{-\left(\frac{x-\gamma}{\alpha}\right)^{\beta}} \tag{6.3}$$

where α (scale parameter), β (shape parameter) and γ (location parameter) are positive constants.

To estimate the parameters that gave the 'best fit' to the data, a procedure involving linear transformation of the above equation, linear regression (to obtain α and β), and a simple

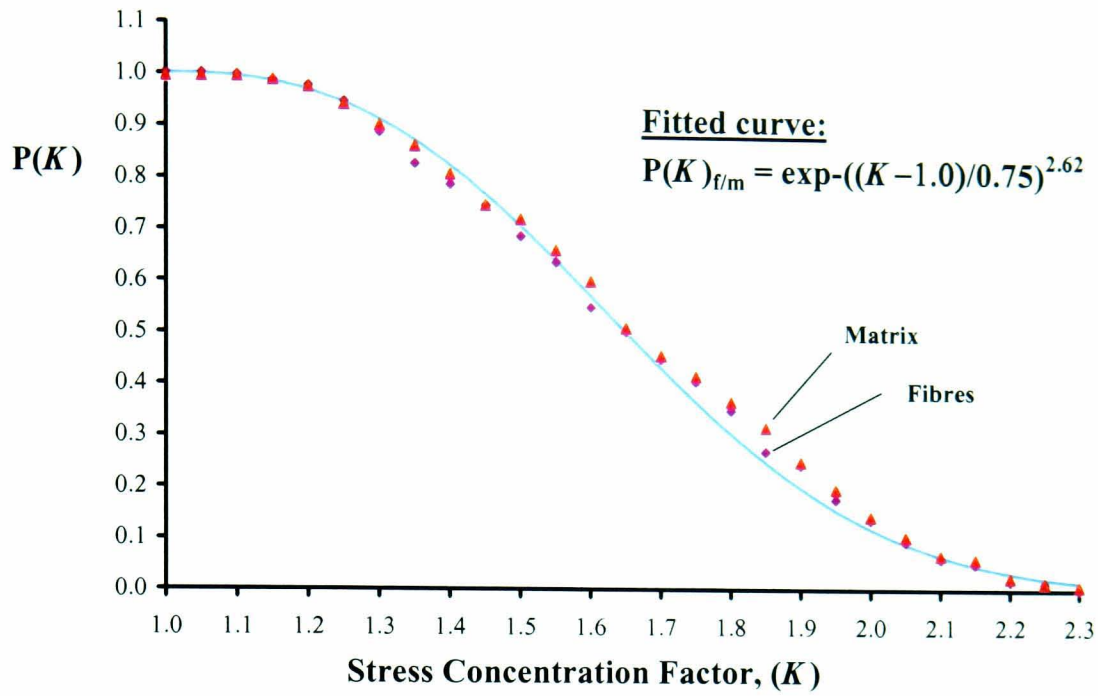

Figure 6.11 Cumulative Weibull distributions of the localised maximum first principal stresses $(S1)_{max}$ within the fibres and matrix. ($V_f = 0.54$, $E_f / E_m = 10$, $\upsilon_f = \upsilon_m = 0.3$)

iterative scheme to minimise any curvature within the transformed data (to obtain γ) was applied. As the results from the fibres and matrix are very similar (see Figure 6.11) a single curve fit was made, using averaged values. From results shown in Figure 6.11, it is first noticeable that the stress concentrations in the fibres and matrix are greater than unity, for all analysed cases. In addition, the shape parameter would seem to indicate that there is a reasonably high degree of variability in the stress concentration factors (taking a value of $\beta \leq 3$ as indicating high degree of scatter).

Effect of the Constituent Elastic Properties on the Local Behaviour

To analyse whether the constituent material properties play a significant role on the local stress concentrations, further simulations were conducted using the values indicated in Table 6.1. As mentioned previously, the elastic moduli ratio (E_f / E_m) and Poisson's ratio mismatch (υ_f / υ_m) of the phases will be isolated, and the maximum first principal stresses $(S1)_{max}$ retrieved from the different fibre packings. Two sets of results were obtained, corresponding to the fibres and matrix (in the same manner as those presented in Figure

6.10).

Constituent Material Properties	**Square (SQ) Arrangement** (25 inclusions)	**Hexagonal (HEX) Arrangement** (19 inclusions)	**Random (RAND) Arrangement** (60 inclusions)
$E_f / E_m = 100$, $\upsilon_f = \upsilon_m = 0.3$	1.855 (m) 1.800 (f)	1.500 (m) 1.426 (f)	3.060 (m) 3.012 (f)
$E_f / E_m = 10$, $\upsilon_f = \upsilon_m = 0.3$	1.675 (m) 1.625 (f)	1.469 (m) 1.397 (f)	2.305 (m) 2.273 (f)
$E_f / E_m = 0.1$, $\upsilon_f = \upsilon_m = 0.3$	4.906 (m) 0.518 (f)	5.047 (m) 0.537 (f)	7.084 (m) 0.916 (f)
$E_f / E_m = 10$, $\upsilon_f = 0.2$, $\upsilon_m = 0.4$	1.798 (m) 1.719 (f)	1.684 (m) 1.564 (f)	2.537 (m) 2.486 (f)
$E_f / E_m = 10$, $\upsilon_f = 0.4$, $\upsilon_m = 0.2$	1.618 (m) 1.590 (f)	1.369 (m) 1.329 (f)	2.231 (m) 2.215 (f)

Table 6.1 **The maximum first principal stresses $(S1)_{max}$ within models consisting of different fibre arrangements and constituent material properties. (*Two sets of results are indicated, where results are taken within the fibres (f), and matrix (m), respectively.*)**

Considering first the effect of the elastic moduli, it is noticeable that for almost rigid fibres ($E_f / E_m = 100$) the maximum stress within the fibres and matrix increases, when compared to the previously analysed case ($E_f / E_m = 10$), as expected. This is prevalent in each of the geometric arrangements, although the effect is greatest for the random-fibre model (~33% increase), and then the square array (~11% increase), and finally the hexagonal array (~2% increase). Next, considering a composite comprised of relatively compliant fibres ($E_f / E_m = 0.1$), the maximum stresses within the fibres decrease, whereas within the matrix the values substantially increase. This is due to the fact that the matrix has to carry the majority of load, and also the transmission of this load is generally across

very small ligament cross sections.

By introducing a Poisson's ratio mismatch the local stress magnitudes are slightly affected, as shown in Table 6.1. If the Poisson's ratio of the matrix is higher than that of the fibres ($\upsilon_f/\upsilon_m = 0.5$), the stresses tended to be between 6-10% higher than the original model, where the Poisson's ratio of the phases were the same ($\upsilon_f/\upsilon_m = 1$). Whereas, if the Poisson's ratio of the matrix is lower than that of the fibres ($\upsilon_f/\upsilon_m = 2$), the stresses tended to be 2-7% lower than the original model.

Analysis of a Composite with a Stiff and Compliant Fibre Mixture

Finally, composite models comprising of 50:50 mixtures of both stiff and compliant fibres relative to that of the matrix have been analysed. Figure 6.12 shows a contour plot of the variation of the first principal stress (S1) within a typical random-fibre embedded cell model with mixed inclusion properties. Comparing Figure 6.9 (contour plot from a model whose geometric characteristics are the same, however, all the fibres have the same material properties) with Figure 6.12, significant differences in the stress distribution are noticeable. In particular, the compliant inclusions are all virtually unstressed, whereas the stiff inclusions are generally experiencing stresses in excess of those present in previous models. This would indicate that the higher moduli inclusions are predominantly carrying the load, and as there are fewer stiff fibres the stresses within each would increase. Furthermore, very high localised stresses can be found in the ligaments between compliant fibres that are generally aligned perpendicular to the applied load plane. In the particular model shown, the local stress concentrations are over six times higher than the applied stress. High stresses in these regions would be due to the transmission of local forces across relatively narrow ligament cross-sections, in a similar manner to the results presented previously in this section for compliant inclusions.

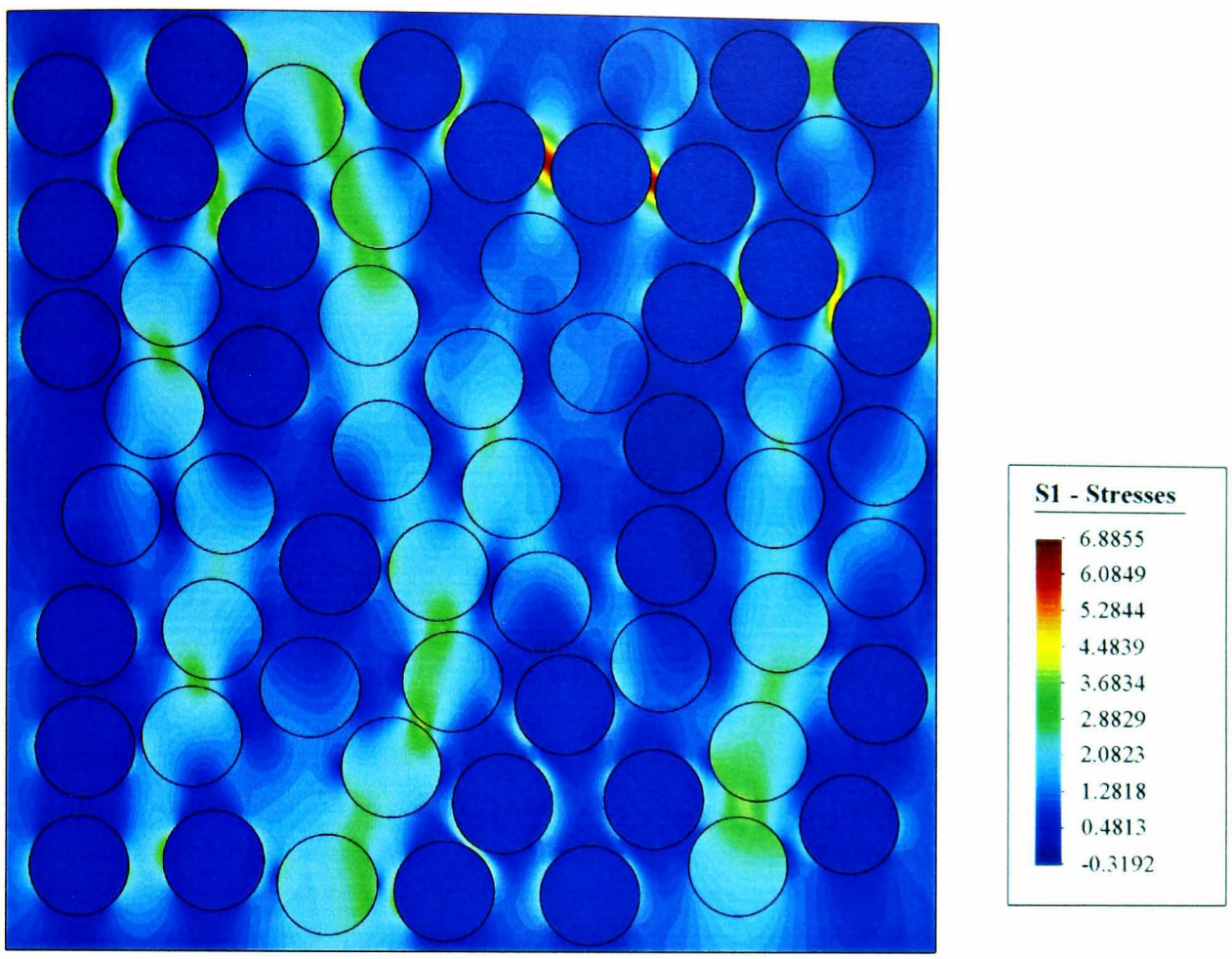

Figure 6.12 Contour plot indicating the variation of first principal stress (S1) within a typical random-fibre embedded cell model. (V_f = 0.54, 50% fibres - E_f / E_m = 10, 50% fibres - E_f / E_m = 0.1, υ_f = υ_m = 0.3)

Statistical analysis of this three-phase system, once again, took the form of a Weibull distribution. Ten different arrangements were examined and in each case the geometric characteristics were kept constant, however the distribution of fibre modulus was randomly varied. Note that the fibre stresses were only taken from the stiff inclusions, as the stresses within compliant inclusions were less than the applied load. A similar Weibull plot to that of the two-phase system (Figure 6.11) can be seen in Figure 6.13 for the aforementioned three-phase system. Note that in this figure the fibre and matrix distributions are distinctly dissimilar, hence two separate curve fits were conducted.

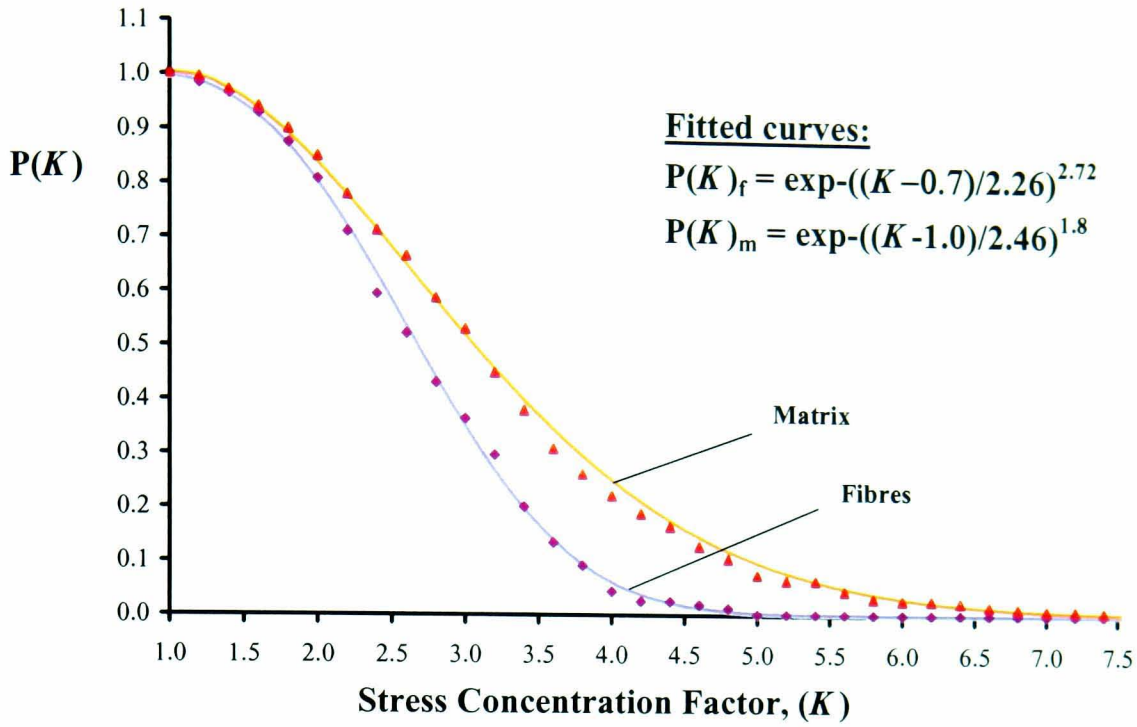

Figure 6.13 **Cumulative Weibull distributions of the localised maximum first principal stresses $(S1)_{max}$ within the fibres and matrix. ($V_f = 0.54$, 50% fibres - $E_f / E_m = 10$, 50% fibres - $E_f / E_m = 0.1$, $\upsilon_f = \upsilon_m = 0.3$)**

Comparing figures 6.11 and 6.13, significant differences in the Weibull distributions are noticeable. In particular, the stress concentrations are substantially higher in the case of the three-phase system. This is indicated by the large difference in the scale parameters α, used in the curve fits ($\alpha = 2.26$ and 2.46 for stiff fibres and matrix, respectively, in the three-phase system, and $\alpha = 0.75$ for both the fibres and matrix of the two-phase system). The shape parameter β would seem to indicate that there is a reasonably high degree of variability in all the results, and in particular, matrix stresses from the mixed-moduli model show a very high degree of variability ($\beta = 1.8$). Finally, the location parameter γ shows that for the two-phase system, and the matrix of the three-phase system, the stress concentration factors (for the analysed cases at least) are always greater than one. However, for the stiff fibres of the mixed-moduli models, there is a higher likelihood of a stress reduction.

For a number of stress concentrations factors, i.e. $K = 2$, 4 and 6, the corresponding probabilities can be calculated using the fitted Weibull functions, as shown in Table 6.2.

Stress Concentration Factor, K	Probability, P(K)		
	Two-phase, fibres and matrix	Three-phase, stiff fibres	Three-phase, matrix
2.0	1.19×10^{-1}	8.01×10^{-1}	8.21×10^{-1}
4.0	3.87×10^{-17}	6.08×10^{-2}	2.39×10^{-1}
6.0	2.64×10^{-63}	3.87×10^{-5}	2.77×10^{-2}

Table 6.2 Calculated probabilities of the two-phase and three-phase systems having a stress concentration factor (K) of 2, 4, and 6.

This highlights the possible adverse effect, in terms of high localised stress concentrations, of mixing both stiff and compliant fibres relative to that of the matrix within a composite. Micro-cracks, which often nucleate in and around the embedded phase, would have a higher probability of initiation in the three-phase system, which in turn could lower the inherent strength of the composite. Note that this result would seem to contradict the findings of the simplified three-inclusion model presented earlier. In the three-inclusion model the fibres are strictly aligned with the applied stress ($\delta = 0^{\circ}$), whereas, in reality fibre alignments would be in the range, $\delta = 0^{\circ}$-90°. In addition, due to the random natural of fibre arrangement and properties, stiff and compliant fibres will also interact with each other. Consequently, the conclusions of the three-inclusion model will be subject to the modelling assumptions and should be interpreted as such.

6.4 Summary

In this study, the localised stress distributions within a multi-fibre composite undergoing transverse deformation are investigated using computational techniques. A combination of the boundary element method (BEM) and an embedded cell approach (ECA) allows a number of idealised (periodic) and more practical (random) discrete phase arrangements

to be analysed in depth. Results obtained are for purely elastic material combinations and calculated stresses are given within the fibres, matrix, and fibre/matrix interfacial zone (assuming no debonding between the fibres and matrix).

The main results obtained from this study are:

- Fibre packing arrangement has a significant effect on the overall stress distribution and the magnitude of localised stress concentrations. For the same fibre volume fraction significantly higher stresses were observed in the non-periodic, compared to the periodic square and hexagonal arrangements.
- Constituent material properties also control the local response. For an elastic moduli ratio greater than unity, stress concentrations were present in the ligaments of near-touching inclusions that have centres aligned in a direction close to that of the applied load. The magnitudes of these stresses increased as the elastic moduli ratio increased. For a system of compliant fibres, very high stresses were present in the ligament of near-touching inclusions that have centres aligned in a perpendicular direction to that of the applied load. Finally, a Poisson's ratio mismatch only slightly affected the local stress distributions and their magnitudes.
- For the random arrangements of stiff fibres, the magnitudes of the stress concentrations seem to have a strong dependence on the ligament length (d), and to a lesser extent on the angle relative to the applied load (δ).
- By mixing a compliant third-phase material into the composite, local stress concentrations substantially increased, which could lead to a reduction in the material's overall strength.

Chapter 7: Interaction between a Propagating Crack and an Uncoated/Coated Inclusion

7.1 Introduction

In many cases, the engineering application of a composite material is closely related to its fracture properties. Hence, in recent years there has been a surge of interest in maximising the 'fracture toughness' of such materials, which is a measure of their resistance to the continued growth of a pre-existing crack. Fracture in these materials is typically associated with three main mechanisms, namely: matrix, reinforcement and interfacial fracture. The first mechanism will be simulated within this investigation.

Studies of the interaction between cracks and inclusions have received much attention in previous years. Analytical approaches have been successfully applied to problems involving cracks inside, outside, penetrating or lying along the interface of an embedded inclusion, within both uniaxial and biaxial stress fields (e.g. *Tamate (1968)*, *Atkinson (1972)*, *Sendeckyj (1974)*, *Erdogan et al. (1974)*, *Kelly et al. (1994*), and *Hwu et al. (1995)*). These studies have clearly identified the effect a second phase inclusion has on the crack tip energetics; in particular, the 'shielding' and 'amplification' effects which are apparent when a crack approaches a relatively stiff or compliant inclusion, respectively. However, all these analyses are based on the assumption of a given crack location and size, and/or a prescribed crack path which is known *a priori,* due the symmetry of the particular problem.

Numerical techniques have also been applied to such problems, for instance the finite element (FE) approach has been used to model a crack approaching and passing through an elastic inclusion (*Li and Chudnovsky (1993a, 1993b)*) and furthermore, crack-particle interaction has been studied in terms of inclusion shape effects and a crack deflection

zone (*Lipetzky and Schmauder (1994)*, and *Lipetzky and Knesl (1995)*). The boundary element technique, which has been used in this study, is particularly well suited to the consideration of crack propagation in linear isotropic solids, as discussed in Section 3.5.3. Although at present it would appear to only have been applied to a composite material composed of Silicon Carbide reinforced Aluminium (Al/SiC) by *Bush (1997)*.

In the present analysis, in accordance with the aforementioned numerical studies, crack propagation is considered to be quasi-static. Hence, dynamic effects, such as elastic waves or strain rate dependent material properties, are not taken into account (e.g. *Meguid and Wang (2000)*).

7.2 Model Description

7.2.1 Geometry and Materials

This investigation analyses the crack tip energetics of an edge crack propagating towards a single embedded inclusion, either coated or uncoated, within a dissimilar matrix. The problem is assumed to be plane strain (which is equivalent to the inclusion representing a fibre), linear elastic and the interface between the phases is fully bonded. The component materials are assumed to behave isotropically, and the cross-section of the inclusion is circular. The embedding matrix material is subjected to a remote uniform tensile stress and the nondimensionalised energy release rate (G/G_o) at the propagating crack tip has been examined as a function of:

- Relative Young's moduli of the material phases (E_i/E_m, E_c/E_m), where i = inclusion, c = coating, and m = matrix,
- Poisson's ratios of the material phases (υ_i, υ_m),
- Normalised crack offset with respect to the inclusion centreline (d/r), and
- Relative coating thicknesses (t).

7.2.2 Boundary Element Modelling

Crack-growth processes, regardless of the physical mechanism involved, invariably require the use of incremental numerical methods for their analysis. Principally there are two main numerical techniques that have been applied to fracture mechanics problems; the finite element and the boundary element method.

The finite element method, whose history in fracture mechanics applications is reported in *Gallagher (1978)*, has been applied to study crack-growth processes, for instance by *Swenson and Ingraffea (1988)* and by *Kocer and Collins (1998)*. However, within most of the present formulations there is a need for continual remeshing to follow the crack extension, which can make this method rather time-consuming.

The boundary element method has also been applied in incremental analyses of crack-growth problems, by the use of sub-regions (*Ingraffea et al. (1983)*), or more recently using a dual formulation (e.g. *Bush (1997)*, and *Portela et al. (1993)*). The latter method, which is incorporated in the present study, is more efficient and has none of the remeshing difficulties mentioned above. Furthermore, by incorporating an efficient scheme to solve the system of equations, such as the incremental LU decomposition method, computational time and resources can be minimised (*de Lacerda and Wrobel (2001)*). This procedure is also adopted in the present linear elastic fracture analysis (see Section 3.5.3 for further information regarding the formulation and implementation of the dual boundary element method for fracture analysis).

In previous studies of crack-growth, the direction of crack propagation has generally been described from information near the crack tip, i.e. localised stress field (*Kocer and Collins (1998)*) or J-integral method (*Portela et al. (1993)*). Alternatively, it can also be determined from a global energy approach, which evaluates the work done by the external loads (*Bush (1997)*). In the present investigation, however, the trajectory is found by the use of a predictor-corrector, maximum principal stress criterion, and the crack tip energetics are evaluated from a modified 'crack-closure' integral method (*de Lacerda and*

Wrobel (2001)). The maximum principal stress criterion predicts the tangential direction of the crack path, so that the crack extension can be approximated by a piece-wise straight curve. The modified crack closure method evaluates the crack-tip stress intensity factors, using the normal and tangential stresses in front of the crack tip and also the relative normal and tangential displacements along the crack path.

To establish the energy release rate (G) for the crack the following equation is then applied, which directly incorporates the calculated stress intensity factors (K):

$$G = \frac{1}{E'}\left(K_I^2 + K_{II}^2\right) \tag{6.1}$$

where $E' = E / (1 - \upsilon^2)$ for plane strain.

In this equation the Young's modulus and Poisson's ratio are assumed to be global parameters of the entire body, hence for a composite material, equivalent values should strictly be applied. However, in the present study the fibre volume fraction (V_f) to be considered is very low, $V_f \approx 3.14\times10^{-4}$, therefore the assumption that these equivalent material properties correspond to those at the crack tip is justified.

In the following study the energy release rate is nondimensionalised by dividing the value obtained in the presence of the embedded inclusion (G) by the corresponding value in the absence of the inclusion (G_o). Hence, the energetics of the propagating crack tip are evaluated from the following relationship:

$$G / G_o \approx \left(K_I^2 + K_{II}^2\right) \Big/ \left(K_I^2\right)_o \tag{6.2}$$

where the subscript o denotes the unreinforced model. Also, $(K_{II})_o$ is neglected as the crack is propagating within an unreinforced plate, and is assumed to be purely Mode I.

The boundary element meshes for the plane strain model have been carefully developed such that the solutions were found to be independent of the elemental size at the crack tip and interface between the inclusion, coating and the dissimilar matrix. Typically, the BE

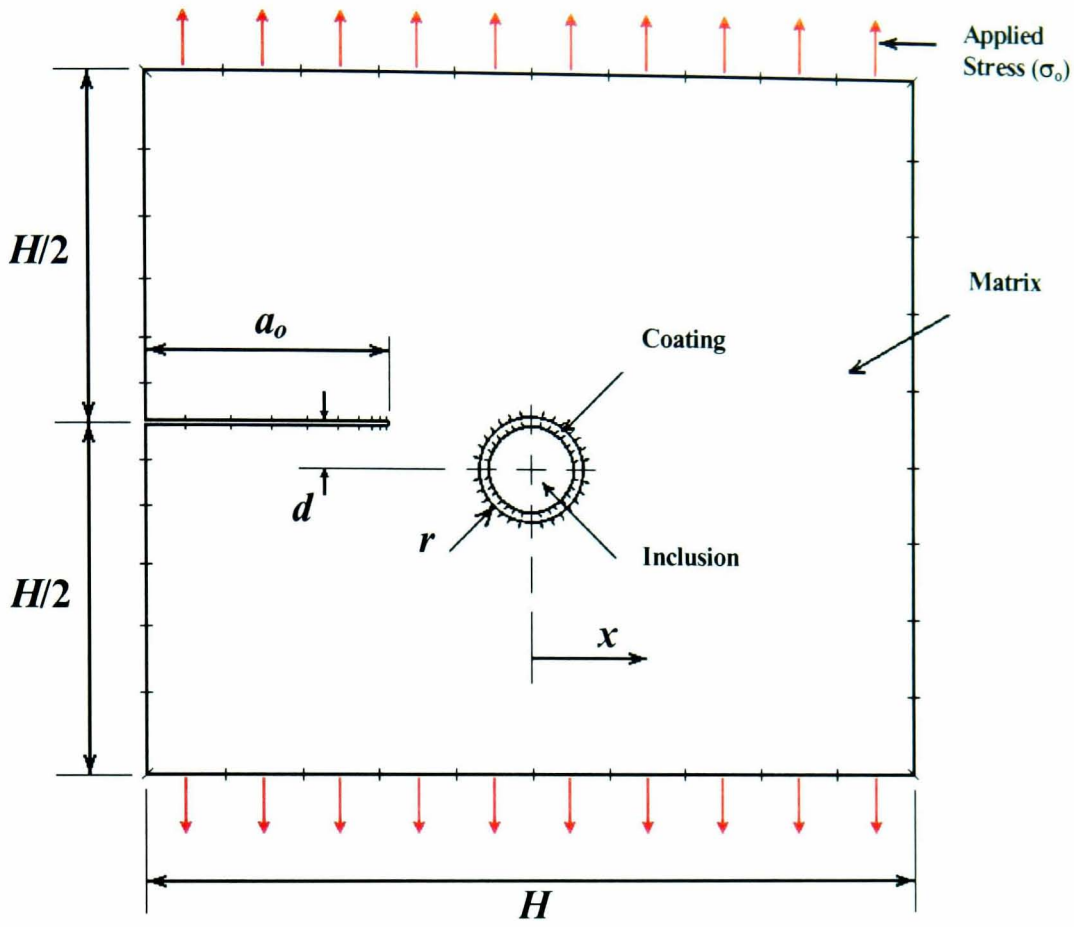

Figure 7.1 Typical 2D Boundary Element model of an edge crack propagating towards an embedded inclusion of dissimilar materials. ($r/H = 0.01$, $a_o = 0.45\ H$)

meshes comprised 90 quadratic elements along the external boundaries, 120 discontinuous linear elements along the initial crack surfaces, and 130 or 260 quadratic interface elements in the case of an uncoated and a coated inclusion, respectively. Figure 7.1 shows a schematic of a typical BE mesh used within this investigation. For modelling purposes, the overall radius of the inclusion (r) is taken as one percent of the plate dimension, i.e. $r/H = 0.01$, and the initial crack length (a_o) is given by $a_o = 0.45\ H$, such that initial propagation commences from $x/r = -5$.

7.3 Results and Discussion

In this section, firstly the problem of an uncoated inclusion (two-phase system) is considered, and then the coated inclusion (three-phase system) problem.

7.3.1 Uncoated Inclusion Problem

Young's Moduli effect: Centred Crack (d/r =0)

The variation in the nondimensionalised energy release rate, G/G_o, of the propagating crack was computed for differing elastic moduli mismatches (Figure 7.2). It is clear from these results that a relatively compliant inclusion ($E_i / E_m < 1$) produces substantial 'amplification' in G/G_o, whereas a relatively stiff inclusion ($E_i / E_m > 1$) shows a corresponding 'shielding' effect. These effects would be expected to lead to respectively either assistance with or impediment to crack growth as the crack approaches the inclusion. In both cases the amplification or shielding effect of the inclusion decreases as the ratio of the inclusion stiffness to matrix stiffness approaches unity. These results are in agreement with both the work of *Li and Chudnovsky (1993a, 1993b)* and *Bush (1997)*.

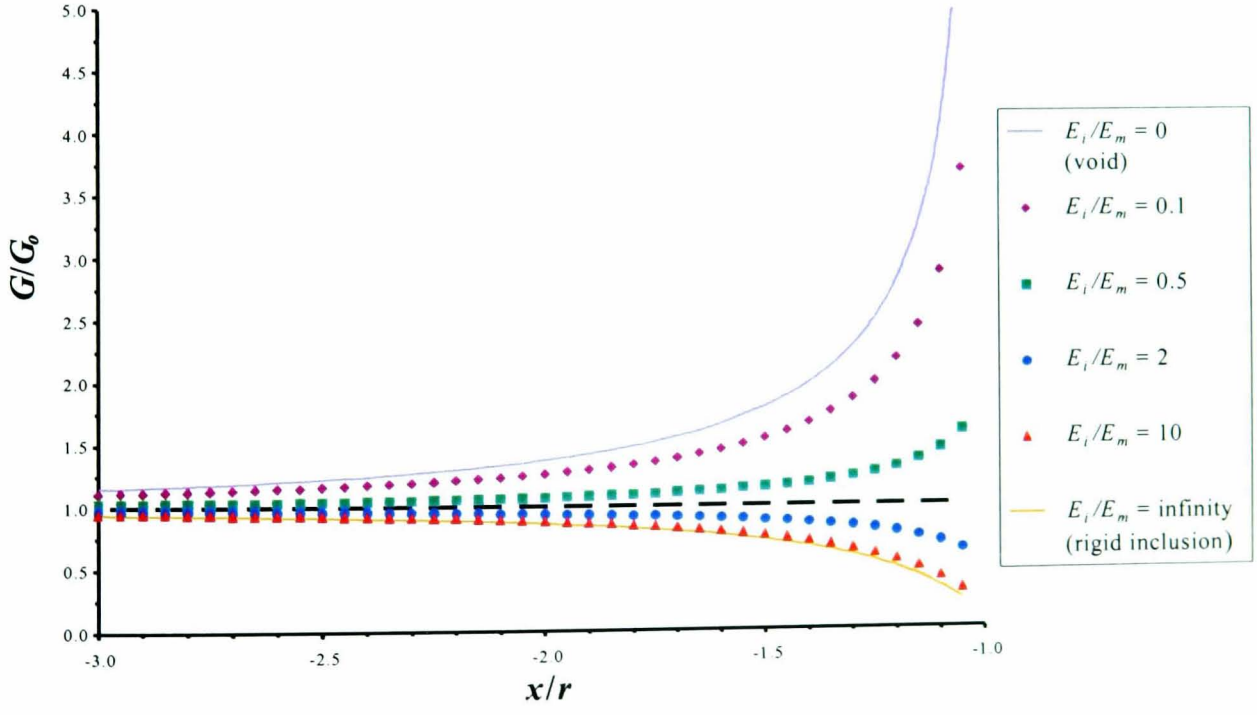

Figure 7.2 **Effect of elastic modulus mismatch (E_i / E_m) on the non-dimensionalised energy release rate (G/G_o) for a crack approaching an uncoated inclusion along its centreline. ($d/r = 0$, $\upsilon_i = \upsilon_m = 0.3$)**

Poisson's Ratio effect: Centred Crack (d/r =0)

Two further series of analyses were conducted to determine if the Poisson's ratios of the individual phases would have an effect on crack propagation. Figure 7.3 shows the variation in the nondimensionalised energy release rate when the Poisson's ratios of both phases (υ_i, υ_m) are modified, in the range 0.1 to 0.4. In this case a rigid inclusion ($E_i/E_m \rightarrow$ infinity) has been modelled, so that the effect of varying the Poisson's ratio could be maximised. From this figure, it is clearly noticeable that the Poisson's ratio has a significant effect on the shielding process. As each phase becomes more incompressible (υ_i, $\upsilon_m \rightarrow 0.5$) the reduction in the energy release rate become less apparent, which would suggest the crack undergoes a reduced shielding effect. Furthermore, as the inclusion is assumed to be rigid, the Poisson's ratio of the matrix can be assumed to be the parameter that is controlling the calculated variations.

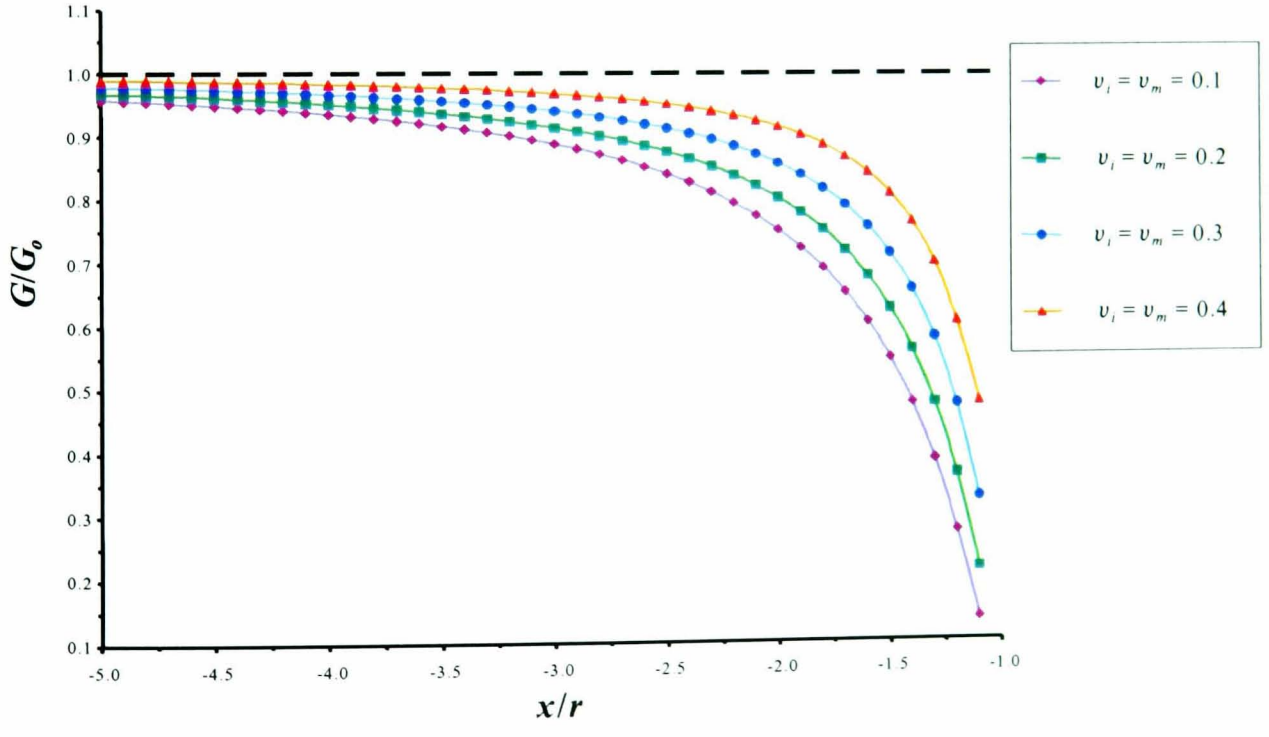

Figure 7.3 Effect of Poisson's ratio on the nondimensionalised energy release rate (G/G_o) for a crack approaching an uncoated inclusion along its centreline. ($d/r = 0$, $E_i/E_m \approx$ infinity)

Figure 7.4 presents the corresponding results for differing Poisson's ratio mismatches (υ_i/υ_m). In this case, $E_i/E_m = 1$, so that the mismatch effect could be isolated. The results

shown in this figure indicate that by simply modifying the Poisson's ratio mismatch, the stress at which the crack propagates can be controlled. For a system in which the Poisson's ratio of the inclusion is higher than that of the matrix ($\upsilon_i/\upsilon_m > 1$), a distinct shielding effect is observed. Whereas, for a system characterised by $\upsilon_i/\upsilon_m < 1$, the effect is reversed and crack amplification is present. The magnitudes of the shielding and amplification effects closely match those found in Figure 7.2, for $E_i/E_m = 2$ and $E_i/E_m = 0.5$, respectively.

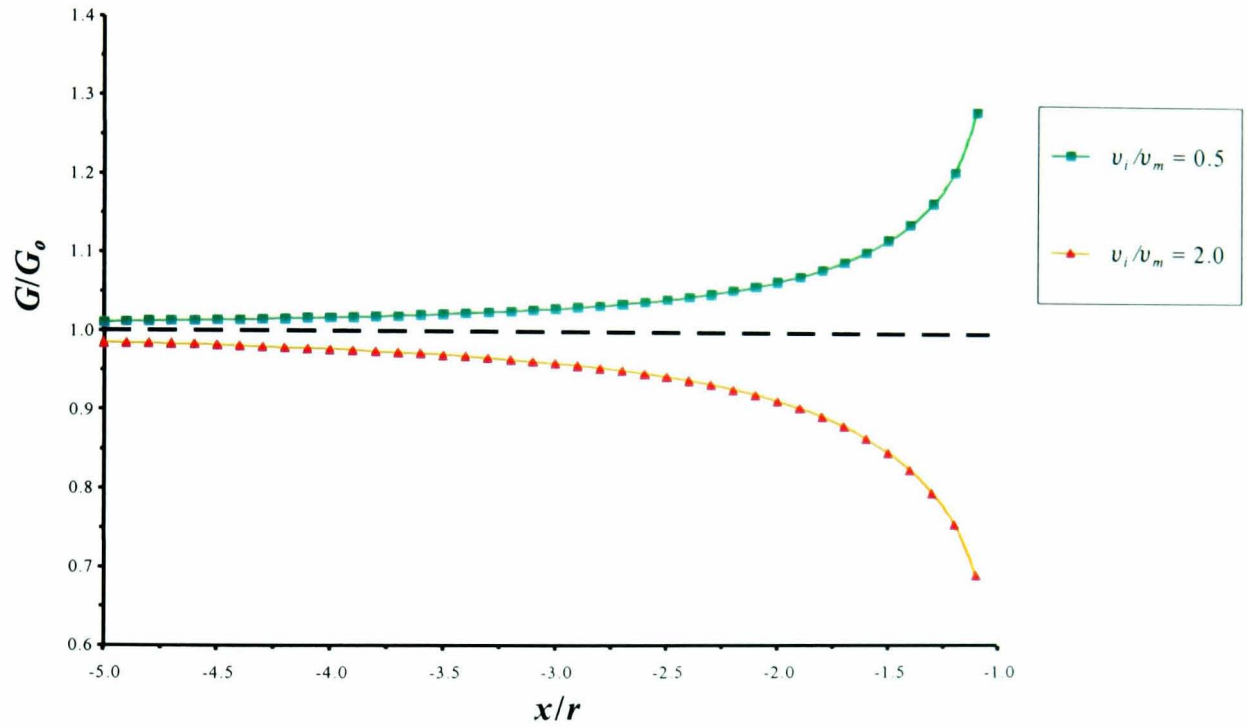

Figure 7.4 Effect of Poisson's ratio mismatch on the nondimensionalised energy release rate (G/G_o) for a crack approaching an uncoated inclusion along its centreline. ($d/r = 0$, $E_i/E_m = 1$)

Poisson's Ratio effect: Arbitrary Offset Crack (d/r =1)

Next, the effect of Poisson's ratio was considered in terms of crack deflection energetics. Most of the cited publications in this present field assume a prescribed linear crack path, which is known *a priori,* due the symmetry of the particular problem. However, if the crack approaches along a path that is offset from the centreline of the inclusion ($d/r \neq 0$), it will deflect as it nears the embedded phase.

The variation in G/G_o with the Poisson's ratio for a rigid inclusion ($E_i/E_m \rightarrow \infty$) and a crack initially offset by one radius, i.e. $d/r = 1$, is presented in Figure 7.5. There is a shielding effect as the crack approaches the fibre as a result of the decrease in G/G_o of ~20% in all cases. The crack trajectories are shown in Figure 7.6. Although the variations in G/G_o are similar in all cases, the crack trajectories are somewhat different, with the lowest values of the Poisson's ratio giving rise to the greatest deflection.

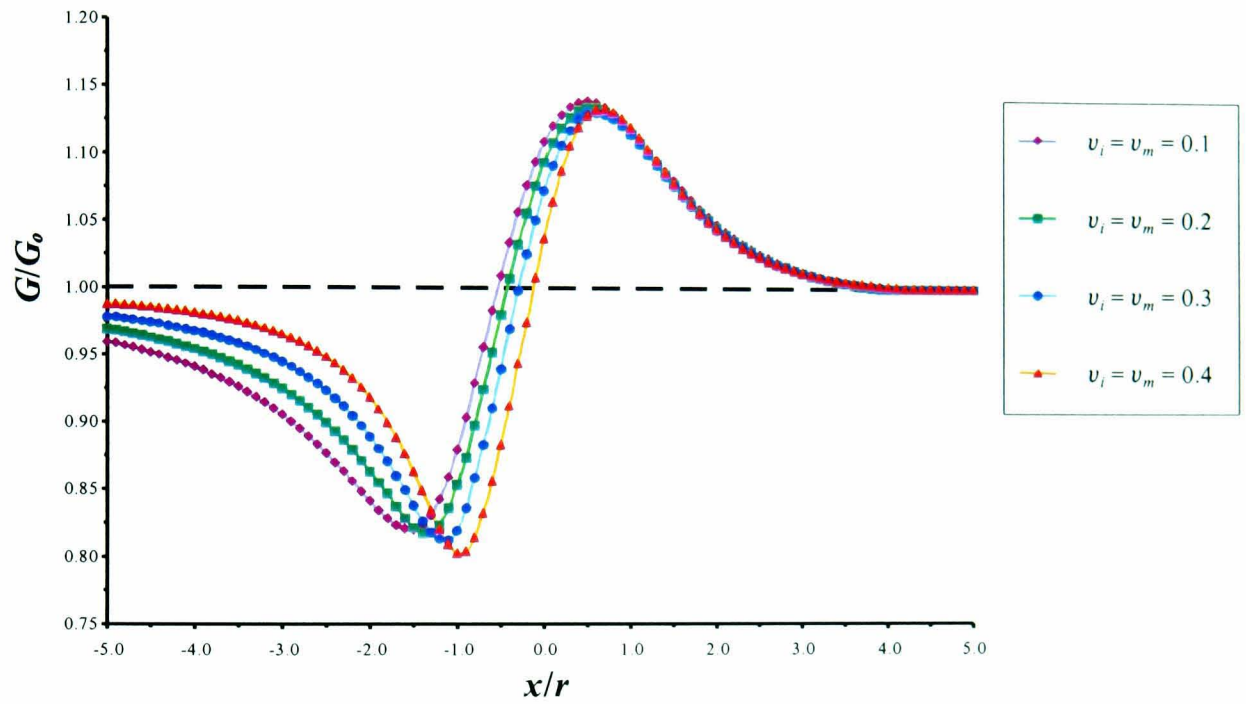

Figure 7.5 **Effect of Poisson's ratio on the nondimensionalised energy release rate (G/G_o) for an offset crack approaching an uncoated inclusion. ($d/r = 1$, $E_i/E_m \approx infinity$)**

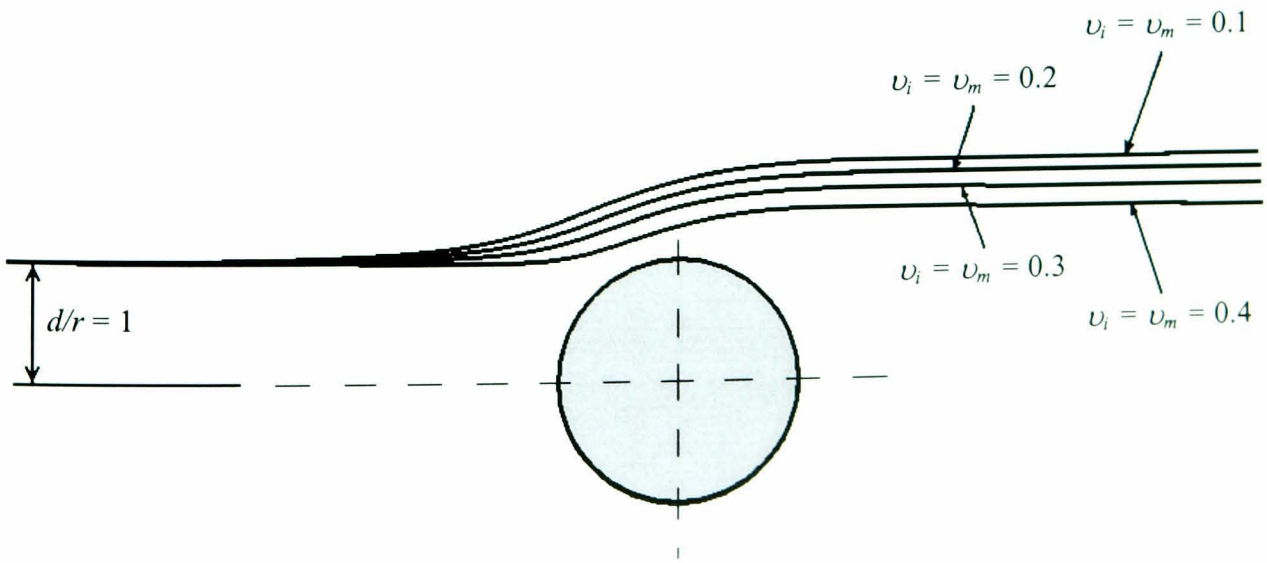

Figure 7.6 **Computed crack trajectories for the cases indicated in Figure 7.5.**

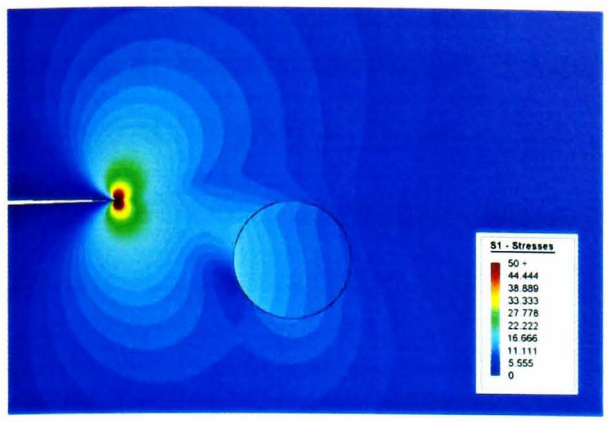

Crack step = 40

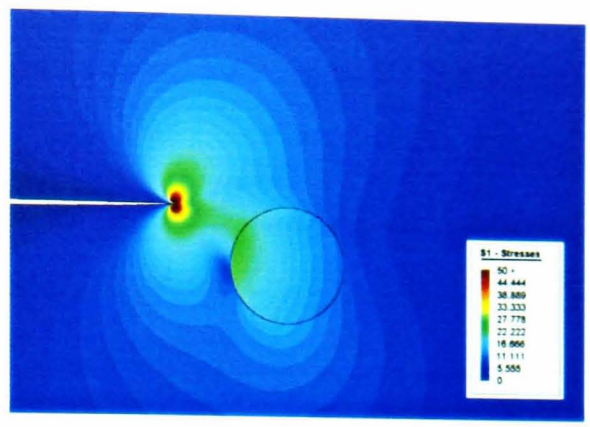

Crack step = 60

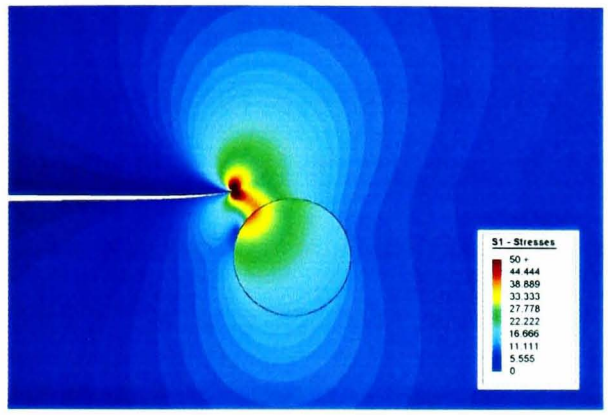

Crack step = 80

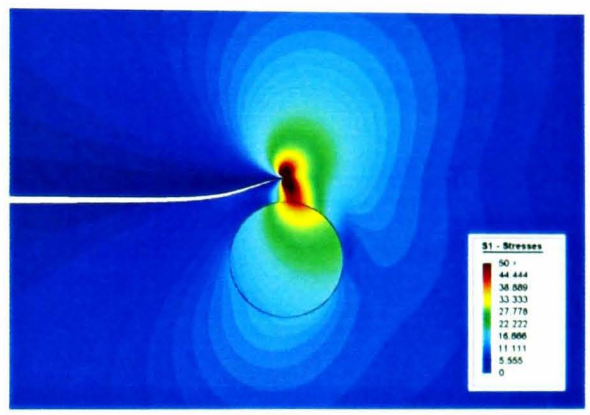

Crack step = 100

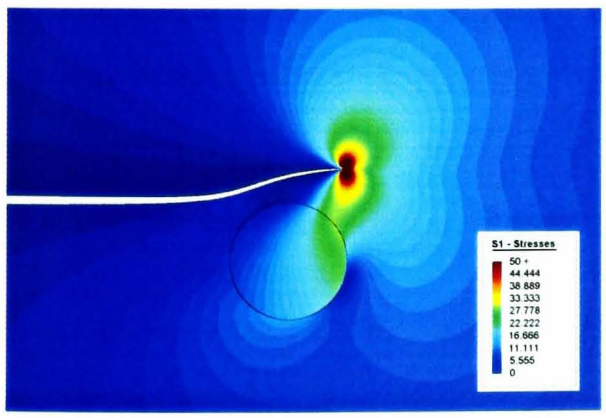

Crack step = 120

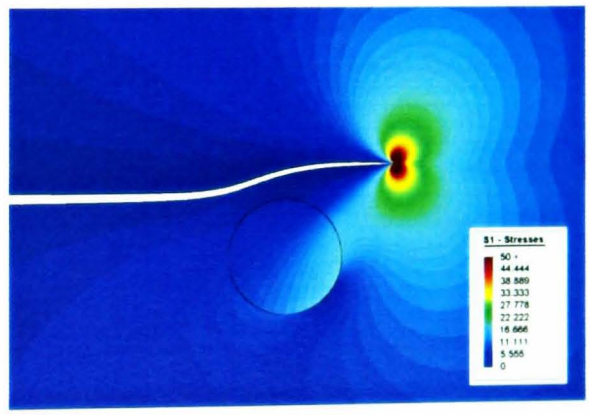

Crack step = 140

Figure 7.7 Contour plots indicating the variation of first principal stress (S1) as the crack passes the inclusion. ($d/r = 1$, $E_i/E_m \approx infinity$, $\upsilon_i = \upsilon_m = 0.1$)

In addition to the variation of the crack path and crack tip energetics, the stresses within the body will be redistributed as the crack passes the inclusion. This is indicated in Figure

7.7 for an arbitrary material combination. From this figure, very high stresses are observed in the localised region around the crack tip. The tip of a crack is effectively a geometrical singularity; therefore, within the limits of linear elasticity the stress field at this point will be unbounded. Also, as the crack approaches and passes the inclusion a secondary stress concentration is observed within the inclusion close to the moving crack tip.

In the present analysis the constituents are assumed to be purely elastic, hence, plastic deformation in the neighbourhood of the crack tip is ignored. For many engineering composites, e.g. metal matrix composites, at least one of the phases is usually ductile and so yielding would occur at and ahead of the crack tip forming a plastic zone. However, the degree of plastic deformation near the crack tip would, in many cases, be severely limited by the presence of the stiff reinforcing phase (*Leggoe et al., (1996)*, and *Kassam et al., (1995)*). It is therefore expected that information obtained from an elastic analysis will be of relevance to composite material design.

The influence of Poisson's ratio differences on the crack propagation was considered by taking a fibre with the same modulus as the matrix, but with Poisson's ratios $\upsilon_i/\upsilon_m = 0.5$ or *2*. Again, an arbitrary initial crack offset of one radius ($d/r = 1$) was chosen. Figure 7.8 shows the variation in G/G_o as the crack approaches the inclusion. Furthermore, Figure 7.9 shows the corresponding crack trajectories for the offset crack propagation.

The crack is attracted to the inclusion if the Poisson's ratio of the matrix phase is higher than that of the inclusion phase ($\upsilon_i/\upsilon_m < 1$), and repelled if this situation is reversed ($\upsilon_i/\upsilon_m > 1$). This confirms the crack tip energetics presented in Figure 7.8, as a dramatic increase in the energy release rate as the crack approaches the material interface, in the case of $\upsilon_i/\upsilon_m = 0.5$. Also, the shielding-amplification curve in Figure 7.8, in the case of $\upsilon_i/\upsilon_m = 2.0$ exhibits only a relatively small change in G/G_o as the crack by-passes the inclusion.

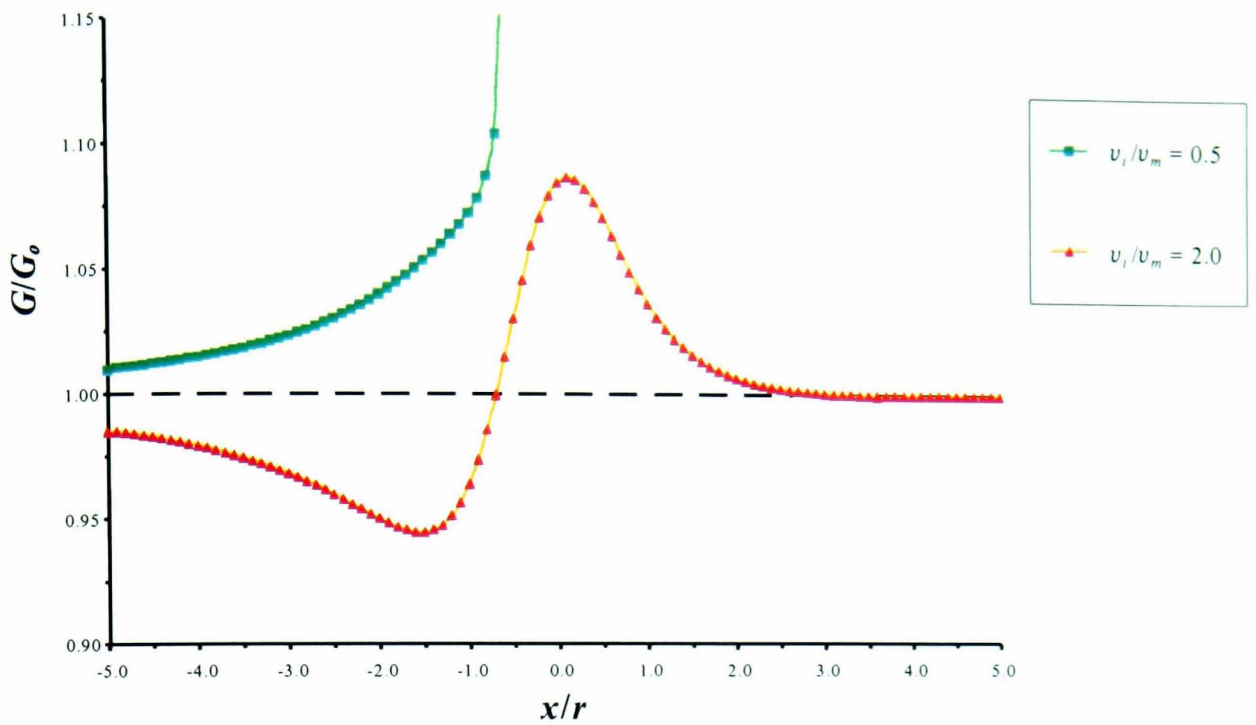

Figure 7.8 **Effect of Poisson's ratio mismatch on the nondimensionalised energy release rate (G/G_o) for an offset crack approaching an uncoated inclusion. ($d/r = 1$, $E_i/E_m = 1$)**

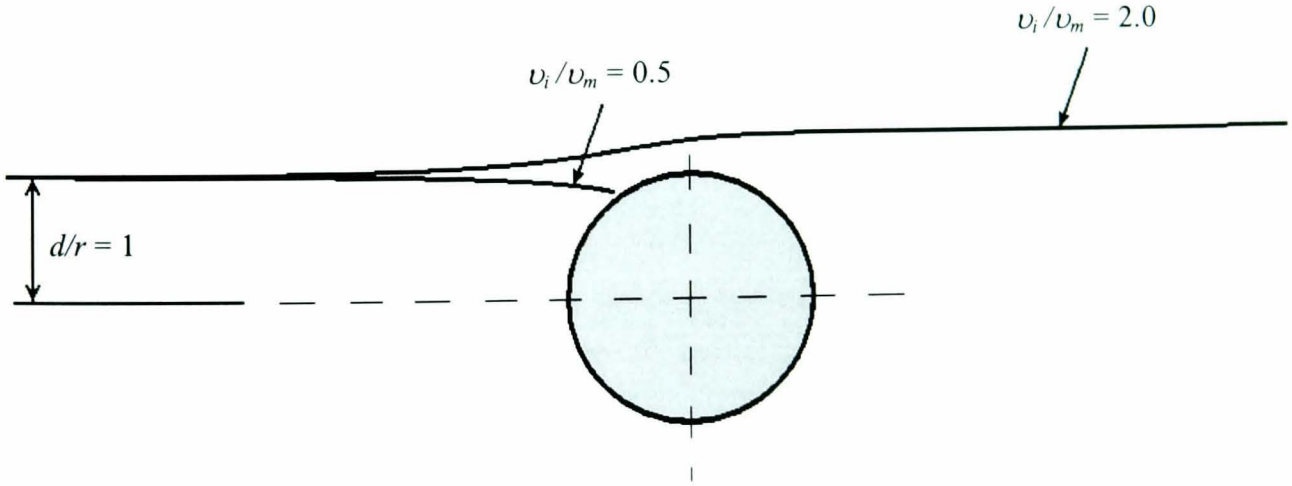

Figure 7.9 **Computed crack trajectories for the cases indicated in Figure 7.8.**

Poisson's Ratio effect: Critically Offset Crack ($d/r = (d/r)_{critical}$)

As matrix fracture is expected to be the predominant mode of final failure, the toughness of a composite will be related to the degree of crack arrest arising from the presence of the reinforcing phase. In the initial models, i.e. a crack propagating with no offset from the

fibre diameter, the crack will impinge upon the obstruction. The subsequent arrest or continued propagation of the crack depends on the relative strength and/or toughness of the matrix, fibre and interface. In general however, the crack will approach the fibre with some degree of offset from a diametral plane. The crack can then either be attracted into the fibre, or it can be deflected such that it continues to propagate in the matrix and bypasses the inclusion. This transition will occur at a particular crack offset from the centre-line of the fibre, $(d/r)_{critical}$.

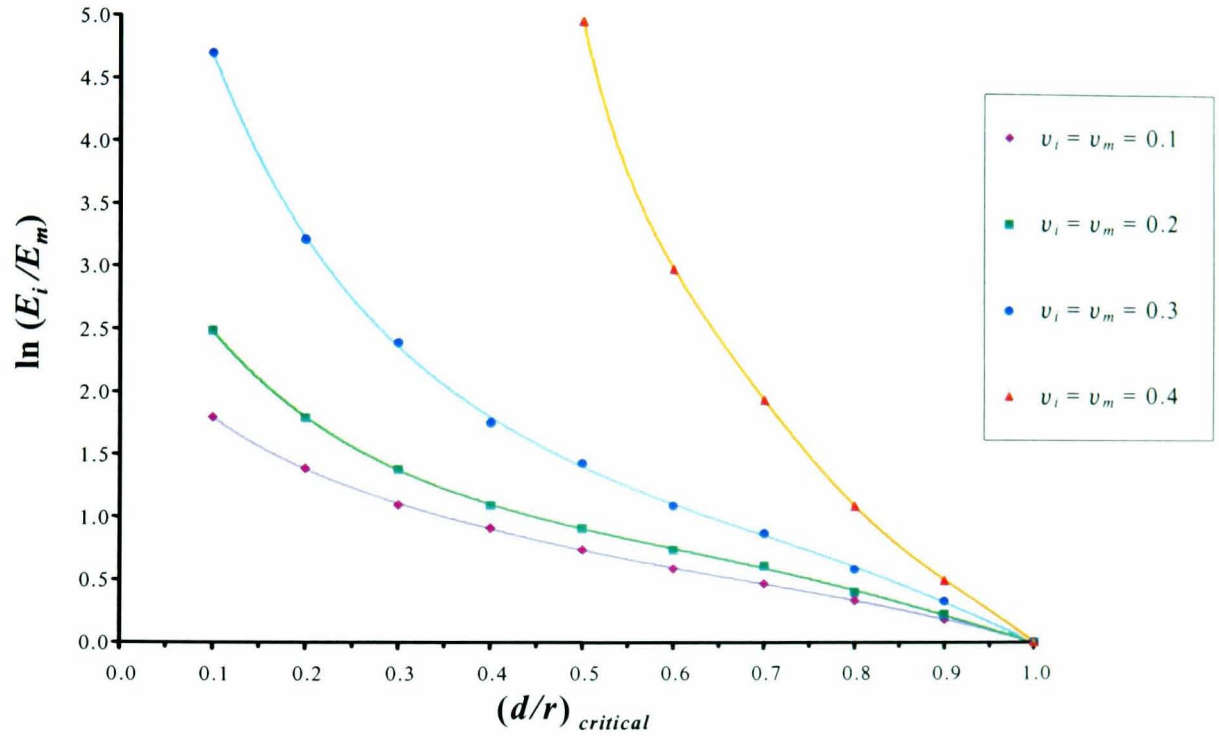

Figure 7.10 The critical offset $(d/r)_{critical}$ that corresponds to the crack passing within one crack tip element length from the uncoated inclusion, for a range of Poisson's ratios and elastic moduli mismatches.

Figure 7.10 depicts the variation of the calculated critical crack offsets, $(d/r)_{critical}$, for a range of elastic moduli ratios ($E_i/E_m>1$) and Poisson's ratios. The critical crack offset was taken as that which corresponded to the crack passing within one crack-tip element length from the inclusion. This value was obtained from many simulations by sequentially varying the elastic constants. It should be noted that since the Poisson's ratios of the inclusion and matrix are taken to be the same, when the elastic moduli are also identical, then the material is uniform, so that the crack will always continue to propagate through

the 'fibre', i.e. $(d/r)_{critical} = 1.0$. It can be seen from Figure 7.10 that as the elastic modulus of the fibre increases relative to that of the matrix then the likelihood of the crack being deflected around the inclusion, rather than attracted towards it, increases. Also apparent from this figure, is the significant effect that Poisson's ratio has on $(d/r)_{critical}$. When the Poisson's ratio is relatively low ($\upsilon_i = \upsilon_m = 0.1$) the crack can still deflect around the inclusion even when the offset is very small, i.e. $(d/r)_{critical} = 0.1$, and the elastic modulus ratio is approximately six. Whereas, when the materials become more incompressible ($\upsilon_i, \upsilon_m \rightarrow 0.5$) the same elastic modulus ratio deflects the crack far less, hence the computed critical offset is much higher ($(d/r)_{critical} \approx 0.7$).

The energy release rates are also affected by the presence of the inclusion, even when the crack propagates entirely in the matrix. Figure 7.11 shows the variation of G/G_o at the critical offset value for the different Poisson's ratios, at a representative E_i/E_m value of 5. G/G_o decreases quite significantly as the crack approaches the inclusion, with its minimum value for $\upsilon_i = \upsilon_m = 0.1$ being only 0.48. Depending upon the particular situation, for example under fatigue conditions, this decrease may even be sufficient to arrest crack growth. Figure 7.12 shows the crack paths at the critical offsets, i.e. $(d/r)_{critical}$, for the different Poisson's ratio values. From this figure it can be seen that particularly for the case of $\upsilon_i = \upsilon_m = 0.1$ the critical offset is relatively low, and the crack trajectory only starts to deviate when the crack is within a short distance from the inclusion, with the consequence that the angle between the crack path and the applied stress decreases markedly. This is presumably the main reason for the significant decrease in G/G_o.

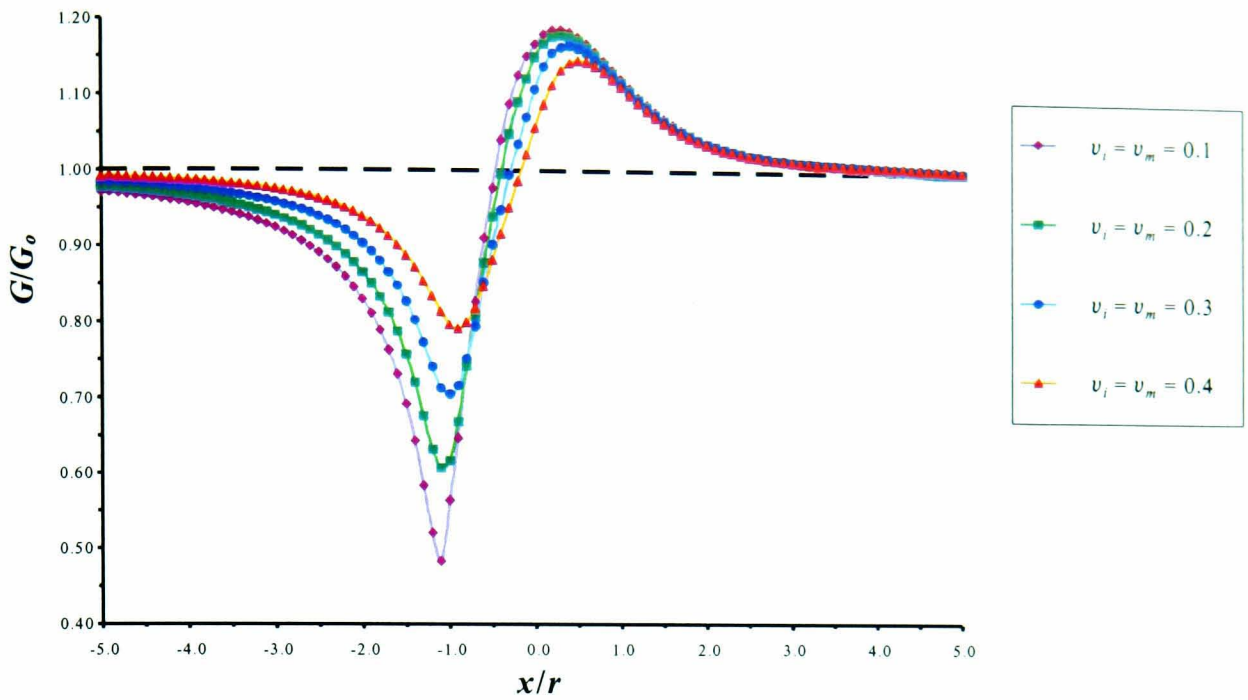

Figure 7.11 Effect of Poisson's ratio on the nondimensionalised energy release rate (G/G_o) for a critically offset crack approaching an uncoated inclusion. ($d/r = (d/r)_{critical}$, $E_i/E_m = 5$)

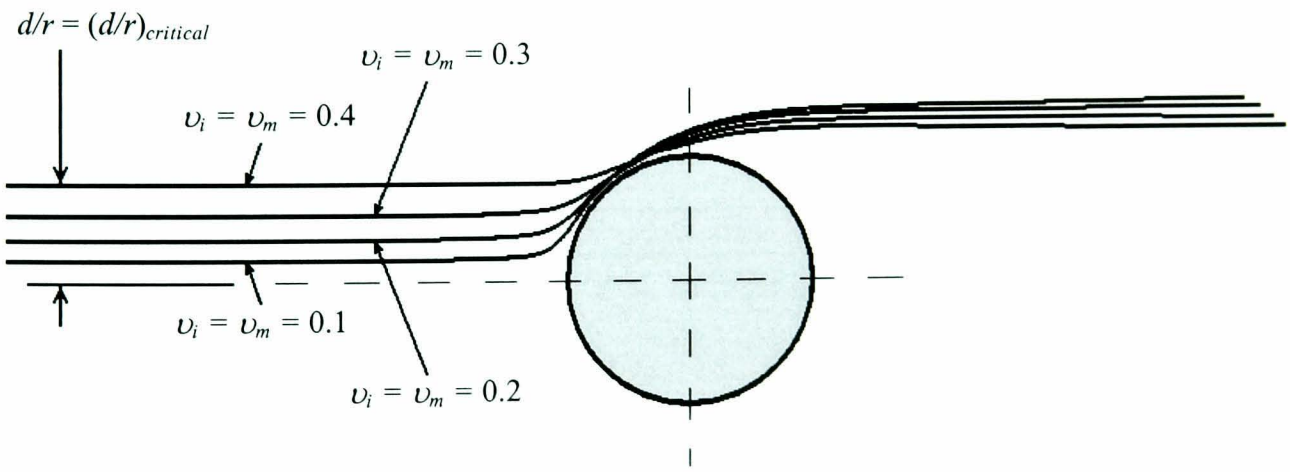

Figure 7.12 Computed crack trajectories for the cases indicated in Figure 7.11.

7.3.2 Coated Inclusion Problem

With the rapid advances in composite materials science, attention has focused not only on two-phase composites, but also on the introduction of a third phase, i.e. coating, applied to the inclusion's surface. From the engineering mechanics approach, some research into

the stress analysis of coated fibres can be found in the literature. For instance the stress distribution around a coated inclusion (*Mikata and Taya (1985)*), or an inclusion that has an interlayer of changing properties (*Vörös and Pukánszky (2001)*). However, it would appear that there is very limited knowledge of the interaction between a propagating crack and a coated inclusion, except for a recent publication that specifically analyses a Griffith crack (*Xiao and Chen (2001)*).

In the present study the influence of relative material properties and thickness of a fully bonded coating on the behaviour of an edge-crack has been investigated.

Young's Moduli effect: Centred Crack (d/r =0)

The variation in the nondimensionalised energy release rate of the propagating crack was computed for a coated inclusion with differing material combinations (Figure 7.13). The coating thickness (t) analysed in each case is 10 percent of the inclusion radius, $t = 0.1r$, and the Poisson's ratios of the three phases are taken to be 0.3. Six particular material combinations have been analysed:

- A progressively graded, compliant inclusion ($E_i/E_m=0.1$, $E_c/E_m=0.5$) or stiff inclusion ($E_i/E_m=10$, $E_c/E_m=5$)
- A compliant inclusion with a stiff coating ($E_i/E_m=0.1$, $E_c/E_m=10$) or a stiff inclusion with a compliant coating ($E_i/E_m=10$, $E_c/E_m=0.1$)
- An inclusion with the same elastic properties as the matrix, but with a compliant coating ($E_i/E_m=1$, $E_c/E_m=0.1$) or with a stiff coating ($E_i/E_m=1$, $E_c/E_m=10$)

The solutions of the two-phase cases ($E_i/E_m=0.1$ and $E_i/E_m=10$) are also shown in Figure 7.13 for comparison. From this figure, it is noticeable that the results for the graded inclusion quite closely follow those for the uncoated inclusion, with only a slight reduction in the shielding or amplification process. This would be expected in the case of a relatively thin coating. For the cases with $E_i/E_m=0.1$, $E_c/E_m=10$, or $E_i/E_m=10$, $E_c/E_m=0.1$ the presence of the coated inclusion has much less effect on G/G_o, and the

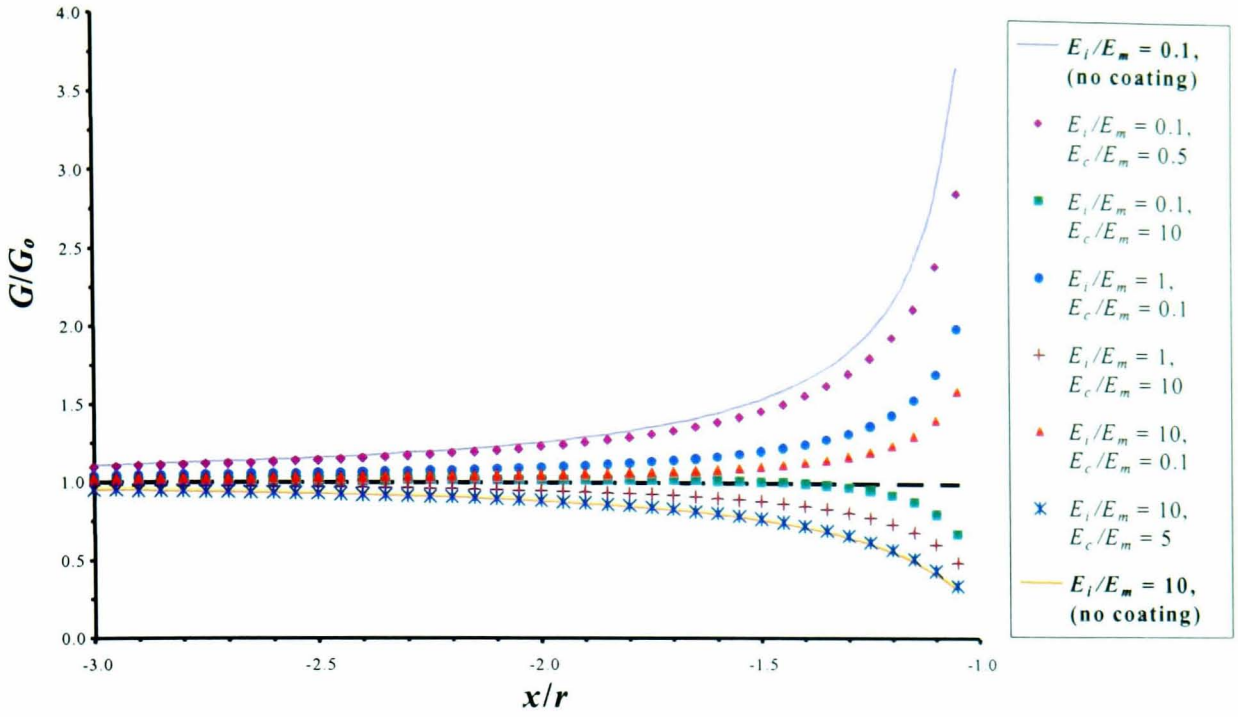

Figure 7.13 Effect of elastic modulus mismatch (E_i/E_m, E_c/E_m) on the nondimensionalised energy release rate (G/G_o) for a crack approaching a coated inclusion along the centreline. ($t = 0.1r$, $d/r = 0$, $\upsilon_i = \upsilon_c = \upsilon_m = 0.3$)

crack only experiences a shielding or amplification effect at distances within $0.5r$ of the inclusion. As described in the following section for these two material combinations, there is a noticeable effect of the coating thickness.

Finally, the last two material combinations were chosen to isolate the effect of the coating, as the material properties of the matrix and inclusion are the same. The results demonstrate that the crack noticeably responds to the presence of the coating, even though its thickness is only 10 percent of the inclusion radius and the moduli are an order of magnitude greater or less that of the fibre/matrix.

Coating Thickness effect: Centred Crack (d/r =0)

To analyse the effect of varying the coating thickness on the crack tip energetics, two material combinations namely, composite A - $E_i/E_m=0.1$, $E_c/E_m=10$, and composite B - $E_i/E_m=10$, $E_c/E_m=0.1$, were simulated using $t/r = 0.02$, 0.05, 0.1, 0.2, and 0.5. The results for the composites A and B are shown in Figures 7.14 and 7.15, respectively. It is

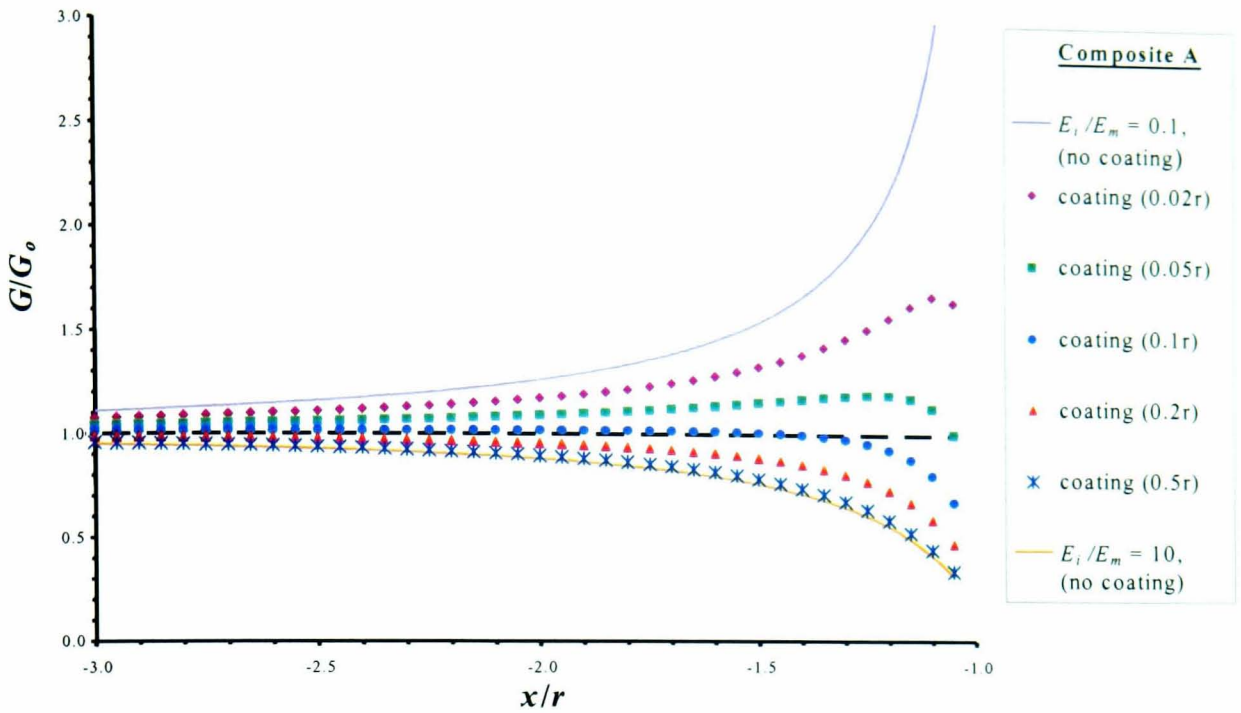

Figure 7.14 **Effect of varying the coating thickness (t) on the non-dimensionalised energy release rate for a crack approaching a coated inclusion with material properties, Composite A - $E_i/E_m=0.1$, $E_c/E_m=10$. ($d/r = 0$, $\upsilon_i = \upsilon_c = \upsilon_m = 0.3$)**

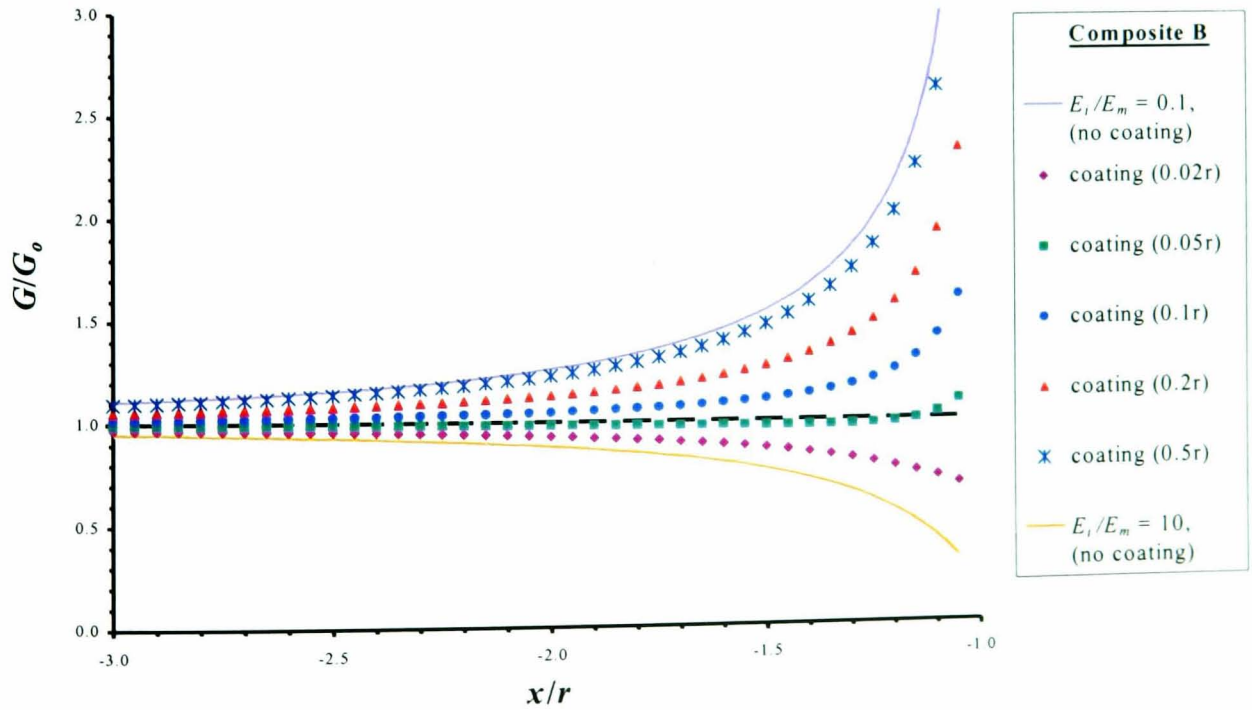

Figure 7.15 **Effect of varying the coating thickness (t) on the non-dimensionalised energy release rate for a crack approaching a coated inclusion with material properties, Composite B - $E_i/E_m=10$, $E_c/E_m=0.1$. ($d/r = 0$, $\upsilon_i = \upsilon_c = \upsilon_m = 0.3$)**

shown from both figures that as the coating thickness increases, the crack responds less to presence of the inclusion, and hence, more to the presence of the coating. Therefore, when the coating is relatively thin the solutions approach those of the two-phase case with the properties of E_i/E_m, but as the coating becomes thicker the trends resemble more the two-phase case with the properties of E_c/E_m.

7.4 Summary

In this study, the interaction between a propagating edge-crack and an embedded elastic inclusion is investigated using computational techniques. Crack deflection/attraction mechanisms and their associated energy release rate variations are examined for differing Young's moduli and Poisson's ratio mismatches, and the crack offset with respect to the inclusion centreline. Furthermore, results are also obtained for both an uncoated and a coated inclusion whose coating thickness and elastic moduli ratio were parametrically varied.

The main results obtained from this study are:

Crack propagation towards an uncoated elastic inclusion

- As the Poisson's ratio chosen for the matrix phase becomes more incompressible (υ_i, $\upsilon_m \rightarrow 0.5$) the crack 'senses' the presence of the inclusion much less, and hence, experiences a reduced shielding effect and crack deflection.
- By simply modifying the Poisson's ratio mismatch the energetics of the propagating crack tip, and also the crack deflection/attraction mechanisms can be controlled. For a system in which the Poisson's ratio of the inclusion is higher than that of the matrix ($\upsilon_i/\upsilon_m > 1$), a distinct shielding effect is observed, which corresponds the mechanism of crack deflection. Whereas, for a system characterised by $\upsilon_i/\upsilon_m < 1$, the effect is reversed and crack amplification/attraction is present.
- Maximisation of the crack deflection mechanism highlights significant differences in

the localised toughening effect, through modification of the Poisson's ratio. By modifying the Poisson's ratio of the phases, the minimum G/G_o value obtained as the crack approaches the inclusion varies considerably. In particular, in the case of $\upsilon_i = \upsilon_m = 0.1$ and $E_i/E_m = 5$, a value of $G/G_o = 0.48$ is obtained. Therefore, depending upon the particular situation, for example under fatigue conditions, this decrease may even be sufficient to arrest crack growth.

Crack propagation towards a coated elastic inclusion

- By introducing a third phase with varied material properties, distinct changes in the crack-tip energetics can be observed.
- As expected, when the coating is relatively thin the solutions approach those of the two-phase case with the properties of E_i/E_m, but as the coating becomes thicker the trends resemble more the two-phase case with the properties of E_c/E_m.

Chapter 8: Interaction between a Propagating Crack and Multiple Inclusions

8.1 Introduction

In the previous chapter, crack deflection/attraction mechanisms and their associated energetics, were analysed for the special case of an edge crack approaching an isolated embedded inclusion (*Knight et al. (2002d)*). However, application of these results to composite materials containing typical fibre volume fractions is limited, as inclusion interaction will influence the local stress fields, which in turn will affect the behaviour of a crack. This chapter will address this situation, by analysing the transverse fracture response of unidirectional multi-fibre composites using the BE technique.

The purpose of this work is to provide an improved knowledge of the fracture characteristics of multiphase materials by investigating the influence of fibre arrangement, phase properties and microcracking on the local stresses and the primary crack-tip energetics. Uniaxial fibre reinforced composites generally have very good properties in the direction of the fibres, but in conventional multi-layer crossply laminates it is cracking in the transverse direction which effectively limits the strength of a stressed body. Therefore, in this study the propagation of a primary crack in the transverse direction is considered, i.e., in a plane containing the fibre axes, rather than perpendicular to the fibres.

Numerical techniques have previously been applied to such problems, for instance three-dimensional simulations of crack growth behaviour in the presence of dispersed particles was studied by *Gao and Rice (1989)* and *Bower and Ortiz (1991)*, using a perturbation analysis. *Kim et al. (1998)* and *Nandy et al. (1999)* have applied the Body Force Method (BFM), which was developed by *Nisitani et al. (1990)*, to the fracture

behaviour of particle-dispersed ceramic composites. The BE technique, which has been used in this study, is particularly well-suited to the consideration of crack propagation in linear isotropic solids. *Bush (1997)* also applied this method to study the interaction between a crack and a particle cluster in a composite material composed of Silicon Carbide reinforced Aluminium (Al/SiC).

Various authors have also considered microcracking in composite materials. Fore instance, *Pijaudier-Cabot and Bažant (1991)* presented an approximation scheme for solving the problem of a single crack situated among solid containing multiple fibres. This work was then extended by *Axelsen and Pyrz (1995)*, to include multiple crack initiation within a distribution of fibres.

In the present analysis, in accordance with the aforementioned numerical studies, crack propagation is considered to be quasi-static. Hence, dynamic effects, such as elastic waves or strain rate dependent material properties, are not taken into account (e.g. *Meguid and Wang (2000)*).

8.2 Model Description

8.2.1 Geometry and Materials

The embedded cell approach (ECA), as discussed Section 6.2.1, has been implemented to predict the microfields in the vicinity of a crack tip within a composite material. Problems of this type are very well suited to this method as it can resolve local stress and strain fields in the core region at high detail (*Wulf et al. (1996)*, *Mishnaevsky et al. (1999)*, and *Ableidinger (2000)*). In addition, far field loads and displacements can be accommodated within the modelling process.

The distribution of the unidirectional fibres is modelled using embedded cells containing either periodic or randomly distributed fibre arrangements. For the embedded cells with uniformly spaced fibre arrangements, the fibres were packed in square (SQ) or hexagonal

(HEX) arrays as shown in Figure 8.1.

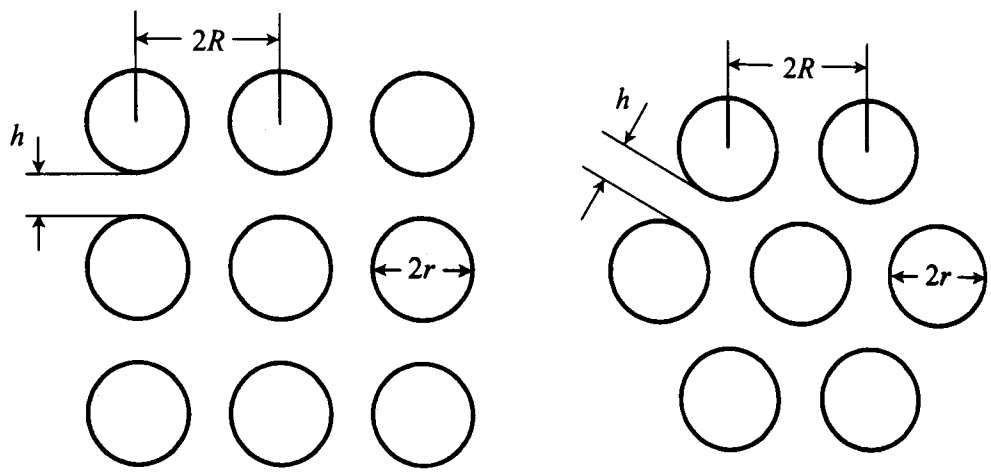

Figure 8.1 Square (SQ) and hexagonal (HEX) packing of unidirectional fibres.

For the ideal arrangements shown in Figure 8.1, the geometric characteristics are related to the fibre volume fraction (V_f) by:

(Square array)
$$h = (R - r) = 2r\left[\left(\frac{\pi}{4V_f}\right)^{1/2} - 1\right] \tag{8.1}$$

(Hexagonal array)
$$h = (R - r) = 2r\left[\left(\frac{\pi}{2V_f\sqrt{3}}\right)^{1/2} - 1\right] \tag{8.2}$$

Using these relationships, both square and hexagonal packed embedded cells were then constructed, consisting of 100 and 99 equally sized fibres, respectively.

In addition to the uniformly spaced fibre arrangements in Figure 8.1, numerical simulations were conducted using embedded cells containing 100 equally sized, randomly (RAND) distributed fibres. These random-fibre embedded cells were generated in a similar manner to those employed in Chapter 6. By stipulating fibre volume fraction and number of inclusions, a simple program determines the size of the embedded cell, and the random location of each fibre, such that fibres neither overlap with each other nor with the cell boundaries. As discussed in Section 6.3.2, this method of generating

random-fibre cells can cause geometric non-uniformities within the cell close to the boundaries. However, as the volume fraction of fibres in the present simulations is lower then this effect would be less significant.

Due to the high computational cost of the simulations, analyses are performed for selected material combinations of practical significance, i.e. *Composite A* - glass fibres embedded in a polyester matrix, and *Composite B* - carbon fibres embedded in an epoxy resin. Glass reinforced polyester is the cheapest and the most widely used composite. Typically it is used in lightweight automotive applications, marine and corrosion-resistant applications, aircraft and aerospace components, and sporting equipment. Carbon reinforced epoxy is an advanced composite, which is generally more expensive to manufacture than glass fibre composites. However, the mechanical properties of specific strength and stiffness are significantly improved. Consequently they are typically used in specialised, high performance applications such as aerospace and automotive components, and for sporting equipment. Constituent material properties for each composite can be seen in Table 8.1.

Constituents	Young's modulus E (GPa)	Poisson's ratio υ
Composite A		
Glass fibre (E-glass)	76.0*	0.22
Polyester	2.0	0.38
Composite B		
Carbon fibre (High modulus)	12.0*	0.20
Epoxy resin	6.0	0.39

* Radially measured value

Table 8.1 Typical constituent material properties used within the present simulations, *Hull and Clyne (1996).*

In addition to the two composite material combinations above, a three-phase composite comprising of a 50:50 mixture of glass and carbon fibres embedded in an epoxy matrix was also analysed. This has direct relevance to the recent development of hybrid mixed fibre composites. A mixture of glass and carbon fibres incorporated into a polymer matrix gives a relatively inexpensive composite, owing to the low cost of the glass fibres, but with mechanical properties enhanced by the carbon fibres. A glass-carbon hybrid is a compromise between the high strength and stiffness of all-carbon composites and the high toughness of all-glass composites. Hence, the resulting three-phase material generally has both reasonable strength and toughness properties.

The volume fraction of fibres (V_f) used within the numerical models is 0.4. This value is considered to be high enough to be representative of typical reinforcement concentrations for fibre-reinforced composites, without impeding the matrix fracture process. Due to the restrictions of the numerical code, the crack cannot penetrate an inclusion or propagate along the matrix/inclusion interface.

For the two-phase models, in accordance with the models presented in Chapter 6, the material properties (E^*, υ^*) employed for the embedding region were obtained using the semi-empirical expressions (Eqs. 6.1 and 6.2) proposed by *Halpin and Tsai (1967)*. While for the three-phase model, the elastic properties employed for the embedding region were determined self-consistently from the behaviour of the core, as discussed previously in Section 6.2.2.

In the present simulations, the different material phases are assumed to be homogeneous and isotropic, and behave purely elastically.

8.2.2 Boundary Element Modelling

The BEM meshes for the plane strain models (which are equivalent to the inclusions representing fibres) have been carefully developed, such that finer elements are placed along the fibre/matrix interfaces in regions where the fibres are nearly touching. This is to

ensure accurate results where possible high stress gradients occur. Typical BEM meshes comprised of up to 5400 linear elements.

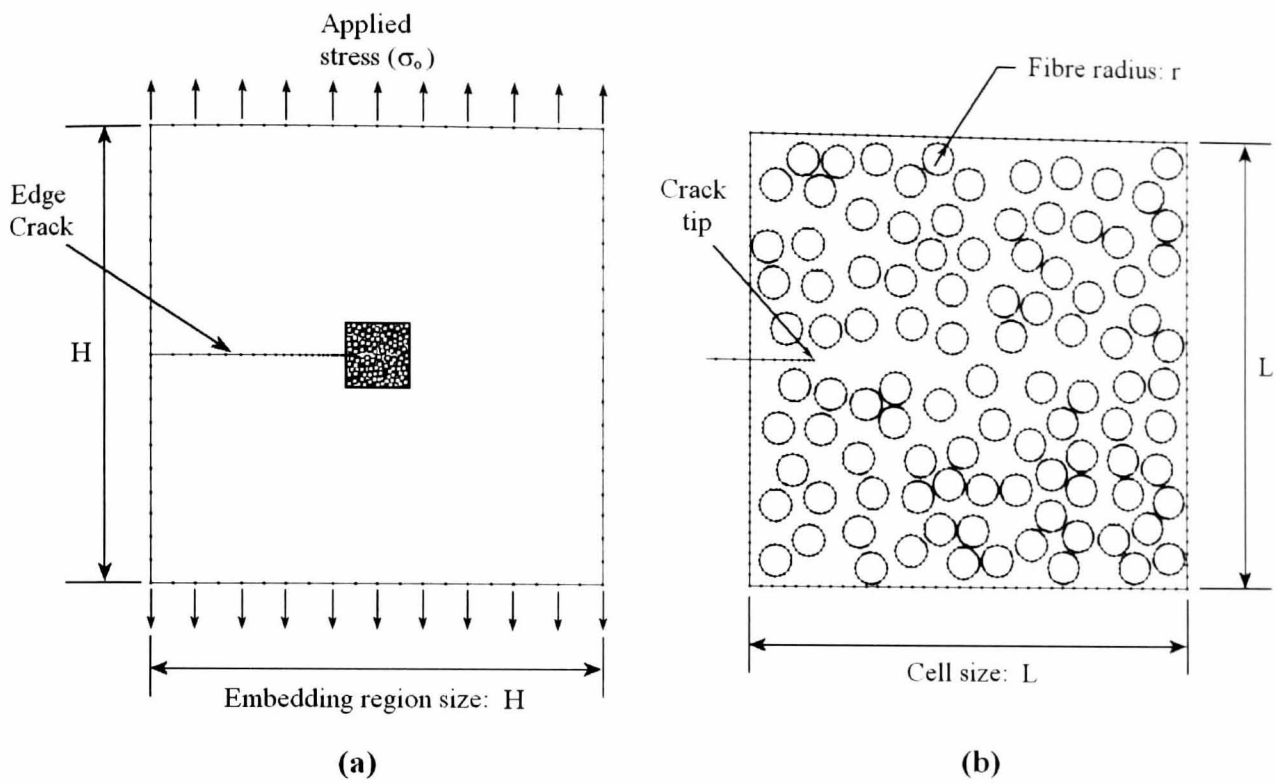

Figure 8.2 Typical 2D BEM model, showing (a) the full discretised model and (b) an enlarged view of the embedded cell. (H/L = 7.136, r/L = 0.0357)

Figure 8.2 illustrates a typical BEM discretisation used to represent a random-fibre composite undergoing transverse failure by fracture. In this model, an edge-crack is modelled, which has passed through the embedding region and is entering the left-hand side of the embedded cell. The upper and lower edges of the embedding region are subjected to a unit tensile stress (σ_o) in the y direction, and the model geometry is defined by: H/L= 7.136, r/L = 0.0357, where H, L and r represent the embedding region size, cell size and the fibre radius, respectively.

In addition, each fibre has the same radius, and the minimum ligament length is defined as ten percent of the fibre radius. The latter condition is stipulated such that the ligament size is of the same order of magnitude or greater than the elemental size in those regions. The reason for this restriction is to avoid the stresses becoming unbounded when the fibres touch, hence the problem to be considered has a contiguity (C) value of zero.

To validate the model stress distributions and crack tip energetics, a convergence study was undertaken using a number of models of different mesh densities. From this study, the boundary element meshes that are adopted within this thesis were found to give mesh-independent results.

8.3 Results and Discussion

In this section, firstly results are presented for a primary crack propagating through embedded cells of different fibre spatial distributions and constituent material properties. This is then followed by an investigation into the effect of secondary microcracks on the local stress fields and the energetics of the primary crack.

8.3.1 Primary Crack Propagation

Effect of the Constituent Material Properties and the Fibre Spatial Distribution

Figures 8.3 to 8.5 show contour plots of the variation in stress concentration (K) within the embedded cell as the crack propagates through the region. In these figures, results pertaining to both composite materials, in three different fibre distributions, i.e. square, hexagonal and random, are illustrated. Comparing these figures, it is first noticeable that the two materials display distinctly differing stress distributions. This difference results primarily from the variation in the constituent Young's modulus ratio (E_f/E_m) of the two materials. The Poisson's ratio mismatches in both composites are very similar, and hence would not contribute to such differences. In the case of composite A, i.e. glass fibre reinforced polyester, the constituent Young's modulus ratio is relatively high ($E_f/E_m = 38$), and therefore the majority of the load is borne by the fibres. This is clearly seen in the figures, as the high stress region links the neighbouring inclusions that stretch away from the crack tip. In the case of composite B, i.e. carbon fibre reinforced epoxy, the ratio is close to unity ($E_f/E_m = 2$), and therefore both the fibres and matrix will share the load. This is shown in the figures, as the high stress region closely resembles the plastic zone

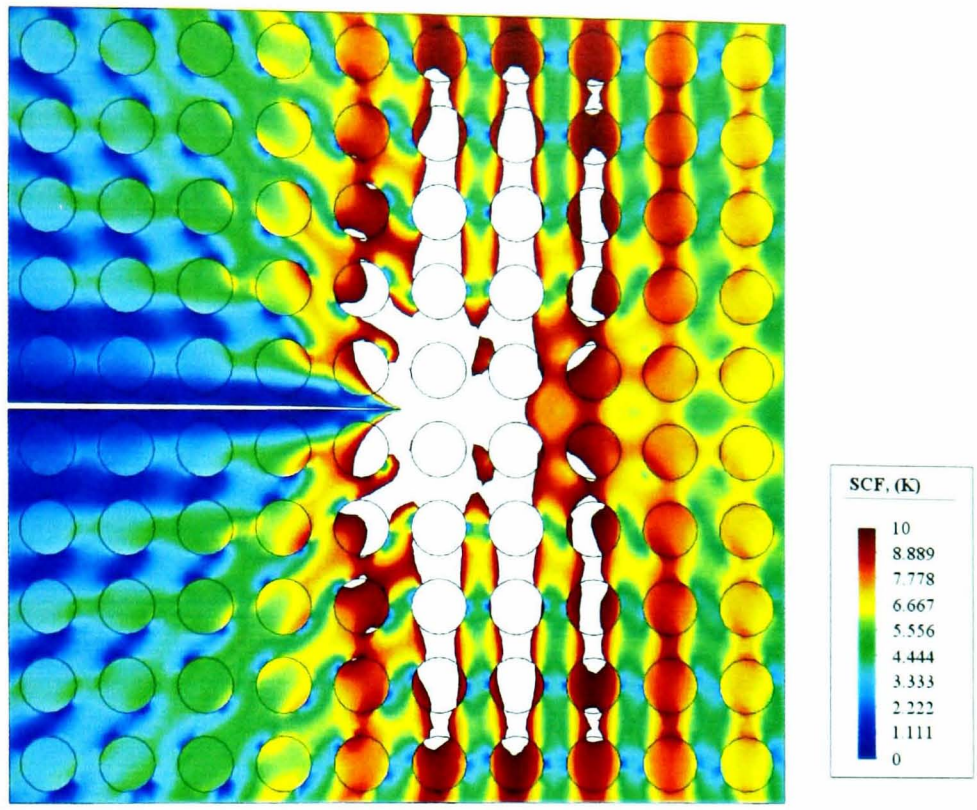

(a)

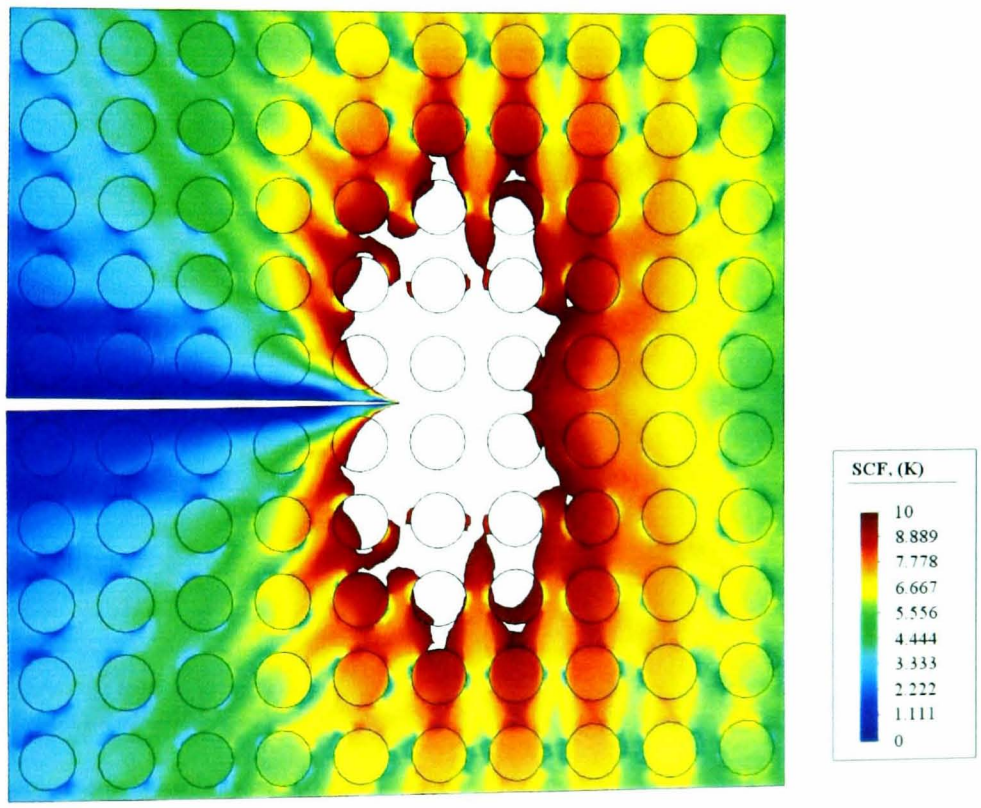

(b)

Figure 8.3 **Contour plot indicating the variation of stress concentration (K), in the proximity of the primary crack, within a square (SQ) array of fibres. Results correspond to: (a) Composite A, and (b) Composite B. (Note: the white-coloured zone indicates a stress concentration above an arbitrarily chosen value of 10)**

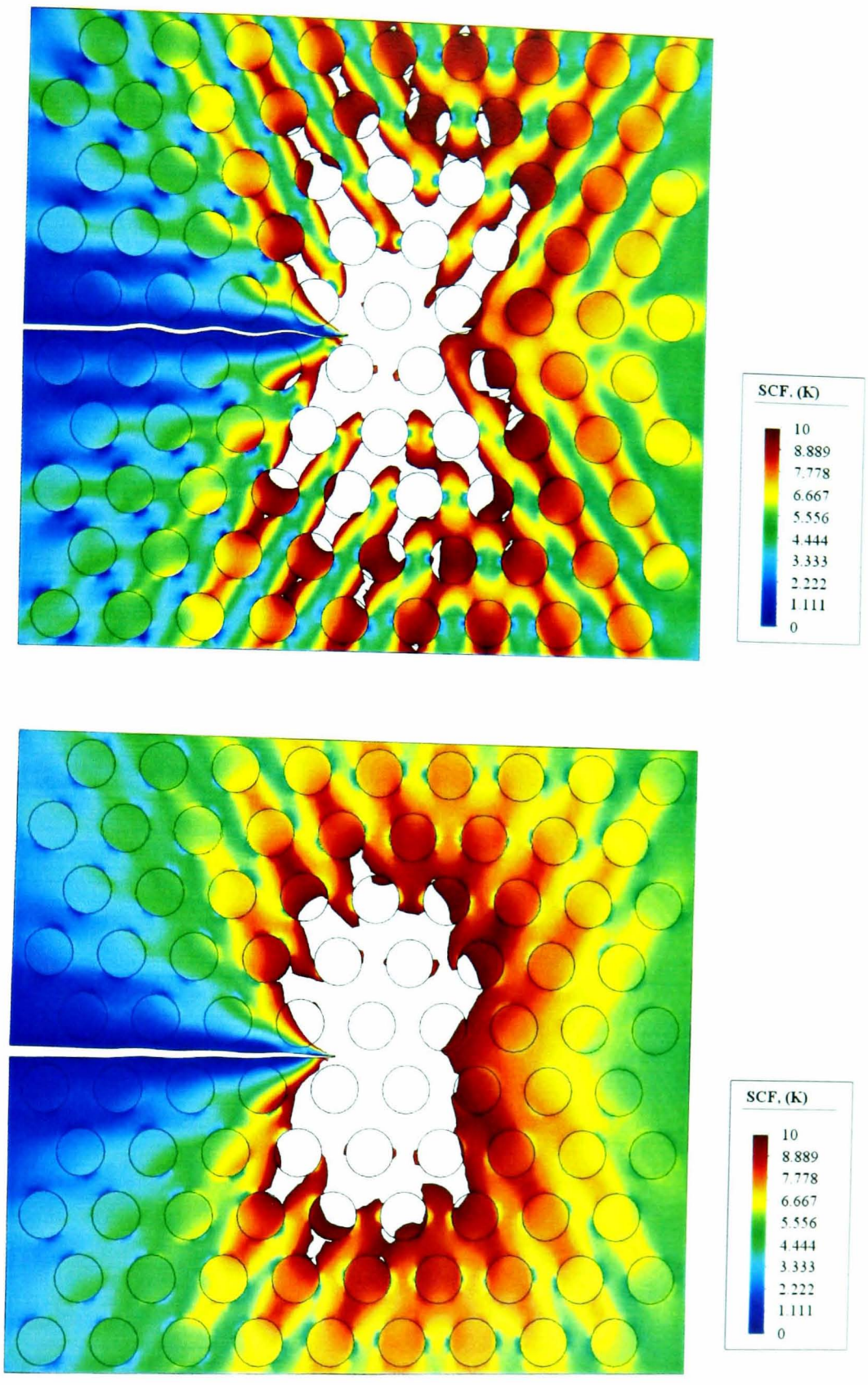

Figure 8.4 **Contour plot indicating the variation of stress concentration (K), in the proximity of the primary crack, within a hexagonal (HEX) array of fibres. Results correspond to: (a) Composite A, and (b) Composite B. (Note: the white-coloured zone indicates a stress concentration above an arbitrarily chosen value of 10)**

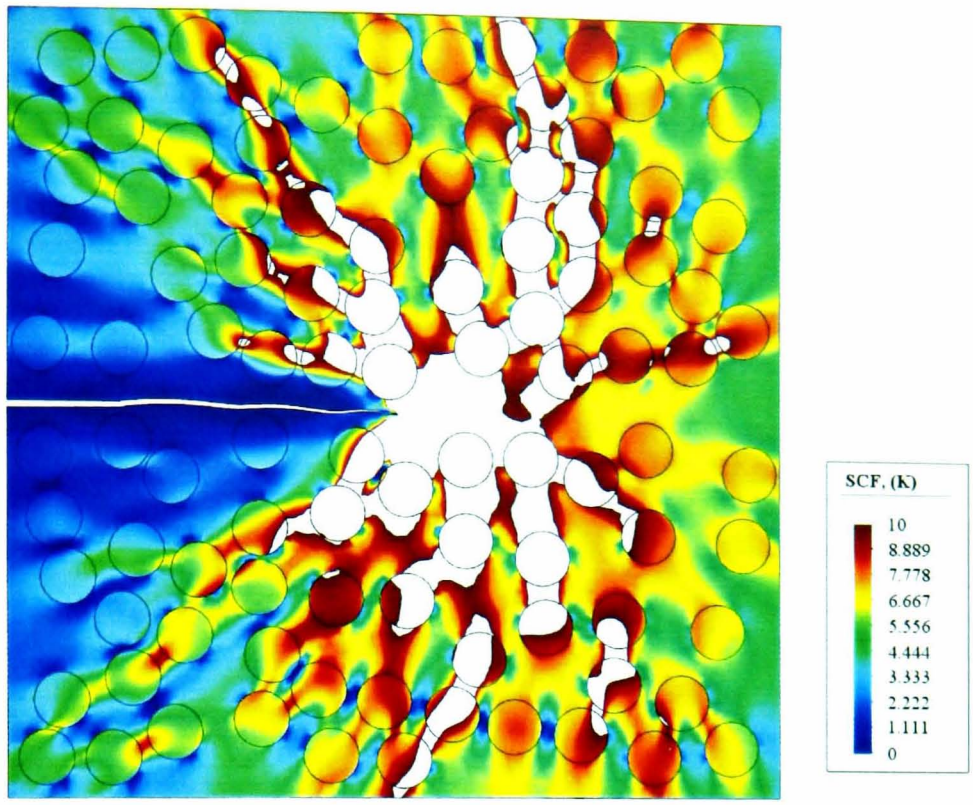

(a)

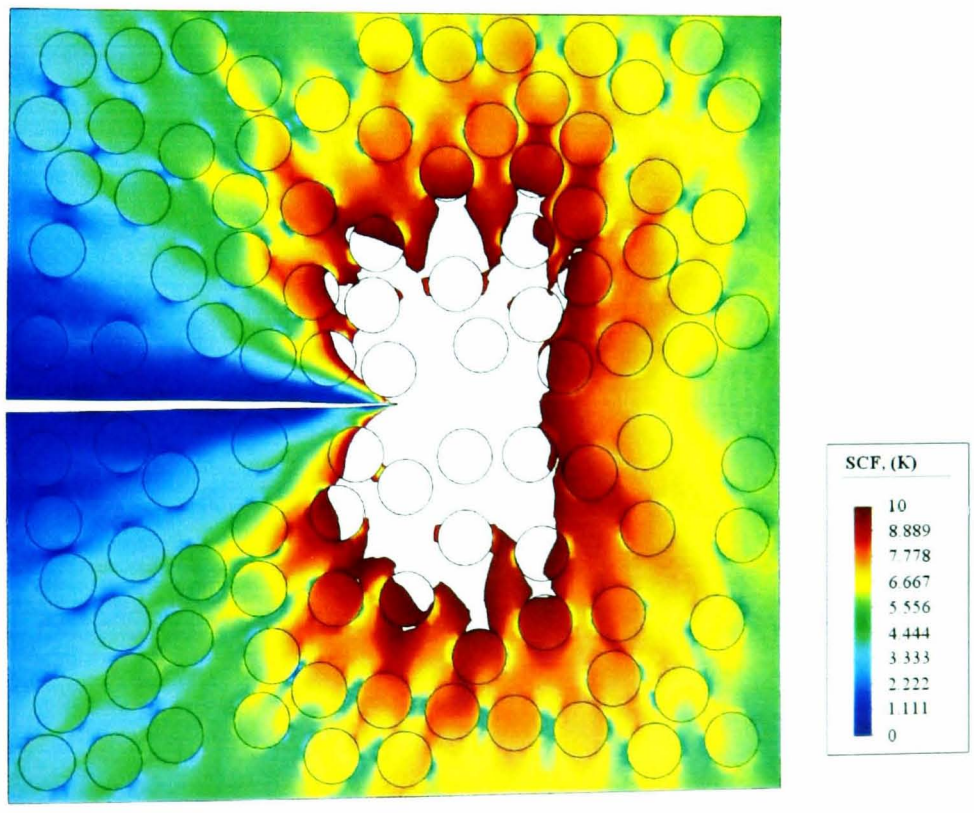

(b)

Figure 8.5 **Contour plot indicating the variation of stress concentration (K), in the proximity of the primary crack, within a random (RAND) array of fibres. Results correspond to: (a) Composite A, and (b) Composite B. (Note: the white-coloured zone indicates a stress concentration above an arbitrarily chosen value of 10)**

observed in monolithic materials.

For composite A, regions of high stress are more widely spread relative to the crack tip, therefore it is reasonable to assume that the damage zone surrounding the crack tip will possibly be greater, compared to composite B. In this zone microcracks could initiate, which could enhance the toughness of the composite. The presence of microcracks relaxes the stress field at the primary crack tip and through interaction with the main crack can even cause crack blunting, branching and deflection (*Matthews and Rawlings (1996)*). The effect of secondary microcracks on the energetics of the primary crack is considered in Section 8.3.2.

In addition, the effect of the fibre spatial distribution is only apparent in composites consisting of a relatively high constituent Young's modulus ratio. The variation of stress concentration computed for composite A is quite strongly affected by the fibre arrangement, whereas in the case of composite B only slight differences are observed.

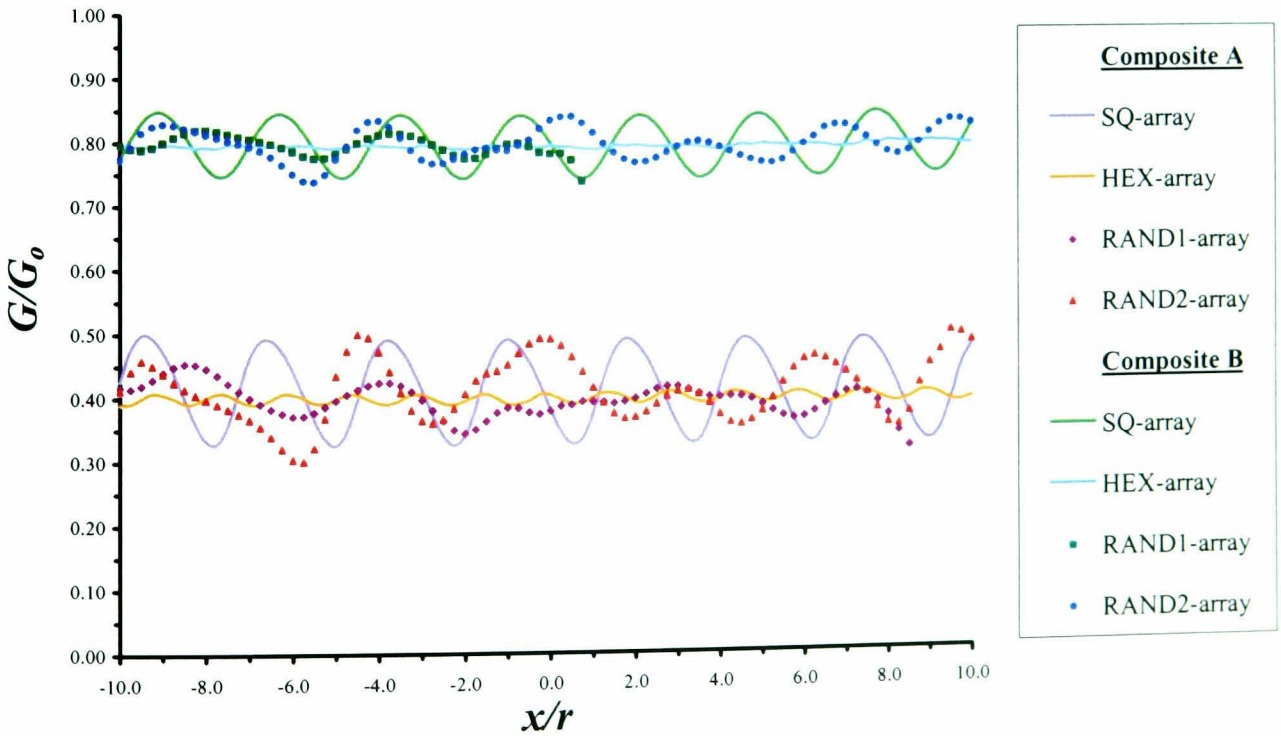

Figure 8.6 **Effect of fibre spatial distribution and constituent material properties on the nondimensionalised energy release rate (G/G_o) of the primary crack.**

The variation in the nondimensionalised energy release rate, G/G_o, of the propagating crack was computed for the various models presented (Figure 8.6). Note that the energy release rate, in this case, is nondimensionalised by dividing the value obtained in the presence of the reinforcing inclusions (G) by the corresponding value in their absence (G_o). From this figure it is noticeable that the existence of the fibres will increase the fracture toughness, as compared with a pure matrix, by lowering the energy release rate at the crack tip. Interestingly, this effect is more pronounced for composite A, as the energetics of the crack tip decrease by approximately 50-70%, whereas for composite B the reduction is only by about 15-28%. In both materials, the effect of the fibre spatial distribution on the crack tip energetics is comparatively small; therefore, the constituent material properties can be considered to be the dominant factor controlling the crack tip energetics.

Analysis of a Three Phase Composite

A composite model comprising a 50:50 mixture of carbon and glass fibres embedded in an epoxy matrix was also analysed. To ensure a uniform distribution of each fibre type, the square (SQ) arrangement was employed where alternating carbon and glass fibres surround each fibre, as shown in Figure 8.7.

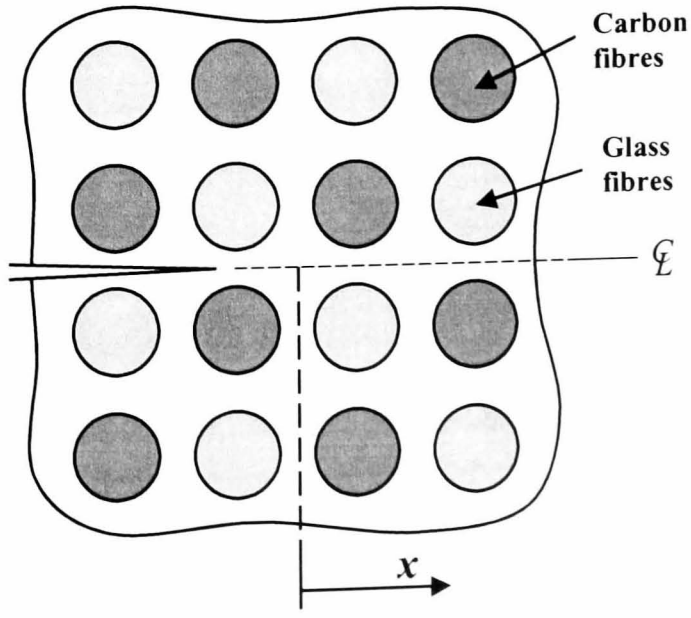

Figure 8.7 Distribution of carbon and glass fibres in the SQ array

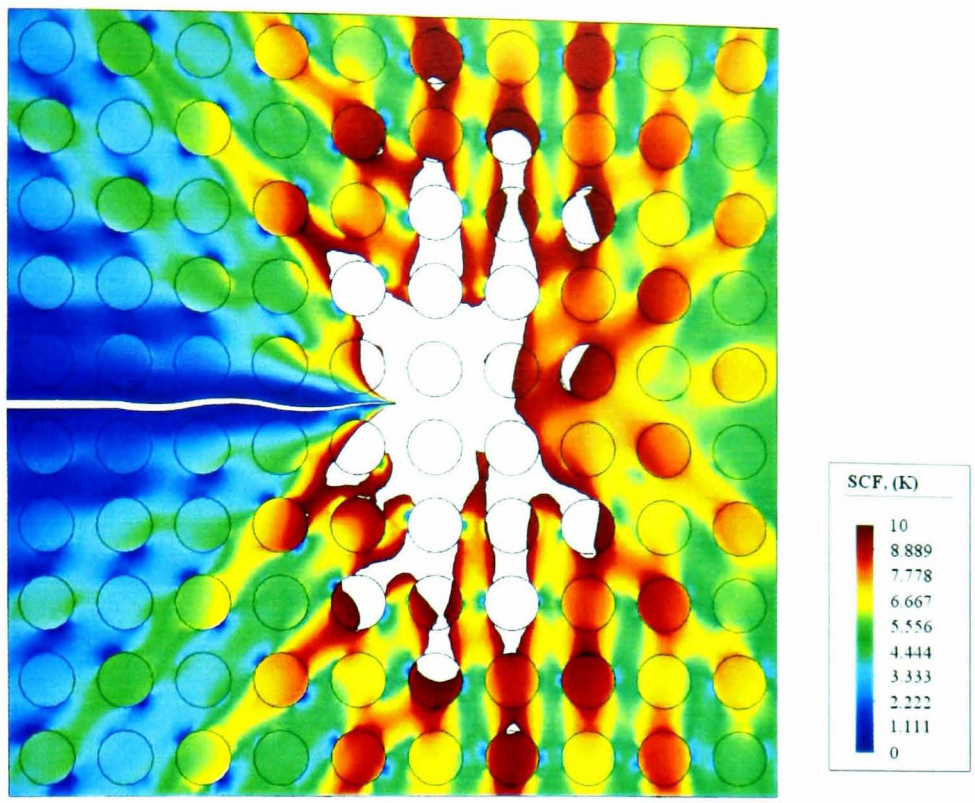

Figure 8.8 Contour plot indicating the variation of stress concentration (K), in the proximity of the primary crack, within a square (SQ) array of fibres. Results correspond to a three-phase composite. (Note: the white-coloured zone indicates a stress concentration above an arbitrarily chosen value of 10)

Figure 8.8 shows a contour plot of the variation of stress concentration (K) within the SQ embedded cell model with mixed fibre properties, as the crack propagates through the region. Comparing figure 8.3 (contour plot from a model whose geometric characteristics are the same, however, all the fibres have the same material properties, i.e. glass (Figure 8.3a) or carbon (Figure 8.3b)) with Figure 8.8, differences in the stress distribution are noticeable. As the all-glass and all-carbon models can be classed as the bounds to the problem, it is expected that the three-phase model would produce an intermediate result.

This is further confirmed when the associated crack tip energetics for the three-phase composite are compared to the previously analysed two-phase materials, see figure 8.9. The variation in G/G_o for the hybrid composite is similar in shape to the all-glass and all-carbon composites, yet the magnitude of the curve lies between the two bounds. For the hybrid composite the energetics of the crack tip decrease by approximately 38-52%,

compared to the unreinforced solid.

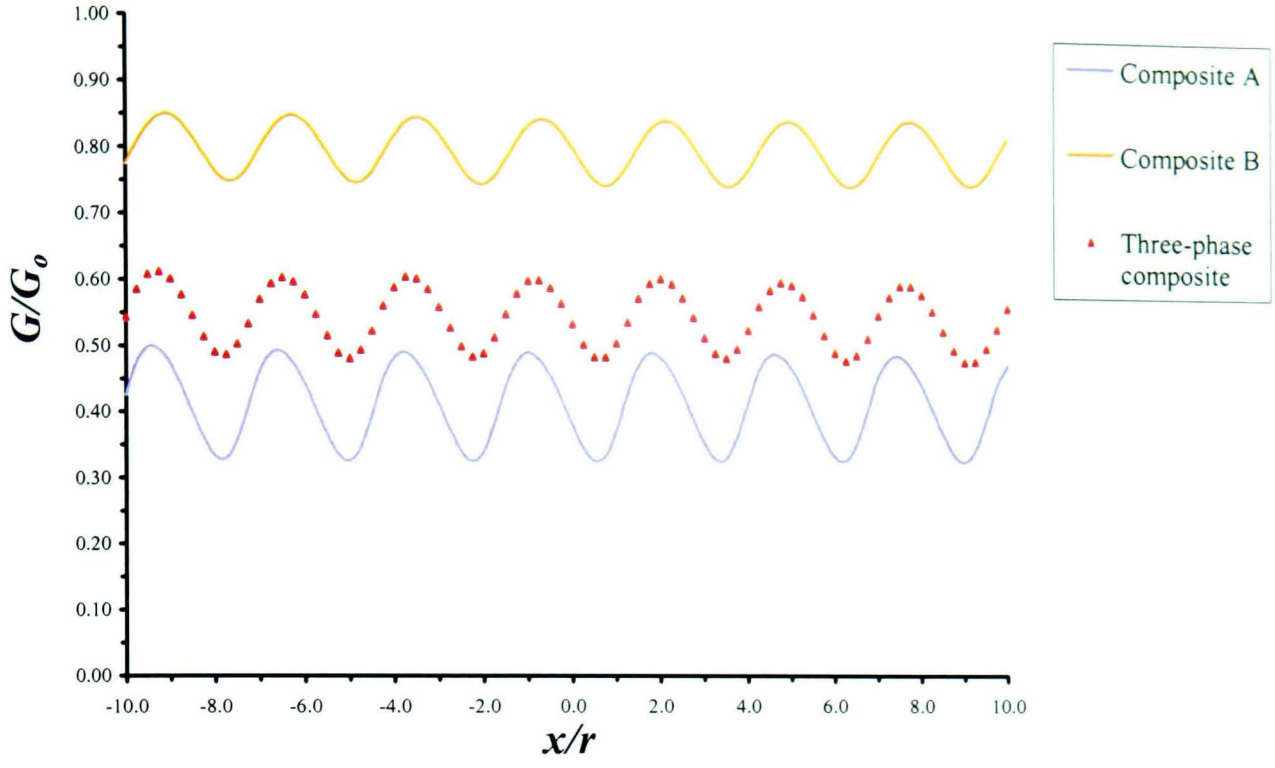

Figure 8.9 Effect of the constituent material properties on the non-dimensionalised energy release rate (G/G_o) of the primary crack.

8.3.2 Primary Crack Propagation with Microcracking

Most particulate or fibre-reinforced composites do not fail by propagation of a single macrocrack. Typically, these materials are capable of sustaining significant loads while multiple microcracks propagate. In concrete loaded in uniaxial tension or compression, acoustic emission analysis (*Maji et al. (1990)*) and X-ray microscopic observations (*Darwin and Dewey (1989)*) show that distributed microcracks and damage localisation exist in the material prior to failure. Distributed cracking is also observed in fibre composites (*Highsmith and Reifsnider (1982)*), which absorbs large amounts of energy, enhancing the toughness of the material.

In the following study, the effect of microcracking on the energetics of the primary crack will be considered. Note that the simulation of crack initiation is not possible within the

present BE code, therefore the locations of nucleated cracks will be based on the local stress field.

Effect of Matrix Microcracking on the Primary Crack Energetics

To analyse the effect of matrix microcracking, a model was constructed in which the primary crack propagates through a zone containing localised damage. The material combination and fibre arrangement employed within this simulation is composite A and a square (SQ) array, respectively. From observations of the stress field for composite A in a SQ array without microcracking (Figure 8.3a), it is apparent that the high stress region extends away from the crack tip along the neighbouring fibres parallel to the applied load. Therefore, it is reasonable to assume that within such regions microcracks could possibly nucleate. For the present simulation two microcracks are positioned within this high stress zone, symmetrically either side of the primary crack plane, in the ligament between the nearest and next nearest rows of fibres, as shown in Figure 8.10.

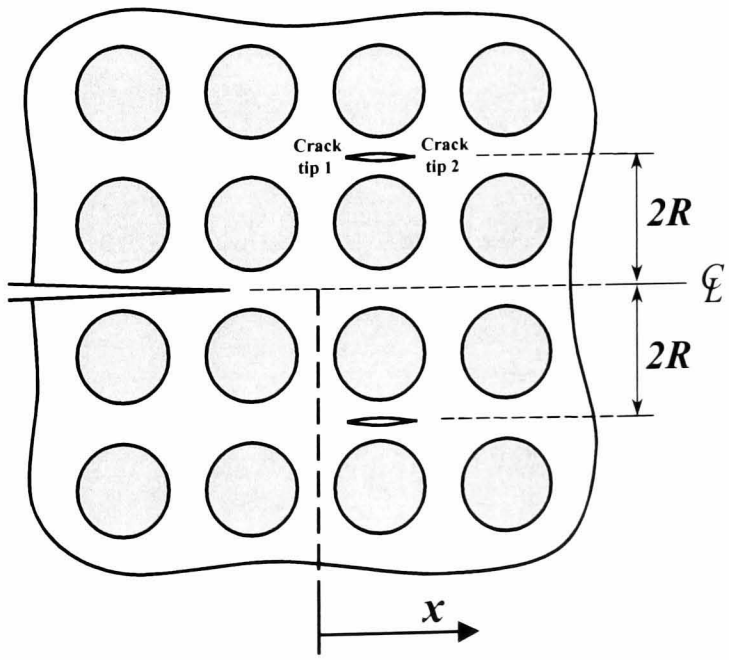

Figure 8.10 Microcrack configuration I – Two symmetrically positioned matrix cracks.

Figure 8.11 shows the variation in the nondimensionalised energy release rate, G/G_o, of the propagating primary crack for three different matrix microcrack lengths (c), i.e. c =

0.5r, r, and 2r. Note that the energy release rate, in this case, is nondimensionalised by dividing the value obtained in the presence of the microcracks (G) by the corresponding value in their absence (G_o).

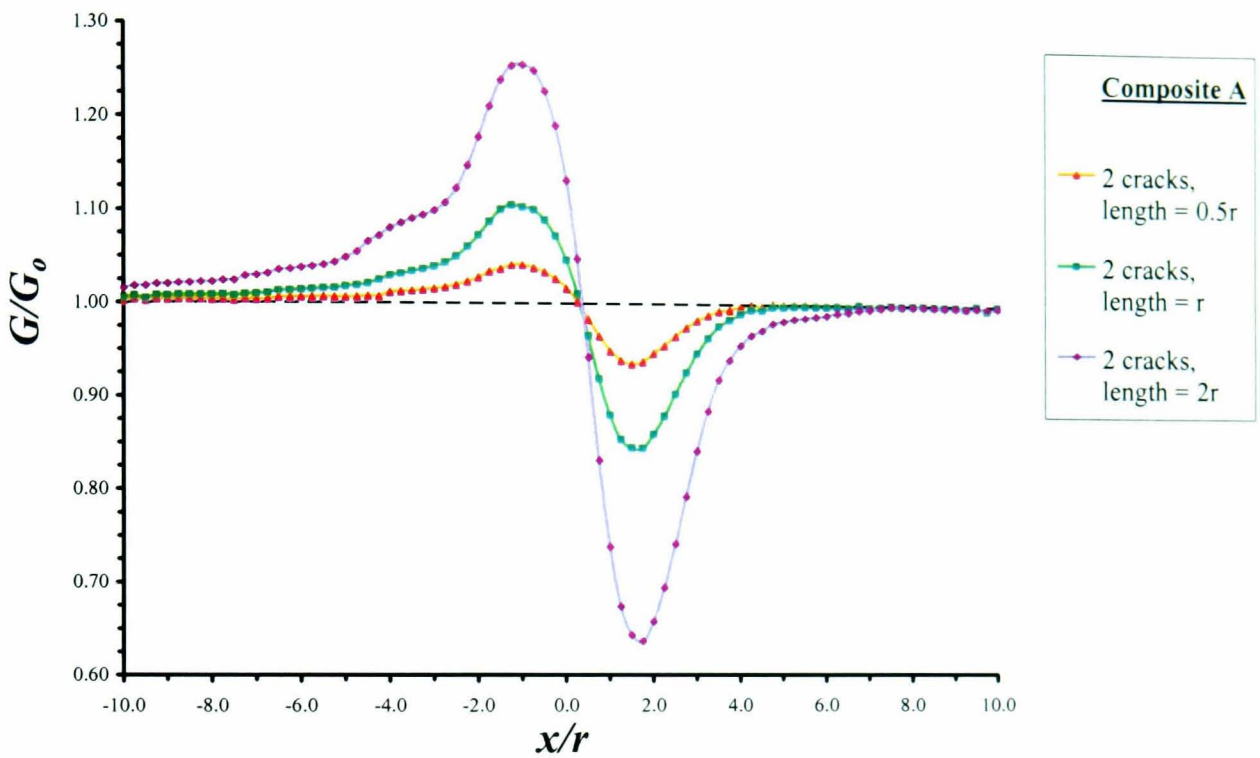

Figure 8.11 Effect of matrix microcracking on the nondimensionalised energy release rate (G/G_o) of the primary crack, (microcrack configuration I).

As the primary crack propagates towards the microcracks an apparent increase (or 'amplification') in the primary crack tip energetics is produced, as the crack 'senses' the presence of the damage zone ahead. However, as the crack enters the damage zone the energetics drop below unity, indicating a 'shielding' effect, which could impede or even arrest crack growth. Interestingly, the variation in G/G_o is similar to the result for an offset crack deflecting around an uncoated fibre (Section 7.3.1, Figure 7.5); however, the processes of amplification and shielding are in reverse order.

The size of the secondary cracks affects the strength of this amplification/shielding process, i.e. as the microcracks increase in length the primary crack becomes more influenced by their presence (Figure 8.11).

Effect of Fibre Microcracking on the Primary Crack Energetics

To analyse the effect of fibre microcracking, a corresponding model was constructed in which two fibres either side of the primary crack plane path are partially fractured, as shown in Figure 8.12.

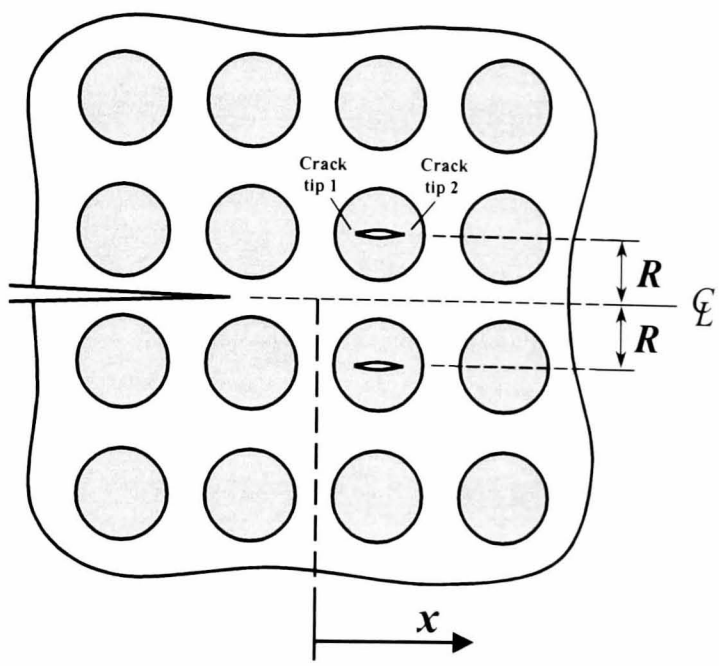

Figure 8.12 Microcrack configuration II – Two symmetrically positioned fibre cracks.

Figure 8.13 shows the variation in the nondimensionalised energy release rate, G/G_o, of the propagating primary crack as it bypasses the cracked fibres. Note that in the present simulation the fibre microcracks are both one fibre radius in length, i.e. $c = r$. Comparing the energetics for both geometric configurations, a similar trend is obtained. However, for the matrix microcracking model the magnitude of the amplification and shielding effect is approximately 10 and 5 times higher for the same microcrack length, respectively.

For both configurations the stress intensity factors (K_I) of the microcrack tips (see Figures 8.10 and 8.12) are plotted against the geometric location of the macrocrack tip, Figure 8.14. Note that as the models are symmetric about the crack plane, the stress intensity factors will be the same for each microcrack; hence results will only be taken from one of the microcracks. As the macrocrack approaches the matrix/fibre microcracks the stress

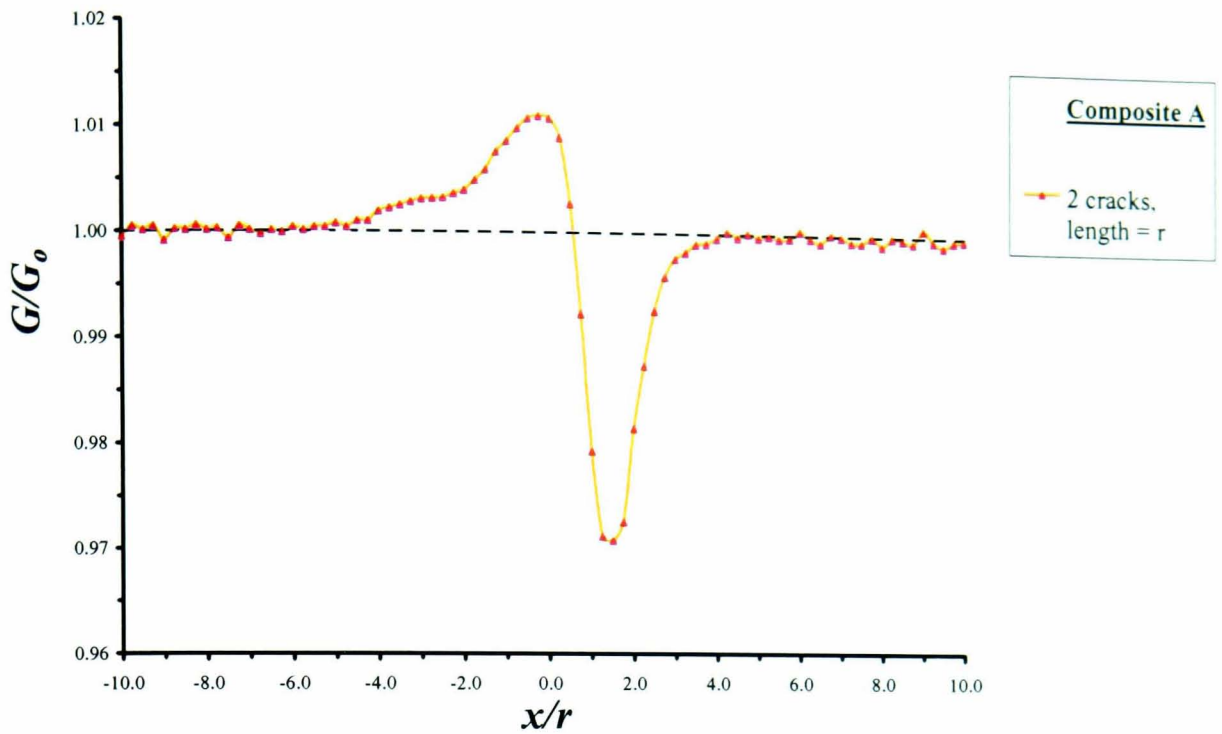

Figure 8.13 Effect of fibre microcracking on the nondimensionalised energy release rate (G/G_o) of the primary crack, (microcrack configuration II).

intensity factors increase, reaching a maximum value when the main crack is close to the leading microcrack tip. In the case of the matrix microcracking model, K_I grows at a relatively steady rate and reaches a maximum value of 16.9, whereas for the fibre microcracking model, K_I initially rises at a similar rate to the matrix microcrack configuration, however, when the main crack is within one fibre diameter the values increase substantially to a maximum of 42.5. For the same geometric location of the macrocrack tip, values obtained from the fibre microcrack model are between two and two and a half times those of the matrix microcracking configuration. Finally, as the macrocrack passes, the value of K_I quickly drops to zero.

Such a result would suggest that pre-existent fibre cracks ahead of the main crack would have a higher probability of growth than matrix cracks, assuming the materials have similar toughnesses. In the case of polymeric composites, the fibres generally have a lower toughness than the matrix; therefore the probability would increase still further.

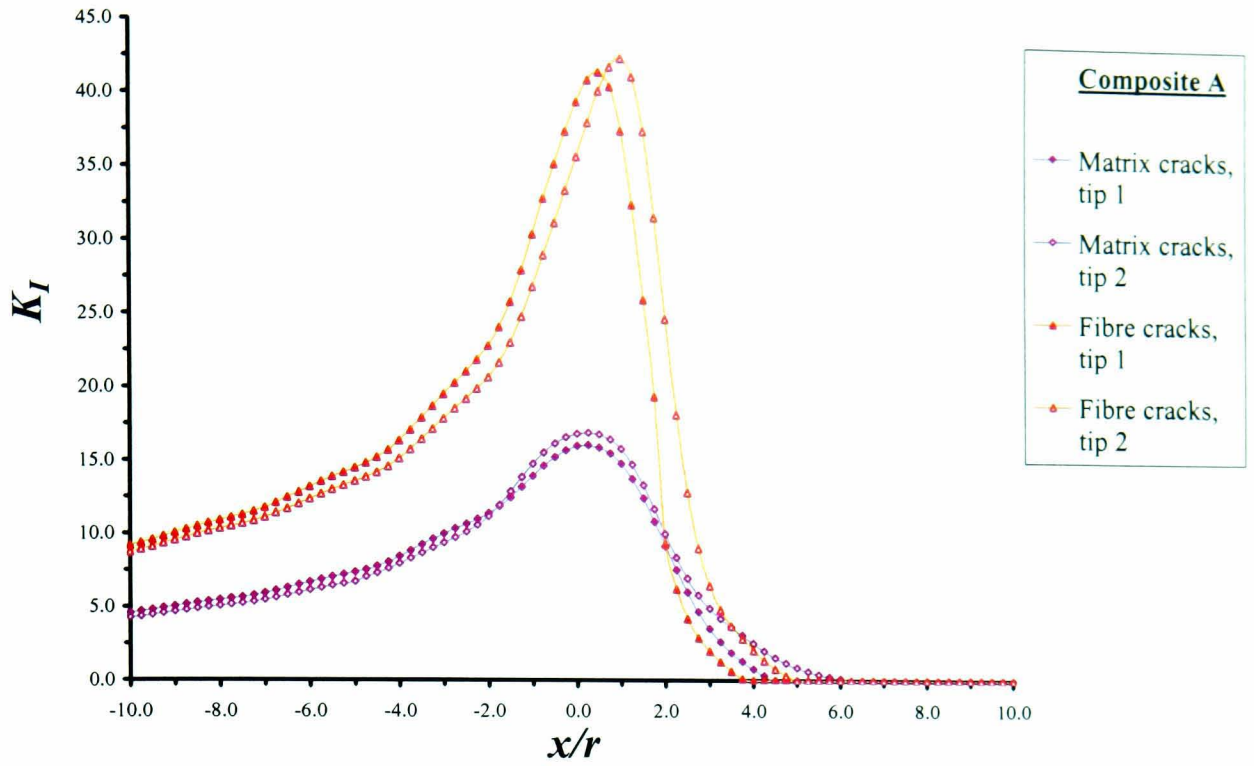

Figure 8.14 Effect of the propagating macrocrack on the stress intensity factors (K_I) of the matrix/fibre microcracks

8.4 Summary

In this study, the localised response of multi-fibre composites undergoing transverse failure by fracture is investigated using computational techniques. Crack tip energetics and local stress fields are examined for two typical composites, i.e. *Composite A* - glass fibres embedded in a polyester matrix, and *Composite B* - carbon fibres embedded in an epoxy resin, as well as a glass-carbon hybrid composite. Furthermore, the effect of secondary microcracking ahead of the main crack is also analysed.

The main results obtained from this study are:

- The local stress distribution calculated for both two-phase composites differ substantially, due primarily to the relative difference in the elastic modulus mismatch of the constituents. For the glass fibre composite, the modulus mismatch is relatively high (E_f / E_m = 38) and therefore the high stress regions link the neighbouring inclusions that stretch away from the crack tip. For the carbon fibre composite, the

mismatch is close to unity ($E_f/E_m = 2$), and therefore the high stress region closely resembles the plastic zone observed in monolithic materials.

- The existence of stiff fibres embedded in a more compliant matrix will increase the fracture toughness of the bulk material, as compared with a pure matrix, by lowering the energy release rate at the crack tip. Interestingly, this effect is more pronounced for the glass fibre composite, as the energetics of the crack tip decrease by approximately 50-70%, whereas for the carbon fibre composite the reduction is only by about 15-28%.

- In both two-phase composites, the effect of the fibre spatial distribution on the crack tip energetics is comparatively small; therefore, the constituent material properties can be considered to be the dominant factor controlling the crack tip energetics.

- The three-phase hybrid composite, consisting of a 50:50 mixture of glass and carbon fibres embedded in an epoxy matrix, exhibited an apparent intermediate fracture toughness value, compared to the all-glass and all-carbon models. The energetics of the macrocrack within the hybrid composite decreased by approximately 38-52%, compared to the unreinforced solid.

- The energetics of the macrocrack lowers as it enters a zone of localised damage (microcracking). The presence of microcracks relaxes the stress field, which can result in a significant reduction in the nondimensionalised energy release rate of the primary crack. The size of the microcracks affects the strength of this process, i.e. as the microcracks increase in length the primary crack becomes more influenced by their presence.

- For a composite with a relatively elastic moduli mismatch (glass fibre reinforced polyester), matrix microcracking influences the macrocrack energetics more so than fibre microcracking. However, pre-existent fibre cracks ahead of the main crack would have a higher probability of growth than matrix cracks, assuming the materials have similar toughnesses.

Chapter 9: Conclusions and Further Work

9.1 Thesis Overview

This thesis presents research into the micro-mechanical modelling of composite materials using numerical techniques. The material behaviour is examined on a microscopic scale, as the properties of interest, i.e. strength and toughness, are dependent on local phenomena. As discussed in **Chapter 2**, the strength and toughness of composite materials is not as well understood as the simpler elastic properties, because in many cases the modes of failure under a given system of external load are not predictable in advance. A composite can fail by one of a combination of often competing mechanisms, which includes debonding of the inclusion-matrix interface, microcracking within one or both of the phases, and fibre pull-out in the case of fibrous materials. The precise mode of failure depends on many factors such as the microstructure of the material, the properties of the constituents, the interfacial bond strength, the presence of microstructural defects, the stress state, and even environmental conditions.

Previous research in this field has typically involved specially designed experiments, theoretical/statistical studies, or the use of numerical techniques. For this research, advanced implementations of numerical methods in continuum mechanics, i.e. the boundary element and the finite element methods, are employed to gain a greater understanding of composite behaviour. The BE and FE approaches, which are presented in **Chapter 3**, are adopted through the utilisation of an in-house developed Boundary Element Analysis program and a commercial Finite Element Analysis software package (ANSYS), respectively. The advantage of using numerical methods, as opposed to experimental studies, is that the geometric and material characteristics can be investigated parametrically, in addition to the reduced time and expense involved. However, to model the complete behaviour of real composites is still not possible, due to

the degree of complexity and uncertainty involved in modelling the various mechanisms of damage and failure, and also due to the immense computational cost. Therefore, simplified models must be employed which are limited by their assumptions.

For the preliminary studies within this thesis (**Chapter 4**), geometrically simplified models, i.e. an isolated circular inclusion embedded within a remotely stressed solid, are presented. From these models a greater understanding of the influence of embedding second phase inclusions on the local stress fields is realised, for a range of controlling factors. For instance, the elastic material properties of the constituents and the bond strength between the materials can strongly affect the local stress concentrations, which play an important role in determining the strength of the composite. In addition, as analytical solutions are readily available for these problems, the accuracy and reliability of the numerical methods could be verified.

These models are then extended to accommodate additional phenomena, such as inclusion interaction, spatial inclusion arrangement, material formulation, i.e. consisting of two- and three-phases of various material properties. In **Chapter 5** the influence of multiple inclusions moving into close proximity with each other is demonstrated, using an aligned three-inclusion model. Stress distributions are calculated around an embedded inclusion that is affected by the presence of two further inclusions, one on either side. The parameters varied include the separation between the inclusions, the interfacial conditions between the phases, and the relative size and stiffnesses of the inclusions. Similar models have been developed using analytical and numerical methods, however are of less general applicability and the consideration of three phase (hybrid) composites has not been found in the literature.

In real composites the fibres are generally non-uniformly packed and the volume fraction of embedded inclusions is such that the application of the results from the previous models is limited. Therefore, to analyse the effect of spatial inclusion arrangement within a typical unidirectional fibre composite, an advanced numerical model is implemented

consisting of up to 60 inclusions embedded within a matrix material, as discussed in **Chapter 6**. A range of geometrical parameters and materials properties has been modelled with a view to designing composite materials with improved properties that are more closely optimised for the particular specification required.

The numerical simulations include several simple geometric arrangements, i.e. square and hexagonally arranged fibres. These models are then extended to accommodate random distributions, so that the effects of fibre clustering on the localised stress distributions could be investigated. In addition, a range of material combinations, i.e. relatively stiff or flexible fibres or a mixture of both, relative to the matrix, is considered. An embedded cell approach (ECA) is employed to apply far field loading and a statistical method, based on the Weibull distribution, has been used to describe the distribution of stress concentrations.

Uniaxial fibre reinforced composites generally have very good properties in the direction of the fibres, but in conventional multi-layer crossply it is cracking in the transverse direction which effectively limits the strength of a stress body. Therefore, in **Chapter 7** the interaction between a propagating crack and an isolated uncoated/coated elastic inclusion is analysed in terms of the localised crack deflection (toughening) mechanism. Studies of the interaction between cracks and inclusions has received much attention in previous years, however in most cases are based on the assumption of a given crack location and size, and/or a prescribed crack path which is known *a priori*, due to the symmetry of the particular problem. In the present investigation, crack growth processes can be modelled efficiently, without such restrictions, using the BE method.

Crack deflection/attraction mechanisms and their associated energy release rate variations are analysed for a range of controlling factors, with the aim of maximising the localised toughening effect. Furthermore, results are also obtained for both an uncoated and a coated inclusion whose coating thickness and elastic moduli ratio were parametrically varied.

Finally, the interaction between a propagating crack with multiple inclusions and microcracks is investigated in **Chapter 8**. This work extends that of the previous chapter and studies the effects of inclusion interaction and localised microcracking within a unidirectional composite, using the BE technique. Two typical composite materials, i.e. glass fibre reinforced polyester and carbon fibre reinforced epoxy, and also a glass-carbon hybrid composite are analysed. Crack tip energetics and local stress fields are considered, with emphasis on the toughening processes. Various authors have previously considered either crack propagation or microcracking in composite materials. However, numerical studies that have investigated their interaction are still lacking.

Through the development of the numerical models a more realistic representation of composite behaviour is achieved, which in turn, provides an improved knowledge of the factors that control strength and toughness. Such information is invaluable to composite material designers, who presently rely heavily on experimental studies to develop composite materials.

9.2 Summary of Main Conclusions

The list below shows the main conclusions drawn from this research:

- The numerical techniques employed within this thesis have shown their versatility and accuracy for the wide range of problems under consideration.
- The presence of a dissimilar second phase inclusion within an otherwise uniformly stressed elastic solid can significantly alter the local stress distributions. The degree of disturbance depends on the material properties of the phases and the interfacial bonding between them.
- Initial studies of inclusion interaction (three inclusion model) have highlighted significant differences in the local stress distributions as inclusions come into close proximity with each other. For rigid inclusions (fully bonded), the stresses within the inclusion interface closest to the neighbouring inclusion, and also

within the ligament, increase markedly as the inclusions move closer together. Conversely, for a three-phase system consisting of relatively stiff and compliant inclusions (fully bonded), the presence of the low modulus inclusion close to the high modulus inclusion dramatically reduces the local stress concentrations. The results from the three-phase material would seem to be beneficial, as microcracks, which often nucleate in and around inclusions, would have a lower probability of initiation, which in turn could lead to an improvement in the fracture strength of the bulk material. Furthermore, the relative size of interacting inclusions detrimentally affects the localised stress concentrations (fully bonded), and in certain circumstances can result in a complete loss of contact within 'shielded' inclusions (non-bonded). Hence, a low variation in inclusional size is recommended in the material design.

- Results from the multi-fibre embedded cell model, indicate that both the fibre packing and the material properties of the constituent phases have a significant effect on the overall stress distribution and the magnitude of localised stress concentrations within a composite. Non-periodic arrangements give rise to higher local stresses, and the magnitudes of these stress concentrations have a strong dependence on the ligament length (distance between the two neighbouring fibres that have a common high-stress region), and to a lesser extent on the angle relative to the applied load (angle between a plane containing the two fibre centres and the applied load). Furthermore, analysis of a three-phase composite, comprised of a mixture of both stiff and compliant fibres, had higher stress concentrations than the equivalent two-phase composites.

- Studies of the interaction between a propagating crack and an uncoated/coated inclusion indicate that the material properties of the phases could have a significant effect on the crack trajectory, and hence the energetics involved in the process of crack deflection are also dramatically altered. This opens up the possibility of enhancing the fracture toughness of fibre reinforced composite

materials by considering the Poisson's ratio of the individual phases when selecting the particular material combination, or by applying a compliant coating to the fibres.

- Finally, an investigation into the transverse fracture response of multi-fibre unidirectional composites has highlighted the importance of constituent material properties and the presence of microcracking on the toughness of multiphase materials. The elastic moduli mismatch of the phases dramatically alters the local stress distribution around a macrocrack and also the associated crack tip energetics. Localised damage (microcracking) ahead of the macrocrack relaxes the local stress field, which can result in a significant reduction in the strain energy of the primary crack. Matrix microcracking influences the macrocrack energetics more so than fibre microcracking. However, pre-existent fibre cracks ahead of the main crack would have a higher probability of growth than matrix cracks, assuming the materials have similar toughnesses.

9.3 Further Work

To further investigate the presented research, additional aspects would need to be considered. For instance, within the numerical models the constituent material properties are assumed to be elastic and isotropic. However, for many engineering composites, one or more of the constituents can undergo appreciable plastic deformation and can exhibit inherent anisotropy as a result of their crystal structure. To introduce plasticity and/or anisotropy within the BE method is not trivial and would involve extensive modifications to the BE code. For elastoplastic problems, domain discretisation would be necessary in the regions of plastic deformation, which in many cases is not known *a priori*. In addition, a rigorous load incrementation and iteration process would be required to obtain a reliable and accurate solution (*Becker (1992)*). While, for anisotropic problems the fundamental solutions are more complicated and implementation is rather computationally intensive (*Wrobel and Aliabadi (2002)*).

Presently, only two-dimensional (single or multiple continuous unidirectional fibres) or axisymmetric (single or multiple aligned spherical inclusions) models have been presented. However, a full three-dimensional simulation is required to consider composites reinforced by non-aligned short fibres or randomly arranged particles (e.g. *Böhm and Han (1999)*). Other aspects that could be investigated include the effect of residual stresses, which develop during the manufacturing process. BE analysis of residually stressed problems can be found in the literature (*Wrobel and Aliabadi (2002)*), however it is yet to be applied to composite materials. Furthermore, the influence of inclusion size/shape and interfacial debonding/cracking could also be considered.

Finally, specially designed experiments could be conducted to validate the results presented herein. However, careful attention would be needed to control the numerous variables, i.e. the inclusions size/shape, the bond strength between the phases, the processing residual stresses, the degree of plastic deformation under load or failure, and others.

References

Ableidinger, A. (2000), Some aspects of the fracture behaviour of metal foams, *Diploma Thesis, Vienna University of Technology, Vienna, Austria.*

Aboudi, J. (1989), Micromechanical analysis of composites by the method of cells, *Appl. Mech. Rev.*, **42**, 193-221.

Achenbach, J. D. and **Zhu, H.** (1989), Effect of interfacial zone on mechanical behaviour and failure of fibre-reinforced composites, *J. Mech. Phys. Sol.*, **37**, 381-393.

Adams, D. F. and **Doner, D. R.** (1967a), Longitudinal shear loading of a unidirectional composite, *J. Comp. Mater.*, **1**, 4-17.

Adams, D. F. and **Doner, D. R.** (1967b), Transverse normal loading of a unidirectional composite, *J. Comp. Mater.*, **1**, 152-164.

Agarwal, B. D. and **Broutman, L. J.** (1974), Three-dimensional finite element analysis of spherical particle composites, *Fibre Sci. Technol.*, **7**, 63-77.

Askeland, D. R. (1996), The Science and Engineering of Materials, *Chapman & Hall, London.*

Atkinson, C. (1972), The interaction between a crack and an inclusion, *Int. J. Eng. Sci.*, **10**, 127-136.

Axelsen, M. S. and **Pyrz, R.** (1995), Correlation between fracture toughness and the microstructure morphology in transversely loaded unidirectional composites, *IUTAM Symposium on Microstructure-Property Interactions in Composite Materials*, *Kluwer Academic Publishers*, 15-26.

Beaumont, P. W. R. (1988), The micromechanics of composite fracture, *Mat. Forum.*, 11, 332-340.

Becker, A. A. (1992), The Boundary Element Method in Engineering - A Complete

Course, *McGraw-Hill, London.*

Beer, J. P. and **Johnston, E. R. Jr.** (1992), Mechanics of Materials, 2nd Ed., *McGraw-Hill, London.*

Benvensite, Y. (1987), A new approach to the application of Mori-Tanaka's theory in composite materials, *Mech. Mater.*, **6**, 147-157.

Biswas, R., Henshall, J. L. and **Wakeman, R. J.** (1997), Finite-element modelling of elastic stress distributions in composite materials, *Mech. Compos. Mater. Struct.*, **4**, 233-249.

Blanford, G. E., Ingraffea, A. R. and **Liggett, J. A.** (1981), Two-dimensional stress intensity factor computations using the boundary element method, *Int. J. Num. Meth. Engng.*, **17**, 387-404.

Böhm, H. J. (2000), A short introduction to basic aspects of continuum micromechanics, *Course notes: Frontiers of Computational Micromechanics in Industry and Engineering, European Advanced Summer School, Galway, Ireland.*

Böhm, H. J. and **Han, W.** (1999), Comparison between three-dimensional and two-dimensional statistics-based unit cell models for particle reinforced MMCs, *CDL-FMD Report, Vienna University of Technology, Vienna, Austria.*

Bower, A. F. and **Ortiz, M.** (1991), A three-dimensional analysis of crack trapping and bridging by tough particles, *J. Mech. Phys. Solids.*, **39**, 815-858.

Brebbia, C. A., Telles, J. C. F. and **Wrobel, L. C.** (1984), Boundary Element Techniques - Theory and Applications in Engineering, *Springer-Verlag, Berlin.*

Budiansky, B. (1965), On the elastic moduli of some heterogeneous materials, *J. Mech. Phys. Solids*, **13**, 223-227.

Bush, M. B. (1997), The interaction between a crack and a particle cluster, *Int. J. Fract.*, **88**, 215-232.

Callister, W. D. Jr. (1994), Materials Science and Engineering: An Introduction, 3rd Ed.,

John Wiley & Sons, New York.

Chati, M. K. and **Mitra, A. K.** (1998), Prediction of elastic properties of fiber-reinforced unidirectional composites, *Engng. Anal. Bound. Elements*, **21**, 235-244.

Chen, C. H. and **Cheng, S.** (1967), Mechanical properties of fiber reinforced composites, *J. Comp. Mater.*, **1**, 30-41.

Chen, H. R., Yang, Q. S. and **Williams, F. W.** (1994), A self-consistent finite element approach to the inclusion problem, *Comput. Mater. Sci.*, **2**, 301-307.

Chen, H. S. and **Acrivos, A.** (1978), The solution of the equations of linear elasticity for an infinite region containing two spherical inclusions, *Int J. Solids Structures*, **14**, 331-348.

Chiang, C. R. (2000), Prediction of the fracture toughness of fibrous composites, *J. Mater. Sci.*, **35**, 3161-3166.

Chow, T. S. and **Hermans, J. J.** (1969), The elastic constants of fibre reinforced materials, *J. Comp. Mater.*, **3**, 382-396.

Christensen, R. M. (1979), Mechanics of Composite Materials, *John Wiley & Sons, New York.*

Christensen, R. M. (1990), A critical evaluation for a class of micro-mechanics models, *J. Mech. Phys. Solids*, **38**, 379-404.

Cook, J. and **Gordon, J. E.** (1964), A mechanism for the control of crack propagation in all-brittle systems, *Proc. R. Soc. London*, **A294**, 519-534.

Cook, R. D. (1995), Finite Element Modeling for Stress Analysis, *John Wiley & Sons, New York.*

Crouch, S. L. (1976), Solution of plane elasticity problems by the displacement discontinuity method, *Int. J. Num. Meth. Engng.*, **10**, 301-342.

Cruse, T. A. (1977), Mathematical foundations of the boundary integral equation method in solid mechanics, *Pratt & Whitney Aircraft Report*, AFSOR- TR-77-1002.

Dandekar, B. W. and **Conant, R. J.** (1992), Numerical analysis of elastic contact problems using the boundary integral equation method - Part II: Results, *Int. J. Numer. Methods Eng.*, **33**, 1523-1535.

Darwin, D. and **Dewey, G. R.** (1989), Image analysis of microcracks, *Cracking and Damage – Eds. J. Mazars and Z. P. Bažant, Elsevier Appl. Science Pub.*, 65-77.

De Lacerda, L.A. and **Wrobel, L.C.** (2000), Frictional contact analysis of coated axisymmetric bodies using the boundary element method, *J. Strain Anal.*, **35**, 423-440.

De Lacerda, L. A. and **Wrobel, L. C.** (2001). Dual boundary element method for axisymmetric crack analysis, *Int. J. Fract.*, **113**, 267-284.

Dong, M. and **Schmauder, S.** (1996), Modelling of metal matrix composites by a self-consistent embedded cell model, *Acta Mater.*, **44**, 2465-2478.

Drugan, J. and **Willis, J. R.** (1996), A micromechanics-based nonlocal constitutive equation and estimates of representative volume element size for elastic composites, *J. Mech. Phys. Sol.*, **44**, 497-524.

Eischen, J. W. and **Torquato, S.** (1993), Determining elastic behaviour of composites by the boundary element method, *J. Appl. Phys.*, **74**, 159-170.

Erdogan, F., Gupta, G. D. and **Ratwani, M.** (1974), Interaction between a circular inclusion and an arbitrarily oriented crack, *J. Appl. Mech.*, **41**, 1007-1013.

Eshelby, J. D. (1957), The determination of the field of an ellipsoidal inclusion and related problems, *Proc. R. Soc. London*, **A241**, 376-396.

Faber, K. T. and **Evans, A. G.** (1983), Crack deflection process - Part I: Theory, *Acta Metall.*, **31**, 565-576.

Foye, R. L. (1966), An evaluation of various engineering estimates of the transverse properties of unidirectional composites, *Proceedings of the 10th National SAMPE Symposium –Advanced Fibrous Reinforced Composites*, 60-67.

Gallagher, R. H. (1978), A review of finite element techniques in fracture mechanics, *Proceedings of the First Conference on Numerical Methods in Fracture Mechanics, University college of Swansea,* 1-25.

Gao, H. and **Rice, J. R.** (1989), A first-order perturbation analysis of crack trapping by arrays of obstacles, *J. Appl. Mech.*, **56**, 828-836.

Goodier, J. N. (1933), Concentration of stress around spherical and cylindrical inclusions and flaws, *J. Appl. Mech.*, **55**, 39-44.

Goree, J. G. (1967), In-plane loading in an elastic matrix containing two cylindrical inclusions, *J. Comp. Mater.*, **1**, 404-412.

Guild, F. J. and **Young, R. J.** (1989), A predictive model for particulate-filled composite materials - Part I, hard particles, *J. Mater. Sci.*, **24**, 298-306.

Gusev, A. A. (1997), Representative volume element size for elastic composites: A numerical study, *J. Mech. Phys. Sol.*, **45**, 1449-1459.

Halpin, J. C. and **Tsai, S. W.** (1967), Environmental factors in composite design, *Air Force Materials Laboratory Technical Report*, AFML-TR-67-423.

Hashin, Z. (1962), The elastic moduli of heterogeneous materials, *J. Appl. Mech.*, **29**, 143-150.

Hashin, Z. and **Rosen, B. W.** (1964), The elastic moduli of fiber-reinforced materials, *J. Appl. Mech.*, **31**, 223-232.

Hashin, Z. and **Shtrikman, S.** (1963), A variational approach to the theory of the elastic behaviour of multiphase materials, *J. Mech. Phys. Solids*, **11**, 127-140.

He, M. Y., Evans, A. G. and **Curtin, W. A.** (1993), The ultimate tensile strength of metal and ceramic matrix composites, *Acta Metall.*, **41**, 871-878.

Hershey, A. V. (1954*), Elasticity of isotropic aggregate of anisotropic cubic crystals, J. Appl. Mech.*, **21**, 236-240.

Highsmith, A. L. and **Reifsnider, K. L.** (1982), Stiffness reduction mechanisms in

composite laminates, *Damage in Composite Materials, ASTM-STP 115 – Ed. K. L. Reifsnider.*

Hill, R. (1965), A self-consistent mechanics of composite materials, *J. Mech. Phys. Solids*, **13**, 213-222.

Hornsby, P. R. and **Premphet, K.** (1997), Fracture toughness of multiphase polypropylene composites containing rubbery and particulate inclusions, *J. Mater. Sci.*, **32**, 4767-4775.

Hornsby, P. R. and **Premphet, K.** (1998), Influence of phase microstructure on the mechanical properties of ternary phase polypropylene composites, *J. Appl. Polym. Sci.*, **70**, 587-597.

Hull, D. and **Clyne, T. W.** (1996), An introduction to composite materials, 2nd Ed., *Cambridge University Press, Cambridge.*

Hwu, C., Liang, Y. K. and **Yen, W. Y.** (1995), Interactions between inclusions and various types of cracks, *Int. J. Fract.*, **73**, 301-323.

Hyer, M. W. (1998), Stress analysis of fiber-reinforced composite materials, *McGraw-Hill, London.*

Ingraffea, A. R., Blandford, G. E. and **Ligget, J. A.** (1983), Automatic modelling of mixed-mode fatigue and quasi-static crack propagation using the boundary element method, *Proceeding of Fracture Mechanics: Fourteenth Symposium, ASTM STP 791,* I407-I426.

Irwin, G. R. (1957), Analysis of stresses and strains near the end of a crack transverseing a plate, *J. Appl. Mech*, **24**, 361-364.

Jones, M. C. L. (1981), Failure mechanisms in filament wound composites, *PhD Thesis, University of Liverpool, Liverpool, UK.*

Jones, R. M. (1999), Mechanics of Composite Materials, *2nd Ed., Taylor & Francis, Inc.*

Kassam, Z. H. A., Zhang, R. J. and **Wang, Z.** (1995), Finite elements simulation to

investigate interaction between crack and particulate reinforcements in metal-matrix composites, *Mater. Sci. Eng.*, **A203**, 286-299.

Keer, L. M., **Dundurs, J.** and **Kiattikomol, K.** (1973), Separation of a smooth circular inclusion from a matrix, *Int. J. Engng Sci.*, **11**, 1221-1233.

Kelly, A. (1994), Concise Encyclopaedia of Composite Materials, *Pregamon Press, London.*

Kelly, P., **Hills, D. A.** and **Nowell, D.** (1994), Curved interface cracks between elastically dissimilar media, with application to the analysis of circular inclusions, *Int. J. Mech. Sci.*, **36**, 173-181.

Kim, B. –N., **Watanabe, M.**, **Enoki, M.** and **Kishi, T.** (1998), Simulation of fracture behaviour in particle-dispersed ceramic composites, *Eng. Fract. Mech.*, **59**, 289-303.

Knight, M. G., **de Lacerda, L. A.**, **Wrobel, L. C.** and **Henshall, J. L.** (2002a), Parametric study of the contact stresses around spherical and cylindrical inclusions, *Comput. Mater. Sci.*, **25**, 115-121.

Knight, M. G., **de Lacerda, L. A.**, **Wrobel, L. C.** and **Henshall, J. L.** (2002b), A parametric study of inclusion interaction in particulate- and fibre-reinforced materials using the boundary element technique, *J. Strain Anal.*, **37**, 47-58.

Knight, M. G., **Wrobel, L. C.** and **Henshall, J. L.** (2002c), Micromechanical response of fibre-reinforced materials using the boundary element technique, *Submitted for publication.*

Knight, M. G., **de Lacerda, L. A.**, **Wrobel, L. C.** and **Henshall, J. L.** (2002d), A study of the interaction between a propagating crack and an uncoated/coated elastic inclusion using the BE technique, *Int. J. Fract.*, **114**, 47-61.

Kocer, C. and **Collins, R. E.** (1998), The angle of hertzian cone cracks, *J. Am. Ceram. Soc.*, **81**, 1736-1742.

Krock, R. H. (1963), Effect of composition and dispersed-phase particle-size

distribution on the static elastic moduli of tungsten-copper composite materials, *ASTM Proc.*, **63**, 605-612.

Kröner, E. (1958), Calculation of the elastic constants of a polycrystalline material from the elastic constants of the single crystal, *Z. Physik*, **151**, 504-518.

Lange, F. F. (1970), The interaction of a crack front with a second-phase dispersion, *Phil. Mag.*, **22**, 983-992.

Lee, H. C. and **Gurland, J.** (1978), Hardness and deformation of cemented tungsten carbide, *Mater. Sci. Eng.*, **33**, 125-133.

Leggoe, J. W., Hu, X. Z. and **Bush, M. B.** (1996), Crack tip damage development and crack growth resistance in particulate reinforced metal matrix composites, *Eng. Fract. Mech.*, **53**, 873-895.

Li, R. and **Chudnovsky, A.** (1993a), Variation of the energy release rate as a crack approaches and passes through an elastic inclusion, *Int. J. Fract.*, **59**, R69-R74.

Li, R. and **Chudnovsky, A.** (1993b), Energy analysis of crack interaction with an elastic inclusion, *Int. J. Fract.*, **63**, 247-261.

Lipetzky, P. and **Knesl, Z.** (1995), Crack-particle interaction in two-phase composites: Part II - Crack deflection, *Int. J. Fract.*, **73**, 81-92.

Lipetzky, P. and **Schmauder, S.** (1994), Crack-particle interaction in two-phase composites: Part I - Particle shape effects, *Int. J. Fract.*, **65**, 345-358.

Liu, S. H. and **Nauman, E. B.** (1990), On the micromechanics of composites containing spherical inclusions, *J. Mater. Sci.*, **25**, 2071-2076.

Love, A. E. H. (1944), A treatise on the mathematical theory of elasticity, *Dover, New York.*

Lu, S. and **Zhang, R.** (1995), A finite-element analysis of toughening and reinforcing effects on particle-filled materials, *Acta Mechanica Sinica*, **27**, 619-623.

Maji, A. K., Ouyang, C. and **Shah, S. P.** (1990), Fracture mechanics of quasi-brittle

materials based on acoustic emission, *J. Mater. Res.*, **5**, 206-217.

Man, K. W. (1994), Contact mechanics using boundary elements, *Comp. Mech. Publ., Southampton.*

Matthews, F. L. and Rawlings, R. D. (1994), Composite Materials: Engineering and Science, *Chapman & Hall, London.*

McMeeking, R. M. and **Evans, A. G.** (1982), Mechanics of transformation-toughening in brittle materials, *J. Am. Ceram. Soc.*, **65**, 242-246.

Meguid, S. A. and **Wang, X. D.** (2000), An elastodynamic analysis of interacting inhomogeneities in advanced composites, *Mech. Mater.*, **32**, 797-805.

Mikata, Y. and **Taya, M.** (1985), Stress field in and around a coated short fiber in an infinite matrix subjected to uniaxial and biaxial loadings, *J. Appl. Mech.*, **52**, 19-24.

Mishnaevsky, L., Dong, M., Hönle, S. and **Schmauder, S.** (1999), Computational mesomechanics of particle-reinforced composites, *Comp. Mater. Sci.*, **16**, 133-143.

Miyata, N., Akada, S., Omura, H., and **Jinno, H.** (1992), Microcrack toughening mechanism in brittle matrix composites, *Fract. Mech. Ceram.*, **9**, 339-355.

Monaghan, J. and **Brazil, D.** (1997), Modelling the sub-surface damage associated with the machining of a particle reinforced MMC, *Comput. Mater. Sci.*, **9**, 99-107.

Mori, T. and **Tanaka, K.** (1973), Average stress in matrix and average elastic energy of materials with misfitting inclusions, *Acta Metall.*, **21**, 571-574.

Mottram, J. T. and **Shaw, C. T.** (1996), Using Finite Elements in Mechanical Design, *McGraw-Hill, London.*

Muskhelishvili, N. I. (1977), Some basic problems of the mathematical theory of elasticity, 4th Ed., *Noordhoff Int. Publ., Leyden.*

Nakamura, T. and **Suresh, S.** (1993), Effects of thermal residual stresses and fibre packing on deformation of metal-matrix composites, *Acta Metall. Mater.*, **41**, 1665-1681.

Nandy, M. -O, Schmauder, S., Kim, B. –N., Watanabe, M. and **Kishi, T.** (1999), Simulation of crack propagation in alumina particle-dispersed SiC composites, *J. Euro. Ceram. Soc.*, **19**, 329-334.

Nisitani, H., Saimoto, A. and **Noguchi, H.** (1990), Versatile method of analysis of two-dimensional elastic problem by body force method, *Trans. Jpn. Soc. Mech. Eng.*, **A56**, 2123-2129.

Park, Y. H., Becker, A. A. and **Fenner, R. T.** (1995), Contact mechanics analysis of frictional slip of inclusions embedded in dissimilar matrices using the boundary element method, *J. Strain Anal.*, **30**, 245-966.

Paul, B. (1960), Prediction of elastic constants of multiphase materials, *Trans. Metall. Soc. AIME*, **218**, 36-41.

Pijaudier-Cabot, G. and **Bažant, Z. P.** (1991), Cracks interacting with particles or fibres in composite materials, *J. Engng. Mech.*, **117**, 1611-1630.

Portela, A. (1993), Dual Boundary Element Analysis of Crack Growth, *Comp. Mech. Publ., Southampton.*

Portela, A., Aliabadi, M. H. and **Rooke, D. P.** (1993), Dual boundary element incremental analysis of crack propagation, *Comput. Struct.*, **46**, 237-247.

Press, W. H., Teukolsky, S. A., Vetterling, W. T. and **Flannery, B. P.** (1992), Numerical Recipes in Fortran, *Cambridge University Press, Cambridge.*

Prewo, K. M. and **Krieder, K. R.** (1972), Transverse tensile properties of boron fibre reinforced aluminium matrix composites, *Metall. Trans.*, **3**, 2201-2211.

Ramakrishnan, N., Kumar, A. M. and **Radhakrishna Bhat, B. V.** (1996), A generalised plane strain technique for estimating effective properties of particulate metal matrix composites using FEM, *J. Mater. Sci.*, **31**, 3507-3512.

Reuss, A. (1929), Calculation of the flow limits of mixed crystals on the basis of the plasticity of mono-crystals, *Z. Angew. Math. Mech.*, **9**, 49-58.

Rosen, B. W. (1965), Mechanics of composite strengthening, *Fibre Composite Materials. ASM: Metals Park, Ohio.*

Rowlands, R. E. (1985), Strength (failure) theories and their experimental correlation, *in Handbook of Composites, Vol 3. - Failure Mechanics of Composites*, 71-125.

Saad, Y. and **Schultz, M. H.** (1986), GMRES: a generalized minimal residual algorithm for solving non-symmetric linear systems, *SIAM J. Sci. Stat. Comput.*, **7**, 856-869.

Sautter, M., Dietrich, C., Poech, M. H., Schmauder, S. and **Fischmeister, H.** (1993), Finite element modelling of a transverse-loaded fibre composite: Effects of section size and net density, *Comput. Mater. Sci.*, **1**, 225-233.

Sendeckyj, G. P. (1974), Interaction of cracks with rigid inclusions in longitudinal shear deformation, *Int. J. Fract.*, **10**, 45-52.

Shelley, J. F. and **Yu, Y. Y.** (1966), The effect of two rigid sperical inclusions on the stresses in an infinite elastic solid, *J. Appl. Mech.*, **33**, 68-74.

Snyder, M. D. and **Cruse, T. A.** (1975), Boundary integral equation analysis of cracked anisotropic plates, *Int. J. Fract.*, **11**, 315-328.

Somigliana, C. (1885), Sopra l'equilibrio di un corpo elastico isotropo, *Il Nuovo Ciemento*, 17-20.

Stippes, M., Wilson, H. B. Jr. and **Krull, F. N.** (1962), A contact stress problem for a smooth disk in an infinite plate, *Proc. Fourth US National Congress of Appl. Mech.*, 799-806.

Swenson, D. V. and **Ingraffea, A. R.** (1988), Modelling mixed-mode dynamic crack propagation using finite elements: theory and application, *Comput. Mech.*, **3**, 381-397.

Tamate, O. (1968), The effect of a circular inclusion on the stresses around a line crack in a sheet under tension, *Int. J. Fract.*, **4**, 257-265.

Tsai, S. W. (1965), Strength characteristics of composite materials, *NASA CR-224.*

Tsai, S. W. and **Wu, E. M.** (1971), A general theory of strength for anisotropic materials, *J. Comp. Mater.*, **5**, 58-80.

Voigt, W. (1889), Über die beziehung zwischen den beiden elasticitätsconstanten isotroper körper, *Ann. Phys. (Leipzig)*, **38**, 573-587.

Vörös, G. and **Pukánszky, B.** (2001), Effect of a soft interlayer with changing properties on the stress distribution around inclusions and yielding of composites, *Composites: Part A – Applied Science and Manufacturing*, **32**, 343-352.

Walpole, L. J. (1966), On the bounds for the overall elastic moduli of inhomogeneous systems - Part I, *J. Mech. Phys. Solids*, **14**, 151-162.

Weibull, W. (1951), A statistical distribution function of wide applicability, *J. Appl. Mech.*, **18**, 293-297.

Wells, J. K. and **Beaumont, P. W. R.** (1985), Debonding and pull-out processes in fibrous composites, *J. Mater. Sci.*, **20**, 1275-1284.

Weng, G. J. (1990), The theoretical connection between Mori-Tanaka's theory and the Hashin-Shtrikman-Walpole bounds, *Int. J. Engng Sci.*, **28**, 1111-1120.

Whitney, J. M. and **Riley, M. B.** (1966), Elastic properties of fiber reinforced composite materials, *AIAA J.*, **4**, 1537-1542.

Willis, J. R. (1977), Bounds and self-consistent estimates for the overall properties of anisotropic composites, *J. Mech. Phys. Solids*, **25**, 185-202.

Wilson, H.B. Jr. and **Goree, J. G.** (1967), Axisymmetric contact stresses about a smooth elastic sphere in an infinite solid stressed uniformly at infinity, *J. Appl. Mech.*, **34**, 960-966.

Wolfenden, A. and **Wolla, J. M.** (1989), Mechanical damping and dynamic modulus measurements in alumina and tungsten fibre reinforced aluminium, *J. Mater. Sci.*, **24**, 3205-3212.

Wrobel, L. C. and **Aliabadi, M. H.** (2002), The Boundary Element Method, *John Wiley*

& Sons, Chichester.

Wulf, J., Steinkopff, T. and **Fischmeister, H.** (1996), FE-simulation of crack paths in the real microstructure of an Al(6061)/SiC composite, *Acta Mater.*, **44**, 1765-1779.

Xiao, Z. M. and **Chen, B. J.** (2001), Stress intensity factor for a Griffith crack interacting with a coated inclusion, *Int. J. Fract.*, **108**, 193-205.

Yu, I. W. and **Sendeckyj, G. P.** (1974), Multiple circular inclusion problems in plane elastostatics, *J. Appl. Mech.*, **41**, 215-221.

Zweben, C. and **Rosen, B. W.** (1970), A statistical theory of material strength with application to composite materials, *J. Mech. Phys. Sol.*, **18**, 189-206.

Appendix A: Two-Dimensional and Axisymmetric Fundamental Solutions

The fundamental solution (Eq. 3.9) is based on the three-dimensional classical solution of a point force in an infinite medium called the *Kelvin solution*. However, by considering the point load as a line load or as a ring load, the two-dimensional and axisymmetric fundamental solutions can be obtained.

Two-Dimensional Formulation

- *Displacement kernels* for plane strain conditions, expressed in tensor notation:

$$U_{ij}(p,Q)=\frac{1}{8\pi\mu(1-\upsilon)}\left[(3-4\upsilon)\ln\left[\frac{1}{r(p,Q)}\right]\delta_{ij}+\frac{\partial r(p,Q)}{\partial x_i}\frac{\partial r(p,Q)}{\partial x_j}\right]$$

- *Traction kernels* for plane strain conditions, expressed in tensor notation:

$$T_{ij}(p,Q)=\frac{-1}{4\pi(1-\upsilon)r(p,Q)}\left[\frac{\partial r(p,Q)}{\partial n}\right]\left[(1-2\upsilon)\delta_{ij}+2\frac{\partial r(p,Q)}{\partial x_i}\frac{\partial r(p,Q)}{\partial x_j}\right]$$

$$+\frac{1-2\upsilon}{4\pi(1-\upsilon)r(p,Q)}\left[\frac{\partial r(p,Q)}{\partial x_j}n_i-\frac{\partial r(p,Q)}{\partial x_i}n_j\right]$$

The plane strain expressions are valid for plane stress if υ is replaced by $\frac{\upsilon}{1+\upsilon}$.

Axisymmetric Formulation

- *Displacement kernels*, expressed in terms of elliptic integrals:

$$U_{rr}(p,Q)=\frac{A}{R_p r_Q^2 C}\left[(3-4\upsilon)\left(R_p^2+r_Q^2\right)+4(1-\upsilon)\left(Z_p-z_Q\right)^2\right]K\left(m,\frac{\pi}{2}\right)$$

$$+\frac{A}{R_p r_Q^2 C}\left[-C^2(3-4\upsilon)-\frac{B\left(Z_p-z_Q\right)^2}{D}\right]E\left(m,\frac{\pi}{2}\right)$$

$$U_{rz}(p,Q)=\frac{A\left(Z_p-z_Q\right)}{R_p C}\left[K\left(m,\frac{\pi}{2}\right)-\frac{H}{D}E\left(m,\frac{\pi}{2}\right)\right]$$

$$U_{zr}(p,Q)=\frac{A\left(Z_p-z_Q\right)}{r_Q C}\left[-K\left(m,\frac{\pi}{2}\right)+\frac{F}{D}E\left(m,\frac{\pi}{2}\right)\right]$$

$$U_{zz}(p,Q)=\frac{2A}{C}\left[(3-4\upsilon)K\left(m,\frac{\pi}{2}\right)+\frac{\left(Z_p-z_Q\right)^2}{D}E\left(m,\frac{\pi}{2}\right)\right]$$

The constants A, B, C, D, F and H are defined as follows:

$$A=\frac{1}{16\pi^2\mu(1-\upsilon)} \qquad D=\left(R_p-r_Q\right)^2+\left(Z_p-z_Q\right)^2$$

$$B=R_p^2+r_Q^2+\left(Z_p-z_Q\right)^2 \qquad F=R_p^2-r_Q^2+\left(Z_p-z_Q\right)^2$$

$$C=\sqrt{\left(R_p+r_Q\right)^2+\left(Z_p-z_Q\right)^2} \qquad H=r_Q^2-R_p^2+\left(Z_p-z_Q\right)^2$$

- *Traction kernels*, expressed in terms of elliptic integrals:

$$T_{rr}(p,Q)=2\mu\left[T_1 n_r+T_2 n_z\right]$$

$$T_{rz}(p,Q)=2\mu\left[T_3 n_r+T_4 n_z\right]$$

$$T_{zr}(p,Q)=2\mu\left[T_5 n_r+T_6 n_z\right]$$

$$T_{zz}(p,Q)=2\mu\left[T_7 n_r+T_8 n_z\right]$$

where the components T_1 to T_8 are defined as follows:

$$T_1=\frac{A}{R_p r_Q^2 C}\left[2\upsilon M-\frac{3}{2}N+\frac{BF\left(Z_p-z_Q\right)^2}{2DC^2}\right]K\left(m,\frac{\pi}{2}\right)$$

$$+\frac{A}{R_p r_Q^2 C}\left[\frac{-2\upsilon}{D}\left[R_p^2 S+\left(Z_p-z_Q\right)^2 V+r_Q^4\right]+\frac{3}{D}\left[R_p^2 F+\left(Z_p-z_Q\right)^2 M\right]\right.$$

$$\left.-\frac{2B^2F}{D^2C^2}\left(Z_p-z_Q\right)^2\right]E\left(m,\frac{\pi}{2}\right)$$

$$T_2=\frac{A\left(Z_p-z_Q\right)}{R_p r_Q CD}\left[D\left(2\upsilon-3\right)+\frac{B}{C^2}\left(Z_p-z_Q\right)^2\right]K\left(m,\frac{\pi}{2}\right)$$

$$+\frac{A\left(Z_p-z_Q\right)}{R_p r_Q CD}\left[3\left(Z_p-z_Q\right)^2-B\left(2\upsilon-3\right)-\frac{4B}{DC^2}\left(Z_p-z_Q\right)^2\right]E\left(m,\frac{\pi}{2}\right)$$

$$T_3=T_2$$

$$T_4=\frac{A}{R_p CD}\left[-D\left(1-2\upsilon\right)+\frac{H}{C^2}\left(Z_p-z_Q\right)^2\right]K\left(m,\frac{\pi}{2}\right)$$

$$+\frac{A}{R_p CD}\left[-\left(Z_p-z_Q\right)^2+H\left(1-2\upsilon\right)-\frac{8FR_p^2}{DC^2}\left(Z_p-z_Q\right)^2\right]E\left(m,\frac{\pi}{2}\right)$$

$$T_5=\frac{A\left(Z_p-z_Q\right)}{CD}\left[\frac{D}{r_Q^2}+\frac{2}{C^2}\left(Z_p-z_Q\right)^2\right]K\left(m,\frac{\pi}{2}\right)$$

$$+\frac{A\left(Z_p-z_Q\right)}{CD}\left[4\left(1+\upsilon\right)-\frac{B}{r_Q^2}-\frac{8B}{DC^2}\left(Z_p-z_Q\right)^2\right]E\left(m,\frac{\pi}{2}\right)$$

$$T_6=\frac{A}{r_Q CD}\left[-D\left(1-2\upsilon\right)-\frac{F}{C^2}\left(Z_p-z_Q\right)^2\right]K\left(m,\frac{\pi}{2}\right)$$

$$+\frac{A}{r_Q CD}\left[-3\left(Z_p-z_Q\right)^2+F\left(1-2\upsilon\right)+\frac{4BF}{DC^2}\left(Z_p-z_Q\right)^2\right]E\left(m,\frac{\pi}{2}\right)$$

$$T_7=T_6$$

$$T_8=\frac{2A\left(Z_p-z_Q\right)}{CD}\left[\frac{-1}{C^2}\left(Z_p-z_Q\right)^2\right]K\left(m,\frac{\pi}{2}\right)$$

$$+\frac{2A\left(Z_p - z_Q\right)}{CD}\left[\left(1-2\upsilon\right)+\frac{4B}{DC^2}\left(Z_p - z_Q\right)^2\right]E\left(m,\frac{\pi}{2}\right)$$

The constants M, N, S and V are defined as follows:

$$M = 2R_p^2 + r_Q^2 + 2\left(Z_p - z_Q\right)^2 \qquad S = 2R_p^2 - 3r_Q^2 + 4\left(Z_p - z_Q\right)^2$$

$$N = 2R_p^2 + 3\left(Z_p - z_Q\right)^2 \qquad V = 3r_Q^2 + 2\left(Z_p - z_Q\right)^2$$